Institut für Erd- und Umweltwissenschaften

Mathematisch-Naturwissenschaftliche Fakultät

Universität Potsdam

The Role of Wind and Water in Shaping Earth's Plateaus

Kumulative Dissertation
zur Erlangung des akademischen
Grades "doctor rerum naturalium"
in der Wissenschaftsdisziplin Geologie

eingereicht an der
Mathematisch-Naturwissenschaftlichen Fakultät
der Universität Potsdam

von
Alexander Rohrmann

Potsdam, Januar 2015

Published online at the
Institutional Repository of the University of Potsdam:
URN urn:nbn:de:kobv:517-opus4-77938
http://nbn-resolving.de/urn:nbn:de:kobv:517-opus4-77938

Erklärung

Hiermit erkläre ich, dass ich die Dissertation “The Role of Wind and Water in Shaping Earth’s Plateaus” selbstständig angefertig und keine anderen, als die von mir angegebenen Quellen und Hifsmittel verwendet habe.

Ich erkläre weiterhin, dass die Dissertation bisher nicht in dieser oder anderer Form in einem anderen Prüfungsverfahren vorgelegt wurde.

Potsdam, 27. Januar 2015

Alexander Rohrmann

Acknowledgements

I am deeply thankful to so many people that helped, supported, and encouraged me to write this dissertation.

Foremost, I would like to thank my doctoral adviser Prof. Manfred Strecker, who enabled me to work on this fascinating research topic. His continuous support, constructive criticism, and seemingly endless time for proofreading were invaluable. Thank you, for the confidence you placed in me, the freedom to follow up on my ideas, and the patience you had with me. I would like to thank Dr. Dirk Sachse and Prof. Dr. Andreas Mulch, who had an important part in this dissertation. Thank you both for your time and effort, your guidance during sample preparation and analysis, and your ideas and suggestions for the manuscripts. Especially, I would like to thank Prof. Paul Kapp and Prof. Richard Herrmance as they continued to place their trust in me and took me to China for field work. A special thanks to my colleague Heiko Pingel, who helped me in so many different ways during the last years. Thanks for your many suggestions and comments and sharing all the emotions during this time. It has been a pleasure to work with you. Many thanks to all my additional co-authors: Prof. Dr. Bodo Bookhagen, Taylor Schildgen, Prof. Dr. Ricardo Alonso, Dr. Cai Fulong and Dr. Carolina Montero. Furthermore, I would like to thank Anne Bernhardt, Andy Wickert, Dr. Rasmus Thiede, and Dr. Wolfgang Schwanghart for proofreading my dissertation. Thanks to Tanja Klaka-Tauscher for all the help with administrative tasks and proofreading, and to all the members of the Paleohydrology Group for your help and support in the lab. I would also like to acknowledge all my office buddies during this time: Euan Mcaulay, Alejandro Bande, Franziska Scheffler, Jonathan Engelhardt and Saswati Sarkar. You were great!

I would like to take this opportunity to thank my parents Helma and Eckhard Rohrmann for their endless and unimaginable support throughout all my education and young carreer as a scientist. I would like to thank my brothers Carsten, Sebastian and Stefan Rohrmann. I cannot thank my family enough for your love and care. Andrea, I don't find the words that would express my gratefulness towards your contribution to the thesis and my life!

Contents

Chapter 5 – Discussion, outlook and conclusion

List of Figures

List of Tables

Abstract

The overarching goal of this dissertation is to provide a better understanding of the role of wind and water in shaping Earth's Cenozoic orogenic plateaus - prominent high-elevation, low relief sectors in the interior of Cenozoic mountain belts. In particular, the feedbacks between surface uplift, the build-up of topography and ensuing changes in precipitation, erosion, and vegetation patterns are addressed in light of past and future climate change. Regionally, the study focuses on the two world's largest plateaus, the Altiplano-Puna Plateau of the Andes and Tibetan Plateau, both characterized by average elevations of >4 km. Both plateaus feature high, deeply incised flanks with pronounced gradients in rainfall, vegetation, hydrology, and surface processes. These characteristics are rooted in the role of plateaus to act as efficient orographic barriers to rainfall and to force changes in atmospheric flow.

The thesis examines the complex topics of tectonic and climatic forcing of the surface-process regime on three different spatial and temporal scales: (1) bedrock wind-erosion rates are quantified in the arid Qaidam Basin of NW Tibet over millennial timescales using cosmogenic radionuclide dating; (2) present-day stable isotope composition in rainfall is examined across the south-central Andes in three transects between 22° S and 28° S; these data are modeled and assessed with remotely sensed rainfall data of the Tropical Rainfall Measuring Mission and the Moderate Resolution Imaging Spectroradiometer; (3) finally, a 2.5-km-long Mio-Pliocene sedimentary record of the intermontane Angastaco Basin (25°45' S, 66°00' W) is presented in the context of hydrogen and carbon compositions of molecular lipid biomarker, and oxygen and carbon isotopes obtained from pedogenic carbonates; these records are compared to other environmental proxies, including hydrated volcanic glass shards from volcanic ashes intercalated in the sedimentary strata.

There are few quantitative estimates of eolian bedrock-removal rates from arid, low relief landscapes. Wind-erosion rates from the western Qaidam Basin based on cosmogenic ^{10}Be measurements document erosion rates between 0.05 to 0.4 mm/yr. This finding indicates that in arid environments with strong winds, hyperaridity, exposure of friable strata, and ongoing rock deformation

and uplift, wind erosion can outpace fluvial erosion. Large eroded sediment volumes within the Qaidam Basin and coeval dust deposition on the Chinese Loess plateau, exemplify the importance of dust production within arid plateau environments for marine and terrestrial depositional processes, but also health issues and fertilization of soils.

In the south-central Andes, the analysis of 234 stream-water samples for oxygen and hydrogen reveals that areas experiencing deep convective storms do not show the commonly observed patterns of isotopic fractionation and the expected co-varying relationships between oxygen and hydrogen with increasing elevation. These convective storms are formed over semi-arid intermontane basins in the transition between the broken foreland of the Sierras Pampeanas, the Eastern Cordillera, and the Puna Plateau in the interior of the orogen. Here, convective rainfall dominates the precipitation budget and no systematic stable isotope-elevation relationship exists. Regions to the north, in the transition between the broken foreland and the Subandean foreland fold-and-thrust belt, the impact of convection is subdued, with lower degrees of storminess and a stronger expected isotope-elevation relationship. This finding of present-day fractionation trends of meteoric water is of great importance for paleoenvironmental studies in attempts to use stable isotope relationships in the reconstruction of paleoelevations.

The third part of the thesis focuses on the paleohydrological characteristics of the Mio-Pliocene (10-2 Ma) Angastaco Basin sedimentary record, which reveals far-reaching environmental changes during Andean uplift and orographic barrier formation. A precipitation- evapotranspiration record identifies the onset of a precipitation regime related to the South American Low Level Jet at this latitude after 9 Ma. Humid foreland conditions existed until 7 Ma, followed by orographic barrier uplift to the east of the present-day Angastaco Basin. This was superseded by rapid (~0.5 Myr) aridification in an intermontane basin, highlighting the effects of eastward-directed deformation. A transition in vegetation cover from a humid C3 forest ecosystem to semi-arid C4-dominated vegetation was coeval with continued basin uplift to modern elevations.

Zusammenfassung

Das übergreifende Ziel dieser Dissertation ist es, ein besseres Verständnis des Einflusses von Wind und Wasser auf die Entstehung orogener Plateaus im Känozoikum zu erlangen. Orogene Plateaus sind hochgelegene, durch geringes Relief und oft endorheische Entwässerung charakterisierte trockene Hochgebirgsregionen. In dieser Arbeit wird vor allem die Rückkopplung zwischen tektonischer Hebung, dem Aufbau von Relief und den daraus resultierenden Veränderungen des Niederschlags, der Erosion und variierenden Vegetationsmustern im Zusammenhang mit vergangenen und zukünftigen Klimaveränderungen untersucht. Der regionale Fokus dieser Arbeit liegt auf den zwei größten Plateaus der Erde, das Altiplano-Puna-Plateau in den Anden und das Tibet Plateau. Beide besitzen eine durchschnittliche Höhe von > 4 km. Als effiziente orographische Barrieren und „Heizflächen“ beeinflussen Plateaus großräumig die atmosphärische Zirkulation und bewirken somit ausgeprägte Gradienten in Niederschlag, Vegetation, Hydrologie und Oberflächenprozessen.

Vor diesem Hintergrund untersucht diese Arbeit das komplexe Zusammenspiel zwischen Tektonik und Klima und damit verbundene Auswirkungen auf Erdoberflächenprozesse auf drei verschiedenen zeitlichen und räumlichen Skalen: (1) die Quantifizierung von Wind-Erosionsraten im Festgestein des ariden Qaidam-Beckens von Nordwest-Tibet mittels kosmogener Nukliddatierungen über Zeiräume von mehreren 10^3 Jahren; (2) die heutige Isotopenzusammensetzung von Niederschläge wird entlang von drei Transekten über die Südzentralanden zwischen 22° und 28° S ermittelt; diese Daten werden modelliert und der Niederschlag mit satellitenbasierten Fernerkundungsdaten der Tropical Rainfall Measuring Mission und des Moderate Resolution Imaging Spectroradiometer ausgewertet; (3) eine 2,5 km mächtige mio-pliozäne Sedimentabfolge des intermontanen Angastaco-Beckens (25°45’ S, 66°00’ W) wird auf die Wasserstoff- und Kohlenstoffzusammensetzungen von molekularen Blattwachsen und hinsichtlich der Sauerstoff- und Kohlenstoffisotopie von Bodenkarbonaten untersucht; diese Datensätze werden mit anderen Umweltindikatoren verglichen, u.a. mit hydratisierten Gläsern vulkanischer Aschen, die in der Sedimentabfolge aufgeschlossen sind.

Es gibt nur wenige quantitative Abschätzungen von Winderosionsraten im Festgestein arider Gebiete mit geringem Relief. Kosmogene ^{10}Be-Messungen im westlichen Qaidam-Becken dokumentieren Erosionsraten zwischen 0,05 bis 0,4 mm/a. Diese Resultate zeigen, dass in ariden Gebieten mit hohen Windgeschwindigkeiten, leicht erodierbaren Gesteinen und andauernder Deformation und Hebung, Wind-Erosionsprozesse die Denudationsraten der fluvialen Erosion bei weitem übersteigen kann. Das große Volumen erodierter Gesteine im Qaidam-Becken und die gleichzeitige Lössablagerung im chinesischen Löss-Plateau veranschaulichen die wichtige Rolle der äolischen Sedimentproduktion in ariden Plateaugebieten und unterstreichen deren Bedeutung für marine und terrestrische Ablagerungsprozesse sowie Nährstoffeinträge in Böden und respiratorische Gesundheitsprobleme.

Die Analyse der Sauerstoff- und Wasserstoffisotopie von 234 Flusswasserproben aus den Südzentralanden belegt, dass Gebiete mit starken konvektiven meteorologischen Ereignissen nicht die erwarteten Isotopenmuster zwischen der Abnahme der Isotopie und der Höhe aufweisen. Diese konvektiven Ereignisse werden über semiariden intermontanen Becken in der Übergangszone zwischen dem zerbrochenen Vorland der Sierras Pampeanas, der Ostkordillere und dem Puna-Plateau im Inneren des Orogens gebildet. Konvektiver Niederschlag dominiert hier den Niederschlagshaushalt und eliminiert jegliche systematische Beziehung zwischen der Isotopie und der Höhe. In den nördlichen Regionen, - in der Übergangszone zwischen dem zerbrochenen Vorland und dem subandinen Falten- und Überschiebungsgürtel, verringert sich der Einfluss konvektiver Niederschläge und hydrometeorologische Extremereignisse gegenüber den orographischen bedingten Niederschlagsmechanismen. Dieser Unterschied wirkt sich in einer besseren Beziehung zwischen Isotopenverhältnissen und Höhe aus. Eine bessere Kenntnis der meteorologischen Einflüsse auf die Wasserisotopie sind der Schlüssel für zukünftige Paläoumweltstudien und zukünftige Bestrebungen, mit Hilfe der Trends in der Isotopie meteorischer Wässer das vertikale Wachstum von Gebirgen zu quantifizieren.

Der dritte Teil der Arbeit behandelt die Isotopenverhältnisse in Blattwachsen und daraus abgeleitete paläohydrologische Eigenschaften des

Anagastaco-Beckens im Mio-Pliozän (10-2 Ma), welche weitreichende Umweltveränderungen während der Hebung der Anden und der Bildung von orografischen Barrieren im Vorland aufzeigen. Als Proxies für Niederschlag und Evapotranspiration dokumentieren Isotopenverhältnisse in Blattwachsen, Bodenkarbonaten und vulkanischen Gläsern den Beginn eines Niederschlagsystems in diesem Teil der Anden, welches durch feuchtebringende Winde des South American Low Level Jet ab 9 Ma etabliert war. Humide Bedingungen existierten bis 7 Ma im Vorland, gefolgt von einer Bildung einer orografischen Barriere im Osten des heutigen Angastaco-Beckens. Als Folge dieser Hebung folgte eine rasche Aridifikation (innerhalb ~0,5 Ma) des nun intermontanen Angastaco-Beckens. Ein Wechsel von einem feuchten C3-Wald-Ökosystem zu semiariden Umweltbedingungen mit einer C4-dominierten Vegetationsdecke vollzog sich gleichzeitig mit der fortlaufenden Hebung des Beckens auf heutige Höhen.

Chapter 1

Introduction

1.1 General background / framework

Earth's orogenic plateaus, elevated low-relief regions in the interior of Cenozoic mountain belts, have always impressed researchers, explorers and naturalists, including Alexander von Humboldt (1808), Walther Penck (1920), Isaiah Bowman (1924), and Heinrich Harrer (1952), to name just a few. Heinrich Harrer, one of the earliest western explorers visiting the Tibetan Plateau, marveled at the sheer endlessness and low-relief plateau landscape:

> "Die Landschaft, durch die wir seit Tagen zogen, war von eigenartiger Schönheit. Weite Ebenen wechselten ab mit hügeligem Gelände und kleinen Pässen, und oft mußten wir durch eiskalte, reißende Bäche waten. [...] Schon lange hatten wir keine Gletscher mehr gesehen, doch als wir uns dem Tasamhaus von Barka näherten, lag eine ganze Kette im Sonnenlicht strahlend da." (Harrer, 1952)

Alexander von Humboldt was moved by the freedom offered by this pristine plateau landscape while he was traveling through the Andes:

> "Auf den Bergen ist Freiheit! Der Hauch der Grüfte
> Steigt nicht hinauf in die reinen Lüfte;
> Die Welt ist vollkommen überall,
> Wo der Mensch nicht hinkommt mit seiner Qual." (Humboldt, 1808)

As part of the ongoing quest for natural resources in orogenic settings, and more than two hundred years after Humboldt's expedition, humans have begun seizing these last vast, virtually untouched areas the planet has to offer and settled on and around all major plateaus. This has fundamentally impacted a very fragile natural environment, which is characterized by pronounced topographic and climatic gradients along the plateau flanks, and low-relief environments with generally low rates of geomorphic processes within the plateau interiors (e.g.,

Strecker et al., 2007; Molnar et al., 2010). Typically, plateaus such as the Tibetan, Anatolian or Andean plateaus are rather dry environments, whereas their flanks are often humid, especially if the orientation of the plateau flanks is perpendicular to moisture-bearing air masses that impinge on their flanks. Changes in plateau landscapes and the processes that shape them are societally relevant. Numerous inhabitants of Asia and South America are increasingly dependent on the water supply provided through runoff by major streams draining the plateau margins for irrigation, energy production, and human consumption (e.g., Immerzeel, 2010; Bookhagen and Burbank, 2010; Viviroli et al., 2011; Hoorn et al., 2010; 2013). These are very important aspects with immediate consequences for humans, but another, equally relevant issue associated with plateaus is the generation of dust particles by erosive processes in these environments, their long-distance transport, and air pollution. This topic has been gaining increased attention in recent years and is rooted in the plateaus' arid interiors that affect faraway regions. Conversely, the influence of soot from distant industrial centers can affect human health across plateaus. This is a major problem for humans that was recently recognized and that might significantly impact the well-being of mountain communities (Beniston, 2003; Kurosaki and Mikami; 2003; Kurosaki et al., 2011; Indoitu et al., 2012). Indeed, the *Intergovernmental Panel on Climate Change (IPCC)* Fourth Assessment (2007) identifies dust and aerosol emission from arid landscapes and water availability in plateau regions as key effects of future climate change that will strongly affect the socio-economic state and future prosperity of humankind (IPCC, 2007; Immerzeel, 2010;) (Fig. 1.1). In this context, the scientific community would like to be able to predict how continued global warming will enhance glacial melting and runoff to major streams, including those draining the Tibetan and Altiplano-Puna plateaus (Fig. 1.1). A warmer climate might change the seasonality of snowfall and snowmelt, potentially causing severe consequences for hydropower generation, water management, and communities due to flooding. The impact of dust and aerosols on future climate change and the role of variations of solar radiation, and thus the potential of a negative feedback on global air temperatures, is highly debated in this context (IPCC, 2007; Seinfeld and Pandis, 2012). Even though the feedback mechanism between the amount of aerosols

and dust in the atmosphere and their impact on lowering global air temperatures is known, climate simulations concerning future dust production amounts and atmospheric concentrations are still fraught with many problems (e.g., Stier et al., 2005; Mahowald et al., 2011; Dufresne et al., 2013). Furthermore, as future climate is expected to warm and aridity in arid core regions and climatic threshold areas is projected to increase, vegetation cover will be reduced.

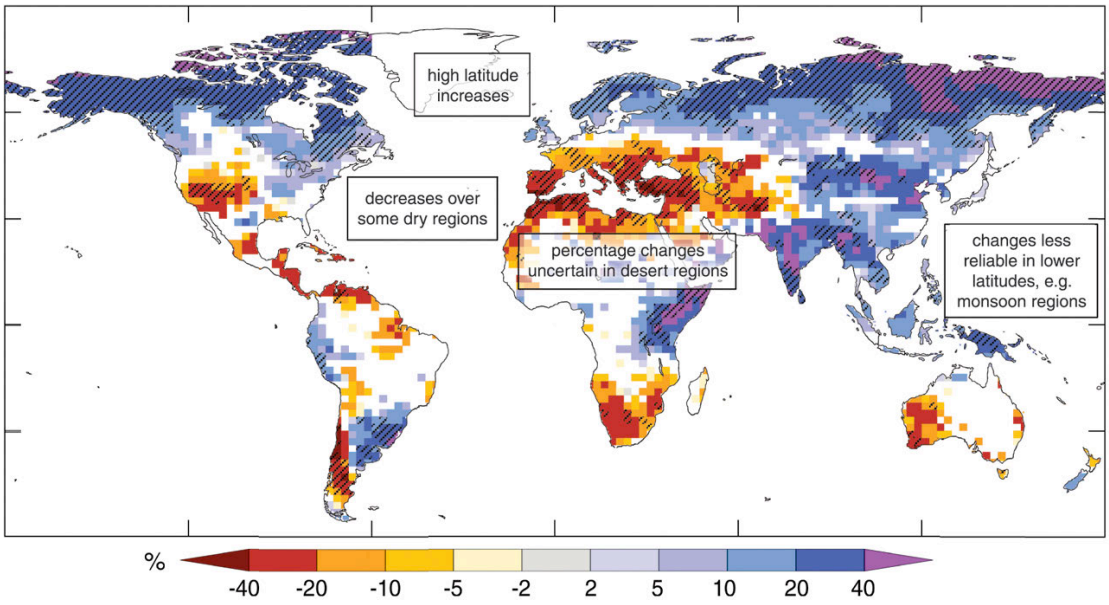

Figure 1.1. Projections and model consistency of relative changes in runoff by the end of the 21st century. Large-scale relative changes in annual runoff (water availability, in percent) for the period 2090-2099, relative to 1980-1999. Values represent the median of 12 climate models using the SRES A1B scenario. White areas are where less than 66% of the 12 models agree on the sign of change and hatched areas are where more than 90% of models agree on the sign of change. The quality of the simulation of the observed large-scale 20th century runoff is used as a basis for selecting the 12 models from the multi-model ensemble. The global map of annual runoff illustrates a large scale and is not intended to refer to smaller temporal and spatial scales. In areas where rainfall and runoff is very low (e.g. desert areas), small changes in runoff can lead to large percentage changes. In some regions, the sign of projected changes in runoff differs from recently observed trends. In some areas with projected increases in runoff, different seasonal effects are expected, such as increased wet season runoff and decreased dry season runoff. Studies using results from few climate models can be considerably different from the results presented here. Figure and figure caption is taken from the IPCC Fourth Assessment Report, Climate Change 2007 (AR4 Synthesis Report, p. 49).

This will lead to more wind erosion and dust emissions, but the impact of hydro-meteorological extreme events and their impact on pulsed erosion is also expected to be exacerbated (Shao et al., 2011; Marticorena, 2014). Dust production and emission continued to be poorly understood and are viewed as a passive response to an ecological response to climate change because missing vegetation covers leaves soil and ground barren and thus susceptible to deflation (e.g., Washington et al., 2006; Cowie et al., 2013).

Often, different characteristics of plateau environments, such as rainfall amount, erosion, vegetation, hydrologic aspects, and their associated landforms, are studied independently of each other, without integrating different forcing factors that might impact these environments (Owen et al., 2006; Dong et al., 2012; Zhang et al., 2012; Yao and Liu, 2014). Previous studies have focused either on landforms, processes, and the overall geologic characterization of humid plateau flanks or on the arid plateau interiors. In addition, some of these studies are limited, because they have not integrated present-day processes and environmental characteristics with past processes that were inferred from proxy indicators in geological archives (e.g., Sun et al., 2008; Duvall et al., 2012; Canavan et al., 2014). *It is here, at the intersection between present-day characteristics of plateau regions and processes in the geological past that are recorded in various proxy indicators, where the research design of this thesis attempts to bridge the gap between different spatial and temporal scales.* The chosen approach addresses the impact of plateaus on hydrologic characteristics and erosional processes from a geological, geomorphic, and isotope geochemical perspective. By using this approach, the study furnishes new information for a unifying view across different plateau environments and their impact on environmental evolution. Against this background, the erosion processes of the flanks of the Tibetan Plateau are analyzed and the characteristics of extreme climate gradients from humid to arid environments across the Altiplano-Puna Plateau of South America are studied with respect to water stable isotopes. The windward flanks of the latter environment receive between 2000 and 6000 mm/year of rainfall, whereas the leeward sides receive less than 100 mm/yr (e.g., Bookhagen and Strecker, 2008; Garreaud et al., 2009). The erosion rates,

vegetation, and hydrology of both plateau environments mimic the pronounced gradients in rainfall (Strecker et al., 2007; Bookhagen and Burbank, 2010; Bookhagen and Strecker, 2012). In turn, the evolution of these gradients through time is recorded in the sedimentary record of the plateau basins and intermontane basins that straddle the plateau flanks (e.g., Jordan and Alonso, 1987; Schemmel et al., 2013; Garzione et al., 2014; Hoke et al., 2014; Schildgen et al., 2014). Knowledge of these extreme climate and surface-process gradients and the plateau's control on the flow of atmospheric circulation in blocking and re-routing air masses is still at an early stage, as is knowledge of associated impacts on erosional processes and thus landscape evolution of plateau margins (Strecker et al., 2007; Bookhagen and Strecker, 2012; Kirby and Whipple, 2012; Gasparini and Whipple, 2014). Especially the feedback processes between tectonic build-up of topography and ensuing changes in precipitation, erosion, vegetation, and the hydrological cycle, are still largely unresolved and subject to ongoing debate (e.g., Whipple and Meade, 2006; Whipple, 2009; Bookhagen and Burbank, 2010; Thiede and Ehlers, 2013; Whipple and Gasparini, 2014). To capture the complex spatiotemporal evolution of rainfall gradients during plateau growth and to better understand the competing influences of eolian vs. fluvial processes in high-mountain environments, this thesis presents investigations of processes that span timescales from years to millions of years. Performing research over more than six orders of magnitude in timescales requires a wide array of methodologies from different fields, such as stable-isotope geochemistry, organic geochemistry of n-alkane leaf-waxes, cosmogenic nuclide dating, geological mapping, and structural and basin analysis, and each of these will be employed to add to the broader picture of plateau feedbacks an evolution.

1.2 Geological setting of the Tibetan and Altiplano-Puna plateaus

There are several definitions of the term plateau. In its most basic form a plateau is defined as "a large flat area of land that is high above sea level" (Cambridge Dictionary, 2014). By this very loose definition, more than 40 percent of the Earth's surface can be classified in terms of plateaus regions. This is unrealistic and underscores the necessity to better characterize plateau environments and their morphotectonic evolution, their forcing of rainfall distribution, amount, and their impact on the evolution of flora and fauna (e.g., Molnar et al., 2010; Hoorn et al., 2010 and 2013; Baker et al., 2014) (Fig. 1.2).

Although plateaus are also found in extensional environments, such as in East Africa (e.g., Wichura et al., 2010), I focus my attention to orogenic plateaus that are formed by continent-continent collision or non-collisional subduction processes beneath the continents (e.g., Cloos, 1993; van Hunen et al., 2000). Next to the Tibetan and Altiplano-Puna plateaus, which constitute the focus of this study, the Colorado and Turkish-Iranian plateaus are also important orogenic plateau regions that fundamentally impact environmental conditions (Figs. 1.2 and 1.3).

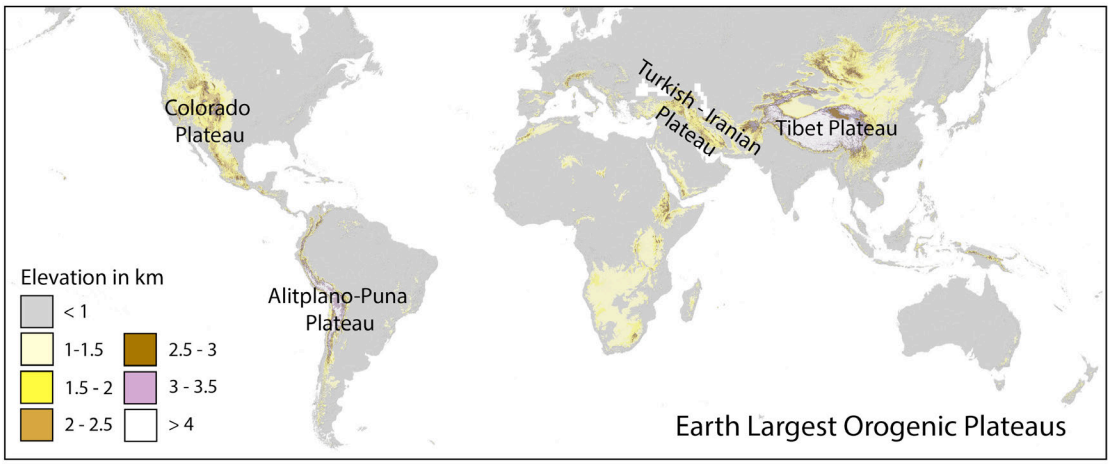

Figure 1.2. Overview of Earth's largest orogenic plateaus. Elevation SRTM-data is modfied from CGIAR SRTM 90 m Digital Elevation Database v4.1 (Jarvis et al., 2008).

The Himalayan-Tibetan collision zone consists of the Himalayas including fourteen principal peaks having elevations above 8 km, the Karakorum ranges in the west, the Himalayan syntaxes in Pakistan and Eastern India, respectively, and the Tibetan Plateau to the north (Figs. 1.2 and 1.3). The Himalayan-Tibetan system spans from ~70° to 105° E and ~40° to 25° N, exhibiting extreme topographic relief of up to 6 km along the Himalayan fronts and syntaxes, and low internal relief of less than 500 m in extensive parts of the central Tibetan Plateau (Burbank et al., 1996; Zeitler et al., 2001; Fielding et al., 1994). The Tibetan Plateau comprises several range uplifts with intermediate-size basins with more than 5 km of sedimentary fill (e.g., Horton et al., 2012). Common to many models of Tibetan Plateau formation is the assumption that most of Tibet was near sea level prior to the India-Asia collision at around 50 Ma and that the plateau grew radially outward from a central core due to the subduction of the Indian plate beneath Asia (Houseman and England, 1996; Tapponnier et al., 2001; Rowley and Currie, 2006). Recent data contradicts this and instead suggests that substantial Cretaceous crustal thickening prior to the early Cenozoic collision at ~50 Ma had already created high topography in large parts of central Tibet (DeCelles et al., 2007; Rohrmann et al., 2012).

The Andes are a continuous, 7000-km-long mountain range along the active convergent margin of South America, extending from ~10°N to 55° S and between ~80° and 60° W (Fig. 1.2). The Andes host some of the highest peaks outside the Himalayan-Tibetan orogen with elevations close to 7 km. In general, the Andes and their present-day elevations are interpreted to result from crustal shortening and thickening, associated with the continuing coupled interaction of the subducting oceanic Nazca plate with the overriding South American continent (e.g., Jordan et al., 1983; Isacks, 1988; Allmendinger et al., 1997).

The Altiplano-Puna Plateau, the second largest orogenic plateau on Earth, is approximately located between 15° and 27° S and has an average elevation of 3.7 km. The plateau has a compressional, low relief basin-and-range topography with numerous internally drained and partly coalesced sedimentary basins (Allmendinger et al., 1997). Although structurally very similar, this contrasts

with the adjacent high-relief intermontane basins and ranges of the Eastern Cordillera and the Santa Barbara and Sierras Pampeanas morphotectonic provinces that are part of the broken Andean foreland (Jordan et al., 1983). The hydrologically closed basins of the Puna have sedimentary fills of up to 5 km thickness and thus lie in stark contrast to much thinner, partially exposed fills in the intermontane basins to the east (e.g., Jordan and Alonso, 1987; Allmendinger et al., 1997; Strecker et al., 2009). The age and deformation mechanism of the Altiplano-Puna plateau uplift is actively debated, with the proposed timing of uplift ranging from early Oligocene to late Miocene (Garzione et al., 2008; Barnes and Ehlers, 2009; Canavan et al., 2014). In addition to crustal shortening and magmatic addition, it has been suggested that the final stages of plateau uplift were associated with the isostatic response to lithospheric delamination processes (Froideveaux and Isacks, 1984; Kay and Mahlburg, 1993; Allmendinger et al., 1997; Sobolev et al., 2005).

1.3 Tibet and Puna-Altiplano plateaus climate conditions

The Altiplano-Puna and Tibet plateaus both exert strong control over atmospheric circulation and moisture distribution (e.g., Hahn and Manabe, 1975; Lenters and Cook et al., 1995; Bookhagen and Burbank, 2006; Takahashi and Battisti, 2007; Bookhagen and Strecker, 2008; Garreaud et al., 2009; Molnar et al., 2010). The topographic distribution of high-standing topography in plateau regions not only blocks and reroutes airflow patterns and thus controls overall moisture supply to the plateau and its flanks, but also often creates its own regional circulation regimes known as monsoons (e.g., Fu and Fletcher, 1985; Lenters and Cook et al., 1995). For example, significant heating over the Tibetan Plateau increases upper tropospheric air temperatures compared to air above the Indian Ocean, driving the flow of warm, moist air toward the orogen as part of the Southeast Asian and Indian summer monsoons (Fig. 1.3 A) (e.g., Fu and Fletcher, 1985). The Indian Summer Monsoon transports moisture during summer (June, July, and August) from the Bay of Bengal toward and along the Himalayan front in a northwestward direction, with far-reaching impacts on surface processes during intensified monsoon years (e.g., Bookhagen and

Burbank, 2006; 2010; Wulf et al., 2010) (Fig. 1.3 A; white arrows). Heavy precipitation of more than 3 m/yr results as the moisture-laden winds encounter the orographic front. In contrast, the Southeast Asian Monsoon has its moisture source in the South China Sea and the Pacific (An, 2000). In the case of China, moisture is transported across Asia and along the eastern Tibetan margin as far north as 35° N (Fig. 1.3 A). Areas north and west of the Tibetan Plateau are influenced by the westerlies. However, here the westerlies are not moisture-laden as farther west, but instead constitute a dry, high speed air-flow, especially during winter (Bryson, 1986; Toggweiler and Russel, 2008).

In South America, the South American Monsoon System (SAMS) is the most important feature controlling moisture supply to the Altiplano-Puna Plateau and the Andean orogen to a latitude of approximately 28° S, but moisture also reaches the orogen from the east due to the influence of the South Atlantic Convergence Zone (Carvalho et al., 2011; Marengo et al., 2012). The SAMS is modulated by the El Niño-Southern Oscillation (ENSO) phenomenon. During positive ENSO cycles, reduced moisture transport into the central Andes has been observed (e.g. Bookhagen and Strecker, 2008). Typically, low-level trade winds drive tropical Atlantic moisture into the Amazon basin, a process that is caused by differential heating between ocean and land (e.g. Marengo et al., 2012), and part of this moisture is recycled and transported southward by the SAMS. The SAMS is most active between December and February (DJF). The heaviest precipitation east of the Andes is formed in the South Atlantic Convergence Zone (SACZ) by convection (Carvalho et al., 2002). The South American Low-Level Jet (SALLJ) as an integral part of the SAMS, however, exerts the greatest control on modulating the moisture supply to the Altiplano-Puna Plateau (Fig. 1.3 B). The Andes deflect low-level flow southward parallel to the strike of the Andes, and when these moisture-laden winds are orographically lifted, there will be heavy rainfall (e.g., Bookhagen and Strecker, 2008; Garreaud et al., 2009; Rohrmann et al., 2014). The largest rainfall amounts are found between ~1 and 1.5 km elevation, whereas higher elevations and leeward sides often receive less than 0.2 m/yr (Bookhagen and Strecker, 2008; Boers et al., 2013; Rohrmann et al., 2014).

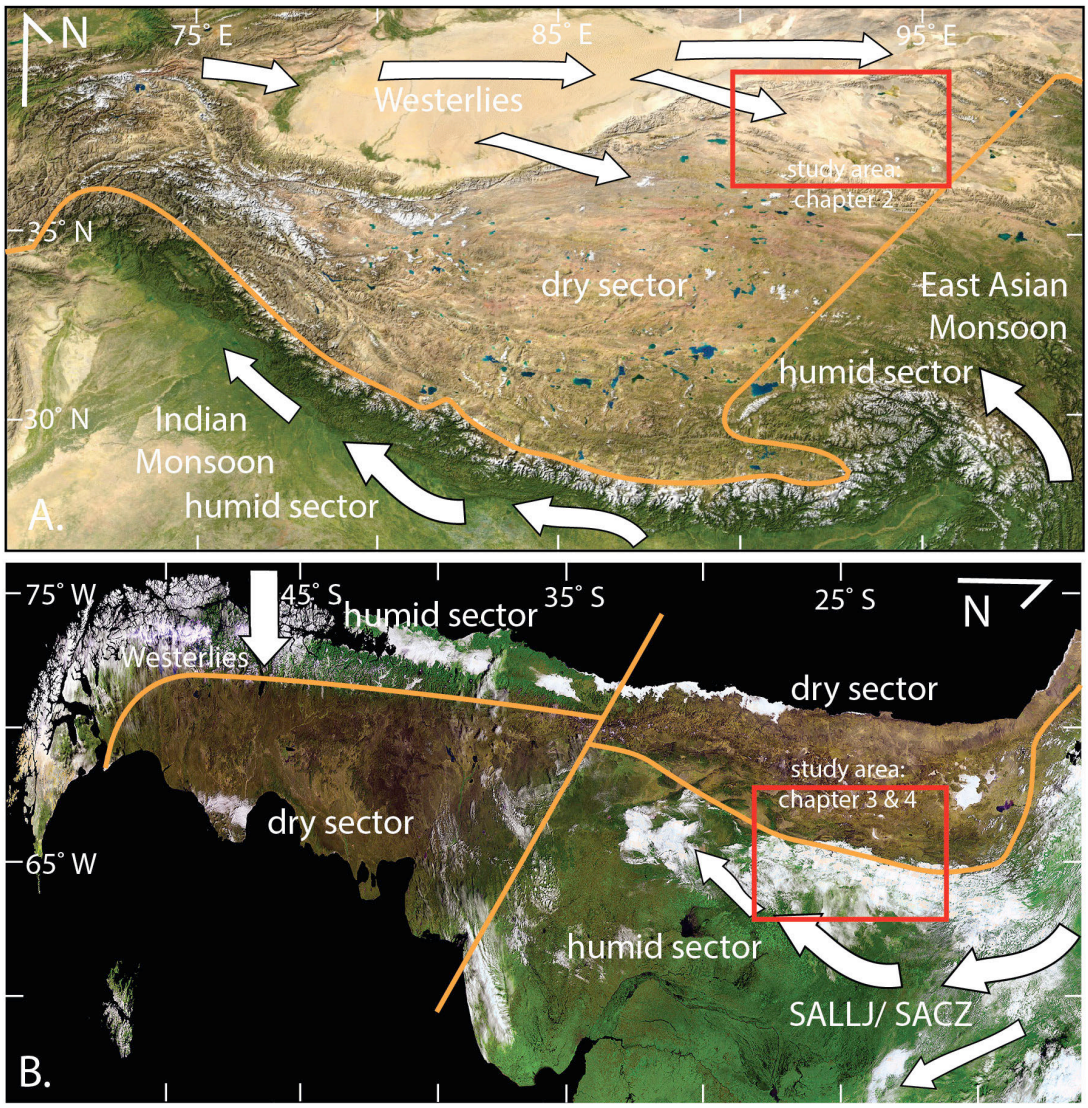

Figure 1.3. The Tibetan (A) and Altiplano-Puna plateaus (B). (A) Satellite composite of the Himalayan-Tibetan system with vegetation and glacial cover (image source: NASA, 2013). (B) Proba-V satellite image acquired on April 23th, 2014 (image source: ESA, 2014). In case of the Andes note the large distortion of the image for more southern regions as Patagonia due to the Mercator projection. White arrows highlight the major atmospheric circulation systems, e.g. monsoon or westerlies, and orange line represents the boundary between dry and wet sectors along Tibet and the Andes, exemplifying the importance of the monsoonal systems in providing moisture and thus controlling the density of vegetation cover in both areas. Red boxes denote study areas for chapters two, three, and four.

Another important component of South American hemispheric-scale atmospheric circulation are the westerlies south of ~28° S (Fig. 1.3). The westerlies transport moisture from the Pacific Ocean into the western Andes, where rain-out takes place along the steep topographic range fronts (e.g.,

Garreaud and Aceituno, 2001; Garreaud et al., 2009). After the westerlies cross from west to east over the Andes, the air masses sink, are adiabatically heated, and become a very dry airmass that is largely responsible for the aridity in the southern-central and southern foreland of the Andes.

1.4 Tibet and Puna-Altiplano plateaus environments

The topography and relief conditions of the Altiplano-Puna and Tibetan plateaus and their impact on airflow patterns and moisture supply have created distinct humid and arid sectors/ environments along and within the plateaus (Fig. 1.3). These sectors vary significantly in vegetation cover, hydrology, and geomorphology. For example, the arid sector of the plateau interiors are more stable, with low streampower and erosion rates, related to a deficit in precipitation and runoff (e.g., Rech et al., 2010; Bookhagen and Strecker, 2012; Jungers et al., 2013). The sparse vegetation cover, in combination with high wind speeds, exposes these areas to wind erosion, but the efficiency of this process has never been fully quantified in the plateau interiors and their arid margins (Isacks et al., 1989; Goudie, 2007). There are few estimates of wind erosion with values between 1 and 10 mm/yr, but these are only crude estimates based on inversion of topographic features or eolian removal of lacustrine sediments from dry lakebeds (e.g., Beresford-Jones et al., 2009; Washington et al., 2006; see in-depth review in chapter 2). In contrast, the wet, windward sectors with their steep topographic flanks acting as orographic barriers, have higher precipitation amounts and erosion rates (e.g., Bookhagen and Strecker, 2012; Blöthe and Korup, 2013).

The nature (i.e. convective or stratiform) and spatio-temporal distribution of precipitation is highly non-uniform in plateau regions (e.g., Bookhagen and Burbank, 2006; Bookhagen and Strecker, 2008; Romatschke and Houze, 2013). For example, precipitation along the Tibetan and Altiplano-Puna plateaus is limited to the summer months – often in combination with an intensification of monsoonal circulation – governing the amount and severity of rainfall. There is little information on the character of precipitation along plateaus especially

regarding convective rainfall (Zipser et al., 2006; Houze et al., 2012). In light of a potentially warmer future, climate air masses in these regions will be able to absorb higher amounts of water vapor, and consequently the number of convective storms and extreme rainfall events will likely be increased. In the Andes, it has been shown that deep convective storms (storms with a cloud height of more than 10 km) develop in the transition zone between the humid flanks and the arid plateau margin (Zipser et al., 2006; Houze et al., 2012). In the Himalaya-Tibetan system, such convective storms are located in the northwestern regions, such as the Karakorum Mountains and Ladakh, where a sparse vegetation cover and high insolation provides an ideal setting to form convective storms (Fig. 1.3). Since precipitation amount in mountainous regions is generally strongly linked to hillslope processes, fluvial erosion and landsliding, it is therefore very important to identify and understand the link between convective rainfall and the mechanisms of mass removal (e.g., Bookhagen and Strecker, 2012; Kirby and Whipple, 2012). The steep topographic and climatic gradients and the transitions between humid and arid high-altitude sectors, in addition to the ongoing tectonic activity, make these areas very vulnerable to the impacts of future climate shifts (e.g., Bradley et al., 2006) and repercussions on infrastructure and populations is to be expected.

The wet and dry sectors of the Tibetan and Altiplano-Puna plateaus are not static, but evolved over time as tectonic shortening caused lateral and vertical topographic growth and thus modified atmospheric circulation systems by establishing orographic barriers and aridifying the orogen interiors (Fig. 1.3) (Vandervoort et al., 1995; Alonso et. al., 2006; DeCelles et al., 2007). The rich sedimentary records of basins on the Altiplano-Puna and Tibetan plateaus and intermontane basins along their margins may potentially record corresponding paleoenvironmental and hydrological changes through time and thus furnish important archives reflecting the impacts and feedbacks of tectonic forcing of climatic conditions (e.g., Isacks et al., 1989; Kleinert and Strecker, 2001; Thiede et al., 2004; Strecker et al., 2007). In the Andes, a general eastward migration of the deformation front from the western parts of the present-day of the orogen toward the eastern foreland is observed, although this eastward migration may

be highly unsystematic and disparate in time and space in the broken foreland sectors (Sempere et al., 1990; Horton, 1998; Kley et al., 2005; Strecker et al., 2009). The formerly continuous foreland was fragmented and filled with synorogenic clastics that were progressively incorporated into the orogen (e.g., Jordan and Alonso, 1987; Reynolds et al., 2000; Carrera et al., 2006; Hain et al., 2011). This led to uplift and exposure of older basin fills within the plateau, the Eastern Cordillera, and adjacent geological provinces to the east of the plateau (Horton, 1998; Horton and DeCelles, 2001; Hilley and Strecker, 2005). Proxy indicators and facies variations in these strata offer the unique opportunity to study hydrologic transitions over time and thus provide an unprecedented archive of paleoenvironmental and biotic evolution for the foreland and orogen interior in response to tectonic and climatic forcing (Fig. 1.3 B). Ultimately, these proxy indicators also furnish information that is needed to better understand the response of plateau environments and their forelands to the impact of global change, as the long-term build-up of topography and ensuing changes in climate may have a similar effect as short-term climate change in a particular location.

1.5 Principal scientific questions addressed in this study

This thesis is an attempt to decipher the role of wind and water in shaping two of the most prominent plateaus on Earth. The approach is based on the study of the humid and arid environments and surface processes in these environments on different timescales, spanning the present-day to millions of years. To help guide me through this process, I developed the following research questions:

1. What is the rate of wind erosion on a local to global scale in the context of plateaus? How does wind erosion operate in plateau settings (i.e. deflation vs. abrasion) and how important are eolian processes in shaping arid plateaus? (Chapter 2)

2. Where do convective rainstorm events occur along plateau environments? Which mechanisms control them? Can these impacts be deciphered by analyzing water stable isotopes and does this information

help to reconstruct plateau paleoenvironments, climate, and topography? (Chapter 3)

3. How is the changeover from a humid to an arid environment accomplished during plateau growth and how do erosion, vegetation, and hydrology respond to tectonic forcing via topographic growth? (Chapter 4)

1.6 Thesis outline

After this general introduction into the topic and the short characterization of the Tibetan and Andean plateaus, wind erosion in the arid Tibetan Plateau environment of the Chinese Qaidam Basin is assessed in Chapter 2 (Fig. 1.3 A). Here, ^{10}Be cosmogenic nuclide surface-dating is used to quantify wind-erosion rates over the last ~15,000 years. Additional issues concerning wind erosion in this environment are considered. These include: (1) the nature and differences of deflation and abrasion processes and how they operate; (2) the significance of wind-erosion rates for the arid Tibetan Plateau environment and the Chinese Loess Plateau; and (3) the obtained wind-erosion rates are compared to global rates of wind erosion from North to South America, Europe, Africa, and Asia, with the objective to highlight their general significance for arid landscape evolution.

After having dealt with the specifics of arid plateau environments and illustrating the role of wind in shaping these environments, the thesis turns to the characterization of humid environments along plateau flanks in South America and the role of water in Chapter 3. The eastern, windward flanks of the Altiplano-Puna Plateau and the Eastern Cordillera of the south-central Andes receive high rainfall amounts, which decreases westward with increasing topography. This represents an ideal setting to first study the present-day characteristics of the humid plateau flanks, and second, their development through time (Fig. 1.3 B). A hydrogen and oxygen water-stable isotope proxy approach is used to identify, analyze, and characterize the nature of precipitation along the eastern Altiplano-Puna Plateau margin. The moisture sources, precipitation gradients, and the

temperature-elevation dependence of stable isotopes of water are evaluated. These help to illustrate where and why deep-convective storms occur along certain parts of the plateau. The data can elucidate which impact present-day convection processes have on isotope proxies based on hydrogen and oxygen in precipitation, but it is equally important for reconstructions of paleotopography, former climate, and past sedimentary environments.

In the fourth chapter, I analyze the evolution of a previously open foreland and its progressive integration into the eastern flanks of the Altiplano-Puna Plateau, with a deep-time perspective. Environmental records from this region suggest that this sector of the formerly contiguous foreland was transformed from humid to arid conditions as the deformation front migrated eastward and orographic barriers were created. The main focus of this chapter is the assessment as to how erosion, vegetation, and the hydrology change over the course of plateau growth and coeval tectonic movements in the broken foreland between the late Miocene and Pliocene. Several stable isotope proxies, including lipid biomarker n-alkanes, pedogenic carbonates, and volcanic glass shards help to reconstruct the paleoenviromental changes. Furthermore, it is demonstrated how the different stable isotope proxies record environmental change, and which components of the paleoenvironment they help to reconstruct.

Chapter 5 synthesizes and discusses the major outcomes of all studied topics and presents an outlook for future research in the realm of stable isotope studies of environmental conditions in actively deforming mountain belts.

1.7 Publications and author contributions

The work presented in the following chapters has been planned, organized, and conducted by myself. The different co-authors contributed to each publication listed below, and provided the analytical equipment for isotope analysis. They also provided guidance during data analysis and interpretation. In addition, several people were involved in fieldwork and sample preparation that I like to

acknowledge. These include Xenophonne Hadeen, Vanesa Niento-Moreno, Stefanie Tofelde, Hanno Meyer, and Ullrich Treffert.

The results presented in chapters 2, 3 and 4 have already been published (chapters 2 and 3) or are sent out for review in international peer-review journals (chapter 4). The published articles' layout has been modified and adjusted to match the thesis format. No changes have been made to either text or figures. The author and co-authors' contributions to chapters 2 to 4 are as follows:

Chapter 2

Rohrmann, A., Heermance, R., Kapp, P. and Cai, F. (2013), Wind as the primary driver of erosion in the Qaidam Basin, China. ***Earth Planetary Science Letters***, 374, 1–10, doi: 10.1016/j.epsl.2013.03.011

A.R. performed fieldwork, sample collection and analysis. R.H. and P.K. and F.C. supported field work and sample collection. A.R. conducted sample preparation for 10Be surface exposure dating, and A.R. and R.H. carried out chemical sample treatment. A.R., R.H., P.K. designed and wrote the manuscript; all authors discussed interpretations and commented on the manuscript. A.R. designed all artwork.

Chapter 3

Rohrmann, A., Strecker, M.R., Bookhagen, B., Mulch, A., Sachse, D., Pingel, H., Alonso, R.N., Schildgen, T.F., Montero, C. (2014), Can stable isotopes ride out the storms? The role of convection for water isotopes in models, records, and paleoaltimetry studies in the central Andes. ***Earth Planetary Science Letters***, 407, 187–195, doi:10.1016/j.epsl.2014.09.021

A.R. conducted field work and sample collection. A.R., M.S. and B.B. collected samples and were responsible for TRMM and MODIS-satellite analysis and A.M. supervised stable isotope measurements. A.R. performed water-stable isotope modeling and analysis. D.S., H.P., R.A., T.S. and C.M. supported field work and

sample collection. A.R., M.S., B.B., A.M., D.S. and H.P. designed and wrote the manuscript; all authors discussed interpretations and commented on the manuscript. A.R. designed all artwork.

Chapter 4

Rohrmann, A., Sachse, D., Strecker, M.R., Mulch, A., Pingel, H., Alonso, R.N., Rapid hydrological response to orographic barrier and central Andean Plateau uplift. Submitted to ***Science***.

A.R. performed fieldwork, sample collection and analysis. M.S., H.P., A.M. and D.S. supported field work and sample collection. A.R. conducted sample preparation for lipid biomarker analysis, and A.R. carried out chemical sample treatment. A.R. and D.S. performed lipid biomarker hydrogen and carbon IRMS-measurements. A.R. and A.M. conducted soil-carbonate stable isotope analysis. H.P. performed volcanic glass shards hydrogen isotope analysis. A.R. designed all artwork and conducted statistical data analysis. A.R., M.R., D.S., A.M., H.P. and R.A. wrote the manuscript; all authors discussed interpretations and commented on the manuscript.

During the course of my PhD I contributed as co-author to the following publication, which is not included in this thesis:

- Pingel, H., Alonso, R.N., Mulch, A., Rohrmann, A., Sudo, M., Strecker, M.R. (2014), Pliocene orographic barrier uplift in the southern Central Andes. ***Geology*** 42, 691–694. doi:10.1130/G35538.1

H.P. performed fieldwork, sample collection and analysis. A.R. M.S., R.A. and A.M. supported field work and sample collection. H.P. conducted sample preparation for volcanic glass shard analysis. H.P. and A.M. performed volcanic glass hydrogen measurements. H.P. performed volcanic glass-shard hydrogen isotope analysis. H.P., R.A., A.R., M.S., A.M., and MA.S. wrote the manuscript; all authors discussed interpretations and commented on the manuscript.

Chapter 2

Wind as the primary driver of erosion in the Qaidam Basin, China

Rohrmann, A., Heermance, R., Kapp, P. and Cai, F. (2013), Wind as the primary driver of erosion in the Qaidam Basin, China. ***Earth Planetary Science Letters***, 374, 1–10, doi: 10.1016/j.epsl.2013.03.011

Abstract

Deserts are a major source of loess and may undergo substantial wind-erosion as evidenced by yardang fields, deflation pans, and wind-scoured bedrock landscapes. However, there are few quantitative estimates of bedrock removal by wind abrasion and deflation. Here, we report wind-erosion rates in the western Qaidam Basin in central China based on measurements of cosmogenic ^{10}Be in exhumed Miocene sedimentary bedrock. Sedimentary bedrock erosion rates range from 0.05 to 0.4 mm/yr, although the majority of measurements cluster at 0.125 ± 0.05 mm/yr. These results, combined with previous work, indicate that strong winds, hyper-aridity, exposure of friable Neogene strata, and ongoing rock deformation and uplift in the western Qaidam Basin have created an environment where wind, instead of water, is the dominant agent of erosion and sediment transport. Its geographic location (upwind) combined with volumetric estimates suggest that the Qaidam Basin is a major source (up to 50%) of dust to the Chinese Loess Plateau to the east. The cosmogenically derived wind erosion rates are within the range of erosion rates determined from glacial and fluvial dominated landscapes worldwide, exemplifying the effectiveness of wind to erode and transport significant quantities of bedrock.

2.1. Introduction

Knowledge of bedrock erosion rates on Earth's surface over timescales of 10^2 – 10^6 years is limited, yet fundamental in assessing the dynamics of landscape evolution and sediment production as a function of tectonic processes, climate, and lithology and their superposed forcing factors (Molnar, 2004; Whipple, 2004). Significant advances have been made in recent decades in quantifying

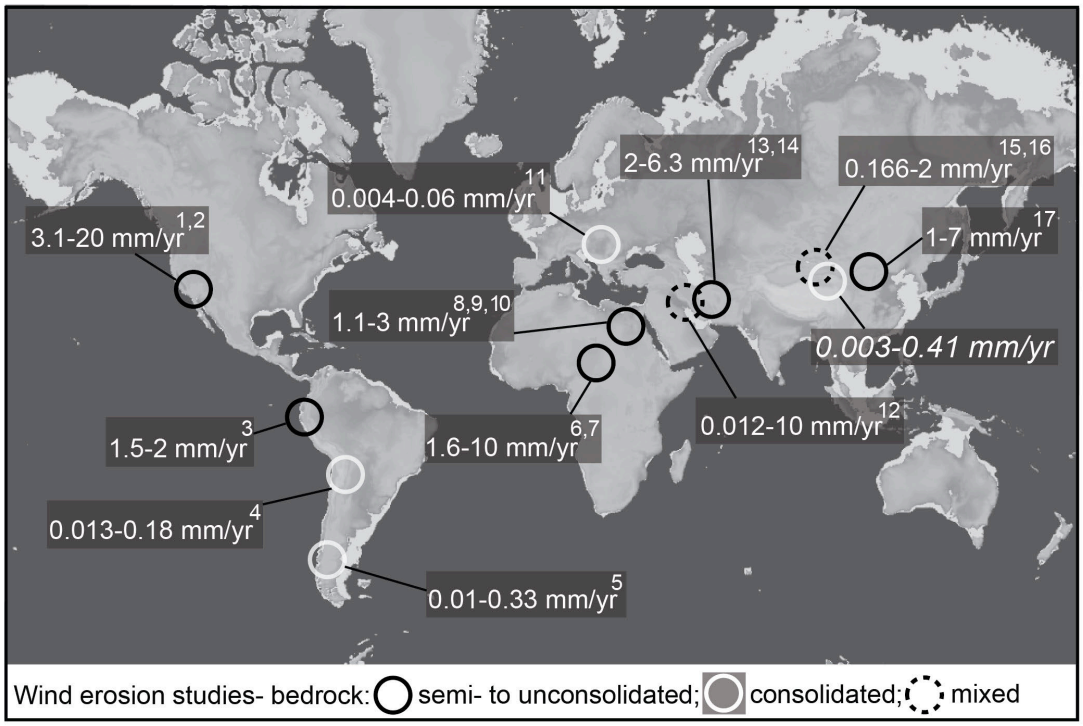

Figure 2.1. Global compilation of wind erosion estimates reporting erosion by deflation (semi- to unconsolidated) and abrasion (consolidated) or both. Erosion rate estimates are based on ^{14}C-dating, optical luminescence-dating (OSL), cosmogenic ^{10}Be-dating or U-Pb dating of eroded rocks. Where no rates were reported, a conservative erosion rate was estimated using the age of the deposit and wind removed material by geometric considerations, e.g. yardang troughs; inverted channels; elevated lake beds or paleo-soils above the general basin floor. Note the order of magnitude difference between wind erosion by deflation and abrasion, suggesting bedrock strength controlling the effectiveness of wind erosion. References: 1. Clarke et al. (1996); 2. Ward et al. (1984); 3. Beresford-Jones et al. (2009); 4. de Silva et al. (2010); 5. Inbar et al. (2001); 6. Washington et al. (2006); 7. Bristow et al. (2009); 8. Haynes et al. (1980); 9. Goudie et al. (1999); 10. Brookes et al. (2003); 11. Ruszkiczay- Rüdiger et al. (2011); 12. Al-Dousari et al. (2009); 13. Krinsley et al. (1970); 14. Kehl (2009); 15. McCaulay et al. (1977); 16. Dong et al. (2012); 17. Rittley et al. (2004).

bedrock and drainage-basin erosion rates in regions where fluvial and glacial processes dominate. Short-term landscape sedimentary flux and erosion rates (10^0-10^2 yr) have been recorded by sedimentary traps and gauging stations on rivers (Meade, 1988; Kirchner et al., 2001; Lavé and Burbank, 2004), whereas on longer timescales (10^3-10^6 yr) concentrations of in situ cosmogenic radionuclides (i.e. ^{10}Be) in fluvial sediments have been used (e.g., Granger et al., 1996; Gosse and Philips, 2001; Blanckenburg et al., 2005, Owen et al., 2001; Portenga and Bierman, 2011). In contrast, few studies have quantified eolian erosion processes in deserts (e.g., McCaulay et al., 1977; Ward et al., 1984; Bristow et al., 2009; Fig. 2.1), particularly on time-scales >5000 yr (Inbar et al., 2001; DeSilva et al., 2010; Ruszkiczay-Rüdiger et al., 2011). This is despite the recognition of wind as an important transport agent (Pye et al., 1995; Uno et al., 2009) that loess is one of the most important fertilizers for plankton growth in the open ocean (Pye et al., 1995; Hanebuth and Henrich, 2009), and the ubiquity of wind-deflated and abraded landforms in many desert regions on Earth (Goudie, 2007) and extraterrestrial bodies such as Mars and Jupiter's moon Titan (e.g. Bridges et al., 2004; Sullivan et al., 2005; Thomson et al., 2008; Rubin and Help, 2009).

The in-situ produced cosmogenic nuclide ^{10}Be can be used to quantify in-situ bedrock erosion because of its long half life (~1.3 x10^6 yrs), short attenuation length (< 2 m), and known production rate in quartz at the Earth's surface (Lal, 1991), making it useful for studying bedrock erosion processes and assessing rates of landscape evolution in general (e.g., Bierman and Caffee, 2002; Bookhagen, 2012). In this study, we quantify eolian erosion rates by measuring cosmogenic ^{10}Be in quartz from wind-scoured and deflated sedimentary bedrock surfaces in the Qaidam Basin (Fig. 2.2). We then compare our results with world-wide bedrock erosion studies in an effort to document the significance of wind as a global erosion agent.

2.1.1 Deflation vs. abrasion and evidence for wind erosion

In general, wind erosion is effective in arid, windy regions characterized by sparse to no vegetation cover. Wind erosion is viewed as being the result of both deflation and abrasion processes (Laity, 2011). Disagreements exist about the correct use of these terms, since both processes can spatially and temporally overlap and contribute to the overall wind-erosion signal. Deflation is defined here as the passive entrainment of loose material at the Earth's surface into the air-flow. In contrast, abrasion is the physical process of actively eroding material by the impact of wind-blown grains onto a bedrock surface (Goudie et al., 2008; Laity et al., 2009). Deflation dominates wind erosion in areas where

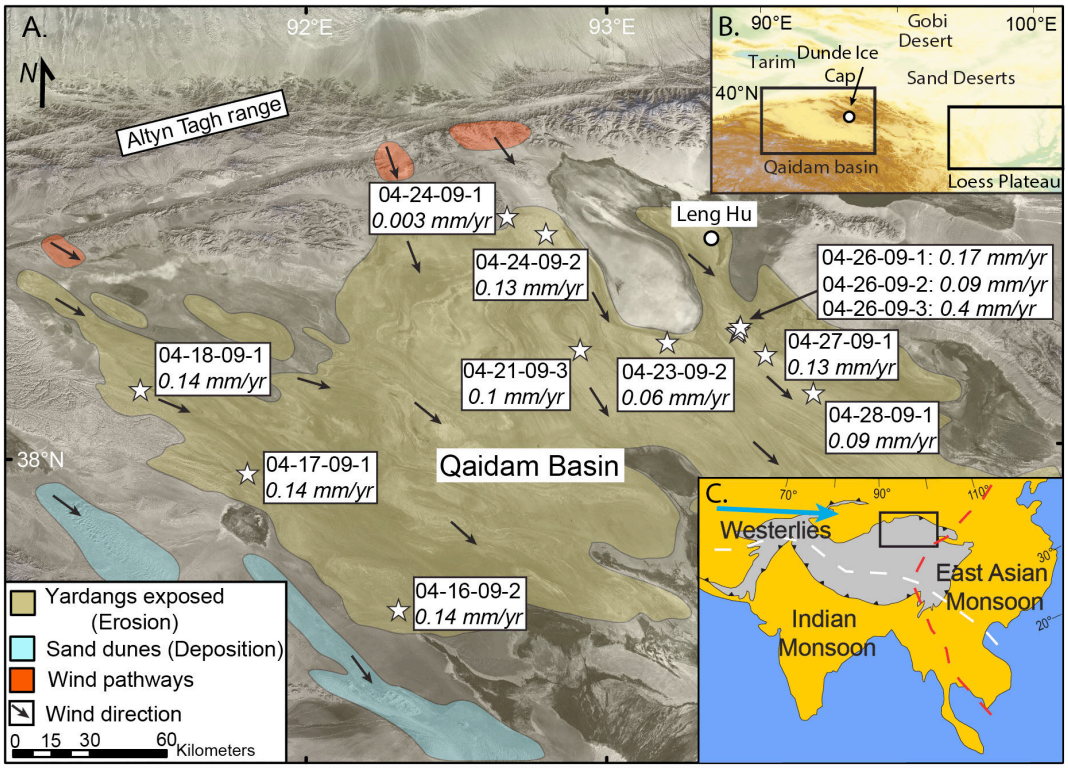

Figure 2.2. A) Landsat image of the Qaidam Basin showing the distribution of yardangs and dune fields, wind directions, and sample locations for ^{10}Be-dating. B) Location of the Qaidam Basin and the Loess Plateau. C) Regional overview of the major circulation systems: The westerlies and dashed lines indicate the maximum modern extent of the Indian and East Asian Monsoon systems (after Gao, 1962).

unconsolidated sediments or poorly lithified rocks are exposed at the surface. In bedrock-dominated areas floored by either consolidated sedimentary or crystalline rocks, only abrasion is able to remove material from bedrock surfaces (Laity et al., 2009 and 2011). However, other factors such as water (e.g. gullying, mudflow, sheet wash), temperature (freeze-thaw), and chemical weathering (salt corrosion and expansion) also impact bedrock surfaces and are able to produce loose material covering bedrock (Aref et al., 2002). Loose sediment is prone to deflation, resulting in bedrock lowering without physical abrasion. In many places it is impossible to distinguish between deflation or abrasion because of the complex relationships among weathering, climate, and bedrock lithology. Thus, information on rates and time scales of either deflation or abrasion alone are scarce.

The primary evidence for wind erosion, and specifically abrasion, in the Qaidam Basin and elsewhere are yardangs (Fig. 2.3 A , B, E), ventifacts (Fig. 2.3 B, foreground), and scoured, low-relief bedrock landscapes devoid of a fluvial network (Fig. 2.3 C and D). Yardangs are wind eroded narrow ridges up to 100 m high and up to hundreds of meters in length (Hedin, 1903; Goudie, 2007). They are sculpted into poor-to-well consolidated bedrock by saltating particles that are transported by strong, uni-directional winds (McCauley et al., 1977; Dong et al., 2012). The few estimates available for the time scales of yardang formation range from thousands of years for small yardangs (1-10 m) (Halimov and Fezer, 1989) to millions of years for large yardangs (>50 m) (Goudie, 2007).

Ventifacts provide evidence for the strong abrasive power of wind at much smaller scales (Laity, 1994; Knight, 2008). Ventifacts are rocks that exhibit grooves, facets, or polishing as a result of abrasion by wind-entrained sand and typically consist of crystalline and well consolidated sedimentary rocks; they are found in most deserts and periglacial environments (Spate et al., 1995; Knight, 2002; Laity, et al. 2009). Reported abrasion rates associated with ventifacts are generally between 0.015 and 6.8 mm/yr (Knight 2008), although one study reported a maximum abrasion rate of 36 mm/yr over a time period of 15 years (Sharp et al., 1980).

Most wind erosion occurs in the large, windy, semi-arid to arid region stretching from North Africa to central China and parts of North and South America (Fig. 2.1). Here, bedrock removal by wind is ubiquitous and reported wind deflation rates from semi- to unconsolidated sediment range from 1 to 20 mm/yr over short (<5000 yrs) time periods (Fig. 2.1; Krinsley et al., 1970; McCaulay et al., 1977; Haynes et al., 1980; Ward et al., 1984; Clarke et al, 1996; Goudie et al., 1999; Inbar et al., 2001; Brookes et al., 2003; Rittley et al., 2004; Washington et al., 2006; Beresford-Jones et al, 2009; Bristow et al., 2009; Al-Dousari et al., 2009; Kehl, 2009; de Silva et al., 2010; Ruszkiczay- Rüdiger et al., 2011; Dong et al., 2012). Most of the presented compilation in Figure 2.1 is based on studies of wind eroded features (yardangs, tree roots, channels, lake beds, lava flows) with ages quantified by ^{14}C-dating, optical luminescence-dating (OSL), and ^{40}Ar-^{39}Ar dating. There are, however, very few studies from well-lithified bedrock in areas affected by wind erosion, where abrasion should be dominant (Inbar et al., 2001; DeSilva et al., 2009, Ruszkiczay-Rüdiger et al., 2011). Recently, Ruszkiczay-Rüdiger et al. (2011) reported cosmogenically derived eolian erosion rates between 0.003 to 0.056 mm/yr from consolidated sedimentary bedrock in the Pannonian Basin of Hungary (Fig. 2.1). Although this technique is promising, there have been few studies of long-term (>5000 year) erosion rates from Central Asia (e.g. Lal et al., 2003). Here, the hyper-arid and windy conditions prevalent in northern Tibet may have enhanced eolian erosion and transport, as testified by the widespread and locally thick (hundreds of meters) accumulations of loess in eastern Asia, including the Chinese Loess Plateau (CLP) (Fig. 2.2 B) and beginning as early as 22 Myr ago (Porter et al., 2001; Guo et al., 2002).

2.1.2 Study area

The Qaidam Basin (QB) is situated at the northern edge of the Tibetan Plateau and covers an area of approximately 120,000 km^2 (Fig. 2.2). Today, the western QB receives less than 70 mm/yr of precipitation and is one of the highest (mean elevation of ~2700 m) and driest deserts on Earth, being shielded by efficient orographic barriers (Sobel et al., 2003). In response to the ongoing Indo-Asian

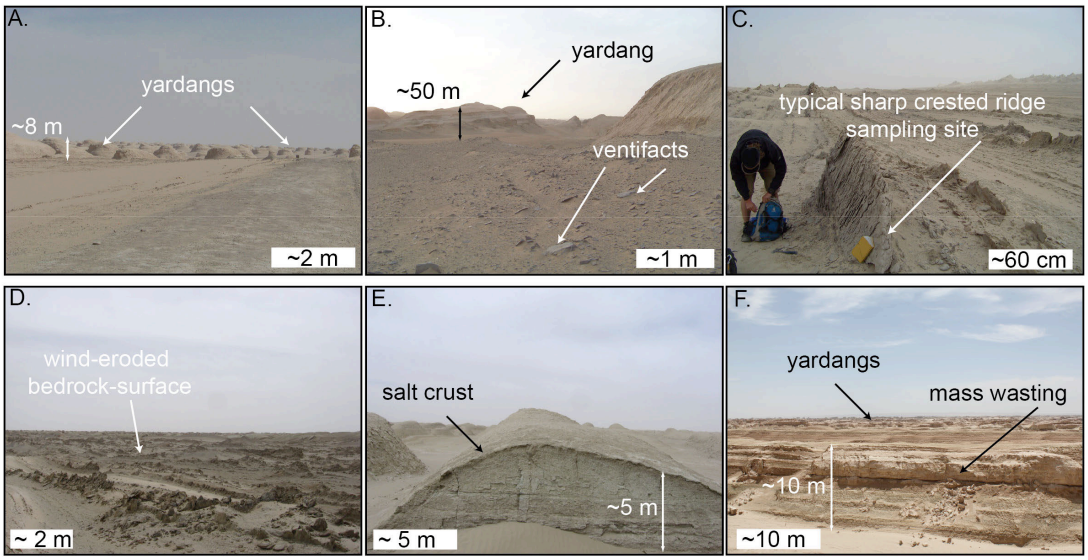

Figure 2.3. Photos from the study area showing: A.) Yardang field with 5 to 8 m high yardangs. B.) Foreground: desert pavement/ ventifacts, with 10-30 cm clasts. Background: ~25-50 m high yardangs and inter-yardang trough. C.) Typical arête sampling side with no visible fluvial network. D.) Vast wind scoured-bedrock landscape exposing sampled Miocene bedrock. E.) Road-cut through a yardang, exposing a ~20-cm-thick layer of salt crust, armoring the landscape from wind erosion. F.) Picture was taken after a strong but very rare rain-event. The yardangs are ~10 m high. Mass-wasting is seen on the side of the front yardang in form of debris-flows and rock fall.

collision, the basin is being shortened in a NE-SW direction (Tapponnier et al., 2001) and its floor exposes folded, friable sedimentary rock of the Miocene Shang Youshashan, Shizigou and Qigequan formations (e.g. Kapp et al., 2011, Wang et al., 2012). The Miocene formations (Shang Youshashan and Shizigou) are characterized by sandstone and conglomerate lenses (i.e. deltaic facies) that pinch out laterally into deeper-water siltstone and shale (i.e. lacustrine facies; Heermance et al., 2013).

Based on its low internal relief (<300 m), internal drainage, intermontane basin setting, and thick accumulations of Cenozoic basin fill, it generally has been inferred that the QB has been dominated by sediment accumulation rather than erosion until recently (Zhou et al., 2006), even though roughly one-third of the modern basin floor (~3.88 × 10^4 km^2) exposes yardangs carved in folded sedimentary strata (Fig 2.2; Kapp et al., 2011). The predominant wind direction

in the basin is from the northwest to southeast, while in the eastern part of the basin the predominant wind direction is more easterly, parallel to the orientation of the >5000-m-high basin-bounding mountain ranges to the north and south (Fig. 2.2). The wind eroded and quartz-rich strata throughout the basin make it ideal to quantify wind erosion and bedrock removal rates with cosmogenic ^{10}Be. In this study, we define wind erosion as being the sum of deflationary and abrasive processes acting on a surface, resulting in lowering and removal of bedrock in a hyperarid landscape marginally affected by rainfall events and fluvial processes. These conditions are met by the QB, where hundreds to thousands of vertical meters of consolidated basin fill may have been removed by wind over the last 2.8 million years (Kapp et al., 2011).

2.2. Methods

2.2.1 Cosmogenic nuclide dating

Terrestrial cosmogenic nuclides are isotopes that form from the interaction of cosmic particles with elements in Earth's atmosphere and surface. In particular, the cosmogenic nuclide ^{10}Be forms from the interaction of cosmogenic particles with quartz (Lal, 1991). Production of ^{10}Be decays exponentially with depth as the penetration of cosmic rays attenuates to zero a few meters below the ground surface. Furthermore, ^{10}Be is radiogenic with a half-life of $\sim$1.3 x 10^6 years (Nishizumi et al., 2007) and thus is not present in buried rocks more than a few million years old. The concentration of ^{10}Be in rocks at the Earth's surface is therefore a function of the production rate, the radioactive decay, and the local erosion rate. Erosion rate can be determined because the production rate (itself a function of altitude and latitude) and the decay rate of the target isotope is known (Lal et al., 1991). This technique has been applied to bedrock within many landscapes (e.g., Bierman et al., 1995; Brown et al., 1995, Nishiizumi et al., 1991; Small et al., 1997), including on bedrock exposed across the Tibetan Plateau (Lal et al., 2003). The calculated erosion rates are essentially a measure of the time required to remove $\sim$2 m of bedrock, which corresponds to the absorption depth for most cosmic rays in typical rocks. Our calculations are

based on the assumption of steady-state erosion, although as discussed later (section 4.1) it is likely that erosion rates have varied significantly over time.

The 250-500 μm sand fraction of quartz was separated from twelve samples distributed across the western QB and processed following the methodology of Kohl and Nishizumi (1992). Samples were spiked with an in-house, low ^{10}Be-concentration carrier (^{10}Be/^{9}Be 4 x 10^{-15} made from Ural Mts. phenacite) at the University of Arizona. ^{10}Be/^{9}Be ratios were measured at the Acceleration Mass Spectrometer at Lawrence Livermore National Laboratories, Berkeley, CA. Erosion rates were calculated using the CRONUS calculator (Balco et al., 2008) and account for ^{10}Be production at the latitude and elevation of the sample location and any potential shielding of the sample site from cosmic radiation by nearby topography.

2.2.2 Sampling method and sites

Twelve bedrock samples were collected for ^{10}Be analysis from the western QB (Fig. 2.2). Here, the basin floor exposes actively growing anticlines, where strata form wind scoured bedrock surfaces or are sculpted into yardangs (Fig. 2.3 A-F). Eleven samples were collected from medium- to coarse-grained sandstones within Miocene fluvio-lacustrine strata. The age of the strata for all our samples is greater than 5.3 Ma based on regional mapping and stratigraphic correlation with magnetostratigraphy (Heermance et al., in 2013; Wang et al., 2012). Miocene bedrock was targeted because these rocks would have been buried to sufficient depths (more than hundreds of meters) for at least the last 5 Myr, such that the ^{10}Be inheritance produced during prior exposure should have decayed to near zero concentration. Most of the targeted samples were located along sharp crested ridges. The ridges in turn are elevated above the mean basin floor, show evidence of wind scouring, and lack any fluvial network (see supplementary data for photos of individual sample sites). By sampling sharp crested ridges that stand above the landscape, we avoided the effects of surface-water runoff that would be focused into low spots within the landscape. Moreover, sharp crested ridges represent points in the landscape that have been

lowered to a lesser degree, and thus lower rate, than their surroundings, and therefore should yield erosion rate minima assuming an initially flat landscape. It is possible that infrequent rain events (Fig. 2.3 F) impact the local erosion signal, although the lack of any continuous catchment area implies that erosion due to runoff, particularly on the tops of the ridges, was very low. Moreover, rain events are not capable of removing sediment from the basin because of the basin's internal drainage; any eroded material must ultimately have been removed from the basin by wind. The basin floor is almost scoured clean of sediment, implying the removal of locally produced sediment by deflation was more efficient than the amount of loose sediment generated by wind abrasion and other erosional/ weathering processes.

Three of the twelve samples were taken from inclined hillslope surfaces. These samples have a higher probability to having been affected by hill-slope and mass-wasting processes in contrast to the remaining samples and we take these into account during our interpretation of the erosion rates. Sample 4-28-09-1 was taken from a 60° dipping side-slope of a yardang. Samples 4-17-09-1 and 4-26-09-1 were collected from well consolidated bedrock exposed on steep (>70°) cliff faces. In order to assess variations in wind erodibility as a function of bedrock cohesiveness/ strength, we also analyzed one granite sample (4-24-09-1) exposed along the northwestern margin of the QB adjacent to the Altyn Tagh Range (Fig. 2.2).

2.3. Results

^{10}Be concentrations for the twelve samples ranged between 6.291×10^4 and 1.054×10^7 atoms/ gram of quartz (Table 2.1). These concentrations, when corrected for topographic shielding, provide cosmogenically derived bedrock erosion rates of 0.003-0.4 mm/yr (Fig. 2.4, Table 2.1). Under the assumption of steady-state erosion, the rates would integrate erosion over a time period of up to 15,000 years for the Miocene bedrock samples and 500,000 years for the Altyn-Tagh granite – the time required to remove the upper 2 m of material (zone of ^{10}Be accumulation).

Table 2.1. Cosmogenic nuclide results.

Sample #	Rock type	Location	Latitude (N)	Longitude (E)	Altitude (m)	^{10}Be concentration (atoms/g)	^{10}Be concentration error (atoms/g)	Erosion rate (mm/yr)[a]	Erosion rate uncertainty (mm/yr)[a]
4-16-09-2	Sandstone	Arête	37.516	92.296	3050	228195	7771	0.138	0.012
4-17-09-1	Sandstone	70°-Cliff	37.967	92.796	2972	107720	4022	0.144	0.011
4-18-09-1	Sandstone	Arête	38.243	92.441	2778	191675	6902	0.145	0.012
4-21-09-3	Sandstone	Arête	38.375	92.897	2786	292823	9714	0.093	0.008
4-23-09-2	Sandstone	Arête	38.400	92.185	2792	485639	15921	0.057	0.005
4-24-09-1	Granite	Arête	38.815	92.655	3306	10544507	331768	0.003	0.000
4-24-09-2	Sandstone	Arête	38.758	92.784	2975	234360	8438	0.133	0.012
4-26-09-1	Sandstone	70°-Cliff	38.434	93.416	2878	86380	3272	0.171	0.014
4-26-09-2	Sandstone	Arête	38.436	93.422	2997	358772	15145	0.087	0.008
4-26-09-3	Sandstone	Yardang top	38.445	93.419	2851	62905	2700	0.401	0.035
4-27-09-1	Sandstone	Arête	38.358	93.510	2988	242840	8721	0.128	0.011
4-28-09-1	Sandstone	60° slope- mount	38.232	93.669	2838	214256	7704	0.092	0.008

a The erosion rate is calculated based on steady-state erosion (see text).

Nine of the twelve samples have bedrock removal rates that cluster between 0.09-0.17 mm/yr within average of 0.125 mm/yr (Fig. 2.4). Among these nine samples, three (4-17-09-1, 4-26-09-1 and 4-28-09-1) were collected from 50-70° dipping surfaces and thus the results are more ambiguous to interpret due to their prominent position with respect to mass-wasting activity. Furthermore, applying shielding correction to these samples is difficult because the surface may have catastrophically failed over the time span of ^{10}Be accumulation. The effect of mass wasting processes for these three samples (samples 4-17-09-1, 4-26-09-1 and 4-28-09-1) is not detectible on the basis of anomalously high erosion rates compared to samples collected from ridges on regionally flat landscapes, however, and implies that hillslope processes may be negligible compared to wind erosion in most places within the western QB. Overall, sampling on sharp crested ridges within overall flat landscapes is advised for future studies to rule out potential mass wasting events during the exposure of the sampled surface.

Whereas most of our samples clustered tightly around 0.125 mm/yr, samples 4-23-09-2 (hard sandstone) and 4-24-09-1 (granite sample) yielded lower rates (0.057 and 0.003 mm/yr, respectively) and 4-26-09-3 yielded a higher rate (0.4 mm/yr; Figure 2.4). These discrepancies can be accounted for by variations in rock strength. Sample 4-23-09-2 is a very coarse grained, well-consolidated sandstone and provides a lower bedrock erosion rate of 0.057 mm/yr, lower than the average (0.09-0.17 mm/yr). This reflects greater resistance to bedrock erosion, which is further supported by its prominent high-elevation position relative to most of the basin floor. The Altyn-Tagh granite 4-24-09-1 exhibits the greatest rock strength of all samples and correspondingly shows the strongest resistance to erosion with an erosion rate of 0.003 mm/yr. This very low erosion rate is consistent with other ^{10}Be-erosion rates determined for granitic bedrock exposed elsewhere adjacent to the Qaidam Basin and on the Tibetan Plateau (Lal et al., 2003, Fig. 2.4). The highest erosion rate of 0.4 mm/yr was obtained from sample 4-26-09-3, collected from a yardang located on a limb of an actively growing anticline in the northwestern part of the basin near Leng Hu (Fig. 2.2).

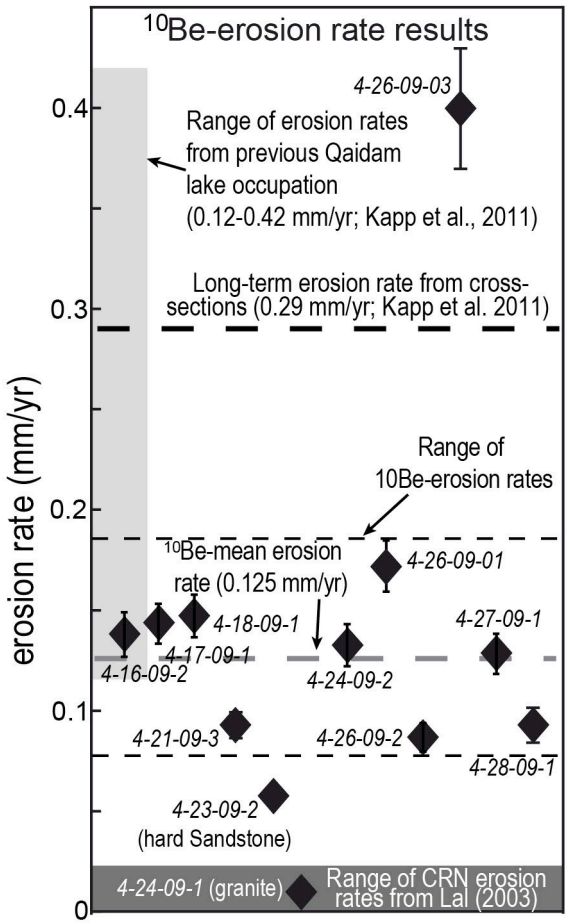

Figure 2.4. ^{10}Be-erosion rate results with 2-s-error bars, showing range of results and mean-erosion rate. In addition, Qaidam erosion rate estimates from yardangs carved into initially flat laying lake sediments (light gray box) and cross-sections both from Kapp (2011). Dark gray box shows, for comparison, the erosion rate range for granite samples from the Qaidam Basin and the Tibetan Plateau (Lal et al., 2003).

2.4. Discussion

2.4.1 Temporal variability of Qaidam wind erosion rates

The erosion rates presented here, with the average being ~0.125 mm/yr, are based on the assumption of steady-state erosion over the past ~15,000 years, resulting in ~2 m of bedrock removal. Based on a number of paleoclimatic and geologic arguments, however, it is likely that erosion in the QB was higher than our determined erosion rates in other parts of the wind-eroded basin and during the last glacial episode.

First, all samples were exclusively collected from indurated and erosion-resistant Miocene bedrock exposed along the axes of anticlines, in contrast to the less consolidated and younger strata exposed along syncline axes. Wind erosion rates would be expected to be greater in troughs that have been lowered to a greater extent than the intra–basin ridges. We did not sample and analyze the more friable Plio-Quaternary strata exposed in the syncline axes because rocks younger than Miocene presumably contain inherited ^{10}Be acquired prior to and during deposition, and would further underestimate overall basin-wide erosion rates.

Second, considering the regional paleoclimatic evidence (e.g. Thompson, 1989; Liu et al., 1994; Shao et al., 2005; Herzschuh et al., 2006; Zhao et al., 2007, 2010; Wang et al., 2008), the greatest factor influencing wind erosion rates and their temporal variability is climate change controlling changes in wind patterns and vegetation cover. Wind patterns and moisture supply in the QB are strongly influenced by the westerlies and in part by the East-Asian summer and winter monsoon system (Fig. 2.2 C; Bryson, 1986). Changes in these systems have resulted in complex impacts on the erosional system. The available climatic records indicate drier conditions during the last glacial in northern Tibet compared to a much wetter Holocene (Herzschuh et al, 2006). This pattern is attributed to a weakening and southward shift of the monsoonal systems during glacial periods, which suppressed moisture supply to NE-Tibet, and a Holocene northward migration of the monsoon with progressively wetter conditions during warming (Thompson et al., 2005; Wang et al., 2008). The southward shift of the monsoonal system in glacial times may have been associated with a >10° southward shift of the polar jet stream compared to its modern position (Shin et al., 2003; Toggweiler and Russel, 2008; Kapp et al., 2011; Pullen et al., 2011). The more southerly position of the jet stream during glacial periods would have favored the passage of large, low-pressure systems over the QB, which likely resulted in high wind speeds that, together with less vegetation cover during dry glacial periods, were able to efficiently erode large quantities of sediment. The increase in wind erosion and removal of material from the western QB during glacials is recorded in the Dunde ice cap located in the Qilian Shan ~100 km east

of the study area (Fig. 2.2 b; Thompson, 1989). The ice-core shows large quantities of dust input throughout the last glacial, followed by a dramatic reduction at the onset of the Holocene. Lake, pollen, and tree-ring records from the QB itself indicate aridity in the basin throughout the glacial until today, not capturing the Holocene northward shift and increased monsoonal precipitation (Phillips et al., 1993; Zhao et al., 2007 and 2010). The prolonged aridity may be explained by the high present-day evapo-transpiration potential of 2000-3000 mm/yr, which also existed during the glacial periods (Phillips et al., 1993). The overall high evapo-transpiration must have suppressed any incoming high moisture fluxes during the Holocene. It is surprising, however, that even as the Holocene climate in the QB stayed dry and favorable to produce dust, dust fluxes and thus wind erosion were dramatically reduced as evidenced by the Dunde ice-core record (Thompson, 1989). Simultaneously, dust emission and loess accumulation in the CLP also decreased substantially as evidenced by the start of paleosol formation at 9.3 ± 0.5 ka (Porter et al., 2001; Yaofeng et al., 2008). The greatest factor for the Holocene reduction in the dust flux and in turn wind erosion may have been the changing wind pattern and reduction of wind speeds in response to a northward shift in the polar jet stream.

Another factor that may have decreased Holocene wind erosion in the QB is the local formation of salt crust. Today, parts of the Qaidam, including yardangs and depressions, are covered with a 10 to 35 cm thick salt crust (Fig. 2.3 E), especially where the salt-rich Qigequan Formation (Pleistocene) is exposed at the surface. Here, the salt-crust potentially armored the landscape and protected the underlying material from erosion. Formation of the salt crust in the QB may have coincide with the massive increase of chloride in the Dunde ice-core record at the Pleistocene-Holocene transition ~10,000 years ago and in turn a significant reduction of dust input (Thompson et al., 1989), resulting in lower erosion rates in areas affected by salt-crust formation throughout the Holocene.

On the basis of the above mentioned climatic and geologic considerations it is reasonable that wind-erosion rates were significantly higher during the last glacial period compared to our determined ^{10}Be-erosion rates covering the past

~15,000 years. This is in line with the dust deposition history in the Dunde ice-core and the CLP, both of which show major changes with the start of the Holocene around ~10^4 years. In general, such a history would translate into higher wind erosion rates during previous glacial conditions compared to determined mean ^{10}Be bedrock erosion rate of 0.125 mm/yr. This interpretation is in line with basin-wide averaged erosion rates from the QB, based on geological cross-sections (0.29 mm/yr, Kapp et al., 2011) (Fig. 2.4). Likewise, 50 m high yardangs carved into 120 to 400 ka flat laying lake deposits, imply similarly high minimum averaged erosion rates (0.12 to 0.42 mm/yr, Kapp et al., 2011, Fig. 2.4).

In summary, variable climate conditions (a drier climate, less vegetation, and stronger wind speeds during the LGM compared to the Holocene) within the QB should directly translate to variable wind erosion rates over time. Similar variability in wind erosion also occurred in southern Argentina, where yardangs are carved into an early Pleistocene lava flow that is overlain by a 1000 year old lava flow that does not show signs of wind erosion (Inbar et al., 2001) or in the Western Pannonian Basin in Hungary, where times of strong wind erosion activity (during glacial periods) varied with times of enhanced vegetation, landform stability, and subdued erosion (during interglacial periods) (Ruszkiczay-Rüdiger 2011). These correlations imply a global climate impact during the last glacial maximum on wind erosion rates worldwide.

2.4.2 The link to the Chinese Loess Plateau

Despite Quaternary wind erosion in the Qaidam Basin and the presence of the Chinese Loess Plateau located downwind from and east of the QB (Fig. 2.2 B, Porter et al., 2001), few studies have argued for a source-sink relationship between the two areas (Liu et al., 1994; Wu et al., 2010; Kapp et al, 2011). A recent study of wind-blown zircons from the CLP has identified the QB and the northern Tibetan Plateau as the principal source areas (Pullen et al., 2011). Kapp et al. (2011) suggested that wind erosion in the QB has been active since 2.6 Ma and estimated from geological cross-sections that roughly two-thirds of the

Loess Plateau volume can be explained by the volume of eroded sedimentary basin fill. Today, roughly one-third (~3.88 × 10^4 km^2) of the modern basin floor exposes yardangs. If we consider our mean basin-wide averaged wind-erosion rate of 0.125 mm/yr, we estimate a wind eroded volume of ~1 x 10^4 km^3 (erosion rate (0.125 mm/yr) x start of erosion (2.6 Ma) x modern yardang area (~3.88 × 10^4 km^2)). The result is equivalent to a volume of one-sixth of the CLP (Loess Plateau volume ~6 x10^4 km^3). However, if the atmospheric circulation pattern was different than today (Shin et al., 2003; Toggweiler and Russel, 2008; Kapp et al., 2011; Pullen et al., 2011) and wind erosion rates were higher during glacial periods in line with QB basin-wide averaged erosion rates from geological cross-sections and yardangs cut in original flat lying lake sediments (Kapp et al., 2011), erosion rates may have been higher over the long-term. This would result in higher volumes of eroded basin material and would account for a higher amount of the Loess Plateau volume, whereas the remaining material could have been derived from northern Tibet and the Gobi and adjacent sand deserts during interglacial periods (Pullen et al., 2011). Overall, the cosmogenically derived volumetric estimates of eroded QB material support the hypothesis that the QB is a major source of loess for the CLP (Bowler et al., 1987; Kapp et al., 2011; Pullen et al., 2011).

2.4.3 Global comparison and control on wind erosion rates

The wind erosion rates determined for the western QB constitute some of the highest erosion rates measured using in-situ cosmogenic nuclide dating in an arid environment (Fig. 2.1, Table 2.1). This contrasts with ^{10}Be bedrock erosion rates in the hyper-arid Atacama Desert of Chile, which vary between 0.0003-0.006 mm/yr (Nishiizumi et al., 2005), cosmogenic nuclide erosion rates from the Tibetan Plateau of < 0.03 mm/yr (Lal et al., 2003), and typical erosion rates for bedrock surfaces not affected by fluvial or glacial processes (~0.01-0.05 mm/yr ; see Small et al., 1997 for a review of other studies). The range of Qaidam bedrock erosion rates (0.05 to 0.4 mm/yr) agrees well with rates of calculated wind abrasion and yardang development in well-consolidated bedrock from Argentina, Chile, Hungary, Saudi-Arabia and other parts of China (0.01-0.18

mm/yr) (Fig 2.1: red circles; Inbar et al., 2001; DeSilva et al., 2009; Al-Dousari et al, 2009; Ruszkiczay-Rüdiger et al., 2011; Dong et al., 2012), but are much lower than global wind deflation rates (1- 20 mm/yr) (Fig 2.1: green circles; e.g. McCaulay et al., 1977; Goudie et al., 1999; Brookes et al., 2003; Washington et al, 2006; Al-Dousari et al, 2009; Bristow et al, 2009). The stark difference in reported wind erosion rates may be attributed to the different bedrock strengths of the eroding material (unconsolidated vs. weakly consolidated and well consolidated). Overall, in comparison with other global studies on yardang development in bedrock-floored deserts, the QB is by far the most erosive, perhaps with the exception of the Lut desert of Iran, where yardangs, having relief of >100 m, have formed in consolidated late Pleistocene strata (Krinsley et al., 1970; Kehl, 2009).

To further investigate the differences between abrasion and deflation and their individual control on wind-erosion efficiency, we plotted the global estimates of wind erosion rates against rock strength of wind eroded material (Fig. 2.5). We used the range of rock tensile strengths determined by Marin and Sauer (1954), Kulhawy (1975), and Larma and Vutukuri (1978), as a measure of bedrock strength and resistance to erosion. There exists a clear break in the efficiency of wind erosion as bedrock tensile strength increases (Fig. 2.5 A and B). Consolidated bedrock, with greater tensile strength, has much lower wind-erosion rates of ~0.003- 0.667 mm/yr compared to semi- to unconsolidated material, which range between 1 to 20 mm/yr. The result is not surprising since deflation should be dominant in semi- to unconsolidated material, whereas deflation is limited in strong material where the generation of loose material available for deflation is supply limited. In contrast, consolidated rocks, having high bedrock strengths, should only erode by the mode of wind abrasion, but in turn at much lower rates. On the basis of Figure 2.5 b, we define domains of predominantly deflation (σ_t < 2 MPa) or abrasion (σ_t > 2 MPa) as a function of rock tensile strength (Fig. 2.5 b).

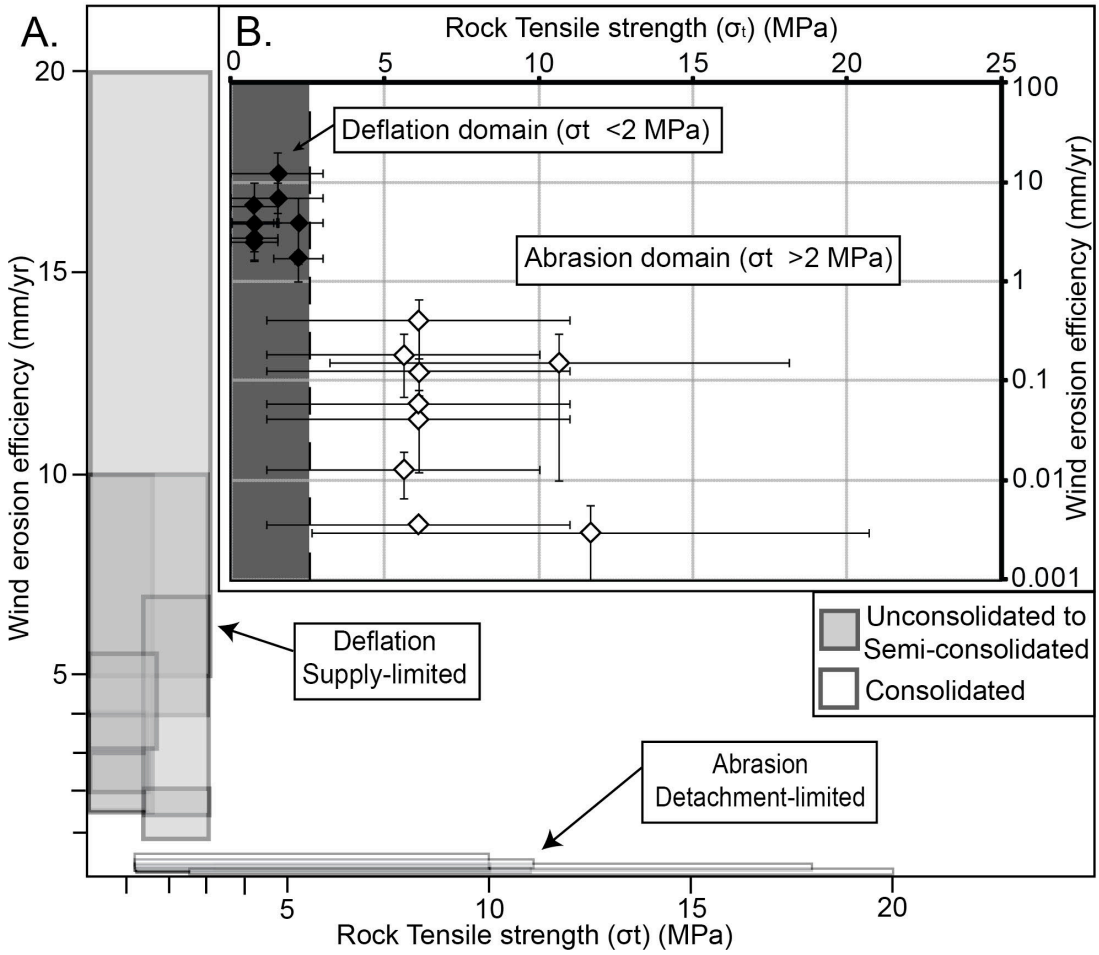

Figure 2.5. A.) Plot of wind erosion rate versus rock tensile strength using the global compilation of wind erosion rates in Figure 2.4 and determined bedrock strengths of the eroding material by Marin and Sauer (1954), Kulhawy (1975), and Larma and Vutukuri (1978). Each box represents a single study and its range of wind erosion estimates and error, as well as the range of determined tensile strengths for the eroding material. Note the large rate difference between semi- to unconsolidated (gray) and consolidated material (white). B) Wind erosion rate is plotted in log-space versus rock tensile strength with error bars. Different colors (black- deflation; white-abrasion) represent individual wind erosion domains controlled by deflation or abrasion.

The exact rock tensile strength at which this transition occurs needs to be systematically investigated in future studies. The relationships depicted in Figure 2.5 b, however, provide a first-order assessment. In summary, deflation processes should be supply-limited, since high rates of up to 20 mm/yr are not sustainable over long periods. This short-term process contrasts with wind abrasion, which is detachment-limited. In general, wind deflation and abrasion should be viewed as two modes of wind-erosion that are not fully distinct from each other, but are controlled by bedrock strength.

2.4.4 Significance of wind erosion and global sediment flux

The role of wind as an erosive agent in significantly contributing to global sedimentary flux has not been analyzed in depth (Goudie, 2008). Nonetheless, wind erosion as shown may be very effective in eroding material in some deserts, and possibly as equally effective as fluvial erosion in many other environments. Our cosmogenically derived wind erosion rates (average 0.125 mm/yr) are within the range of those reported worldwide from glacial (~ 0.08 to 1000 mm/yr) and fluvial (~0.001 to 100 mm/yr) dominated regions (Koppes and Montgomery, 2009). Wind erosion rates are on the same order as glacial erosion rates obtained from the mountains of the Pacific Northwest of North America, for example (~0.1 mm/yr). Compared to fluvial erosion rates, wind erosion rates are on the same order as fluvial erosion measured in rivers from the Apennines (~0.1 mm/yr), they are higher than fluvial erosion rates in cratons (<0.1 mm/yr), and they are comparable to the lower end of the spectrum of fluvial erosion of rivers in tectonically active regions.

The effectiveness of wind as an erosional agent is further highlighted by the thick loess deposits of the CLP as well as large accumulations of dust offshore in the Pacific, Atlantic, and Indian oceans (Porter et al., 2001; Rea et al., 1998; Hanebuth and Henrich, 2009). Loess production itself is today viewed as a direct product of sand grain abrasion and subsequent grain-size reduction, because during the impact of saltating grains the grain size is reduced (Anderson et al., 1986; Crouvi et al., 2008). Under modern conditions, only sand seas and deflating lake basins have been recognized to be major sources and production areas of loess in mid-latitude deserts where loess is not sourced from glacial environments (Crouvi et al., 2010, Enzel et al., 2010). Our study shows that areas with yardangs are also a major source for loess. It is in this type of environment that material is actively being eroded and subsequently experiencing a grain size reduction from sand to fine silt due to the impact of saltating grains during wind storm events.

2.5. Conclusions

New ^{10}Be cosmogenic erosion rates obtained from well consolidated Miocene sedimentary rocks on the Qaidam Basin floor yield eolian bedrock erosion rates between 0.05 and 0.4 mm/yr, with a mean rate of ~0.125 mm/yr. Rates are highest along an actively growing anticlines in Miocene sedimentary strata, and lowest in resistant, granitic bedrock, with a rate of 0.003 mm/yr. Our results provide the first quantification of eolian bedrock erosion rates associated with yardang fields in central Asia. The virtual absence of fluvial erosion on the sharp crested ridges and yardang tops sampled suggest that the erosion is dominated by wind processes. Paleoclimate and geologic evidence, together with the enhanced formation of salt crust at the start of the Holocene, suggest that wind erosion rates may have been highly variable and were likely significantly higher during past, especially during cold, glacial conditions. Our study identifies the Qaidam Basin as an environment of severe wind erosion and implies that wind erosion can occur at rates comparable to fluvial and glacial processes in specific climatic and tectonic settings. Based on existing global long-term (>5000 years) datasets, the Qaidam Basin is one of the most erosive deserts on Earth. Calculated volumes of eroded material from the Qaidam Basin during the Quaternary suggest that at least 16% and potentially more of the Chinese Loess Plateau deposits may have been derived from the Qaidam Basin. In addition, a relationship between wind deflation and abrasion rates was established in relation to the bedrock strength of the eroding material. Our new data will help to calibrate numerical models of wind erosion and yardang development and contribute to a better understanding of abrasion vs. deflation processes in general.

Acknowledgements

The research was funded by donors to the American Chemical Society Petroleum Research Fund (grant ACS PRF# 48729-ND8). We gratefully acknowledge the help of Andrew McCallister during sample collection. Furthermore, we thank Jay Quade for the use of the cosmogenic isotope lab at the University of Arizona, and Bodo Bookhagen for assistance with sample preparation advice. In addition, we thank the DFG-Leibniz Center for Surface Processes and Climate Studies at the Universität Potsdam, Germany, for their support.

Chapter 3

Can stable isotopes ride out the storms? The role of convection for water isotopes in models, records, and paleoaltimetry studies in the central Andes

Rohrmann, A., Strecker, M.R., Bookhagen, B., Mulch, A., Sachse, D., Pingel, H., Alonso, R.N., Schildgen, T.F., Montero, C. (2014), Can stable isotopes ride out the storms? The role of convection for water isotopes in models, records, and paleoaltimetry studies in the central Andes. ***Earth Planetary Science Letters***, 407, 187–195, doi:10.1016/j.epsl.2014.09.021

Abstract

Globally, changes in stable isotope ratios of oxygen and hydrogen ($\delta^{18}O$ and δD) in the meteoric water cycle result from distillation and evaporation processes. Isotope fractionation occurs when air masses rise in elevation, cool, and reduce their water-vapor holding capacity with decreasing temperature. As such, d18O and dD values from a variety of sedimentary archives are often used to reconstruct changes in continental paleohydrology as well as paleoaltimetry of mountain ranges. Based on 234 stream-water samples, we demonstrate that areas experiencing deep convective storms in the eastern south-central Andes (22 - 28° S) do not show the commonly observed relationship between $\delta^{18}O$ and δD with elevation. These convective storms arise from intermontane basins, where diurnal heating forces warm air masses upward, resulting in cloudbursts and raindrop evaporation. Especially at the boundary between the tropical and extra-tropical atmospheric circulation regimes where deep-convective storms are very common (~ 26° to 32° N and S), the impact of such storms may yield non-systematic stable isotope-elevation relationships as convection dominates over adiabatic lifting of air masses. Because convective storms can reduce or mask the depletion of heavy isotopes in precipitation as a function of elevation, linking modern or past topography to patterns of stable isotope proxy records

can be compromised in mountainous regions, and atmospheric circulation models attempting to predict stable isotope patterns must have sufficiently high spatial resolution to capture the fractionation dynamics of convective cells.

3.1. Introduction

The use of oxygen and hydrogen stable isotopes ($\delta^{18}O$ and δD) in the meteoric water cycle has become common practice when assessing the complex relationships among tectonics, climate, topography, atmospheric circulation, and evapotranspiration of the biosphere (e.g. Dansgaard, 1964; Gonfiantini et al., 2001; Bowen and Wilkinson, 2002; Cerling et al., 1993; Dettman et al., 2003; Garzione et al., 2008; Mix et al. 2013). Despite the plethora of applications of these isotopes as proxies for earth surface and atmospheric processes, there is still a lack of understanding of the key factors that affect isotope distillation in orographic rainfall (Rozanski et al., 1993; Worden et al., 2007). This problem is especially relevant in high-elevation mountain ranges and plateau regions, where a systematic decrease in $\delta^{18}O$ and δD of meteoric waters with elevation is not observed, even though large temperature gradients as a function of elevation exist (Poage and Chamberlain, 2001; Rowley et al., 2001; Hren et al., 2009; Lechler et al., 2012; Schemmel et al., 2013). Explanations for this phenomenon have included mixing of different moisture sources (Hren et al., 2009), high-elevation evaporation (Schemmel et al., 2013), and snow sublimation (Lechler et al., 2012). Beyond these factors that likely contribute to discrepancies between expected/ modeled and observed $\delta^{18}O$ and δD patterns in the geologic proxy record, the isotope-enabled atmospheric circulation and climate models themselves suffer from limitations that are attributed to (1) the low spatial resolution of General Circulation Models (> 50 km), in which mesoscale circulation patterns, e.g., convective storms, cannot be reproduced and local topography is smoothed; (2) oversimplifications in models that tie temperature-dependent isotope fractionation directly to surface elevation; and (3) the low density of meteorological stations in arid and/ or high-elevation terrains, which results in over-representation of station data from humid lowlands and valleys.

Here, in a combined empirical and modeling approach, we investigate the effects of topographic relief, storminess, rainfall mode, moisture recycling, and airflow patterns on modern $\delta^{18}O$ and δD patterns in stream waters sampled along three E-W transects across eastern margin of the south-central Andes between ~ 22 and 28° S (Fig. 3.1) to unravel the relationships between $\delta^{18}O$ and δD values and storminess.

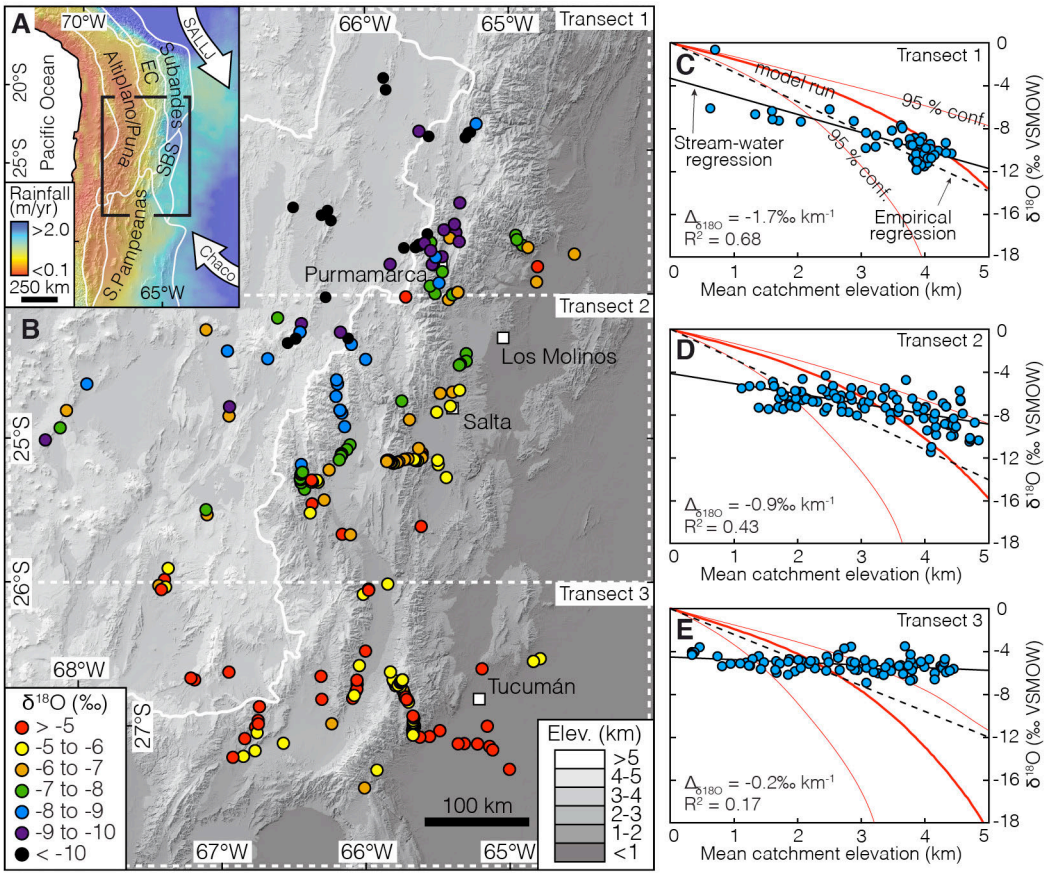

Figure 3.1. Topography, rainfall, and stream-water $\delta^{18}O$ data for the south-central Andes. A. TRMM 3B42 annual rainfall and morphotectonic provinces (SBS: Santa Barbara System). Arrows highlight moisture transport (SALLJ - South American Low Level Jet) (Vera et al., 2006) and orogenward-moisture transport controlled by the Chaco low (Vuille et al., 2003). GNIP-stations from Fig. 3.2 are represented by white squares. B. SRTM DEM and stream-water color-coded $\delta^{18}O$ values (VSMOW). Right diagrams (C-E) represent mean-catchment elevation versus $\delta^{18}O$ (blue circles represent catchment samples), linear regression (solid black line) and global empirical fractionation curve (-2.8 ‰ km^{-1}, black dashed line) for each transect. Rowley et al. (2001) thermodynamic atmospheric model simulations based on DJF MOD11C2 night-temperature and NCEP-NCAR 1000 mbar re-analysis relative humidity data (%) from 2008 to 2013 (Kalney et al., 1996) as starting model input parameters are shown in red.

3.1.1 Precipitation and wind patterns along the south-central Andes

Extending from ~7° N to 45° S, with elevations rising to over 6 km, the Andes constitute a major orographic barrier to southern-hemisphere atmospheric circulation, exerting fundamental control on wind and precipitation patterns (Figs. 3.1 a, 3.2 and figs. B.1, B.2). For at least the last 7 to 8 Myr, the Andes have deflected moisture-bearing trade winds from the equatorial Atlantic and Amazonia towards the south to form the South American Low-Level Jet (SALLJ, Fig. 3.1 a) (Vera et al., 2006; Uba et al., 2007; Mulch et al. 2010), which transports moisture to the eastern Andean flanks and accounts for annual rainfall of up to 3 m/yr (Fig. 3.1 a) (Bookhagen and Strecker, 2008). High seasonality results in >80% of the annual precipitation falling during the austral summer (December to February; Fig. 3.2) (Prohaska et al., 1976). To the south of the region affected by the SALLJ, a secondary jet (Chaco Jet) controlled by the Chaco Low influences moisture transport for the south-central Andes (Fig. 3.1 a) (Salio et al., 2002; Saulo et al., 2004). The Chaco low forms in response to continental heating of the Andean foreland (Chaco plains) in northern Argentina and Paraguay (Salio et al., 2002). To the west, above the ca. 4-km high Altiplano-Puna Plateau, a dry and stable westerly atmospheric airflow occurs at >500 mbar (>5 km; Figs. B.1 and B.2) (Garreaud et al., 2003). After crossing the plateau, the air descends along the eastern Andean flanks forming an orographic wave (Romatschke and Houze, 2013). To the east of the plateau, generally north-south oriented intermontane basins of the Eastern Cordillera and northern Sierras Pampeanas extend over areas of up to ~ 10^4 km^2. These basins are often bounded by ranges with topographic relief in excess of 3 km, rendering them very favorable to high nocturnal heat storage. The descent of upper atmospheric dry and stable air crossing the plateau prohibits orographic ascent of heated and moist air from the foreland and the plateau-parallel intermontane basins (Fig. 3.3 and figs. B.1 and B.2). As a result of the different air-mass properties, an inversion develops. In such a scenario, rainfall is only produced by deep convective storms, which allow warm and humid air below the inversion to break through the overlaying lid (Fig. 3.3 b) (Zipser et al., 2006; Romatschke and Houze, 2013).

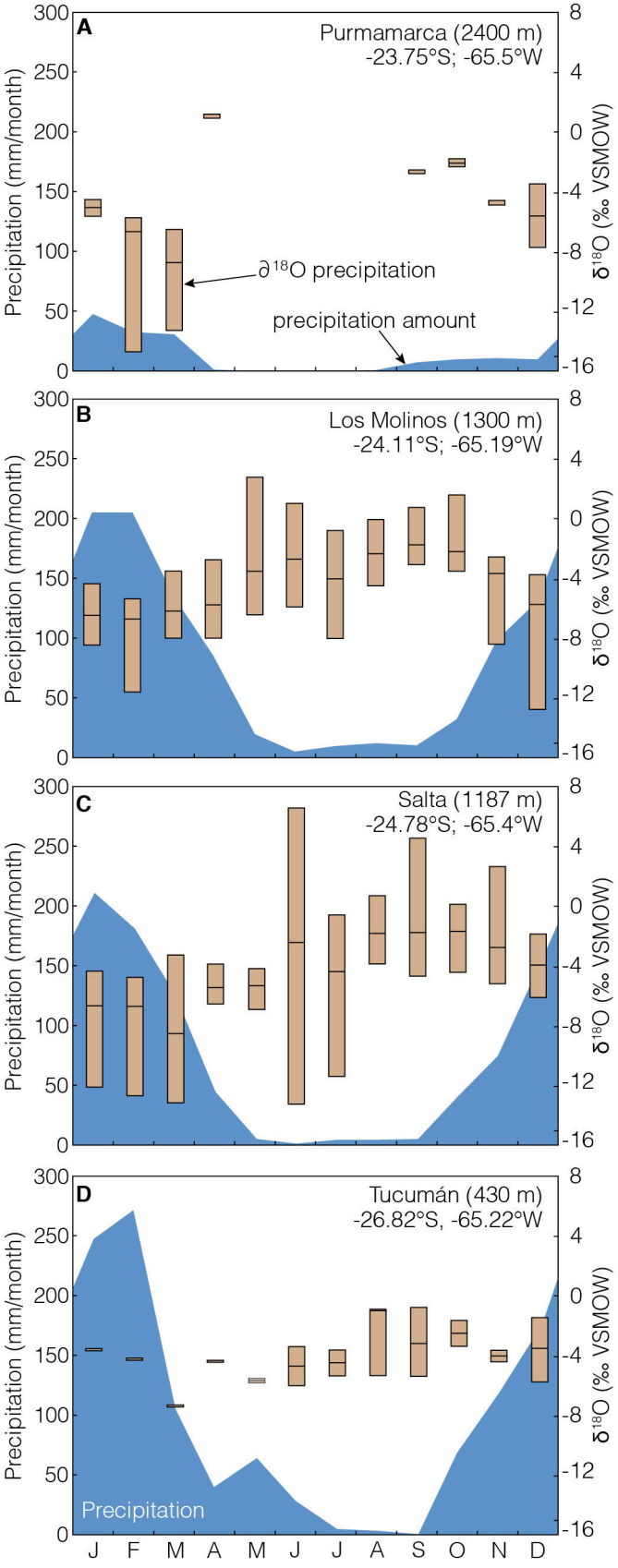

Figure 3.2. Oxygen stable isotope and precipitation data for the GNIP-station from Tucumán, Salta, Los Molinos, and Purmamarca (IAEA, April 2012) (cf. Figure 3.1). Brown boxes show oxygen stable isotope data in precipitation and blue boxes represents the mean monthly rainfall data. Tucumán station data represents 2 yrs of data from 01/05/2001 until 12/01/2002, Salta represents 22 yrs of data from 01/15/1981 to 12/15/2002, Los Molinos 9 years of data from 01/01/1981 to 2/01/1989 and Purmamarca 3 yrs of data from 01/01/1998 to 04/01/2000. Data are taken from the global IAEA/WMO website of Global Network of Isotopes in Precipitation. The GNIP Database is accessible at: http://www.iaea.org/water (IAEA, April 2012).

3.2. Methods

We established an extensive dataset of $\delta^{18}O$ and δD values of stream-water samples across the eastern border of the NW-Argentine Andes between ca. 22°S and 28°S. Our stream-water sampling strategy included individual catchments along the eastern Andean flanks and the internally drained interior of the Puna Plateau with upstream areas between 10 and 100 km^2 and contained flowing water. Field campaigns took place during the months of October through March from 2010 to 2013 with a sampling focus during December, January and February (DJF; Fig. 3.2; Table B.1). As more than 80 % of the mean annual rainfall occurs during DJF contrasted with generally dry austral winter (JJA) months (Fig. 3.2), we were able to capture the bulk of the annual signal of stream-waters.

Samples were collected in 10 ml centrifuge tubes, sealed with plastic caps, and wrapped with parafilm and PTFE tape to prevent sample loss and evaporation prior to analysis. The elevation of each sampling location was recorded and catchment mean elevations were calculated using standard GIS methods. Mean catchment elevations range from 340 m in the east to 4836 m in the west, with high peak elevations well represented in all three transects.

Samples were analyzed at the joint Goethe University-BiK-F Stable Isotope facility at Goethe University Frankfurt. Stable hydrogen and oxygen isotope ratio measurements were made on 1 ml aliquots using an LGR 24d liquid isotope water analyzer. δD and $\delta^{18}O$ values were corrected based on internal laboratory standards calibrated against VSMOW (Vienna Standard Mean Ocean Water). The absolute analytical precision was typically better than 0.6 ‰ and 0.2 ‰ (both 2σ) for δD and $\delta^{18}O$, respectively. Absolute stable isotope values of the sample set range from -24 to -96 ‰ for δD and -4.5 to -13.0 ‰ for $\delta^{18}O$. Detailed results for all samples are presented in Table B.1.

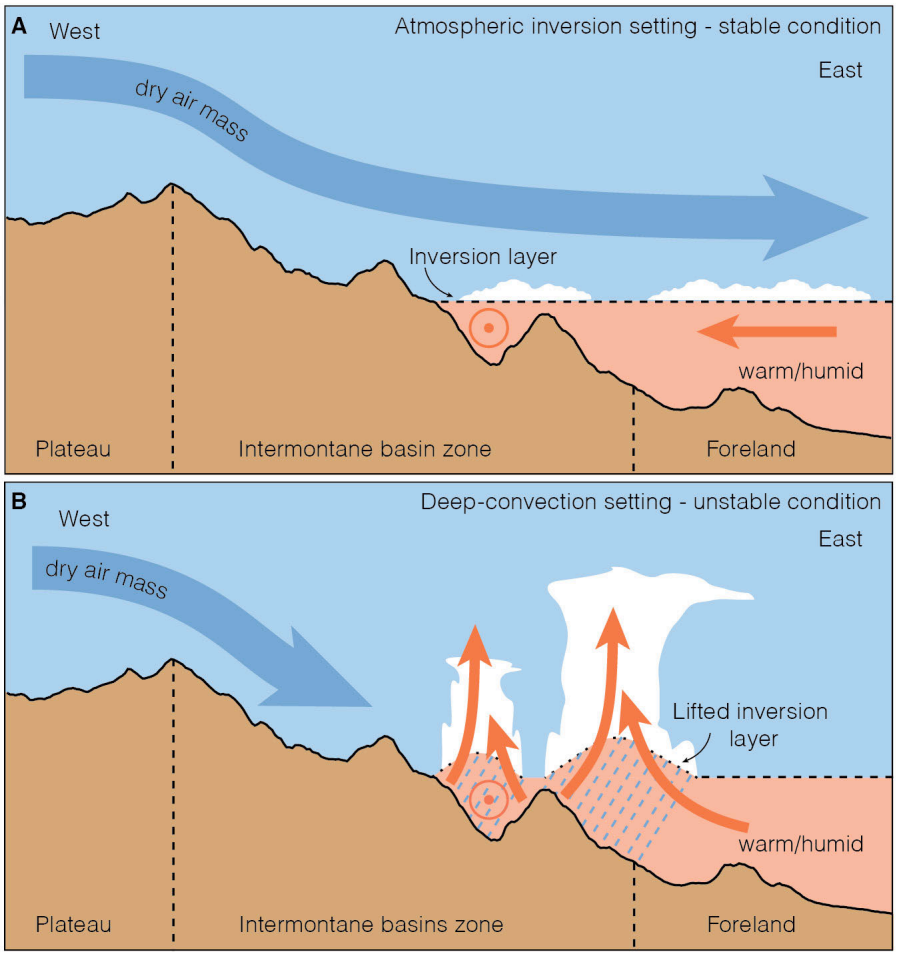

Figure 3.3. Conceptual framework of the orographic wave, inversion ("capping") and lifting ("triggering") across the eastern Andean plateau margin. A: Inversion in place showing intact cap/boundary layer (heavy dashed line) between dry and adiabatically heated sinking air above and advected warm humid air below. B: Reduced orographic airflow and lifting of inversion (light dashed line) with strong upward lifting of warm humid air and eruption of deep-convective storms. Warm humid air in the intermontane basins below the inversion is connected with the foreland through topographic lows (river valleys), which help to advect the humid air mass into the interior (indicated by black circles with point). The large basins south of 24°S act as reservoirs for potential energy (resulting from daily solar heating) from which deep-convective storms can erupt.

3.3. Results

To characterize the spatial distribution of $\delta^{18}O$ and δD in meteoric water (reported in VSMOW), we sampled 234 streams, lakes, springs, snow, and rainfall events over a period of four years along three E-W transects (Figs. 3.1 b, 3.4 a and Fig. B.3; Table B.1). All transects have the same easterly moisture source, but differ in topography, with relatively small intermontane basins and a distinct plateau margin in the north transitioning to large intermontane basins and a highly irregular plateau margin in the south (Figs. 3.1, 3.5 and Fig. B.1). $\delta^{18}O$ values from stream waters range from -0.6 to -11.5 ‰ along transect 1 (22 to 24° S), -4.3 to -11.4 ‰ along transect 2 (between 24 to 26° S), and -2.3 to -6.9 ‰ along transect 3 (26 to 28° S; Figs. 3.1 and 3.5). As we focus on studying the relationships of $\delta^{18}O$ and δD stream water with elevation, we define isotope lapse rates, $\Delta(\delta^{18}O)$ and $\Delta(\delta D)$, which reflect the change of $\delta^{18}O$ (or δD) as a function of elevation. A significant negative correlation between $\delta^{18}O$ and elevation exists in transect 1 with $\Delta(\delta^{18}O)$ = -1.7 ‰ km^{-1} (R^2= 0.68). Along transect 2, $\Delta(\delta^{18}O)$ is reduced to -0.9 ‰ km^{-1} (R^2= 0.43), while there is no significant relationship between elevation and $\delta^{18}O$ for transect 3 ($\Delta(\delta^{18}O)$ = -0.2 ‰ km^{-1} with R^2= 0.17).

Each transect deviates from the global empirical relationship between $\delta^{18}O$ and elevation ($\Delta(\delta^{18}O)$ = -2.8 ‰ km^{-1}; Fig. 3.1), although deviations are much larger in the south (transect 3) compared to the north (transect 1) (Poage and Chamberlain, 2001). In general, there is an increase from -0.2 to -2.4 ‰ km^{-1} in the isotopic lapse rate from 28° S to 15° S along the eastern Andes when the data are compared to stable isotope stream-water data from Bolivia (Gonfiantini et al., 2001). South of 28° S, it is difficult to obtain data as aridity limits perennial stream flow. Stream-water data from a study near Mendoza ca 33° S indicate an isotopic lapse rate of up to -3.9 ‰ km^{-1}; however, sample elevations below 2 km are strongly underrepresented and a spill-over effect of Pacific moisture has been reported there, complicating the comparison with our data from NW Argentina (Hoke et al., 2013).

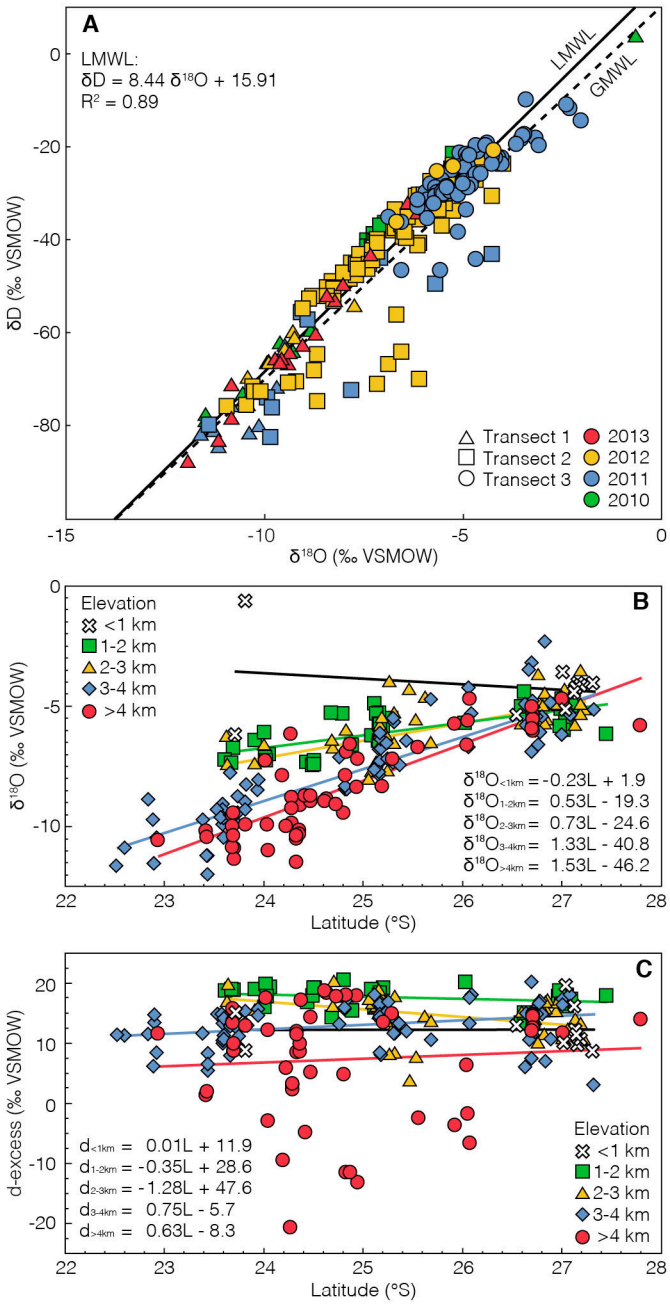

Figure 3.4. Stream-water $\delta^{18}O$, δD, and D-excess data and latitudinal distribution. A. $\delta^{18}O$ versus δD values shape-coded for different water transects and color-coded for their sampling year. Dashed black line represents the global meteoric water line (GMWL) and solid black line is the local meteoric water line (LMWL). B. $\delta^{18}O$ values of stream-water data against latitude. Symbol-color coded objects represent 1-km bins and illustrate the large latitudinal gradient in stream-water. C. 1-km binned D-excess values of stream water data with latitude. Note the scatter in data from elevations >4 km potentially showing Pacific moisture mixing.

3.4. Interpretations

3.4.1 Spatial patterns in oxygen and hydrogen stable isotope composition

Although all low-elevation foreland locations have similar $\delta^{18}O$ values of ~ -4 ‰ (Global Network of Isotopes in Precipitation (GNIP) stations; Fig. 3.2), our data

show a strong north-south gradient in $\delta^{18}O$, isotopic lapse rate, and deuterium excess for the higher-elevation regions (Figs. 3.1 b, 3.4 b-c and 3.5) (IAEA/WMO, 2012). Deuterium excess (defined as $d = \delta D - 8 * \delta^{18}O$) is a parameter determined by non-equilibrium fractionation indicative of sub-cloud evaporation, moisture recycling, snow sublimation, or changes in moisture source (Stewart, 1975; Froehlich et al., 2008; Lechler et al., 2012).

The large decrease in $\delta^{18}O$ (< -10 ‰) along transect 1 (northern transect) compared with $\delta^{18}O$ water values in the foreland is - to a first-order - similar to Rayleigh fractionation. Rayleigh distillation treats the isotopic composition as an open-system distillation, where precipitation is successively removed from the vapor as it condenses and the residual vapor is consistently depleted in ^{18}O and D (Dansgaard, 1964). This process is reflected in the good correlation of $\delta^{18}O$ with elevation (Figs. 3.1 b and 3.5). The westward decrease in *d* from ca. 19 ‰ to -13 ‰ in transect 1 on the plateau is expected for ascending easterly humid air masses that progressively rainout above increasingly drier air. During rainout, sub-cloud evaporation of the falling rain droplets occurs, lowering the deuterium excess values (Fig. 3.5) (Stewart, 1975; Froehlich et al., 2008).

Along transect 2, the relationship between $\delta^{18}O$ and elevation weakens and it essentially disappears along transect 3. There, $\delta^{18}O$ and deuterium excess values from the foreland to the plateau margin are virtually constant (Figs. 3.1 b and 3.5). Such a pattern is inconsistent with simple orographic lifting of warm, humid air masses and associated rainout. Rather, it is indicative of upward convective mixing, resulting in limited open-system distillation necessary for Rayleigh fractionation and hence limited oxygen (and hydrogen) isotope fractionation of precipitation falling at the Earth's surface. Across the entire latitudinal swath from 22° to 28° S, a strong $\delta^{18}O$ gradient is prominent (Figs. 3.1 and 3.4 b-c). Moreover, there are systematic relationships of the $\delta^{18}O$ values at different elevation intervals as the gradient in the amount of ^{18}O depletion (and hence the isotopic lapse rate) increases with elevation from south to north (Fig. 3.4 b-c). This trend suggests that convection is not only limited to the southernmost transect, but also that the amount of convective rainfall decreases northward,

thus directly affecting the observed oxygen-isotope lapse rates (Fig. 3.1). D-excess (*d*) shows no trend with latitude, illustrating that the moisture source along all three transects is similar and derived from the Amazon Basin (Figs. 3.1 and 3.4 b-c). However, several samples at elevations > 4 km show much more negative *d* values, likely resulting from mixing with a Pacific moisture source.

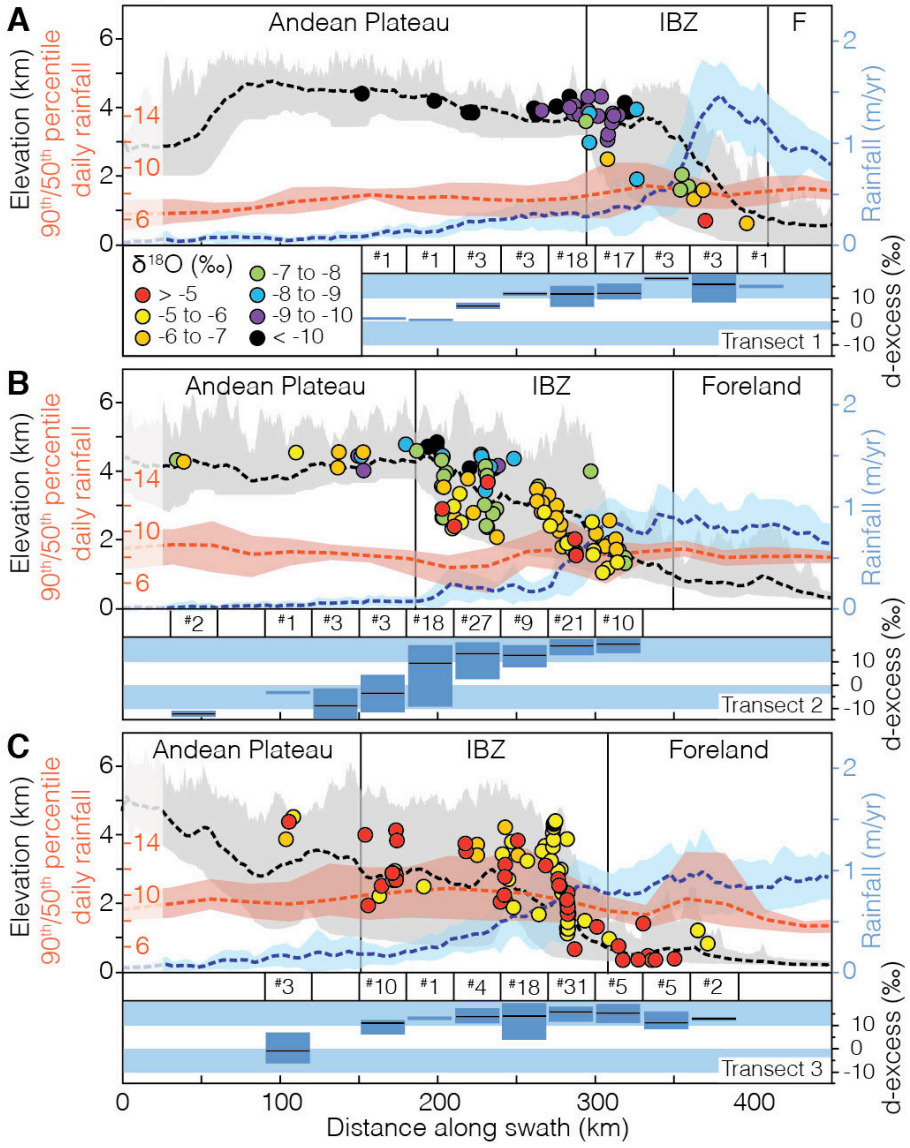

Figure 3.5. Swath profiles showing maximum, minimum (gray shading), and mean elevation (black) TRMM-2B31 rainfall data (blue) (Bookhagen et al., 2008), and TRMM 3B42 V7 90th/50th percentile ratio of daily rainfall (red) across the south-central Andes (Huffmann et al., 2007; Boers et al., 2013). Stable isotopic values ($\delta^{18}O$) have the same color scale as in Figure 3.1. Blue bins below each transect show range and mean (gray line) of deuterium excess values along the profile. Each box represents samples located in a 30-km-wide interval with numbers of samples for each bin shown above.

3.4.2 Temperature-lapse rates and modeling of stable isotopes in precipitation

To gain additional insight into the controls on $\delta^{18}O$ and δD values of meteoric water in the Central Andes, we use a numerical thermodynamic Rayleigh condensation model to predict stable isotopic compositions along the sampled transects (Fig. 3.1 b; and supplementary materials for further details) (Rowley et al., 2001). First, we define a surface temperature-lapse rate for each transect based on 12 yrs of satellite-derived DJF land-surface temperature data (MOD11C2) to obtain input starting temperatures for the model (Figs. 3.6 a and 3.7; and Supplementary materials for further details) (Wan et al., 2002). The MODIS satellite data are calibrated against surface stations and have accuracies of better than 1°C (Wan et al., 2008). In general, temperature-lapse rates below 2000 m are in line with a dry adiabatic cooling trend of ~ 1.0 °C per 100 m, whereas at elevations above 2000 m, they follow a moist-adiabatic cooling trend of 0.5 °C per 100 m (Fig. 3.7). Consequently, the obtained data set was subdivided into elevations above and below 2000 m based on the different temperature lapse-rate trends. For transect 1, lapse rates <2000 m are -0.92°C/100 m ($n = 134$, $R^2 = 0.85$, $p << 0.01$) and -0.21°C/100m for > 2000 m ($n = 855$, $R^2 = 0.63$, $p << 0.01$); transect 2 lapse rates < 2000 m are -0.80°C/100 m ($n = 346$, $R^2 = 0.55$, $p << 0.01$) and -0.38°C/100 m for > 2000m ($n = 1965$, $R^2 = 0.63$, $p << 0.01$); transect 3 lapse rates < 2000m are -0.64°C/100m ($n = 748$, $R^2 = 0.74$, $p << 0.01$) and -0.47°C/100 m for > 2000m ($n = 2121$, $R^2 = 0.68$, $p << 0.01$) (Fig. 3.7). The null hypothesis for the p-values was that the elevation (x) and temperature (y) are derived from independent, random samples from normal distributions with equal means and equal, but unknown variances. For the model input humidity starting parameters, we used the NCEP-NCAR 1000 mbar re-analysis relative humidity data (%) from 2008 to 2013 (Kalney et al., 1996).

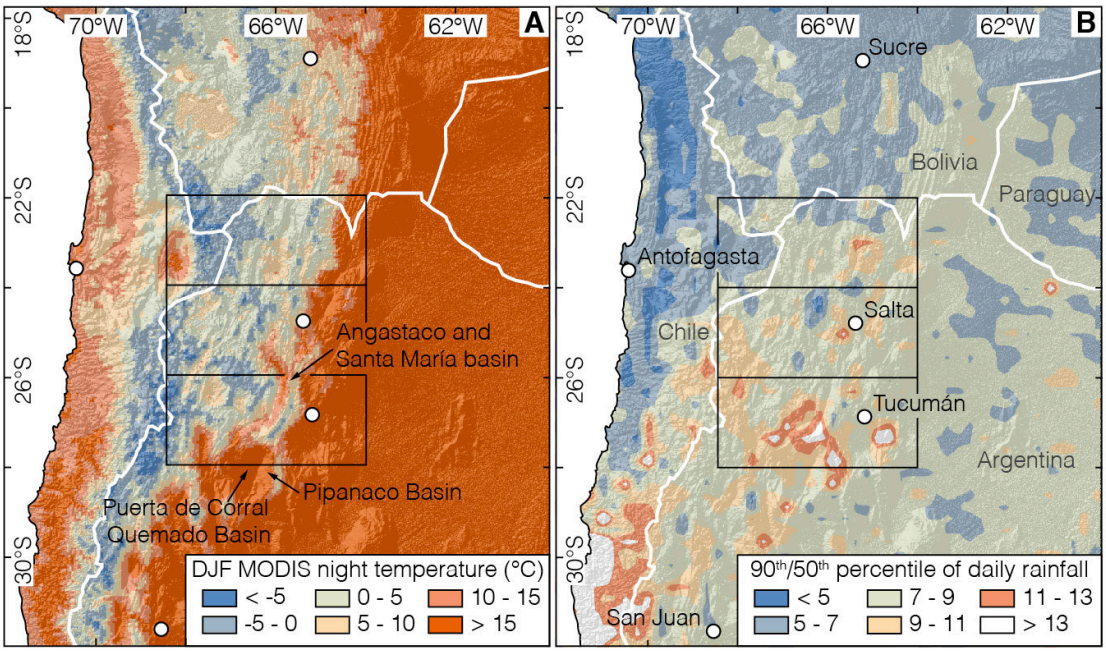

Figure 3.6. A. TRMM-3B42 V7 90th/50th percentile of daily rainfall data averaged over 15 yrs (Huffmann et al., 2007; *Boers et al., 2013*). Low ratios indicate a narrow rainfall distribution (i.e., stratiform rainfall), whereas high ratios indicate a 'heavy-tail' rainfall distribution (i.e., deep convective storms). White lines represent international borders. B. Night land surface temperatures (MOD11C2) (*Wan et al., 2002*) for DJF averaged over 12 yrs. Note the intermontane basins between 26° and 30°S storing excess heat and potential energy for convection.

The thermodynamic Rayleigh condensation model based on atmospheric temperature-lapse rates and fractionation with elevation as rising air masses cool provides a reasonable prediction of observed isotopic compositions along transect 1 (red lines; Fig. 3.1 c-e). Isotope $\delta^{18}O$ values >3 km are well represented, whereas lower elevations show a mismatch between observed and modeled values, likely due to downstream mixing of higher-elevation stream water. However, in transect 2, the fit of predicted $\delta^{18}O$ and δD values weakens, as high-elevation samples obtained in locations >4 km start to fall outside the model's 95% confidence level. In transect 3, the model does not match the observed $\delta^{18}O$ pattern at all. Especially, elevations > 3 km plot outside the model bounds, implying that fractionation here does not follow open-system behavior, which is a prerequisite for Rayleigh fractionation (Fig. 3.1 e).

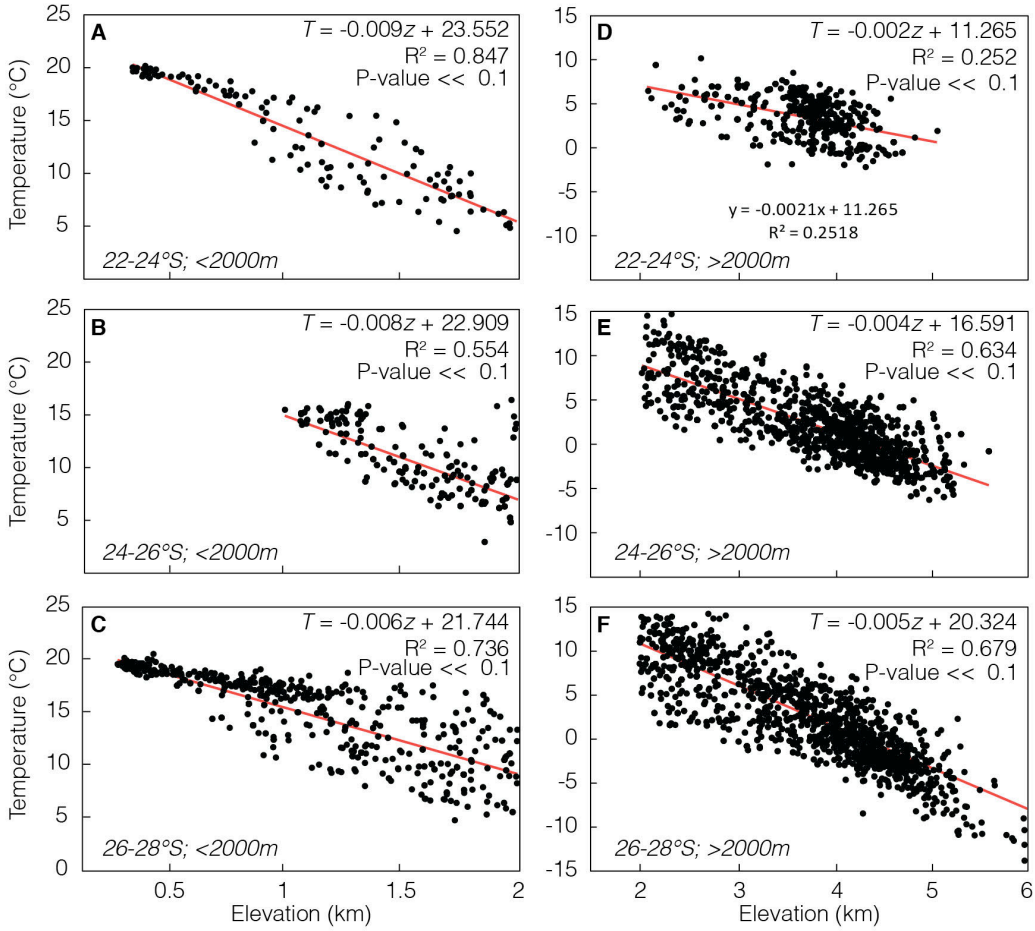

Figure 3.7. MOD11C2 night land surface temperatures for December, January, and February (DJF) averaged over 12 yrs from 2000 to 2012. The temperature data are divided into elevations above and below 2 km. Raster resolution is 5.5 km and black points represent temperature information of individual cells. Only cells overlapping sampled catchments are used for calculating temperature-lapse rates. Note the differences between lapse rates above and below 2 km. Lapse rates below 2 km are much closer to dry adiabatic cooling trend, whereas above 2 km, a very suppressed wet adiabatic cooling trend is observed.

3.4.3 Tracing convective rainfall and storminess

Similar to other plateau margins worldwide, strong insolation, high humidity, and pronounced topographic and relief gradients along the windward flanks of the Andean plateau result in frequent and extreme hydro-meteorological events (Zipser et al., 2006; Bookhagen and Strecker, 2008; Romatschke and Houze, 2013). High-spatial resolution TRMM-2B31 and 2A25 satellite data (Tropical Rainfall Measuring Mission - TRMM) allows for examination of convection

processes and precipitation patterns between 36° N and 36°S (Huffman et al., 2007; Bookhagen and Strecker, 2008; Romatschke and Houze, 2013). We use TRMM 3B42V7 $90^{th}/50^{th}$ percentile ratios for daily rainfall as a proxy for deep-convective rainfall and to define patterns of strong convection and storminess (Huffman et al., 2007; Boers et al., 2013) (Fig. 3.6 b). We normalize extreme rainfall amounts associated with convective storms (90^{th} percentile) by the median (50^{th} percentile) for each pixel to document distinct spatial patterns in rainfall extreme events (Fig. 3.6 b). The $90^{th}/50^{th}$ percentile ratio is a measure of how skewed the rainfall distribution is for a particular area and thus cannot identify the mode of precipitation. Therefore, it is necessary to identify the source (e.g., convection) of the skewness in the rainfall data to interpret the $90^{th}/50^{th}$ percentile data accurately. For example, the high $90^{th}/50^{th}$ percentile ratios along the western flank of the Andes do not exhibit convective nature, but reflect very strong, infrequent wintertime frontal rainfall events producing a skewed rainfall distribution (Fig. 3.6 b).

In the Eastern Andes, the high $90^{th}/50^{th}$ percentile ratios south of 26°S (Fig. 3.6 b) agree well with TRMM-Precipitation Radar data (PR, product 2A25), which characterizes the nature of rainfall in South America and also shows frequent deep-convective storms south of 26° S (Romatschke and Houze, 2013). There, the trigger for convection is not diurnal heating as elsewhere in the tropics, but rather conditions favorable to lifting the inversion found along the south-central Andes over intermontane basins (Fig. 3.3 and B.4) (Romatschke and Houze, 2013). Specifically, daytime warming of large intermontane basins stores significant potential heat, which is available at night to lift the inversion and promote deep-convective storms (Fig. 3.6 a). The rapid lifting of warm, humid air from beneath the inversion causes rapid upward convective mixing of moisture, resulting in limited open system distillation. As a result, convective rainfall does not systematically deplete the air mass of heavy isotopes, because moisture recycling replenishes the depleted air at high elevation (Risi et al., 2008). Hence, convective air circulation allows storms to cross high topography without major depletion in ^{18}O or D, as illustrated by consistently high deuterium-excess values

along transect 3 and only slightly decreasing deuterium-excess values in transect 2 (Figs. 3.4 and 3.5).

3.5. Discussion

3.5.1 Controls on stable-isotope systematics

Our results demonstrate that despite general agreement with globally observed stable isotope-elevation relationships in transect 1, elevation does not exert a first-order control on $\delta^{18}O$ values in the southernmost transects across the southern-central Andes (Figs. 3.1, 3.4 and 3.5). This interpretation is supported by the virtual absence of a relationship between rainfall amount and topographic relief (Fig. 3.5). In contrast, $\delta^{18}O$ and δD stream-water samples along transect 1 agree with other available studies of $\delta^{18}O$ and δD located north of 22° S, where the climate is generally more humid and the tropical atmosphere regime is characterized by lower storm frequencies (Fig. 3.6 b) (Gonfiantini et al., 2001; Insel et al., 2012). In the region of transect 1, the temperature-lapse rate with elevation drives rainout and stable-isotope fractionation, but this is not the case south of 26°S along transect 3, which is influenced by the extra-tropical atmospheric circulation regime and increased convection (Fig. 3.5). These contrasting patterns in our data between the northern and southern transects exemplify how studies of $\delta^{18}O$ and δD at the boundary between the tropics and extra-tropics (~ 26° to 32° N and S) can be strongly affected by deep convective storms (Fig. 3.6). Consequently, repeated convective storms may yield unexpected and non-systematic oxygen-isotope lapse rates as a function of elevation. In such cases, the assumption of temperature-controlled rainout with elevation producing a systematic isotopic lapse rate can be severely compromised. Our data are the first to demonstrate the causes and consequences of missing oxygen (and hydrogen) isotope depletion in the presence of large temperature gradients with elevation, and particularly how deep-convection can overprint isotope systematics in precipitation as upward moisture mixing in storms violates the open-system assumption in Rayleigh fractionation.

3.5.2 Implications for isotope-enabled atmospheric circulation models, paleoenvironmental studies, and paleoaltimetry studies

Reconstructions of paleo-environmental conditions and the topographic evolution of mountain belts are often derived from stable isotope proxies in materials such as pedogenic carbonates, volcanic glass, mammal-tooth enamel, or organic compounds. Each of these materials retains the $\delta^{18}O$ or δD composition of ancient meteoric waters (e.g. Lee-Thorpe and van der Merwe, 1987; Cerling et al., 1993; Garzione et al., 2008; Mulch et al., 2008; Sachse et al., 2012). Especially for materials that capture short-term variations in the isotopic composition of rainfall, the absence of systematic stable isotope-elevation relationships may render any paleoaltimetry interpretation complex, if not impossible (Blisniuk and Stern, 2005). Our results therefore have major implications for understanding, interpreting, and modeling present and past $\delta^{18}O$ and δD data, especially regarding paleoelevation and paleoenvironment assessments within and along the Andean orogeny and beyond.

First, current stable-isotope enabled General Circulation Models rely solely on adiabatic cooling and temperature fractionation induced by changes in elevation. Our results demonstrate the need for sufficiently high resolution in these models to capture regional mesoscale convective cells, which would far more accurately reflect regional stable isotope values of precipitation. Otherwise, modeled $\delta^{18}O$ and δD values will substantially deviate from observation data, a phenomenon observable for the region along our transect 3, which is characterized by highly convective rainfall (Insel et al. 2012).

Second, in regions with deep convection, it will be difficult to reliably reconstruct topography or paleoenvironmental conditions through stable-isotope approaches, because strong convection may reduce or mask any elevation signal in the geologic proxy record. Therefore, interpretations of $\delta^{18}O$ and δD records (e.g., from pedogenic carbonates, lipid-biomarkers, or tooth enamel) that assume simple Rayleigh fractionation in areas influenced by deep convection at the

tropical-extratropical boundary may provide misleading information on the elevation and/or climate history and should be validated against additional proxy records. As an example, $\delta^{18}O$ values from pedogenic carbonate and mammal teeth of Tertiary sediments within the deep-convective zone of transect 3 at 27.5°S / 67°W (Fig. 3.1) at the Puerta de Corral Quemado intermontane basin show little variability (-7.5 to -4.5 ‰) between ~ 8 to 3 Ma (Latorre et al., 1997; Hynek et al., 2012). Nonetheless, several lines of evidence indicate a pronounced phase of mountain building and surface uplift during that time. At ~ 6 Ma, low-temperature thermochronology data derived from adjacent basement ranges and sediment characteristics of the adjacent basins indicate that ranges to the north and east of the basin were uplifted and started forming orographic barriers (Strecker et al., 1989; Bossi et al., 2001; Kleinert and Strecker, 2001; Sobel and Strecker, 2003). These range uplifts blocked moist easterly airflow and induced changes from C3 to C4 plant communities in the basin (Hynek et al., 2012). The lack of concurrent significant variation in the $\delta^{18}O$ record likely indicates that the region was influenced by convective storms, both between ~ 8 to 3 Ma as well as today.

In the context of these paleoenvironmental studies, we caution that only those areas that are not affected by deep-convection may be appropriate for stable isotope paleoaltimetry -- an approach whose applicability and reliability has been intensely discussed over the past decade (e.g., Poage and Chamberlain, 2001; Blisniuk and Stern, 2005; Rowley and Garzione et al., 2007; Ehlers et al., 2009). We also conclude that the complicating effects of convective rainfall have not been fully considered in a variety of stable isotope paleoaltimetry studies in the southern-central Andes (e.g., Canavan et al. 2014; Carrapa et al., 2014). This oversight may potentially lead to oversimplified misinterpretations of quasi-constant stable isotope – elevation relationships in regions that today (and likely in the past) were strongly subjected to convective rainfall conditions. Conversely, farther north, where extensive intermontane basins are less frequent and deep convective storms are typically not generated (e.g., regions adjacent to the Subandean fold-and-thrust belt or in the Eastern Cordillera), our identification of

Rayleigh fractionation in modern precipitation is encouraging for stable isotope paleoaltimetry studies.

3.6. Conclusions

Overall, our results add a new element in the interpretation of stable isotope data from precipitation along elevation/ temperature transects, particularly when attempting to interpret past records of $\delta^{18}O$ and δD. Such present-day validation studies of water stable-isotope patterns are crucial for extra-tropical regions that are affected by deep-convection, as convection can disrupt simple patterns of rainout and Rayleigh isotopic fractionation with increasing elevation. Understanding atmospheric circulation patterns along plateau margins with pronounced rainfall gradients, such as the Altiplano-Puna or Himalaya-Tibetan Plateau, is of particular importance, as strong convection cells can arise not only from areally extensive intermontane basins and foreland regions, but also from steep topographic barriers. In summary, our results illustrate that (1) atmospheric convection can strongly affect $\delta^{18}O$ and δD in precipitation and overprint simple relationships between stable isotopes in precipitation and elevation that are due to temperature-controlled fractionation and orographic lifting; (2) isotope-in-precipitation models based on temperature-related fractionation alone that do not have sufficient spatial resolution to capture convective storms can deviate substantially from the observed $\delta^{18}O$ and δD patterns; and (3) in regions with convective rainfall, we emphasize the necessity for careful assessments of modern $\delta^{18}O$ and δD data before attempting to interpret $\delta^{18}O$ and δD data in the geologic record.

Acknowledgements

This study was funded by the Deutsche Forschungsgemeinschaft (DFG joint grants: STR 373/32-1, MU2845/4-1) with support from the DFG-Leibniz Center for Surface Processes and Climate Studies at Universität Potsdam, Germany (DFG 373/18-1) and the LOEWE funding program (Landes-Offensive zur Entwicklung wissenschaftlich-ökonomischer Exzellenz) of Hesse's Ministry of Higher

Education, Research, and the Arts. D. Sachse was supported by a DFG Emmy-Noether grant (SA1889/1-1). We acknowledge the support of J. Fiebig at the Joint Goethe University - BiK-F stable isotope facility Frankfurt and H. Meyer at the Alfred-Wegener-Institute in Potsdam. We thank D. Rowley, M. Hren and an anonymous reviewer for insightful reviews.

Chapter 4

Rapid hydrological response to orographic barrier and central Andean Plateau uplift

Rohrmann, A., Sachse, D., Strecker, M.R., Mulch, A., Pingel, H., Alonso, R.N. (submitted), Rapid hydrological response to orographic barrier and central Andean Plateau uplift. ***Science***

Abstract

Orogenic plateaus and their flanking ranges may strongly impact regional and global hydrology, vegetation, and erosion. Yet, the detailed temporal characteristics of topographic growth and possible feedbacks between tectonics and climate are not well understood in these regions (Molnar et al., 2010; Garzione et al., 2008; Hoorn et al., 2010). During the last decade reconstructions of the topographic evolution of mountain belts and orogenic plateaus and ensuing environmental changes have been increasingly retrieved from stable isotope proxies in sedimentary deposits from basins within and along the plateaus. These proxies retain the oxygen ($\delta^{18}O$) or hydrogen (δD) composition of ancient meteoric waters or they reflect former vegetation covers ($\delta^{13}C$), in case of pedogenic carbonates (e.g. Cerling et al., 1993; Friedman et al., 1993; Kleinert and Strecker, 2001; Hoke et al., 2014; Zhuang et al., 2014). Sedimentary fills with intercalated volcanic ash horizons in the intermontane basins east of the Andean Plateau of NW Argentina (Puna) record the eastward-directed lateral growth of the central Andes and their impact on hydrologic, sedimentary and ecological changes through time (Jordan and Alonso, 1987; Baby et al., 1997; Hilley and Strecker, 2005; Hain et al., 2011). We reconstructed paleohydrological changes from a sedimentary sequence exposed in the intermontane Angastaco Basin of NW Argentina (25°45 S, 66° W) deposited during Andean plateau uplift and adjacent orographic barrier formation (10-2 Ma) by using an array of stable water isotope proxies (lipid biomarker δD and $\delta^{13}C$; soil carbonate $\delta^{18}O$ and $\delta^{13}C$; and volcanic glass δD). Combined, these proxies provide a unique precipitation – evapotranspiration record that reveal the onset of a monsoonal precipitation

regime related to the South American Low Level Jet at this latitude by 9 Ma. This was accompanied by protracted, seasonally humid foreland conditions until 7 Ma, followed by orographic barrier formation upwind of the basin and later, rapid (~0.5 Myr) intermontane aridification, with a shift to semi-arid conditions. For the first time, our new high-resolution multi-proxy isotope approach enables the reconstruction of the response of the hydrologic cycle, ecosystem, and erosion to Mio-Pliocene Andean tectonism in unprecedented detail.

4.1 Introduction

With average elevations of ~4 km, low internal relief, closed, and partially coalesced sedimentary basins, and high, deeply incised flanks, the Cenozoic Andean plateau constitutes the world's second largest orogenic plateau. The topographic growth of the plateau and the adjacent mountain ranges has generated steep climatic gradients across the orogen, with a humid foreland and increasing aridity towards the orogen interior. The Cenozoic uplift of the Andean orographic barrier has been instrumental in establishing the modern atmospheric circulation and rainfall patterns throughout South America (Lenters and Cook, 1995; Garreaud et al., 2003; Bookhagen and Strecker, 2008) (Fig. 4.1 a). Today, the eastern flanks of the central Andes receive up to 3 m of annual precipitation during the austral summer via the South American Monsoon System and the southward transport of Amazonian moisture along the eastern flanks of the orogen by the South American Low-Level Jet (SALLJ) (Carvalho et al., 2011; Marengo et al., 2012). In contrast, basins to the west of the orographic barrier receive less than 0.2 m/yr (Bookhagen and Strecker, 2008). This pattern characterizes the climate in the region between 13° and 27 ° S and is thought to have been established with the onset of the SALLJ due to surface uplift of the Altiplano-Puna Plateau at 9 Ma (Garzione et al., 2008; Mulch et al., 2010). However, it is unclear as to how far south SALLJ moisture transport reached during an episode of pronounce Miocene mountain building, and when humid conditions were established along the inherently arid southeastern flank of the Puna. Following the hydrological patterns found along the windward flanks of

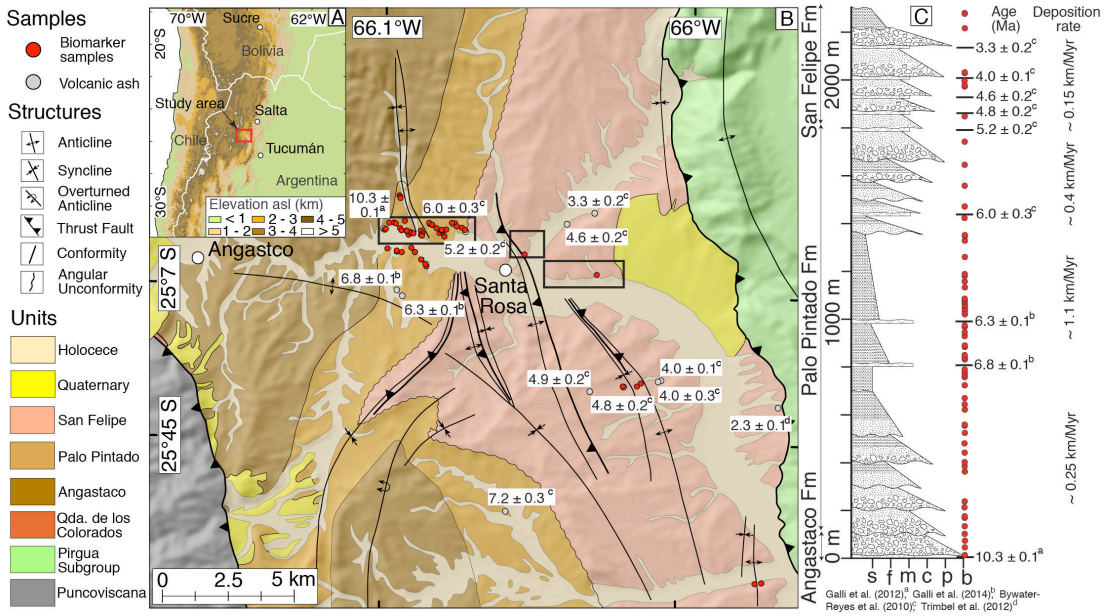

Figure 4.1. Regional tectonic overview of the study area and stratigraphy. A. Elevation binned SRTM-data and location of the study area. B. Geological map of the Angastaco Basin with lipid-biomarker sample locations and volcanic ash dates (for soil-carbonates samples locations see Table C.2). See legend for symbols and colors. Black boxes mark location of the measured stratigraphic log. C. Measured stratigraphic profile from the Angastaco Basin with lipid-biomarkers sample levels marked with red dots, volcanic ashes with U-Pb zircon and $^{40}Ar/^{39}Ar$-ages. All samples and ashes outside the measured stratigraphic profile are projected along strike of the bed into the stratigraphic section.

the southern-central Andes a dense C_3 vegetation developed here, whereas the leeward sectors host a C_3/C_4 vegetation mosaic, reflecting a semi-arid to arid environment (Ruthsatz and Hofmann, 1984; Starck et al., 2001; Kleinert and Strecker, 2001).

Here, we identify the timing of hydrological changes in response to Andean plateau and orographic barrier uplift through a stable water isotope proxy array from terrestrial sediments exposed in the semi-arid Angastaco intermontane basin (AB) at 25°45 S and 66° W. The basin, located at ca. 2 km elevation, with up to 6 km of lacustrine and fluvial sediment fill, contains one of the best chronologically constrained sedimentary sections in the region. Importantly, organic material and pedogenic carbonates make the Angastaco sequence an ideal site for a multi-proxy stable isotope study to decipher the evolution of

environmental conditions along the eastern flank of the Andean plateau (Starck et al., 2001; Coutand et al., 2006) (Figs. 4.1 and 2; C.1).

4.2 Results and Discussion

The AB record contains abundant terrestrial lipid biomarkers, specifically the nC_{27} to nC_{33} alkanes derived from the leaf waxes of higher terrestrial plants that originated in the basin's paleo-catchment area at the eastern Andean plateau margin (Eglington and Hamilton, 1967; Sachse et al., 2012) (Figs. 4.2; C.2-7; Table C.1). Our analysis focuses on the nC_{29} and nC_{31} alkanes because their high abundance allowed measurement of the wax's hydrogen isotope values (δD_{wax}) reflecting paleohydrologic changes (Sachse et al., 2012). In addition to the wax's δD_{wax} and carbon isotopes ($\delta^{13}C_{wax}$), we provide high-resolution soil-carbonate oxygen ($\delta^{18}O_{carb}$) and carbon ($\delta^{13}C_{carb}$), and hydrogen volcanic glass (δD_{volc}) isotope values sampled on the same section (Fig. 4.2; Table C.2-3).

The combined stable isotope records reveal three distinct stages in environmental conditions: (1) the integration of sedimentary units of a formerly contiguous foreland into the eastern flanks of the plateau; (2) the formation of an orographic barrier, followed by (3) the development of an intermontane sedimentary basin, similar to a predicted scenario in the lateral plateau-growth model by Sobel et al. (2003) (Fig. 4.2). During early deposition of the Palo Pintado formation in a contiguous foreland δD_{wax} and $\delta^{18}O_{carb}$ values all decreased from high values at ~10 Ma to reach a first isotope minimum after ~8.8 Ma (Fig. 4.2). The data suggest the existence of a foreland-basin setting characterized by humid conditions during the late Miocene, although this region should have been arid, considering its latitudinal position and proximity to cold upwelling along the Pacific coast (Strecker et al., 2007). A humid climate regime at that time is furthermore supported by the character of sedimentary strata from other basins farther north along the eastern Andean flanks, as in the Iruya basin at 22°53 S and 64°36 W (Echavarria et al., 2003) or the Rio Pilcomayo region of southern Bolivia at 21°S (Mulch et al., 2010). These observations support the notion that a southward moisture transport by a paleo SALLJ, similar

to present-day foreland conditions in Argentina, reached as far south as 26 °S at approximately ~8.5 Ma.

Next, we reconstructed the proxy source-waters (SW) and established $\delta D_{leafwater}$ and $\delta D_{preciptation}$, as well as $\delta^{18}O_{soil\text{-}water}$ from δD_{wax}, δD_{volc} and $\delta^{18}O_{carb}$, respectively, providing unique insights into the changes that impacted the hydrological cycle (Figs. 4.3, C.8 and C.9; for source-water reconstruction see supplementary). Converting $\delta^{18}O_{carb\ SW}$ to δD using the local meteoric water line from Rohrmann et al. (2014) and assuming that $\delta D_{volc\ SW}$ and $\delta^{18}O_{carb\ SW}$ are representative of precipitation and soil water, respectively, the isotopic difference between both values reflects the effects of soil evaporation (Cerling et al., 1993; Friedman et al., 1993). Instead, the difference between $\delta^{18}O_{carb\ SW}$ and $\delta D_{wax\ SW}$ reflects leaf-water deuterium isotope enrichment above soil water, and thus transpiration (Cerling et al., 1993; Sachse et al., 2012; Kahmen et al., 2013) (Fig. 4.3). The relative difference between reconstructed source-waters $\delta D_{volc\ SW}$ and $\delta D_{wax\ SW}$ therefore documents regional trends in evapotranspiration (Fig. 4.3). The evapotranspiration record fits well with the different isotopic phases mirroring the foreland-intermontane basin transition. Plant transpiration was high between ~10 to 8.5 Ma and decreased to low levels after 8.5 Ma, which is compatible with the regional increase in humidity via the SALLJ (Fig. 4.3).

Subsequently, δD_{wax} and $\delta^{18}O_{carb}$ values showed a trend towards more positive values suggesting slightly drier conditions (Fig. 4.2). The larger variability in $\delta^{18}O_{carb}$ compared to δD_{wax} values may result from the fact that the $\delta^{18}O$ signal is derived from within the basin, whereas the δD_{wax} reflects organic material from overbank deposits supplied by western catchments along the plateau flanks. This signal is consequently interpreted to integrate runoff from the basin, the uplifting eastern flanks of the Puna, and the Eastern Cordillera, thus dampening the overall magnitude of change (Coutand et al., 2006; Deeken et al., 2006; Galli et al., 2014; Ponton et al., 2014) (Fig. 4.2). The $\delta^{13}C_{wax}$ and $\delta^{13}C_{carb}$ values during this period range between -31 to -35 ‰, and -17 to -10 ‰, respectively, representative of an exclusively C_3 vegetation cover (e.g. Cerling et al., 1993; Chikaraishi and Naraoka, 2003) (Fig. 4.2).

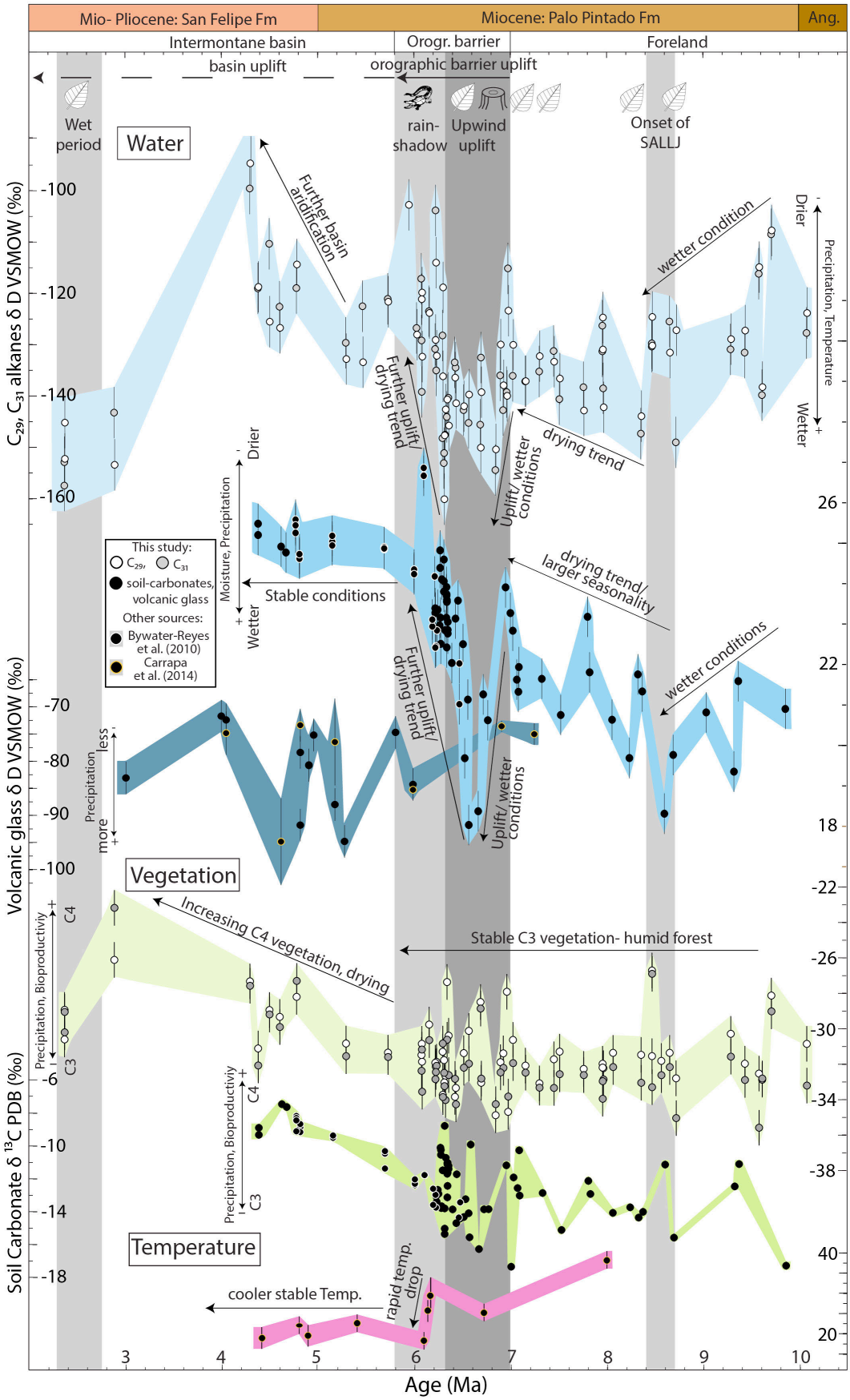
Mio- Pliocene: San Felipe Fm
Miocene: Palo Pintado Fm
Ang.
Intermontane basin
Orogr. barrier
Foreland
basin uplift
orographic barrier uplift
Wet period
rain-shadow
Upwind uplift
Onset of SALLJ
Water
Further basin aridification
wetter condition
Further uplift/ drying trend
drying trend
Uplift/ wetter conditions
Drier
Wetter
Precipitation, Temperature
Moisture, Precipitation
Stable conditions
drying trend/ larger seasonality
wetter conditions
This study:
C29, C31
soil-carbonates, volcanic glass
Other sources:
Bywater-Reyes et al. (2010)
Carrapa et al. (2014)
Precipitation
less
more
Vegetation
Increasing C4 vegetation, drying
Stable C3 vegetation- humid forest
Precipitation, Bioproductiviy
C4
C3
Temperature
cooler stable Temp.
rapid temp. drop
C29, C31 alkanes δ D VSMOW (‰)
Volcanic glass δ D VSMOW (‰)
Soil Carbonate δ 13C PDB (‰)
Soil Carbonate δ 18O VSMOW (‰)
C29, C31 alkanes δ 13C PDB (‰)
Δ47 Temperature (°C)
Age (Ma)

Figure 4.2. Stable isotope data and compilation of all proxy materials of δD_{wax}, $\delta^{13}C_{wax}$, $\delta^{18}O_{carb}$, $\delta^{13}C_{carb}$ and δD_{volc}. Each record has a precise age model based on tephrochronology shown in figure 4.1. All δD and $\delta^{18}O$ data are represented according to the Vienna Standard Mean Ocean Water (VSMOW) scale; $\delta^{13}C$ data are reported according to the Pee Dee Belemnite (PDB). 1-sigma dating error for all isotope proxies of ± 0.1 to 0.3 Ma. Error bars represent pooled precision for δD_{wax} (5 ‰) and $\delta^{13}C_{wax}$ (0.5 ‰) of external isotope standards. Analytical errors are being used for $\delta^{18}O_{carb}$, $\delta^{13}C_{carb}$ and δD_{volc}. See supplementary data and tables for isotope proxies sources and analytical values. Alligator fossil information and location is from Bona et al. (2014). Fossil leaf and tree-trunk data is derived from the measured stratigraphic log in this study.

The fit between $\delta^{13}C_{wax}$ and $\delta^{13}C_{carb}$ has a slope of 0.94 (R^2 = 0.48), supporting the inference that pedogenic carbonates reflect plant CO_2 respiration and track the amount of C_3 and C_4 vegetation in the landscape (e.g., Cerling et al., 1993). Together with a high estimated clumped isotope temperature of 38°C (biased towards summertime temperatures) obtained from the basin strata (Carrapa et al., 2014), tree trunks, leaf morphologies, and pollen assemblages from the same section record a humid C_3 forest-ecosystem, potentially similar to the present-day Paranaense flora of southwest Brazil (e.g. Herbst et al., 1987; Starck et al., 2001; Hoorn et al., 2010) (Fig. 4.2). Plant transpiration must have been low between ~8.5 to 7 Ma, suggesting high humidity during this time interval (Fig. 4.3). The stable isotope proxy data together with available paleoenvironmental indicators therefore suggest a low-elevation (< 0.5 km), humid open foreland for this area during the late Miocene.

Sediments of the Palo Pintado formation deposited between approximately 7 and 6.3 Ma record a rapid decrease in δD_{wax}, $\delta^{18}O_{carb}$, and $\delta^{13}C_{wax}$ and $\delta^{13}C_{carb}$ with the lowest isotope values measured in the section. These trends were coupled with an increase in sedimentation rate from ca. 0.4 to > 1 km/Myr, corresponding to the transition from the contiguous foreland to the orographic barrier stage as rapid accumulation space was created (Figs. 4.1 and 4.2). The fluvial network of the basin changed dramatically due to orographic barrier uplift of the León Muerto and Los Colorados ranges to east of the present-day AB.

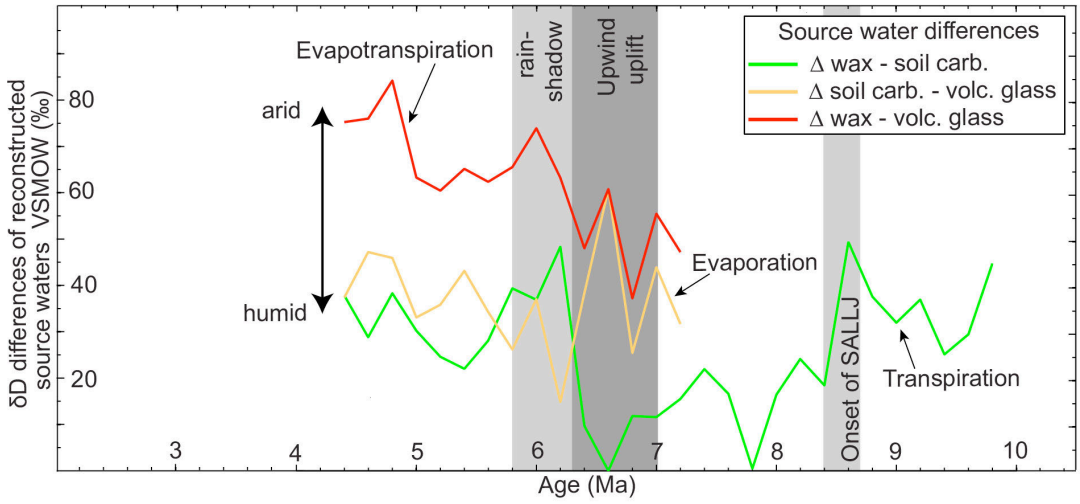

Figure 4.3. Reconstruction of evaporation, transpiration and evapotranspiration over time based on proxy source-water reconstruction. Reconstructed source-waters for lipid-biomarkers, pedogenic carbonates and volcanic glass shards, suggest different source-waters for the individual proxies: volcanic glass: precipitation; pedogenic carbonates: soil-water; lipid biomarkers: leaf /soil –water (Figs. C.8, C.9 and supplementary data repository). Note that $\delta^{18}O_{carb\ SW}$ is converted to δD values for comparison with $\delta D_{wax\ SW}$ and $\delta D_{volc\ SW}$. The relative source-water differences track the paleohydrological evolution over time, i.e. volcanic glass - pedogenic carbonates = evaporation; pedogenic carbonates – lipid biomarkers = transpiration; volcanic glass – lipid biomarkers = evapotranspiration.

The uplift severed the connectivity between the eastern flanks of the Puna, the Eastern Cordillera, and the open foreland (Coutand et al., 2006; Deeken et al., 2006; Carrapa et al., 2011; Hain et al., 2011) (Fig. 4.1). Fining-upward sediments and wetland and lacustrine facies assemblages document this stage (Fig. 4.1). Today, the threshold elevation for effective orographic barriers in the southern-central Andes is ~2 km (Bookhagen and Strecker, 2008; Hain et al., 2011). Since sufficient moisture still reached the AB during the early uplift of the proto Sierra de León Muerto to support a C_3 vegetation, as indicated by $\delta^{13}C_{wax}$ values spanning from -30 to -34 and low plant transpiration, the proto Sierra de León Muerto did not yet constitute an effective orographic barrier (< 2 km) between 7 and 6.3 Ma (Figs. 4.2 and 4.3). The reductions in δD_{wax} and $\delta 18O_{carb}$ at that time therefore record growth of the Sierra de León Muerto and not uplift of the basin sensu stricto (Fig. 4.2). Therefore, a minimum estimate for the uplift of the orographic barrier between 7 to 6.3 Ma, may correspond to ca. 1.5 km (previous

foreland < ~0.5 km), since an effective orographic barrier (> 2 km) was established after 6.3 Ma. Orographic barrier uplift on the order of 1.5 km was accompanied by a ~30 ‰ decrease in δD_{wax} and a 5 ‰ decrease in $\delta^{18}O_{carb}$. Thus, a surface uplift of about 1 km in the southern-central Andes was accompanied by a 20 ‰ change in δD_{wax} or a 3.3 ‰ change in $\delta^{18}O_{carb}$. However, other effects, such as the amount affect, changing moisture source or overall wetter conditions, can similarly influence the signal, but might not have the first-order control on isotope values in rainfall in such a tectonically active region (e.g. Poage and Chamberlain, 2001; Risi et al., 2008).

After 6.3 Ma the basin aridified rapidly, evidenced by increasing δD_{wax} and $\delta^{18}O_{carb}$ values from -160 to -102 ‰ and 18 to 31 ‰, respectively. This happened likely in response to uplift of the Sierra de León Muerto as an effective orographic barrier and occurred over a time span of only 0.5 Ma, (Fig. 4.2). At the same time plant transpiration quickly increased responding to reduced humidity as a result of orographic barrier formation (Fig. 4.3). During the same time Δ_{47} temperatures decreased from 29° to 11 °C (Carrapa et al., 2014). Despite these severe environmental changes toward more arid conditions the AB still supported a diverse fauna and a C_3 vegetation indicative of sufficiently high water availability, which may have been sourced from run-off generated at higher elevations (Herbst et al., 1987; Starck et al., 2001) (Fig. 4.2). The inference of sustained humid conditions is supported by a recent alligator fossil find *(Caiman latirostris)*. Today, living relatives of this species exist in the low-elevation foreland, suggesting that the basin itself had not gained any significant elevation yet (Bona et al., 2014).

At approximately 5.8 Ma the region transitioned into the intermontane basin stage as the basin started to be uplifted along west-verging back thrusts (Fig. 4.2) (Carrera et al., 2006). Between ~6 to 4.5 Ma an overall 20 ‰ reduction in δD_{volc} is observed, possibly reflecting uplift of the basin itself. However, increased aridity and the observation of convection in present-day stable isotope meteoric waters from this region indicate no significant isotope lapse rate (Fig. 4.2) (Poage and Chamberlain, 2001; Rohrmann et al., 2014). During this time the

sedimentation rate significantly decreased from 0.4 km/Myr to ca. 0.15 km/Myr. In addition, the basin further aridified as documented by δD_{wax} value increase to -98 ‰ and sediment coarsening up-section, with increasing deposition of conglomerates and saline lacustrine sediment in the superseding San Felipe formation (Figs. 4.1 and 4.2). Δ_{47} temperatures also stabilized at values around 18 to 20°C, similar to the present-day, with little variability throughout the remaining intermontane basin stage (Carrapa et al., 2014). During this episode $\delta^{13}C_{wax}$ values indicate further aridification expressed through a change from a C_3 to a C_4 dominated ecosystem, in line with tooth-enamel isotope data from the AB (Fig. 4.2) (Bywater-Reyes et al., 2010; Diefendorf, et al. 2011). Furthermore, the level of plant transpiration stabilized at a high level, related to new plant species populating the area in response to increased aridity (Fig. 4.3). Overall, the paleoenvironmental evapotranspiration appears to have been mainly driven by plant transpiration in response to basin aridification, as the evaporation seems to be relatively stable over the entire time-period signal (Fig. 4.3). The stable evaporation signal throughout the record likely reflects the overall seasonal climate as soil carbonates preferentially form at the end of the wet season when evaporation increases (Peters et al., 2013).

4.3. Conclusions

Our new multi-isotope proxy record highlights specific paleohydrological and ecological changes and their timing in response to tectonic deformation and surface uplift in the southern-central Andes. These observations emphasize the potential to reconstruct spatiotemporal changes in evapotranspiration trends in the context of tectonic forcing. Interestingly, the large δD_{wax} inferred increase in leaf-water isotope enrichment of > 50 ‰ throughout the Palo Pintado sedimentary section is similar to the present-day difference between the Amazonian rainforest and the semi-arid environments of the intermontane basins on the western flank of the Andes (Kahmen et al., 2013). The precipitation – evapotranspiration record obtained from our analysis reveals that in regions with monsoonal climates the overall degree of evaporation remains rather constant. In contrast, transpiration rapidly reacts to a decrease in available

moisture related to orographic barrier uplift and tectonically induced environmental changes. For the first time, our results deconvolve the complex links between environmental changes and their imprint on stable isotopes in the hydrological cycle, as well as vegetation changes and tectono-climatic feedback processes in the southern-central Andes.

Acknowledgements

This study was funded by Deutsche Forschungsgemeinschaft (DFG joint grants: STR 373/32-1, MU2845/4-1) with support from the DFG-Leibniz Center for Surface Processes and Climate Studies at Universität Potsdam, Germany (DFG 373/18-1) and the LOEWE funding program (Landes-Offensive zur Entwicklung wissenschaftlich-ökonomischer Exzellenz) of Hesse's Ministry of Higher Education, Research, and the Arts. D. Sachse was supported by a DFG Emmy-Noether grant (SA1889/1-1). We acknowledge the support of J. Fiebig at the Joint Goethe University - BiK-F stable isotope facility Frankfurt.

Chapter 5

Discussion, Outlook and Conclusion

The main goal of this thesis was to understand the impact of eolian and fluvial processes on the evolution of orogenic plateaus and the impact of tectonic processes on forcing hydrologic conditions during the build-up of orographic barriers to rainfall. One of the most important issues in this undertaking is to understand present-day hydrological processes with the goal of better understanding the environmental impact of similar processes in the geological past. This will ultimately help to assess present-day climate variability and future climate change. Such a complex task can be best achieved by integrating geological, geomorphic, paleontological, and isotope geochemical data. Thus, retrieving and generating interdisciplinary data sets from a variety of geological archives may provide the raw material to decipher the full spectrum of forcing factors that drive the surface-process regime in orogenic plateaus. Below, I summarize my findings of chapters 2, 3, and 4 by discussing the newly generated information that assists in efforts to provide new, unifying view across different plateau environments. Since the direct implications have already been discussed in the individual chapters, I will now focus on the outcome of my investigation, particularly in the context of remaining challenges in characterizing plateau paleoenvironments. I will also discuss the implications of my research with respect to the environmental evolution of high-mountain regions and their forelands in light of future climate change, as envisioned in the IPCC's fourth assessment. Finally, I will present an outlook for future studies, followed by a conclusion.

5.1. Discussion

My results highlight the existence of hydrological, vegetation, and surface-process regimes in the different elevational sectors of plateau regions and their

flanking mountain ranges, spanning humid to arid environments. First, wind erosion is one of the most important processes for eroding arid plateau interiors, as low amounts of rainfall, low streampower, and internal drainage conditions prevent material evacuation toward the foreland (e.g., Goudie, 2007; Kapp et al., 2011). In contrast to these environments, fluvial processes and protracted fluvial connectivity within the foreland dominate in the fully humid plateau flanks and their arid to wet transitional regions, (e.g., Ouimet et al., 2010; Gasparini and Whipple, 2014). The erosional gradient from wet to arid environments across plateau margins and the reduction of fluvial erosive power is complemented by the greater efficiency of wind erosion in arid regions. However, it will be difficult to quantify each erosive agent independently, since mixing between fluvial and wind erosion will occur in the climatic transition zones (de Silva et al., 2010). In this context, it is important to note that the water stable isotope results of chapter 3 show that the strongest convective storms are located in semi-arid transition zones. These extreme hydrometerological events aid further to increase the erosivity in such climatic environments, which are characterized by a sparse vegetation cover and steep hillslopes (Bookhagen and Strecker, 2012; Carretier et al., 2013; Whipple and Gasparini, 2014). Corresponding observations were made in the Angastaco Basin paleorecord (chapter 4). Here, deposition rates and by inference, erosion rates were found to be highest during orographic barrier uplift and the tectonically forced transition from wet to dry conditions. It is noteworthy that the effects of reduced fluvial connectivity and the creation of sediment-accommodation space have a similar control on the deposition rate (e.g., Sobel et al., 2003). It is known that vegetation cover has a stabilizing effect on the landscape and protects the underlying soil or sediments from erosion (e.g., Langbein and Schumm, 1958; von Blanckenburg et al., 2004; Vanacker et al., 2007). In the Angastaco Basin record, this stabilizing effect may have been greatest during the humid foreland stage and is documented by leaf-wax carbon isotope values and supporting paleoecological evidence, which suggest humid, dense C3 vegetation covers at this time (e.g., Herbst et al., 1987; Starck and Anzótegui, 2001). It is conceivable that the dense vegetation would have potentially limited erosion, although precipitation and fluvial runoff would have been greatest. A similar, present-day pattern is also seen parallel to the western

flanks of the Chilean Andes, where erosion rates decrease with increasing vegetation cover and rainfall (Rehak et al., 2010; Carretier et al., 2013).

Interestingly, in arid landscapes a positive feedback between the degree of wind erosion, dust production, and plant bioproductivity should exist as dust is transported towards the vegetated humid foreland. Indeed, desert dust and loess are often rich in calcite and other minerals and fertilize soils (e.g., Pye, 1995; Ridgwell, 2002). Therefore, dust production in arid plateau landscapes, such as the Tibetan and Altiplano-Puna plateaus, has a positive effect on vegetation and bioproductivity in the humid foreland sectors. It is important to point out that today a significant portion of agricultural land is situated in these humid lowland areas downwind from the source regions in arid highlands, providing a major contribution to Argentina's, Bolivia's, China's, and India's Gross Domestic Product and food supply (Fischer Weltalmanach, 2003). Desert dust therefore provides an important supply of nutrients and prevents soil leaching over time.

Erosional processes forced by wind and water in tectonically active plateau regions result in different landscape characteristics. Wind erosion has the tendency to reduce overall relief and topography, because wind homogeneously attacks exposed surfaces (e.g., Goudie, 2007; Kapp et al., 2011; Laity et al., 2011). Fluvial erosion is focused on channels and riverbeds, where stream incision undercuts hillslopes, leading to steeper slopes, intensified mass transfer, and ultimately more relief (e.g., Burbank et al., 1996; Whipple et al., 1999). Both processes operate on a plateau-wide scale. Filling of the arid, internally drained basins of the Tibetan and Altiplano-Puna plateaus has produced a setting where wind erosion lowers and smooths relief by selectively eroding topographic features above the basin floor (Goudie, 2007; Kapp et al., 2011). Basin filling and wind erosion are thus synergistic and create low-relief plateau landscapes. In contrast, the role of fluvial incision and its tendency to increase relief is exemplified along the three major Tibetan rivers, Yangtze, Mekong, and Yellow River (e.g., Clark et al., 2004; 2005; Craddock et al., 2010; Ouimet et al., 2010). Here, high amounts of orographic precipitation result in high fluvial runoff and erosion. These observations match the results of chapter 3 along the eastern

flank of the south-central Puna margin, where high relief and rainfall amounts covary north of 25 ° S (e.g., Bookhagen and Strecker, 2008; Strecker et al., 2009; Hain et al., 2011). These regions also produce the highest erosion rates as determined by cosmogenic nuclide dating (Bookhagen and Strecker, 2012).

The modulation of moisture availability forced by tectonic uplift and orographic barrier formation is exemplified by the deposition of intermontane Angastaco Basin sediments (chapter 4). The study demonstrated how humid plateau flanks and associated sedimentary environments might become isolated from moisture supply by orographic barrier uplift. In the case of Angastaco this process was coeval with rapid ecologic and hydrologic responses. Ensuing environmental adaption to the reduced water availability occurred on millennial timescales. These changes are also reflected in changes in the spatiotemporal trends of depositional systems and sedimentary basin fills. Clearly, tectonic processes and related topographic growth significantly govern moisture availability along plateaus by modulating moisture pathways, thereby impacting environmental conditions. These trends match those of previously published records in the southern-central Andes (Strecker et al., 2007; Hain et al., 2011; Pingel et al., 2014), but these recorded changes have never been shown in such temporal resolution as the new stable isotope data presented in chapter 4. Outward plateau growth along fold-and-thrust belts (e.g., central Andes of Bolivia) or isolated block uplifts along steep reverse faults (e.g., Sierras Pampeanas) would result in orographic barriers and exacerbated aridification of plateau interiors (e.g., Isacks, 1989; Jordan and Alonso, 1987; Sobel et al., 2003). These processes are vividly demonstrated by my new multi-proxy data set, as initial rapid 0.5 Ma aridification in the context of orographic barrier formation, and a second later aridification pulse during basin uplift is observed.

As shown in this study and previous investigations on various aspects of plateau growth, changes in topography have a major impact on atmospheric circulation systems as plateaus form orographic barriers and are extensive heating surfaces at high elevation that impact seasonal changes in air pressure (e.g., Prell and Kutzbach; 1997; Ruddiman et al., 1997; Molnar et al., 2010). General circulation

models (GCM) have highlighted the topographic importance of the Himalayan-Tibetan system and Andes for re-routing atmospheric flow and initiating the South American, Indian, and East Asian monsoons (e.g., Lenters and Cook, 1995; Insel et al., 2009; Poulsen et al., 2010; Boos and Kuang, 2010). For the Andes, GCMs have shown that a threshold elevation of ~2 km must be reached before monsoonal circulation patterns start to operate (Poulsen et al., 2010). The South American Low Level Jet (SALLJ), as an integral part in the South American Monsoon circulation system, transports moisture into inherently arid regions in the southern central part of the orogen (Strecker et al., 2007; Garreaud et al., 2009; Silva et al., 2009). My stable isotope multi-proxy study (chapter 4) indicates that this moisture-transport system must have started to operate after 9 Ma and began transporting humid air masses as far south as 26° S. It has been suggested by Mulch et al. (2010) that the SALLJ was established in response to significant topographic uplift of the Central Bolivian Andes. Combined with observations made in NW Argentina, this highlights how plateau topography and atmospheric circulation are strongly connected. A change in either topography or atmospheric circulation would lead in turn to changes in vegetation, hydrology, and/or the form and magnitude of Earth-surface processes, similar to observations made in the Angastaco Basin paleorecord (chapter 4). It remains to be seen if hydrological and vegetation-cover changes in response to the onset of the SALLJ after 9 Ma have had an impact along the entire length of the south-central Andes and if this was a synchronous event. This is an important issue, because there exists little paleoclimatological information for the transition zone between the SALLJ and the westerlies to the south of 28° S (Garreaud et al., 2009). Furthermore, it is important to recognize that with the establishment of the South American Monsoon System there exists not only a stronger moist airflow from the ocean towards the continent during summer, but also a counter-flow from the plateau to the ocean during winter (e.g., Garreaud et al., 2009). This would increase dust transport from the arid plateau interiors towards the foreland and to the Atlantic Ocean. The impact of such dust transport is demonstrated along eastern Tibet, where severe winter dust storms transport sediment far eastward across China and into the Pacific Ocean (e.g., Sun et al., 2001; Wang et al., 2004).

The results of my study have implications for how to view future climate change and climate variability in an increasingly warm world. The *Intergovernmental Panel on Climate Change Fourth Assessment* claims that global warming will lead to reduced water availability and precipitation along the Andean and Tibetan plateaus (IPCC, 2007) (Fig. 1.1). This will have implications for the plateaus' erosion processes, hydrology, and vegetation cover. The reduced water availability and precipitation are expected to lead to further aridification of the plateau interiors, where wind erosion and dust production will then likely increase because of the disappearance and destruction of a protective vegetation cover (e.g., Wolfe and Nickling, 1993). Such a scenario may lead to a local negative feedback cycle in which air temperatures along plateaus may be lower than expected, because of increased albedo (e.g., IPCC, 2007; Seinfeld and Pandis, 2012). Corresponding observations have been made concerning high atmospheric aerosol concentrations in China, where a cooling of air temperatures in response to high atmospheric dust concentrations is observed (e.g., Menon et al., 2002; Qian et al., 2004). The second effect of a projected increase in aridity along plateaus will be the potential for more frequent convective hydrometerological extreme events. As highlighted in Chapter 3, deep-convective storms develop in semi-arid basins along the Eastern Cordillera of Argentina. These environments may foster excessive heat storage, which in turn fuels deep convection. If arid landscapes and environments will expand due to synergistic climatic and tectonic processes, the number of convective storms can be expected to increase and will lead to greater, event-based fluvial runoff and erosion.

5.2. Outlook for future studies

The fields of arid landscape geomorphology, paleoecology, and Earth surface processes have experienced a revival in recent years as new analytical techniques such as cosmogenic ^{10}Be-dating and stable isotope applications to paleohydrology have opened up new possibilities to study complex environmental history (e.g., Ruszkiczay-Rüdiger et al., 2011; Sachse et al, 2012).

In the context of these new developments, the results presented in chapter 2 are the first quantitative wind-erosion estimates using cosmogenic ^{10}Be-dating. As such, this is a promising approach that can be applied to other arid, low-relief landscapes that are impacted by high-speed surface winds. With more quantitative wind-erosion data it will be possible to redefine global sediment fluxes more rigorously (Koppes and Montgomery, 2009). This is particularly important in efforts to better understand the links between sediment sources and sinks for the reconstruction of paleoenvironmental and climatic conditions using loess records (e.g., Porter, 2001; Yaofeng et al., 2008; Kapp et al., 2011; Pullen et al., 2011). The establishment of a source-to-sink relationship, however, has been hampered by a lack of appropriate analytical methods resulting in limited analyses, which are often focused on chemical composition (e.g., Ding et al., 2001; Sun, 2002). Cosmogenic ^{10}Be-dating in wind-eroded landscapes can also help to directly identify the dust sources and quantify wind-erosion rates. At present, many loess records have received little attention, such as the Andean loess record in the Pampean foreland in Argentina (e.g., Smith et al., 2003). For this record, there exists several hypotheses from where the loess might have originated and under what atmospheric conditions it was deposited (e.g., Smith et al., 2003; Gaiero et al., 2013). Further cosmogenic work on yardang fields and wind-abraded bedrock surfaces on the Altiplano-Puna Plateau will help to elucidate wind-erosion rates and dust production in these areas to establish a more reliable source-to-sink relationship (e.g., Greene, 1995; Goudie, 2007; de Silva et al., 2010; Gaiero et al., 2013).

With respect to the water stable isotope studies along and across the south-central Andes (chapter 3), the reduction or masking of the stable isotope-altitude effect in convective regions could be shown to play a significant role for water stable isotope values in precipitation in other regions as well. These include the Karakorum, NW India, and Pakistan (e.g., Poage and Chamberlain, 2001; Houze, 2012). A similar morphotectonic setting and atmospheric conditions exist in these regions and deep-convective storms are frequent (e.g., Houze et al., 2012). Future paleoelevation studies in these regions and elsewhere should take these

issues into consideration. In the South American context, the role of deep-convective storms along strike of the eastern Andes should be systematically analyzed in future studies. Such an analysis of stable isotopes in precipitation spanning southern Argentina to regions as far north as Colombia would be greatly supplemented by several recently published stable isotope data sets (Gonfiantini et al., 2001; Saylor et al., 2009; Hoke et al., 2013). The combination of new and published data would help to identify and understand the complex controls on isotope fractionation and its relationship with topography, climate, and atmospheric conditions. Eventually, such an analysis might furnish information on the controlling atmospheric conditions, i.e. convection, that would be reflected in stable isotope paleorecords. Only then, changes of oxygen and hydrogen isotopes retrieved from ancient records would provide an unambiguous view of topographic changes through time. Recently analyses of atmospheric water-vapor isotope composition in South America using satellite-data products show that modern atmospheric water vapor does not follow simple Rayleigh fractionation, because the reported vapor-isotope composition is too enriched (Worden et al., 2007; Galewsky et al., 2014; Samuels-Crow et al., 2014). The reasons for such enriched atmospheric water vapor are still debated. In general, these studies lack the systematic linkage of the stable isotope composition in atmospheric water vapor and stable isotope composition in precipitation. Open future questions in interdisciplinary studies of this subject therefore are: does the enriched atmospheric water vapor result from convection, and are the enriched isotope values in convective regions a result of enriched atmospheric water vapor? Again, if we are ultimately interested in understanding long-term stable isotope records in the context of surface uplift, it is important to study present-day conditions with several caveats that prevent us from over-interpreting paleoisotope data sets.

The high-resolution Angastaco Basin stable isotope record (chapter 4) was derived from a single basin along the eastern flanks of the Andean Puna Plateau. There is, however, an ambiguity as to how representative the information from a point source (basin) is for the broader regional context of the eastern flanks of the plateau. Fortunately, there are many basins along the Eastern Cordillera,

Sierras Pampeanas and Altiplano-Puna Plateau that expose thick Miocene sedimentary sequences. In light of my studies in the Angastaco Basin and the results that I was able to obtain from organic materials in Miocene sediments, similar sedimentary sequences in the Toro and Humahuaca basins as well as basins farther north in Bolivia or on the Puna Plateau (e.g., the Hombre Muerto, Pocitos, and Pastos Grandes basins) would be excellent locations for future multi-proxy stable isotope studies to identify environmental changes associated with plateau uplift (e.g., Vandervoort et al., 1995; Echavarria et al., 2003; Hilley and Strecker, 2005; Mulch et al., 2010).

5.3 Conclusion

In light of the spatial and temporal environmental changes along and across the eastern flanks of the Altiplano-Puna Plateau and wind erosion processes in Tibet, I reached the following conclusions:

(1) ^{10}Be-erosion rates on wind-eroded bedrock surfaces in the Qaidam Basin range from 0.05 to 0.4 mm/yr, with the majority of these values clustering at 0.12 mm/yr. These rates are comparable to global estimates of wind erosion rates and highlight their general significance for arid landscape evolution.

(2) The reduced importance of fluvial erosion in many semi-arid low-relief environments within or at plateau margins, as demonstrated in the case of the Qaidam Basin, suggests that wind erosion may outpace rates of fluvial erosion. These findings reveal that from a surface-process perspective, these environments are far from being stable, contradicting a long-held paradigm that arid, low-relief environments have generally low erosion rates.

(3) There exists a large difference regarding how deflation and abrasion operate. Abrasion is the process of physical erosion of the underlying bedrock due to particle impacts, and corresponds to erosion rates several orders of magnitudes lower than deflation, which requires only the motion of sediment grains. This relationship is governed by the bedrock strength of the material being eroded.

(4) Precipitation in the arid sectors along the Andes (22-28° S) is low. However, the precipitation that does fall is mainly related to deep-convective storms that are related to day-time heating of intermontane basins.

(5) Hydrological changes and aridification can occur rapidly (~0.5 Ma) along plateaus as moisture availability is modulated by uplifting orographic barriers.

Regarding processes and characteristics of humid plateau flanks, I have reached the following conclusions:

(1) The eastern, windward flanks of the Altiplano-Puna Plateau and the Eastern Cordillera of the south-central Andes receive large amounts of precipitation, decreasing westward with rising topography. Here, the stable isotope–altitude effect in fractionation is expected; however, this pattern is not observed in water stable isotopes of oxygen and hydrogen, and other patterns emerge in the Andes between 22 and 28° S. In this environment, convective storms reduce or mask the depletion of heavy isotopes in precipitation as a function of elevation.

(2) In regions with convective rainfall, I emphasize the need to carefully assess the modern oxygen and hydrogen relationships before attempting to reconstruct plateau paleo-elevations, environmental conditions, climate, or topography.

(3) The $\delta^{13}C_{wax}$ of plant material contained in Neogene sediments in NW Argentina suggests sustained C3 vegetation along former humid plateau flanks that were superseded by arid environments following orographic barrier uplift.

(4) The large inferred leaf-water isotope enrichment of >50 ‰ in the Mio-Pliocene strata of the Angastaco Basin of NW Argentina is similar to the present-day difference between the humid Amazon rainforest and semi-arid intermontane basins in the arid orogen interiors. This exemplifies the large environmental transformations that typically affect laterally and vertically growing plateau margins.

Appendix A

Supplementary material to chapter 2

Sampling sites

Sample site 4-16-09-2

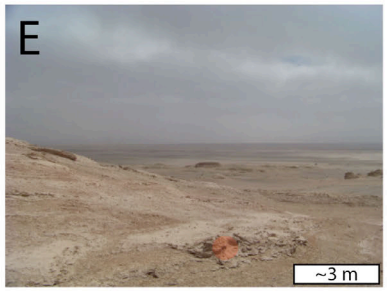

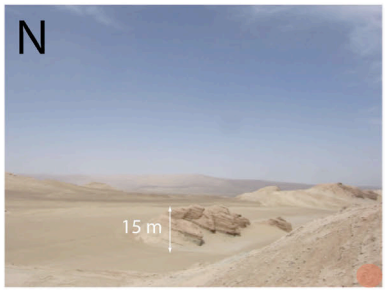

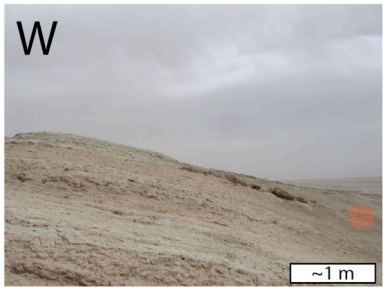

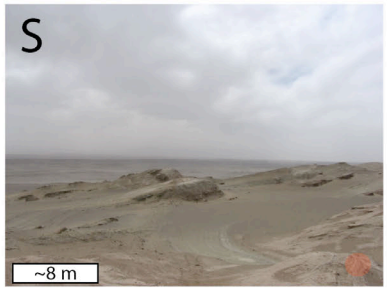

Sample site 4-17-09-2 (70°-cliff face)

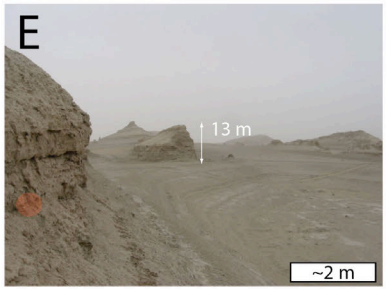

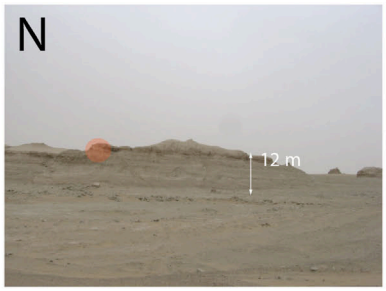

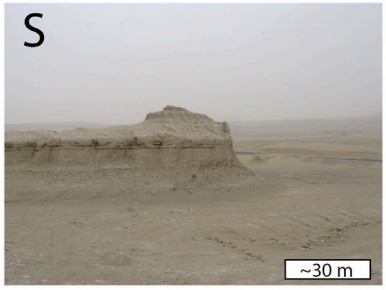

Sample site 4-18-09-2

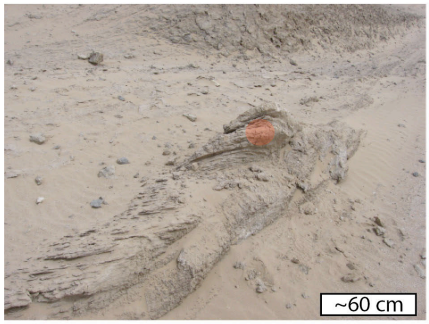

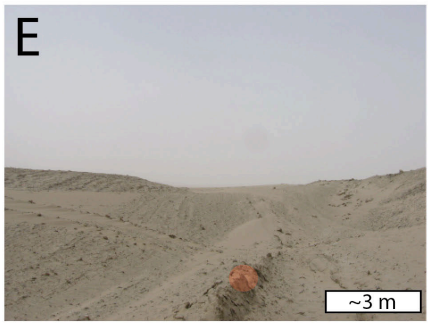

Sample site 4-21-09-2

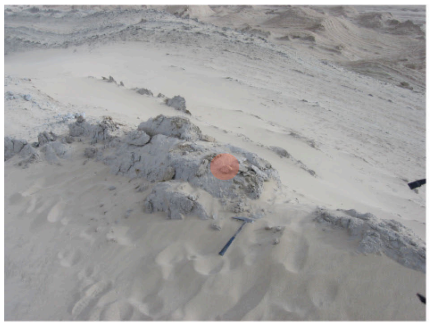

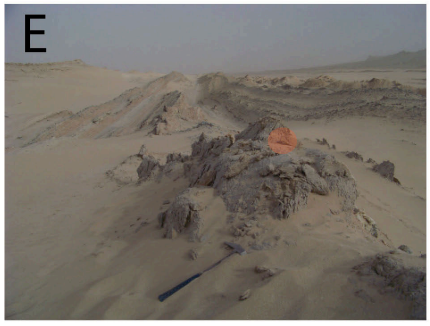

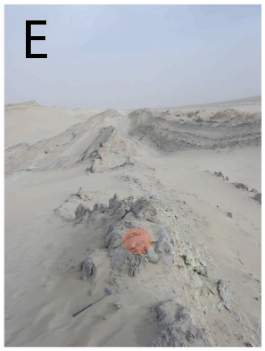

Sample site 4-23-09-2

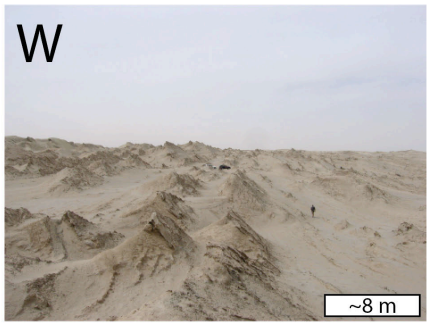

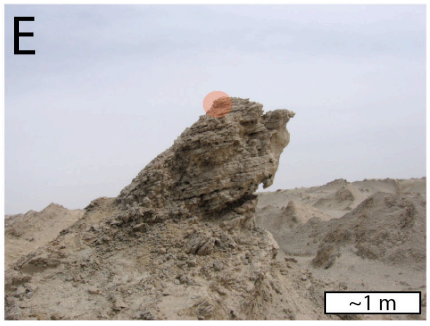

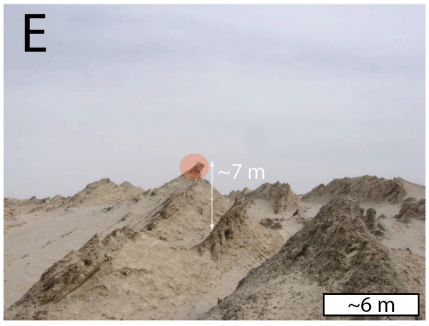

Sample site 4-24-09-1 (Granite sample)

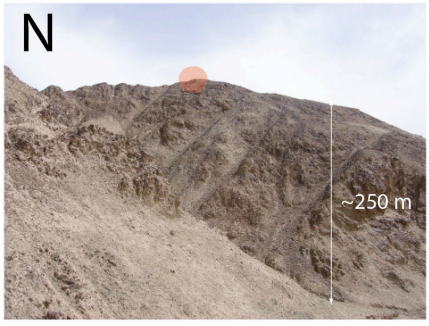

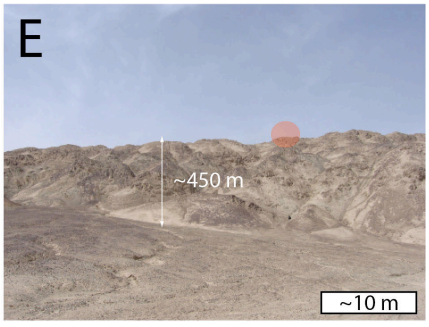

Letter in the upper left corner indicates view direction: S- south; W- west; N- north; E- east. Red dot shows the sampling location for cosmogenic ^{10}Be dating.

Sample site 4-24-09-2

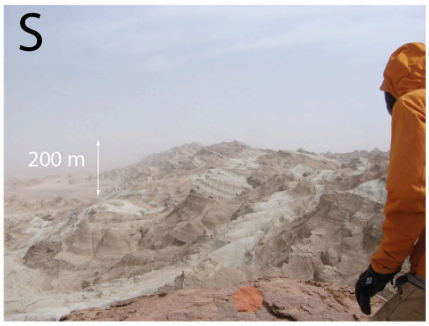

Sample site 4-26-09-1 (70°-cliff face)

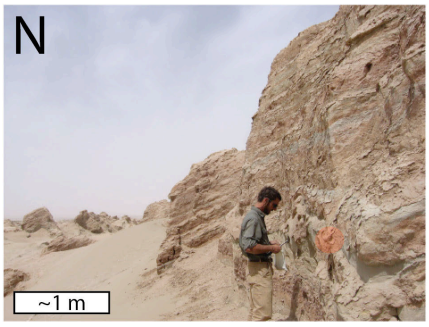

Letter in the upper left corner indicates view direction: S- south; W- west; N- north; E- east. Red dot shows the sampling location for cosmogenic ^{10}Be dating.

Sample site 4-26-09-2

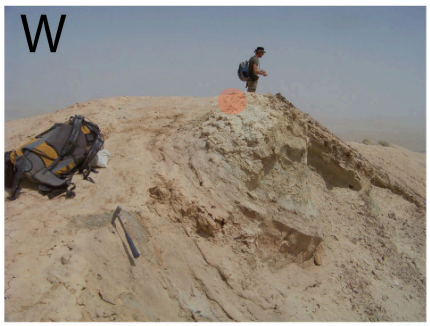

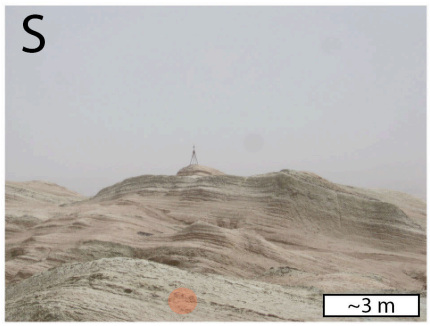

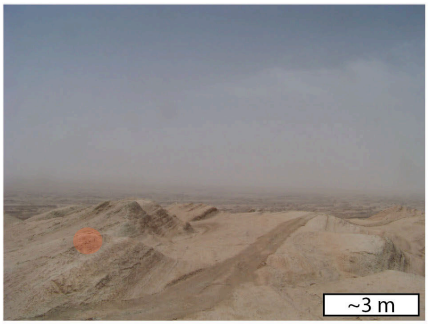

Sample site 4-26-09-3 (Yardang top)

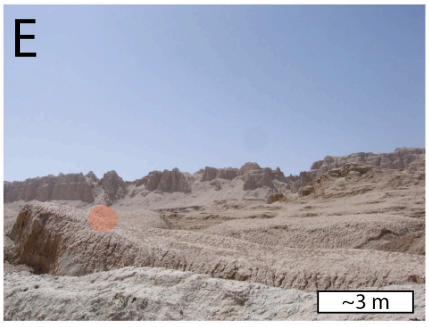

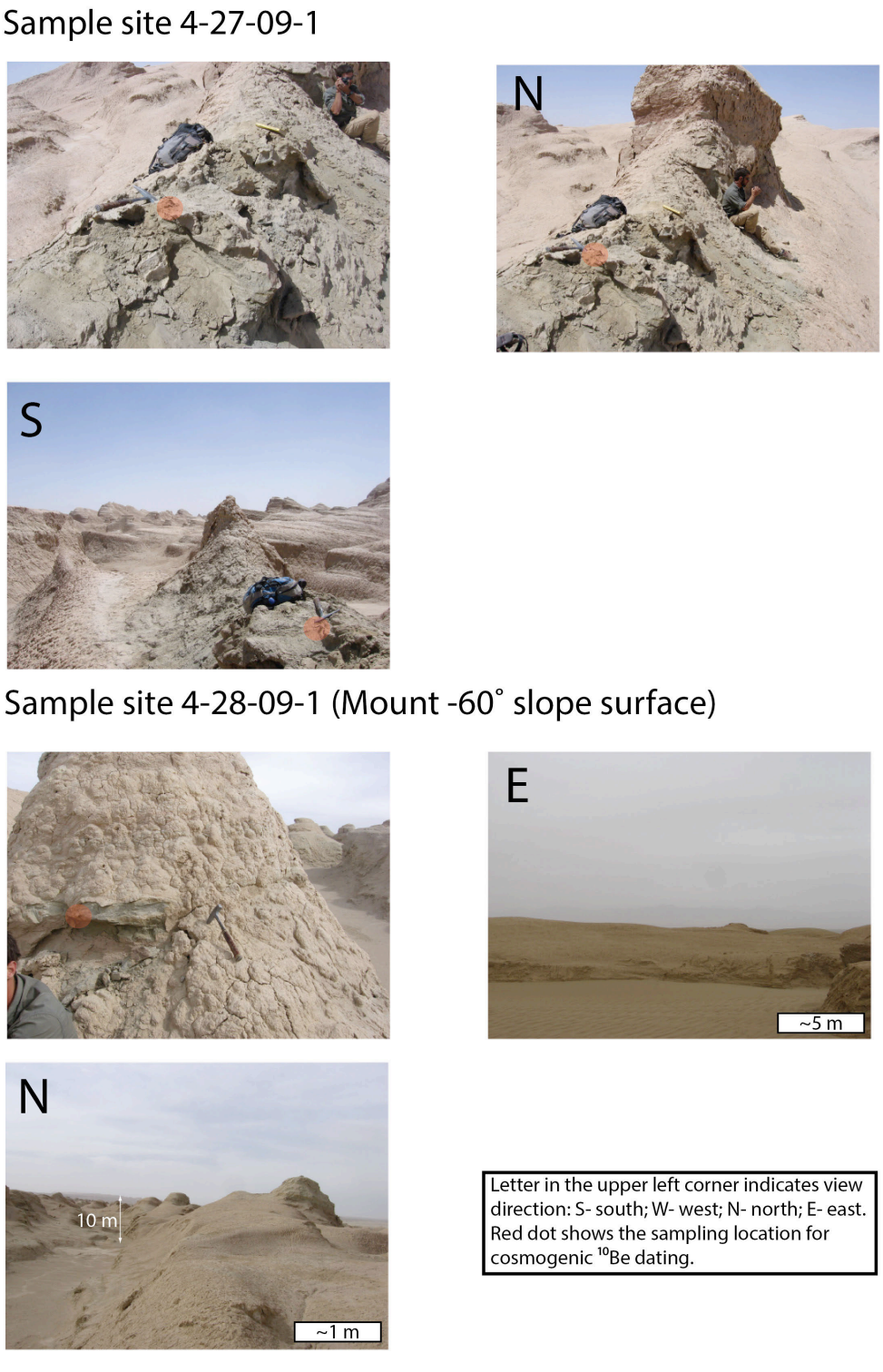

Fig. A.1. Overview of sampling sites for ^{10}Be cosmogenic nuclide dating

Sample	latitude	longitude	elevation (m)	rock type	Location	sample thickness (cm)	sample density (g/cm3)	shielding factor (0-1)	Quartz used in dissolution (g)	Be Carrier (mg)	ratio 10Be/9Be	ratio 10Be/9Be error	10Be conc.	10Be conc. Error (atom/g)	production rate spallation (atoms/g/yr)	production rate muons (atoms/g/yr)	erosion rate (mm/yr)	erosion rate uncertainty (mm/yr)
4-16-09-2	37.5158	92.2958	3050	sandstone	Arête	3	2.2	0.9985	38.100	0.422	3.15E-13	6.30E-15	228195	7771	36.01	0.46	0.13835	0.01185
4-17-09-1*	37.9667	92.7961	2972	sandstone	Cliff	3	2.2	0.4468	34.890	0.430	1.38E-13	3.13E-15	107720	4022	15.57	0.45	0.14382	0.01149
4-18-09-1	38.2428	92.4412	2778	sandstone	Arête	3	2.2	0.9994	37.400	0.430	2.56E-13	5.82E-15	191675	6902	31.23	0.43	0.14468	0.0124
4-21-09-3	38.3753	92.8973	2786	sandstone	Arête	3	2.2	0.9811	34.450	0.424	3.63E-13	6.79E-15	292823	9714	30.91	0.43	0.09333	0.00793
4-23-09-2	38.3996	92.1852	2792	sandstone	Arête	3	2.2	0.9996	37.700	0.425	6.52E-13	1.22E-14	485639	15921	31.65	0.43	0.057	0.00488
4-24-09-1	38.8146	92.6552	3306	granite	Arête	3	2.2	0.9998	35.700	0.424	1.33E-11	2.25E-13	10544507	331768	43.45	0.50	0.00303	0.00031
4-24-09-2	38.7584	92.7842	2975	sandstone	Arête	3	2.2	0.9988	33.400	0.426	2.82E-13	6.44E-15	234360	8438	35.69	0.46	0.13349	0.01155
4-26-09-1*	38.4338	92.4160	2878	sandstone	Cliff	3	2.2	0.4403	38.000	0.428	1.22E-13	2.78E-15	86380	3272	14.71	0.44	0.17161	0.01364
4-26-09-2	38.4362	92.4223	2997	sandstone	Arête	3	2.2	0.9999	43.100	0.426	5.50E-13	1.77E-14	358772	15145	35.88	0.46	0.08719	0.00783
4-26-09-3	38.4453	92.4185	2851	sandstone	slope on top of yardang	3	2.2	0.8449	35.100	0.437	8.23E-14	2.24E-15	62905	2700	27.77	0.44	0.40135	0.03502
4-27-09-1	38.3582	92.5104	2988	sandstone	Arête	3	2.2	0.9958	38.000	0.424	3.33E-13	7.65E-15	242840	8721	35.46	0.46	0.12804	0.01107
4-28-09-1	38.2320	92.6693	2838	sandstone	55-60 degree slope	3	2.2	0.7008	40.500	0.424	3.14E-13	7.19E-15	214256	7704	23.79	0.45	0.09191	0.00772
4-2-10-blank									0	0.427	6.90 E-15	8.64E-16	LLNL*		calculated in CRONUS calculator			

shielding factor: based on the horizon line taken at each sample site.
LLNL*: 10Be/9Be determined at Lawrence Livermore Center for Acceleration Mass Spectrometry, June 18, 2010
Erosion Rates based on time-dependent production-rate model after Lal (1991) and Stone (2000) and calculated in CRONUS. See Balco et al. (2008) for details.
The blank 4-2-10-blank had a 10Be-concentration of 197823 atoms with an error of 25200 atoms.

Table A.1. Detailed cosmogenic ^{10}Be nuclide results table

Appendix B

Supplementary material to chapter 3

Temperature lapse rate analysis

The MOD11C2 night land surface temperatures for DJF, averaged over 12 years from 2000-2012, was used for temperature-lapse rate analyses (*Wan et al., 2003)*. The raster resolution of this dataset is 5.5 km and all analyses were performed using ArcGIS software (Version 10 by ESRI) and MATLAB software (Version R2013b by MathWorks). Sampled catchments were extracted from the DEMs (AsterDTM 30x30m) using ArcGIS's watershed and pour-point function where sample locations defined pour points. In MATLAB, temperature from the MOD11C2 raster set was extracted for each catchment. Catchments with a catchment size ≤10 km^2 were dilated to represent at least 4 pixels (ca. 20 km^2) to obtain a more appropriate local temperature gradient that better reflects the atmospheric conditions above the catchment. Instead of using all temperature data along a transect, this approach has the advantage to obtain a more meaningful temperature-lapse rate along the sampled water transects. The obtained data set was subdivided into elevations above and below 2000 m, because the lapse rate below this elevation is following a drier adiabatic cooling trend. Results for each transect are plotted in Fig. 3.7. Finally, we used the obtained temperature lapse rates to calculate the starting input temperature (T_0) for the thermodynamic Rayleigh condensation model by Rowley et al. (2001). We obtained starting temperature input values for transect 1: 23.5 °C; transect 2: 22.9 °C; and transect 3: 21.7 °C.

Stable isotope modeling

A numerical thermodynamic atmosphere model based on a Rayleigh adiabatic condensation process was used to compare sampled stream-water data with model predictions of rain-isotopic compositions with altitude (Fig. 3.1). Here, we applied the numerical model from Rowley et al. (2001). A full mathematical description of the model and all fractionation factors are found therein (Rowley et al., 2001). The model considered the simplest case of Rayleigh fractionation, where the liquid phase formed by vapor condensation is removed from the system by precipitation. We obtained the model starting parameters for temperature from the MOD11C2 data (see above: temperature lapse-rate analysis), the humidity starting values (RH_0) where derived from the NCEP-NCAR 1000 mbar re-analysis relative humidity (%) composition from 2008 to 2013 for DJF (*Kalney et al., 1996*). The obtained humidity starting values were for transect 1: 85 % RH, for transect 2: 78 % RH, and for transect 3: 67 % RH. Model results are presented in Figure 3.1 c-e.

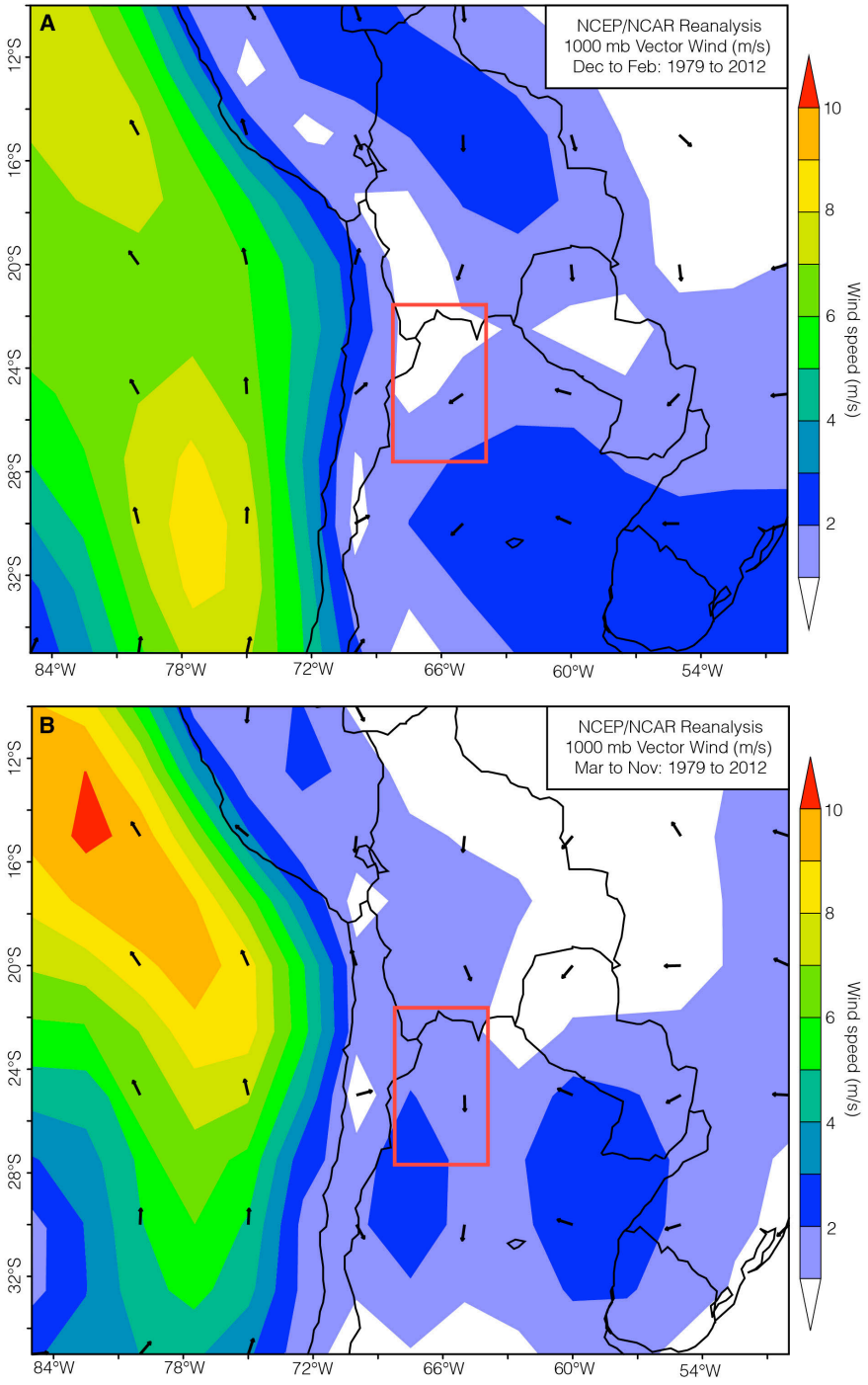

Fig. B.1.

NCEP-NCAR 1000 mbar reanalysis winds (m/s) composition from 1979 to 2012 (*Kalney et al., 1996*). Image provided by the NOAA/ESRL Physical Sciences Division, Boulder Colorado from their web site at http://www.esrl.noaa.gov/psd/.

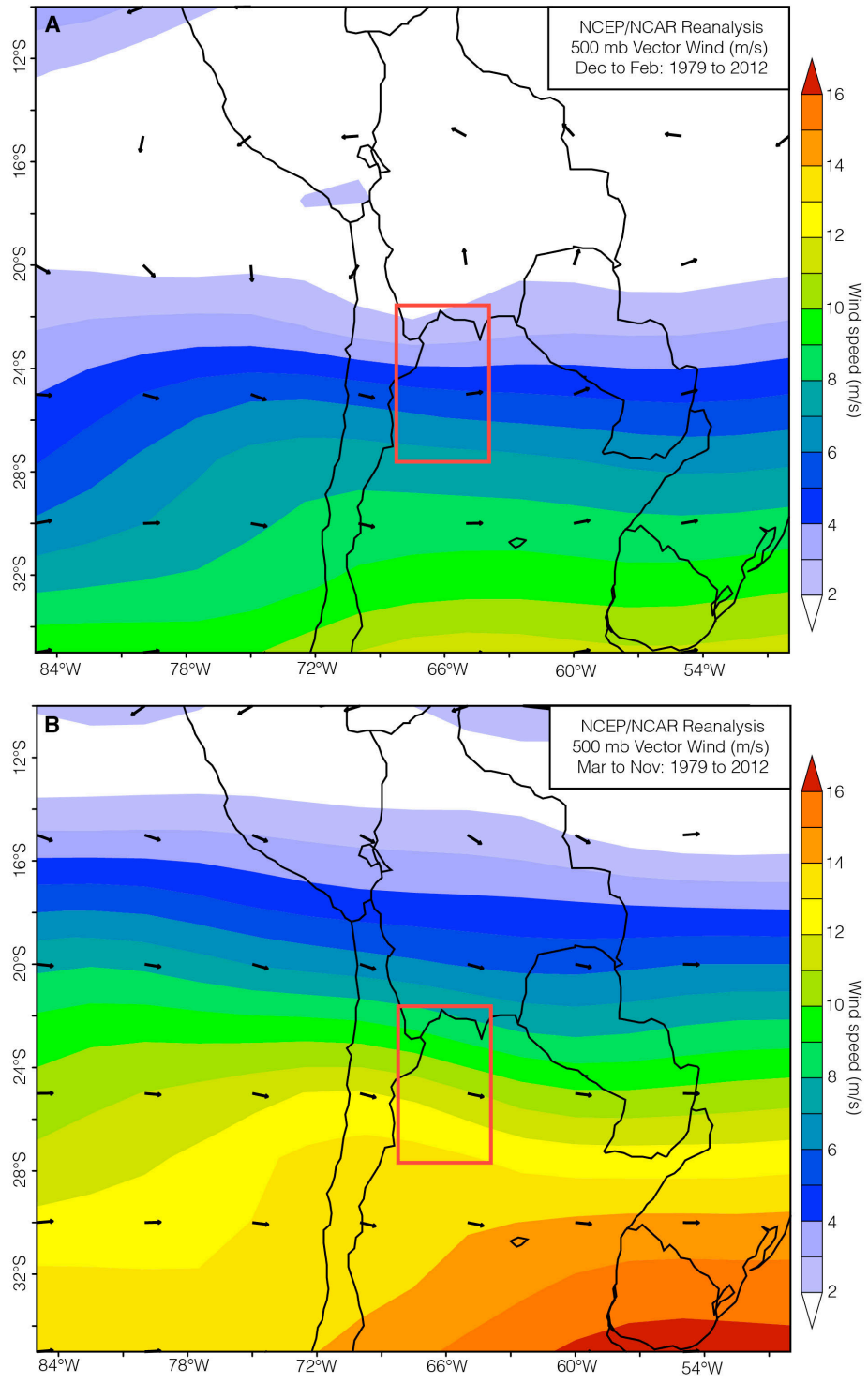

Fig. B.2.

NCEP-NCAR 500 mbar re-analysis winds (m s^{-1}) composition from 1979 to 2012 (*Kalney et al., 1996*). Image provided by the NOAA/ESRL Physical Sciences Division, Boulder Colorado from their web site at http://www.esrl.noaa.gov/psd/.

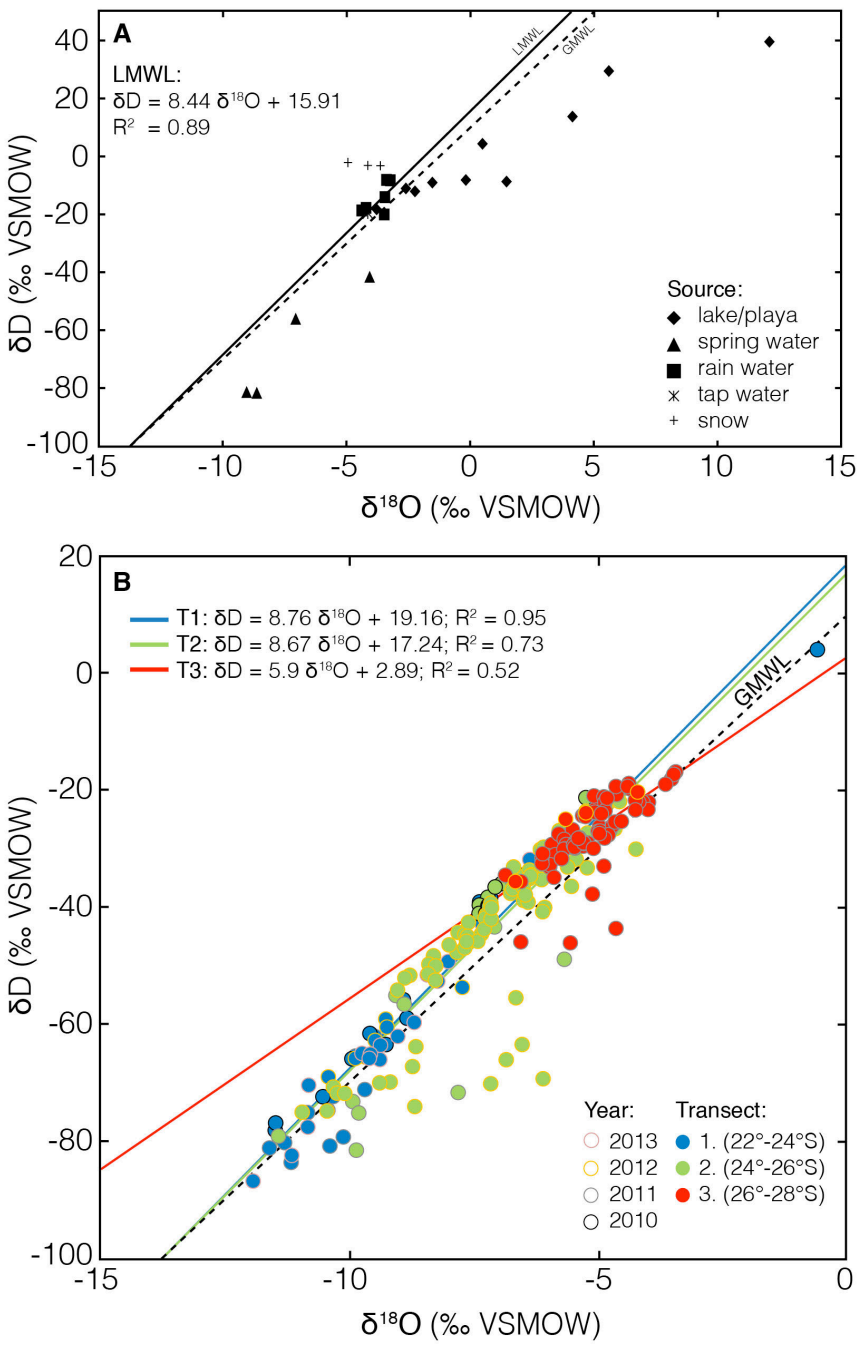

Fig. B.3.

(A) $\delta^{18}O$ versus δD values shape-coded for different water sources (lake/playa, spring, rain, tap and snow). Solid black line represents the global meteoric water line (GMWL) and dashed line is the local meteoric water line (LMWL). Note the strong evaporation trend of Puna lakes and playas. Snow samples are enriched in deuterium indicating minor snow-sublimation at high altitude. (B) $\delta^{18}O$ versus δD values of stream-water data (coded for sampling year and transect). Solid line

is the GMWL and dashed lines represent the LMWL for each transect and goodness of each fit. At first glance all stable isotopes from stream waters are following the same trend, as they all have similar starting $\delta^{18}O$ and δD compositions, however, there is a clear divergence in the amount of isotopic depletion of ^{18}O and D-isotopes from north to south.

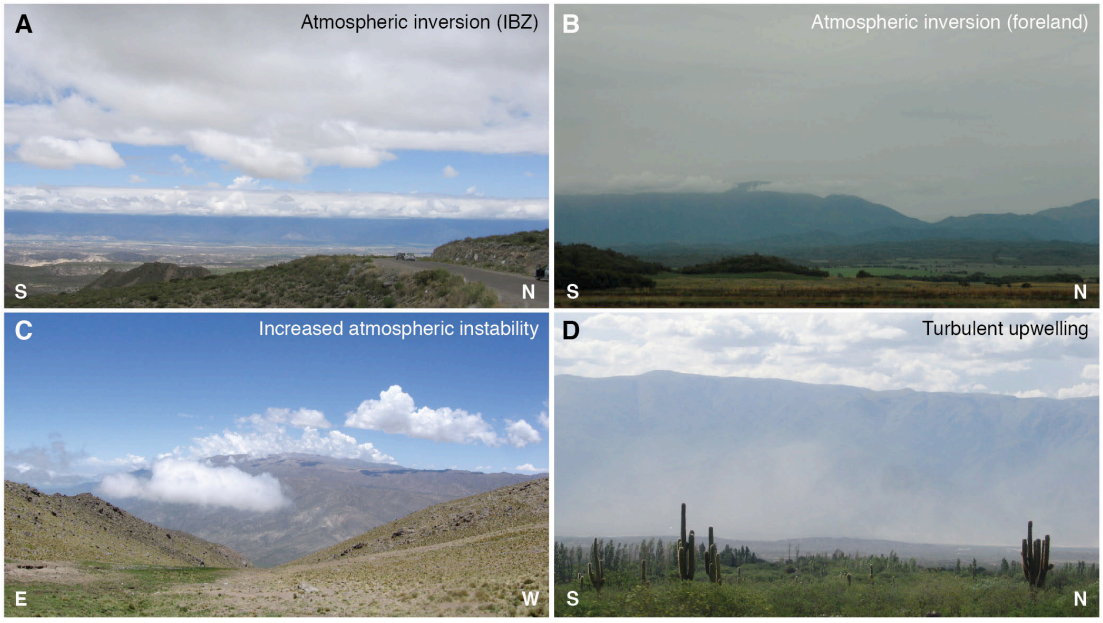

Fig. B.4.

Example of the development of deep-convective storms along the south-central Andes during a sampling campaign in January 2011 in the Santa María Basin (Sierras Pampeanas). All pictures were taken within 24 hours.

Table B.1. Water stable isotopes results table

Sample #	Year collected	Location	Latitude (S.)	Longitude (W.)	Sample elevation (m)	Mean catchment elevation (m)	Sample type	$d^{18}O$ (o/oo) vs. SMOW	1 s	dD (o/oo) vs. SMOW	1 s	d-excess
Paraje Mucar	2011	transect A	23.4265	66.9537	4120	4416	stream	-10.4	0.1	-81.3	0.3	2.0
SdT	2011	transect A	23.4176	66.4988	4000	4207	stream	-10.1	0.1	-79.8	0.4	1.4
AB1	2011	transect A	22.8883	65.6236	3600	3829	stream	-9.7	0.1	-71.7	0.2	6.1
AB2	2011	transect A	22.5982	65.8553	3736	3812	stream	-10.9	0.1	-75.6	0.3	11.3
AB3	2011	transect A	22.5172	65.8724	3860	3988	stream	-11.6	0.1	-81.7	0.2	11.3
AB4	2011	transect A	22.9230	65.5558	3670	3859	stream	-10.5	0.1	-75.2	0.5	8.4
Rio Huichara	2011	transect A	23.5898	65.4101	2551	3069	stream	-9.9	0.1	-65.9	0.4	13.3
Lipan_1	2011	transect A	23.6792	65.6213	3530	4080	stream	-9.5	0.1	-62.5	0.3	13.7
Lipan_2	2011	transect A	23.6938	65.6496	4150	4330	stream	-10.4	0.1	-72.9	0.3	10.0
Lipan_3	2011	transect A	23.6975	65.7289	3790	4040	stream	-11.3	0.1	-80.7	0.2	9.8
Sus1	2011	transect A	23.4372	66.2585	3660	3855	stream	-11.2	0.1	-84.1	0.2	5.4
W10 PUR01	2010	transect A	23.6825	65.6275	3760	4086	stream	-10.0	0.1	-66.4	0.2	13.4
W10 PUR02	2010	transect A	23.7052	65.6699	4100	4197	stream	***5.0***	0.1	***-8.4***	0.2	***-48.6***
W10 SMARTIN	2010	transect A	23.8154	64.7952	476	701	stream	-0.6	0.1	3.7	0.2	8.8
W10 CALI01	2010	transect A	23.6936	64.8682	1120	1331	stream	-6.7	0.1	-34.9	0.2	18.9
W10 CALI02	2010	transect A	23.6742	64.9021	1660	1703	stream	-7.3	0.1	-39.6	0.2	19.0
W10 CALI03	2010	transect A	23.6391	64.9423	1478	2049	stream	-7.4	0.1	-39.5	0.2	19.8
W10 CALI04	2010	transect A	23.6100	64.9523	1478	1603	stream	-7.2	0.1	-38.9	0.2	18.7
W10 HUICHAIRA	2010	transect A	23.5714	65.4509	2800	3812	stream	-9.6	0.1	-62.1	0.2	14.8
W10 CAF01	2010	transect A	22.9306	65.3014	3540	4150	stream	-10.6	0.1	-72.9	0.2	11.6
W10 CAF02	2010	transect A	22.8982	65.2805	3680	3880	stream	-11.5	0.1	-78.6	0.2	13.4
W10 CAF03	2010	transect A	22.8928	65.2671	3780	3941	stream	-11.5	0.1	-77.4	0.2	14.6
W10 CAF04	2010	transect A	22.8357	65.2292	3130	3954	stream	-8.9	0.1	-59.4	0.2	11.5
W10 PA01	2010	transect A	23.8104	65.5231	2520	3837	stream	-8.9	0.1	-56.3	0.2	15.3
W10 MAIMARA	2010	transect A	23.6274	65.4105	2390	2500	stream	-6.3	0.1	-33.0	0.2	17.0
W10 ALF01	2010	transect A	23.5899	65.3670	2930	3790	stream	-9.3	0.1	-64.0	0.2	10.4
YAC	2012	transect A	23.3842	65.3407	2723	3835	stream	-9.7	0.1	-66.1	0.1	11.6
JUE	2012	transect A	23.5323	65.3776	2530	3795	stream	-9.3	0.1	-59.6	0.1	14.8
PUR1	2012	transect A	23.6589	65.5423	2967	3623	stream	-7.8	0.1	-54.2	0.2	7.9

Table B.1. Water stable isotopes results table (continued)

PUR2	2012	transect A	23.6012	65.5661	3576	3984	stream	-10.4	0.1	-69.5	0.1	14.1
PUR3	2012	transect A	23.6646	65.5859	3030	3918	stream	-9.5	0.1	-63.3	0.1	12.8
TUM	2012	transect A	23.8115	65.5326	2549	3918	stream	-9.3	0.1	-61.0	0.1	13.2
Rio Morino 1	2012	transect A	23.8106	65.8243	3650	4013	stream	-9.9	0.1	-66.3	0.2	12.9
AR13-W37	2013	transect A	23.4349	66.2858	3760	3867	stream	-12.0	0.1	-87.3	0.1	8.3
AR13-W38	2013	transect A	23.4308	66.2662	3728	3873	stream	-11.2	0.1	-82.9	0.2	6.5
AR13-W39	2013	transect A	23.6972	65.7322	3716	4040	stream	-10.9	0.1	-78.1	0.2	8.8
AR13-W40	2013	transect A	23.6943	65.6480	4104	4326	stream	-9.4	0.1	-66.5	0.3	8.8
AR13-W41	2013	transect A	23.6816	65.6294	3913	4098	stream	-10.8	0.1	-70.9	0.2	15.8
AR13-W42	2013	transect A	23.7104	65.5319	2629	3224	stream	-9.8	0.1	-65.5	0.2	12.7
AR13-W43	2013	transect A	23.7401	65.5073	2442	3231	stream	-8.7	0.1	-60.2	0.1	9.6
AR13-W44	2013	transect A	23.5856	65.4063	2458	3761	stream	-9.1	0.1	-62.5	0.5	9.9
AR13-W46	2013	transect A	23.7427	65.4699	2241	3572	stream	-9.4	0.1	-64.1	0.1	11.2
AR13-W47	2013	transect A	23.8283	65.4729	2131	3480	stream	-8.3	0.1	-53.1	0.1	12.9
AR13-W48	2013	transect A	23.9136	65.4662	2092	2880	stream	-7.4	0.1	-43.3	0.2	15.6
ST13-003-W1	2013	transect A	23.5936	65.3829	2657	3770	stream	-9.6	0.1	-65.6	0.3	11.2
ST13-004-W1	2013	transect A	23.5949	65.3701	2736	3803	stream	-9.6	0.1	-66.3	0.3	10.7
ST13-005-W1	2013	transect A	23.9458	65.5286	2817	3644	stream	-8.0	0.1	-49.7	0.3	14.6
ST13-008-W1	2013	transect A	23.9428	65.4930	2393	3074	stream	-8.5	0.1	-52.0	0.1	15.7
ST13-021-W1	2013	transect A	23.9068	64.8088	406	1595	stream	-6.4	0.1	-32.3	0.5	19.0
ST13-022-W1	2013	transect A	23.7116	64.5354	313	625	stream	-6.2	0.1	-34.1	0.2	15.1
AR-11-W_87	2011	transect B	25.9985	67.3896	3480	4439	stream	***-4.3***	0.1	***-43.0***	***0.2***	***-8.6***
AR-11-W_89	2011	transect B	25.9205	67.3643	3591	4538	stream	-5.7	0.1	-49.4	0.2	-3.6
Salar Rincon	2011	transect B	24.0354	66.9742	3930	4443	stream	-9.9	0.1	-82.0	0.4	-3.0
Rio Tocomar	2011	transect B	24.1838	66.6049	4165	4587	stream	-7.8	0.1	-72.2	0.5	-9.4
SA1	2011	transect B	24.2217	66.4416	4150	4402	stream	-10.0	0.1	-73.7	0.3	6.0
SA2	2011	transect B	24.2827	66.1696	3940	4168	stream	-9.8	0.1	-75.7	0.6	3.0
Toro1	2011	transect B	24.3258	66.1176	4010	4085	stream	-11.4	0.1	-79.6	0.2	12.0
Toro2	2011	transect B	24.3658	66.0933	3750	4163	stream	-9.1	0.1	-55.6	0.2	17.2
Toro3	2011	transect B	24.4717	65.9941	3400	4367	stream	-8.9	0.1	-57.0	0.5	14.4
Toro4	2011	transect B	24.7608	65.7448	2190	3003	stream	-7.1	0.1	-43.8	0.2	13.1
Toro5	2011	transect B	24.8553	65.7101	1780	2304	stream	-6.7	0.1	-36.0	0.4	18.0
Toro6	2011	transect B	24.8894	65.6895	1640	1856	stream	-6.6	0.1	-37.4	0.2	15.4
W10 MT01	2010	transect B	24.5109	65.3458	1515	1688	stream	-7.2	0.1	-38.7	0.2	19.2

Table B.1. Water stable isotopes results table (continued)

W10 MT02	2010	transect B	24.5045	65.3360	1480	1768	stream	-7.4	0.1	-40.1	0.2	19.3
W10 MT03	2010	transect B	24.4855	65.2962	1239	1538	stream	-7.4	0.1	-41.5	0.2	17.9
W10 MT04	2010	transect B	24.4321	65.2963	1238	1382	stream	-7.3	0.1	-41.5	0.2	16.8
W10 HUM01	2010	transect B	24.0556	65.4194	1580	1864	stream	-7.0	0.1	-36.4	0.2	19.4
W10 HUM02	2010	transect B	24.0056	65.3542	1613	2068	stream	-6.6	0.1	-35.0	0.2	17.7
W10 HUM03	2010	transect B	24.0063	65.3501	1620	1775	stream	-6.1	0.1	-32.6	0.2	16.1
W10 HUM04	2010	transect B	24.0189	65.3914	1788	1879	stream	-7.1	0.1	-37.0	0.2	19.8
W10 HUM05	2010	transect B	24.0229	65.3899	1750	1971	stream	-7.2	0.1	-40.2	0.2	17.8
W10 SALTA	2010	transect B	24.7960	65.4047	1180	1236	stream	-5.3	0.1	-21.7	0.2	20.6
W10 SALTA 20	2010	transect B	24.0148	65.5118	2032	4006	stream	-7.2	0.1	-40.3	0.2	17.5
San An-1 (San-1)	2012	transect B	24.0394	66.2727	3630	4093	stream	-11.0	0.1	-75.5	0.4	12.2
AnInc	2012	transect B	24.2811	66.4501	4400	4455	stream	-9.2	0.1	-70.4	0.2	3.3
AnInc II	2012	transect B	24.2811	66.4501	4400	4352	stream	-8.8	0.1	-67.7	0.1	2.3
AdG I	2012	transect B	24.3258	66.4784	4560	4836	stream	-10.3	0.1	-71.2	0.2	11.5
AdG II	2012	transect B	24.3283	66.4816	4567	4693	stream	-10.5	0.1	-75.3	0.1	8.5
AdG III	2012	transect B	24.3573	66.5349	4270	4710	stream	-10.3	0.1	-72.3	0.1	9.9
AdG IV	2012	transect B	24.3573	66.5352	4280	4698	stream	-10.1	0.1	-72.3	0.2	8.6
SRPG-1	2012	transect B	24.4663	66.6739	3970	4775	stream	-8.7	0.1	-64.3	0.1	5.2
Ari-1	2012	transect B	24.8259	68.0703	3830	4276	stream	-6.9	0.1	-66.5	0.2	-11.5
Ari-2	2012	transect B	24.9460	68.1141	4240	4328	stream	-7.2	0.1	-70.7	0.6	-13.1
ATR-1	2012	transect B	25.5492	67.0948	4115	4553	stream	-6.7	0.1	-55.9	0.1	-2.5
HM-1	2012	transect B	24.8637	66.9420	3868	4550	stream	-6.6	0.1	-63.9	0.2	-11.5
Pocitos I	2012	transect B	24.7996	66.9394	3733	4028	stream	-9.4	0.1	-70.5	0.2	4.8
PoCav-1	2012	transect B	24.2658	67.1018	3710	4108	stream	-6.1	0.1	-69.8	0.2	-20.7
Qui-1	2012	transect B	24.4127	66.9537	3783	4439	stream	-8.7	0.1	-74.6	0.3	-4.9
QE001	2012	transect B	25.1172	65.6029	1373	1603	stream	-4.9	0.1	-23.2	0.3	15.8
QE002	2012	transect B	25.1363	65.6053	1455	1627	stream	-5.3	0.1	-24.8	0.1	17.5
QE003	2012	transect B	25.1474	65.6057	1479	1704	stream	-6.4	0.1	-34.1	0.1	17.2
QE004	2012	transect B	25.0816	65.6284	1557	1777	stream	-6.2	0.1	-30.5	0.1	19.0
QE005	2012	transect B	25.1676	65.6344	1565	2051	stream	-5.8	0.1	-28.3	0.3	18.1
QE006	2012	transect B	25.1661	65.6492	1599	1972	stream	-5.7	0.1	-27.6	0.1	18.4
QE007	2012	transect B	25.1614	65.6606	1627	1965	stream	-6.4	0.1	-35.6	0.1	15.9
QE008	2012	transect B	25.1586	65.6601	1641	1953	stream	-5.7	0.1	-27.8	0.1	17.9
QE009	2012	transect B	25.1545	65.7010	1756	2485	stream	-6.1	0.1	-30.2	0.1	18.9

QE010	2012	transect B	25.1575	65.7260	1807	3030	stream	-6.8	0.1	-38.1	0.2	16.3
QE011	2012	transect B	25.1597	65.7273	1810	2676	stream	-6.2	0.1	-34.3	0.3	15.0
QE012	2012	transect B	25.1736	65.7651	2067	2445	stream	-5.8	0.1	-30.5	0.1	15.8
QE013	2012	transect B	25.1793	65.7774	2152	3328	stream	-6.4	0.1	-34.9	0.1	16.1
QE014	2012	transect B	25.1861	65.8027	2398	2837	stream	-5.5	0.1	-29.2	0.1	14.4
QE015	2012	transect B	25.1783	65.8160	2630	3112	stream	-6.8	0.1	-37.3	0.1	16.7
QE016	2012	transect B	25.1771	65.8202	2691	2845	stream	-6.6	0.1	-36.5	0.2	15.9
QE017	2012	transect B	25.1667	65.8325	2847	3373	stream	-7.3	0.1	-41.8	0.3	16.5
QE018	2012	transect B	25.1647	65.8346	2857	3451	stream	-7.9	0.1	-48.2	0.1	14.8
QE019	2012	transect B	25.1628	65.8407	2875	3573	stream	-7.7	0.1	-47.4	0.1	14.3
QE020	2012	transect B	25.1664	65.8500	2954	3490	stream	-6.1	0.1	-40.5	0.1	8.4
QE021	2012	transect B	25.1730	65.8488	3010	3153	stream	-6.1	0.1	-41.2	0.1	8.0
VC022	2012	transect B	24.9310	66.1421	2622	4132	stream	-8.3	0.1	-48.8	0.1	18.0
VC023	2012	transect B	24.8370	66.1610	2718	3737	stream	-8.4	0.1	-50.2	0.1	17.3
VC024	2012	transect B	24.8170	66.1726	2754	3975	stream	-8.3	0.1	-50.5	0.1	15.9
VC025	2012	transect B	24.8175	66.1730	2749	4150	stream	-7.8	0.1	-44.7	0.1	18.0
VC026	2012	transect B	24.6344	66.1911	3192	4307	stream	-8.8	0.1	-52.1	0.1	18.4
VC027	2012	transect B	24.6069	66.1980	3249	4427	stream	-8.9	0.1	-52.5	0.1	18.8
VC028	2012	transect B	24.7208	66.2014	3032	4482	stream	-9.1	0.1	-54.6	0.1	17.9
VC029	2012	transect B	24.8171	66.1740	2761	3453	stream	-8.4	0.1	-51.9	0.2	15.7
VC030	2012	transect B	25.0574	66.1046	2451	2925	stream	-8.0	0.1	-46.9	0.2	17.3
VC031	2012	transect B	25.0900	66.1261	2414	2793	stream	-7.7	0.1	-45.1	0.1	16.6
VC032	2012	transect B	25.1181	66.1634	2350	3883	stream	-7.6	0.1	-43.0	0.2	18.1
VC033	2012	transect B	25.1241	66.1613	2334	2413	stream	-7.7	0.1	-45.4	0.1	15.8
VC034	2012	transect B	25.1343	66.1678	2336	2451	stream	-7.3	0.1	-42.3	0.3	16.1
VC035	2012	transect B	25.1616	66.1791	2302	3048	stream	-7.4	0.1	-45.0	0.1	14.0
VC036	2012	transect B	25.2315	66.2496	2145	2822	stream	-6.2	0.1	-35.7	0.1	13.6
VC037	2012	transect B	25.3160	66.3261	2437	2549	stream	-5.3	0.1	-33.7	0.1	8.4
VC038	2012	transect B	25.3032	66.3348	2345	3364	stream	-5.5	0.1	-32.2	0.1	11.6
VC039	2012	transect B	25.3152	66.3644	2573	2657	stream	-6.5	0.1	-39.3	0.2	13.0
VC040	2012	transect B	25.3650	66.4203	2341	3972	stream	-7.4	0.1	-46.3	0.2	13.3
VC041	2012	transect B	25.3207	66.4442	2470	2690	stream	-7.2	0.1	-39.8	0.1	17.7
VC042	2012	transect B	25.2989	66.4476	2492	3583	stream	-7.3	0.1	-44.2	0.2	14.4
VC043	2012	transect B	25.2900	66.4488	2521	4323	stream	-7.2	0.1	-42.5	0.1	15.0

Table B.1. Water stable isotopes results table (continued)

Table B.1. Water stable isotopes results table (continued)

VC044	2012	transect B	25.2616	66.4447	2616	2930	stream	***-4.0***	0.1	***-23.7***	***0.1***	***8.2***
VC045	2012	transect B	25.2506	66.4371	2650	2684	stream	-7.7	0.1	-46.3	0.2	15.1
VC046	2012	transect B	25.2407	66.4357	2677	3552	stream	-6.5	0.1	-37.0	0.2	15.3
VC047	2012	transect B	25.1942	66.4426	2904	4444	stream	-8.3	0.1	-52.9	0.3	13.5
VC048	2012	transect B	25.2477	66.4349	2672	3869	stream	-7.2	0.1	-40.5	0.1	16.9
VC049	2012	transect B	25.3150	66.3732	2554	3004	stream	-5.6	0.1	-33.5	0.2	11.6
VC051	2012	transect B	25.4397	66.2839	2044	3794	stream	-6.4	0.1	-39.6	0.4	11.9
VC052	2012	transect B	25.4673	66.3684	2158	2435	stream	-4.3	0.1	-30.5	0.1	3.7
VC053	2012	transect B	25.5299	66.3812	2200	2376	stream	-5.6	0.1	-36.9	0.2	7.7
VC054	2012	transect B	25.6778	66.1586	1862	3695	stream	-4.7	0.1	-27.0	0.1	10.6
VC055	2012	transect B	25.6816	66.1015	1826	2126	stream	-6.5	0.1	-38.3	0.2	13.6
VC059	2012	transect B	25.6235	65.6105	1173	2071	stream	-4.6	0.1	-22.3	0.1	14.5
VL060	2012	transect B	25.2840	65.4363	1054	1112	stream	-5.5	0.1	-30.0	0.3	13.9
VL061	2012	transect B	25.1951	65.4921	1176	1739	stream	-5.8	0.1	-27.3	0.1	19.2
VL062	2012	transect B	25.1648	65.4964	1192	1620	stream	-5.3	0.1	-24.0	0.1	18.2
VL063	2012	transect B	24.8305	65.5025	1248	2560	stream	-6.0	0.1	-30.2	0.1	17.6
VL064	2012	transect B	24.6998	65.4781	1403	2229	stream	-6.7	0.1	-33.5	0.2	20.3
VL065	2012	transect B	24.6908	65.3934	1240	2601	stream	-6.4	0.1	-35.1	0.2	16.1
VL066	2012	transect B	24.6783	65.3432	1258	1411	stream	-5.3	0.1	-27.7	0.2	14.3
AR-11-W_2	2011	transect C	26.6192	65.1870	549	1385	stream	-4.4	0.1	-20.1	0.3	15.1
AR-11-W_3	2011	transect C	26.5894	64.8447	548	1187	stream	-5.0	0.1	-26.6	0.5	13.4
AR-11-W_4	2011	transect C	26.5481	64.7826	535	812	stream	-5.4	0.1	-29.9	0.2	12.9
AR-11-W_6	2011	transect C	27.0137	65.1569	372	460	stream	-3.6	0.1	-18.5	0.1	10.0
AR-11-W_7	2011	transect C	27.1565	65.1344	332	340	stream	-4.0	0.1	-22.4	0.2	9.8
AR-11-W_8	2011	transect C	27.1854	65.1107	329	349	stream	-4.1	0.1	-22.4	0.4	10.7
AR-11-W_9	2011	transect C	27.3095	64.9911	329	379	stream	-4.0	0.1	-23.7	0.3	8.6
AR-11-W_11	2011	transect C	27.1429	65.2185	336	353	stream	-4.2	0.1	-22.4	0.4	11.3
AR-11-W_12	2011	transect C	27.1332	65.3154	338	341	stream	-4.3	0.1	-22.1	0.1	12.2
AR-11-W_13	2011	transect C	27.1240	65.3423	344	740	stream	-4.4	0.1	-19.3	0.4	16.1
AR-11-W_14	2011	transect C	27.0479	65.4781	388	1290	stream	-4.7	0.1	-21.1	0.1	16.2
AR-11-W_15	2011	transect C	27.0918	65.5539	413	1466	stream	-5.0	0.1	-22.5	0.5	17.4
AR-11-W_16	2011	transect C	27.0948	65.6182	572	653	stream	***-3.4***	0.1	***-10.0***	***0.3***	***17.6***
AR-11-W_17	2011	transect C	27.0837	65.6658	787	3804	stream	-5.3	0.1	-24.8	0.3	18.0
AR-11-W_18	2011	transect C	27.0731	65.6637	807	1097	stream	-5.1	0.1	-23.7	0.3	17.1

Table B.1. Water stable isotopes results table (continued)

AR-11-W_19	2011	transect C	27.0333	65.4016	1022	946	stream	-5.1	0.1	-21.4	0.5	19.6
AR-11-W_20	2011	transect C	27.0463	65.6673	1087	1249	stream	-5.3	0.1	-24.5	0.4	18.0
AR-11-W_21	2011	transect C	27.0341	65.6588	1174	1232	stream	-5.3	0.1	-24.9	0.2	17.4
AR-11-W_22	2011	transect C	27.0340	65.6606	1274	1420	stream	-5.6	0.1	-28.0	0.2	17.0
AR-11-W_23	2011	transect C	27.0178	65.6560	1316	1665	stream	-6.0	0.1	-29.7	0.2	18.0
AR-11-W_25	2011	transect C	27.0106	65.6610	1409	1660	stream	-4.9	0.1	-21.9	0.2	17.0
AR-11-W_27	2011	transect C	26.9979	65.6628	1499	1866	stream	-4.7	0.1	-19.8	0.3	17.7
AR-11-W_28	2011	transect C	26.9935	65.6628	1560	1715	stream	-5.1	0.1	-24.2	0.4	16.7
AR-11-W_29	2011	transect C	26.9772	65.6632	1684	1952	stream	-5.8	0.1	-27.9	0.4	18.7
AR-11-W_30	2011	transect C	26.9630	65.6598	1754	1848	stream	-4.9	0.1	-21.5	0.4	17.8
AR-11-W_32_1	2011	transect C	26.9489	65.6621	1833	2259	stream	-4.9	0.1	-22.5	0.1	16.8
AR-11-W_32_2	2011	transect C	26.9461	65.6656	1847	2063	stream	-4.9	0.1	-23.9	0.4	15.3
AR-11-W_34	2011	transect C	26.8497	65.6971	2012	2267	stream	-5.5	0.1	-27.2	0.3	17.2
AR-11-W_35	2011	transect C	26.8321	65.7050	2235	2934	stream	-5.7	0.1	-28.8	0.4	16.9
AR-11-W_36	2011	transect C	26.8293	65.7095	2289	2452	stream	-4.4	0.1	-19.8	0.2	15.8
AR-11-W_37	2011	transect C	26.8174	65.7215	2401	2663	stream					
AR-11-W_38	2011	transect C	26.8138	65.7158	2499	2480	stream	-5.0	0.1	-24.4	0.4	15.3
AR-11-W_39	2011	transect C	26.8000	65.7230	2574	2888	stream	-5.7	0.1	-29.7	0.3	15.7
AR-11-W_40	2011	transect C	26.7775	65.7290	2779	3647	stream	-6.1	0.1	-31.6	0.4	17.0
AR-11-W_41	2011	transect C	26.7658	65.7351	2871	3799	stream	-6.6	0.1	-36.1	0.4	16.6
AR-11-W_42	2011	transect C	26.7424	65.7552	3021	3981	stream	-5.4	0.1	-28.5	0.3	14.8
AR-11-W_43	2011	transect C	26.7360	65.7861	3009	3254	stream	-6.0	0.1	-33.6	0.5	14.5
AR-11-W_44	2011	transect C	26.7110	65.7979	2888	3429	stream	-5.0	0.1	-27.4	0.3	12.9
AR-11-W_45	2011	transect C	26.7062	65.7954	2905	3074	stream	-5.5	0.1	-30.3	0.2	13.7
AR-11-W_46	2011	transect C	26.7044	65.7998	2843	3047	stream	-4.8	0.1	-27.0	0.5	11.3
AR-11-W_47	2011	transect C	26.6939	65.8029	2881	3611	stream	-5.2	0.1	-29.4	0.3	12.5
AR-11-W_48	2011	transect C	26.6410	65.8223	2629	3458	stream	-5.8	0.1	-31.4	0.4	14.9
AR-11-W_49	2011	transect C	26.5085	66.0099	1768	2537	stream	***-2.0***	0.1	***-14.5***	***0.3***	***1.8***
AR-11-W_50	2011	transect C	26.5924	66.0331	1822	2654	stream	-5.7	0.1	-30.4	0.3	15.2
AR-11-W_51	2011	transect C	26.6979	66.0541	1877	3072	stream	***-3.2***	0.1	***-18.1***	***0.3***	***7.4***
AR-11-W_52	2011	transect C	26.7335	65.7663	3102	3187	stream	-5.9	0.1	-31.5	0.3	15.7
AR-11-W_53	2011	transect C	26.7149	65.7543	3556	3583	stream	-5.3	0.1	-30.0	0.3	12.7
AR-11-W_54	2011	transect C	26.7101	65.7508	3604	3785	stream	-5.7	0.1	-30.5	0.2	15.3
AR-11-W_55	2011	transect C	26.7092	65.7497	3604	4142	stream	-6.0	0.1	-33.2	0.4	14.8

Table B.1. Water stable isotopes results table (continued)

AR-11-W_56	2011	transect C	26.7092	65.7497	3604	4233	stream	-5.3	0.1	-29.5	0.4	13.0
AR-11-W_57	2011	transect C	26.7066	65.7480	3714	4250	stream	-5.5	0.1	-29.3	0.2	14.7
AR-11-W_58	2011	transect C	26.7035	65.7443	3861	4268	stream	-5.5	0.1	-29.8	0.2	14.4
AR-11-W_59	2011	transect C	26.6991	65.7404	4013	4291	stream	-5.0	0.1	-27.4	0.4	12.6
AR-11-W_60	2011	transect C	26.6950	65.7384	4116	4320	stream	-5.9	0.1	-35.3	0.1	12.0
AR-11-W_64	2011	transect C	26.7244	66.0535	1906	2044	stream	-5.5	0.1	-30.1	0.2	13.9
AR-11-W_65	2011	transect C	26.8226	66.0836	1982	2007	stream	-4.7	0.1	-26.5	0.4	11.5
AR-11-W_66	2011	transect C	27.0024	66.2301	2174	3342	stream	-6.2	0.1	-32.0	0.4	17.3
AR-11-W_67	2011	transect C	26.8281	66.2999	2300	3452	stream	***-2.3***	0.1	***-11.7***	***0.5***	***6.9***
AR-11-W_68	2011	transect C	26.6708	66.3043	2456	3675	stream	-3.5	0.1	-17.2	0.5	10.6
AR-11-W_69	2011	transect C	27.1894	66.7614	1981	2832	stream	-5.3	0.1	-29.4	0.3	13.2
AR-11-W_70	2011	transect C	27.2243	66.8447	1831	2172	stream	-5.1	0.1	-30.4	0.5	10.7
AR-11-W_71	2011	transect C	27.2327	66.9145	1849	1904	stream	***-3.1***	0.1	***-19.7***	***0.5***	***5.1***
AR-11-W_72	2011	transect C	27.1013	66.8305	2148	2462	stream	***-2.4***	0.1	***-11.1***	***0.4***	***8.3***
AR-11-W_74	2011	transect C	27.0243	66.7608	2384	2630	stream	-4.3	0.1	-23.8	0.5	10.5
AR-11-W_75	2011	transect C	27.0008	66.7400	2432	4057	stream	-4.7	0.1	-25.8	0.4	11.7
AR-11-W_76	2011	transect C	26.9779	66.7399	2488	2776	stream					
AR-11-W_77	2011	transect C	26.8819	66.7340	2955	3765	stream	-4.8	0.1	-28.0	0.4	10.6
AR-11-W_79	2011	transect C	26.6317	66.9330	3194	3926	stream	-4.9	0.1	-33.4	0.5	6.0
AR-11-W_82	2011	transect C	26.6809	67.2040	3939	4176	stream	***-1.1***	0.1	***-22.0***	***0.4***	***-13.2***
AR-11-W_85	2011	transect C	26.0688	67.4121	3352	4302	stream	-4.7	0.1	-44.1	0.4	-6.6
AR-11-W_86	2011	transect C	26.0495	67.3852	3442	4437	stream	-5.6	0.1	-46.5	0.3	-1.8
AR-11-W_90	2011	transect C	26.0412	67.4305	3393	4142	stream	-6.6	0.1	-46.4	0.2	6.3
AR-11-W_91	2011	transect C	27.0008	66.7400	2432	2630	stream	-4.6	0.1	-25.7	0.4	10.8
AR-11-W_92	2011	transect C	27.1894	66.7614	1981	2832	stream	-4.9	0.1	-28.6	0.3	10.7
AR-11-W_93	2011	transect C	27.1894	66.7614	1981	2832	stream	-3.5	0.1	-17.7	0.6	10.5
AR-11-W_94	2011	transect C	27.0024	66.2301	2174	3342	stream	-6.2	0.1	-32.9	0.3	16.4
AR-11-W_95	2011	transect C	26.8045	66.0717	1957	3370	stream	-5.4	0.1	-28.6	0.3	14.9
AR-11-W_96	2011	transect C	26.7705	66.0601	1942	2199	stream	-4.9	0.1	-21.8	0.3	17.1
AR-11-W-97	2011	transect C	26.7587	66.0558	1939	2725	stream	-3.7	0.1	-19.4	0.2	10.1
AR-11-W-98	2011	transect C	26.6979	66.0541	1877	3072	stream	-6.9	0.1	-35.0	0.3	20.2
Rio Vilavil	2011	transect C	27.0599	66.7470	2200	2891	stream	-5.0	0.1	-27.8	0.3	12.3
Rio Puerta C. Q.	2011	transect C	27.1352	66.5653	1924	2444	stream	-5.8	0.1	-32.1	0.4	14.0
Rio Guanchin	2011	transect C	27.7853	68.0836	3013	4378	stream	-5.8	0.1	-32.1	0.4	14.0

Acon_1	2011	transect C	27.4457	66.0021	1540	1845	stream	-6.1	0.1	-31.3	0.2	17.9
Acon_2	2011	transect C	27.3223	65.9152	1100	3180	stream	-5.2	0.1	-38.2	0.3	3.0
CAF	2012	transect C	26.0660	65.9738	1626	3756	stream	-6.7	0.1	-36.0	0.1	17.5
VC056	2012	transect C	26.0946	66.0126	1795	3728	stream	-5.3	0.1	-24.3	0.1	18.0
VC057	2012	transect C	26.0654	65.9752	1643	3764	stream	-4.2	0.1	-20.7	0.1	13.2
VC058	2012	transect C	26.0239	65.8428	1533	1647	stream	-5.7	0.1	-25.4	0.2	20.1

Table B.1. Water stable isotopes results table (continued)

Table B.1. Water stable isotopes results table (continued)

Other data											
Sample #	**Year collected**	**Latitude (S.)**	**Longitude (W.)**	**Sample elevation (m)**	**Sample type**	**$d^{18}O$ (o/oo) vs. SMOW**	**1 s**	**dD (o/oo) vs. SMOW**	**1 s**	**d excess**	**Note**
AR-11-W_24	2011	27.0178	65.6560	1316	rain	-3.4	0.1	-8.1	0.3	19.1	
AR-11-W_26	2011	26.9979	65.6628	1499	rain	-3.2	0.1	-8.2	0.3	17.8	
AR-11-W_31	2011	26.9630	65.6598	1754	rain	-4.4	0.1	-18.6	0.3	16.6	
AR-11-W_61	2011	26.6956	66.0462	1888	rain	-3.5	0.1	-14.0	0.3	13.7	
AR-11-W_62	2011	26.6956	66.0462	1888	rain	-4.2	0.1	-17.7	0.3	16.1	
AR-11-W_63	2011	26.5924	66.0331	1822	rain	-3.5	0.1	-20.0	0.4	7.9	
AR-11-W_1	2011	26.6154	65.1968	607	lake	-3.8	0.1	-18.2	0.4	12.1	
AR-11-W_10	2011	27.5134	64.9011	329	lake	-2.2	0.1	-12.0	0.3	5.9	
AR-11-W_33	2011	26.9233	65.6834	1887	lake	-2.6	0.1	-11.0	0.3	9.9	
AR-11-W_73	2011	27.0243	66.7608	2384	lake	4.1	0.1	13.8	0.3	-19.2	saline
AR-11-W_78	2011	26.8518	66.7571	3199	lake	0.5	0.1	4.4	0.4	0.5	saline
AR-11-W_80	2011	26.6317	66.9330	3194	lake	-1.5	0.1	-9.0	0.4	3.4	
AR-11-W_81	2011	26.6951	67.1800	3782	lake	1.5	0.1	-8.6	0.4	-20.3	
AR-11-W_83	2011	26.6264	67.2432	3700	lake	5.6	0.1	29.6	0.3	-15.2	
AR-11-W_84	2011	26.1113	67.4280	3331	lake	12.1	0.1	40.0	0.5	-56.8	saline
VC050	2012	25.3023	66.3709	2569	lake	-0.2	0.1	-8.1	0.4	-6.6	saline
AR-11-W_88_#2	2011	25.9985	67.3896	3480	spring	-4.1	0.1	-41.6	0.4	-8.9	
CAS-1	2012	25.0301	68.2176	4075	spring	-9.1	0.1	-81.4	0.4	-9.0	
Abra de Navarro	2012	24.6415	67.9292	3950	spring	-8.6	0.1	-81.7	0.2	-12.5	
ATR-2	2012	25.5144	67.1017	4043	spring	-7.1	0.1	-56.1	0.1	0.5	
AR-11-W_5	2011	26.8260	65.2220	459	tap water	-4.2	0.1	-19.5	0.4	13.7	
W10 SALTA 21	2010	24.0368	65.7161	4615	snow	-3.6	0.1	-3.2	0.3	26.0	
W10 SALTA S.	2010	24.0630	65.7458	5953	snow	-4.2	0.1	-3.1	0.3	30.1	
W10 SALTA High	2010	24.0469	65.7522	5304	snow	-5.0	0.1	-2.1	0.3	37.6	

Appendix C

Supplementary material to chapter 4

Sampling and stratigraphic profile logging

Samples for leaf-wax and pedogenic carbonate oxygen, hydrogen, and carbon stable isotope analyses were collected during two field seasons in 2011 and 2013 from the sedimentary basin record of the Angastaco Basin (~25.5°S). Sampling and section measurements (thickness and bedding orientation) were performed along an E-W transect in exposed successions of the Mio-Pliocene Angastaco, Palo Pintado, and San Felipe formations along the Río Calchaquíes near the town of Santa Rosa (Fig. 4.1). We focused our attention on organic-rich layers of the Angastaco basin strata with abundant paleosoils and lacustrine sediments intercalated with volcanic ash deposits. Overall, 66 leaf-wax samples and 64 pedogenic carbonate samples were collected from paleosoils, overbank deposits and lacustrine sediments. Our aim to collect equidistant samples was limited by suitable organic-rich material or soil-carbonate horizons for analysis. However, whenever possible, well-consolidated nodules were sampled at least 30 cm below paleosoil horizons. Sampling intervals for leaf-wax samples vary between 20 to 150 m, with higher sampling rates in sections with evidence for more humid depositional environments. Samples collected north and south of the measured stratigraphic profile were projected into the stratigraphic log, as individual beds can be traced along strike on satellite imagery.

Sample preparation for leaf-wax δD_{wax} and $\delta^{13}C_{wax}$ analyses and measurement.

Samples were crushed using DCM-cleaned (dichloromethane) equipment and pulverized (ca. 40 to 60 μm) in a shatterbox with agate grinding chamber. Soluble organic matter was extracted from samples (100 g) at the University of

Potsdam using an accelerated solvent extractor (ASE350, Dionex Crop., Sunnyvale, USA) with a dichloromethane/ methanol mixture of 9:1 at 100°C and 1500 psi. Total extracts of three 18-minute cycles were captured in 250 ml bottles, later concentrated to 4 ml in a Turbovap, and then separated on silica gel using a solid phase extraction (SPE). SPE-columns preparation included the use of 1.5 g of silica gel (0.040-0.063 mesh; Alfa Aesar, Ward Hill, USA) filled into 6 ml glass columns (Macherey-Nagel, Düren, Germany). Columns were cleaned with three times the column volume of acetone and DCM and then dried overnight at 60°C. The column was again flushed with three times the column volume of acetone, DCM, and hexane prior to transferal of the total lipid extract onto the column. n-Alkanes and alcohols were eluted in 15 ml hexane and DCM, respectively, and the remaining substances were flushed with 15 ml methanol. Two out of three separated fractions were stored for later analysis. The remaining n-alkane fraction was treated with 6 µg 5α-androstane standard for gas chromatographic quantification. The identification and quantification of individual compounds was performed using a gas chromatograph with a coupled flame ionization and mass-selective detector (GC-FID/MSD Agilent 7890A GC, 5975C MSD, Agilent Technologies, Palo Alto, USA) flushed with helium carrier gas. Temperatures in the GC oven were programmed to increase at a rate of 12°C/min starting from 70°C to 320°C at which temperatures were held constant for 21 min. The PTV injector had a split ratio of 5:1 at an initial temperature of 70°C. The injector was heated up to 300°C at a programmed rate of 7.2°C/min and held constant at this temperature for 2.5 min. The n-alkane FID-peak areas were compared with the previously added 5α-androstane standard from which n-alkane concentrations were calculated. The n-alkane concentrations are reported as µg per gram dry sediment. In addition the average chain-length (ACL) and the carbon preference index (CPI) were calculated in Mathlab®.

For all samples δD_{wax} and $\delta^{13}C_{wax}$ were measured using a coupled gas chromatography-isotope ratio mass spectrometer (GC-IRMS) Delta V Advantage (ThermoFisher Bremen, Germany) at the University of Potsdam. The n-alkane fractions were dried and concentrated to 200 µg/µl per compound in hexane for δD measurements. The n-alkane fraction was injected (1 µl) into an TRACE 1310

Gas Chromatograph equipped with an Agilent DB-5 column, 30 m x 0.25 mm x 25 µm film. The injector was operated in splitless mode at 300°C and the oven was held at 70°C for 2 min. The oven was heated at 15°C/min until 150°C, and then heated with 5°C/min to 320°C. The final temperature was held for 10 min. The column effluent was transferred via a ConFlo IV interface (ThermoFisher, Bremen, Germany) into an isotope ratio mass spectrometer after conversion to H_2 in a high-temperature oven at 1420 °C. In general, triplicate analysis of 25 samples was performed, however, for 31 samples we performed only duplicate analysis. All results are reported using the conventional delta notation in permil (‰) units. δD values were corrected using a calibrated and known standard mixture of n-C_{16} to n-C_{30} alkanes obtained from the Biogeochemical Laboratories of the University of Indiana (A_3, A_4 and A_5) as well as a concentration depended standard mixture (B_2, B_3). A linear regression was produced using the known vs. measured values of the A_4 and A_5 standards, having a linear regression slope of 1 ± 0.021 for all analyzed standards. Three standards were measured after every sixth to ninth injection, where an $A_{3\text{-}5}$ standard was measured in the beginning and at the end and a B_2 standard in the middle of each sequence. The H_3^+ factor was determined at the start and end of the sequence and was very robust over the measurement period at 4.4 ± 0.25 (Hilkert et al., 1999). The analytical standard deviation for all single measurements was typical better than ± 3‰ (Table C.1). We report averaged sample duplicate and triplicate measurements with a standard deviation of ± 5‰ that represents the total variability in all measured n-alkane standard mixtures of the $A_{3\text{-}5}$ standards and is more than the analytical standard deviation of each single measurement of ± 3‰.

δ^{13}Cwax values were measured using the same fractions used for δDwax. The n-alkane fractions were concentrated to 60 µg/µl in hexane for δ^{13}C measurements. The same instrumental setup (GC-IRMS) and temperature programming was used as for the δ^{13}C measurements, only the oxidation oven was run at a lower temperature of 960°C. Duplicates were measured for each sample and a CO_2 gas with known isotopic composition was used as reference gas. The same n-alkane standard mixtures ($A_{3\text{-}5}$ and B_2 standard) were used as for δD measurements with the same standard setup in the measured sequence.

Only duplicate analysis for each sample was performed. The standards were used to correct the analyzed samples to Vienna Standard Pee Dee Belemnite scale (VPDB). A Linear regression was produced using the known vs. measured values of the A_4 and A_5 standards and linear regression had a slope of 1 ± 0.14 for all analyzed standards. The results are reported in delta notation in permil (‰). The analytical precision of each single measurement had a typical standard deviation of ± 0.5‰. We report all measured samples with a standard deviation of ±1‰, which represents the total variability in all measured n-alkane standard mixtures of the $A_{3\text{-}5}$ standards and is more than the analytical standard deviation of ±0.5‰. All lipid-biomarker n-alkane data of δD and $\delta^{13}C$ and ACL, CPI and cross-correlation plots are reported in Table C.1; Figs. C.2-C.3 and 4.2. ACL, CPI and cross-correlation plots are reported in Figs. C.4-C.6.

Sample preparation for soil-carbonates $\delta^{18}O$ and $\delta^{13}C$ analyses and measurement.

In total 64 pedogenic carbonates were selected from the Angastaco Basin, ranging from ~10 to 4 Ma. Pedogenic carbonate nodules were cut in half and bulk carbonate powder was extracted with a diamond tip dental drill. 100 to 180 µg untreated pedogenic carbonate was reacted with 98% H_3PO_4 for 90 min at 70°C in continuous flow mode using a Thermo MAT 253 mass spectrometer interfaced to a Thermo GasBench II at the Goethe University-BiK-F Joint Stable Isotope Facility Frankfurt. Analytical precision was typically ±0.1‰ for $\delta^{18}O$ and ±0.2‰ for $\delta^{13}C$ based on replicate measurements of international and in-house standards. Stable isotope values are presented with respect to VSMOW ($\delta^{18}O$) and PDB ($\delta^{13}C$). All pedogenic carbonates $\delta^{18}O$ and $\delta^{13}C$ values are reported in Table C.2 and Figure 4.2.

Reconstruction of lipid biomarker, pedogenic-carbonates, and volcanic glass source water.

There has been an increasing effort to develop an empirical equation instead linking isotope depletion in lipid biomarker n-alkanes to source water through

apparent fractionation (Sachse et al., 2012; Garcin et al., 2012) (Fig. C.8). We use the empirical equation $\delta D_{wax\ SW}$ = 1.08 x δD_{wax} – 140 from Garcin et al. (2012), derived from along a large temperature, rainfall and moisture gradient in tropical Africa (Ghana), to reconstruct lipid-biomarker source water (SW). We prefer this equation because a global compilation by Sachse et al. (2012) is dominated by mid-latitude data underrepresenting semi-arid and arid regions. Reconstructed source waters are presented in Table C.1 and Figs. C.3 and C.9.

Pedogenic carbonates usually form in soil depths of ~20 to 30 cm as the result of evaporating surface water. As calcite forms it records a signal of $\delta^{18}O$ and $\delta^{13}C$ stable isotopes. The $\delta^{18}O$ signal reflects the isotopic composition of the surface water and the $\delta^{13}C$ signal has been interpreted to reflect bioproductivity, CO_2 plant respiration or C_4/C_3 vegetation type. The calcite formation and the $\delta^{18}O$ isotope values are strongly controlled by temperature-dependent isotope fractionation between water and carbonate (e.g., Cerling and Quade, 1993; Liu and Ku, 1997). Therefore, for the reconstruction of paleosurface water the carbonate formation temperature needs to be known. Here, we use reconstructed clumped-isotope temperatures from Carrapa et al. (2014) for deciphering the temperature-dependent isotope fractionation using the fractionation factor of Kim and O'Neil (1997). Calculated values of the $\delta^{18}O_{carb\ SW}$ are reported in Table C.2 and Figs. 4.3 and C.9. For comparison with δD_{SW} of lipid-biomarker n-alkanes and volcanic glass shards the pedogenic carbonate $\delta^{18}O_{carb\ SW}$ were converted to $\delta D_{carb\ SW}$ using the local meteoric water line of $\delta D = 8.44 * \delta^{18}O + 15.91$ for 26°S from Rohrmann et al. (2014) (Table C.2 and Figure 4.3 and C.9).

After deposition rhyolitic glass incorporates large amounts of meteoric water (3 to 8 wt%) over a time frame of 5 to 10 ky (Friedman et al., 1993; Mulch et al., 2008; Cassel et al., 2009). The final δD_{volc} signal represents an integrated meteoric water signal during hydration over geological time scales. To compare δD_{volc} with other isotope proxy materials, e.g. lipid-biomarker and soil-carbonates, we converted the δD_{volc} signal to ancient meteoric water (source water), using the equation $\delta D_{SW} = 1.0343\ [1000 + \delta D_{volc}] - 1000$ by Friedman et

al. (1993). Converted meteoric-water and $\delta D_{volc\ SW}$ values are presented in Table C.3 and Figs. 4.3 and C.9. A time series is constructed using the reconstructed source waters with a time resolution of 200 k and used for calculating the source water differences in figure 4.3. All isotope relationships between source waters and the single isotope proxies and evaporation, transpiration and evapotranspiration are schematically sketched in figure C.8.

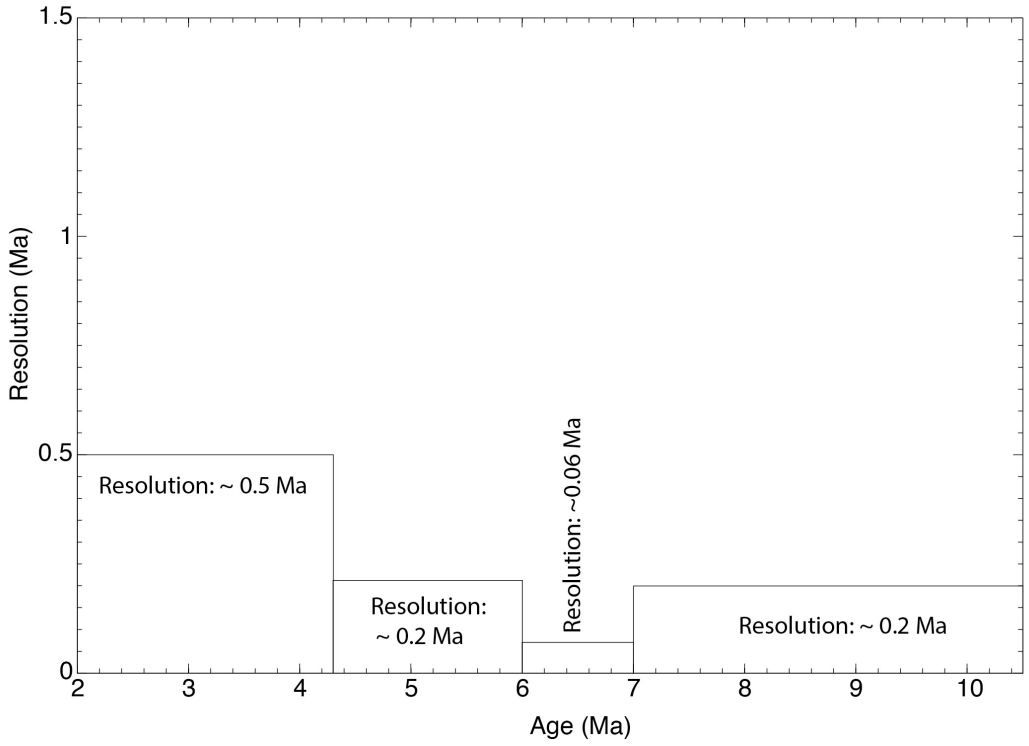

Fig. C.1. Lipid biomarker n-alkane record resolution through time.

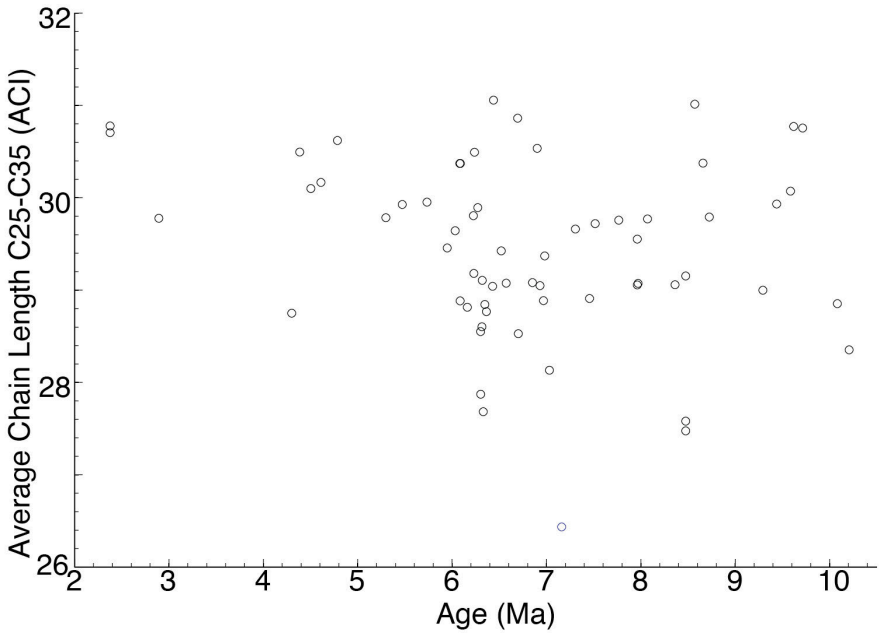

Fig. C.2. Average chain lengths (ACL) for n-alkane records C_{25} to C_{35}.

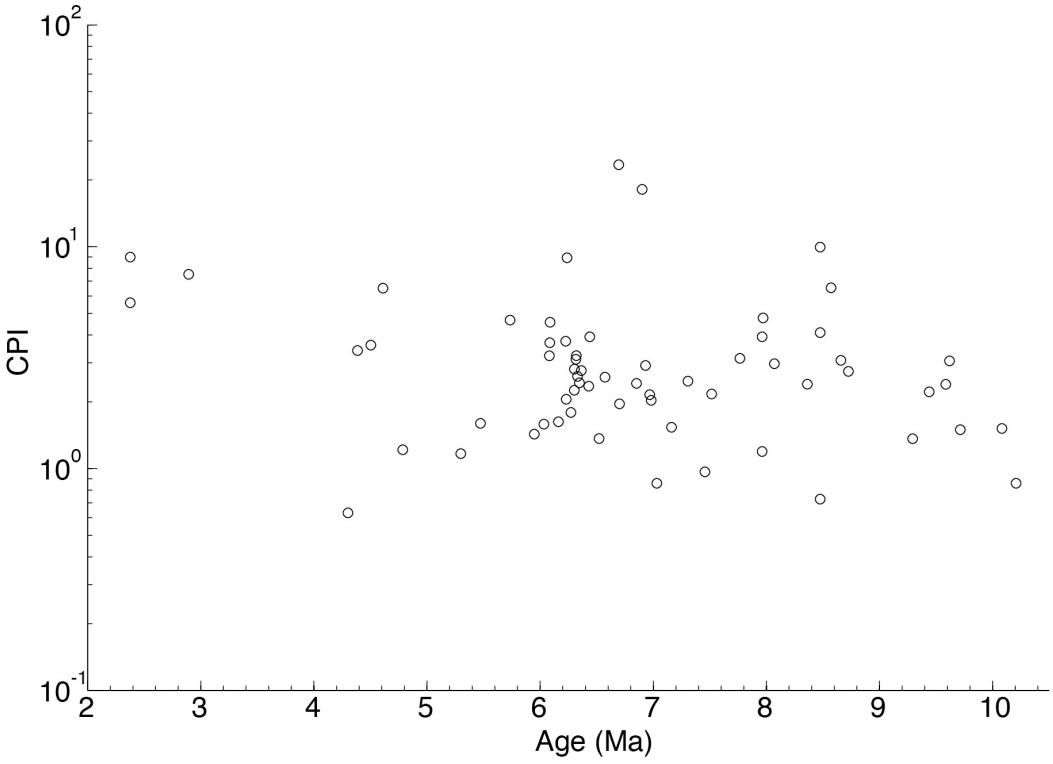

Fig. C.3. Carbon preference index (CPI) for n-alkane records.

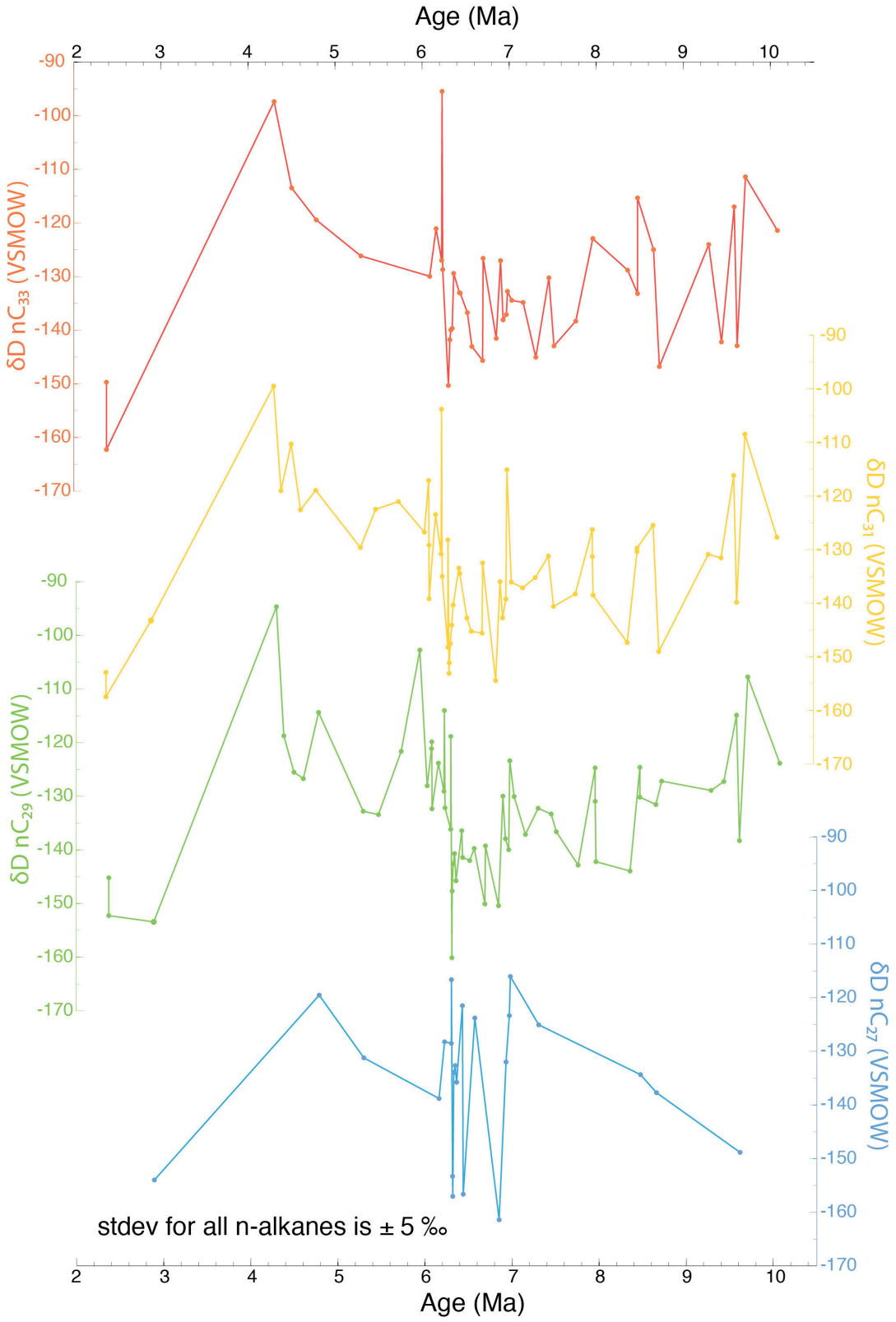

Fig. C.4. Hydrogen lipid biomarker data for n-alkanes C_{27} to C_{33} versus age. The standard deviation for all δD n-alkane values is ± 5 ‰, and not plotted for better comparison between different n-alkanes.

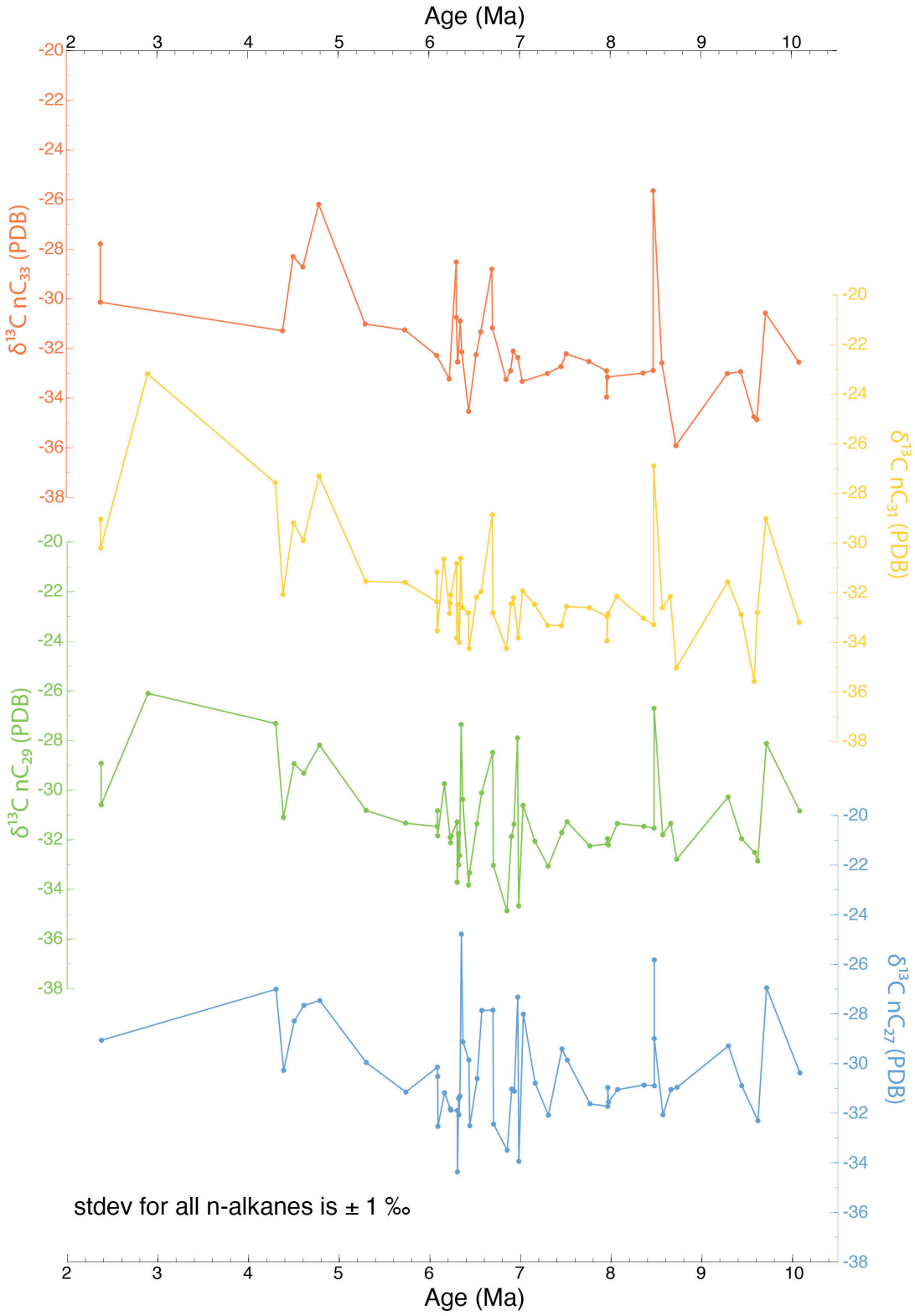

Fig. C.5. Carbon lipid biomarker data for n-alkanes C_{27} to C_{33} versus age. The standard deviation for all $\delta^{13}C$ n-alkane values is ± 1 ‰ and not plotted for better comparison between different n-alkanes.

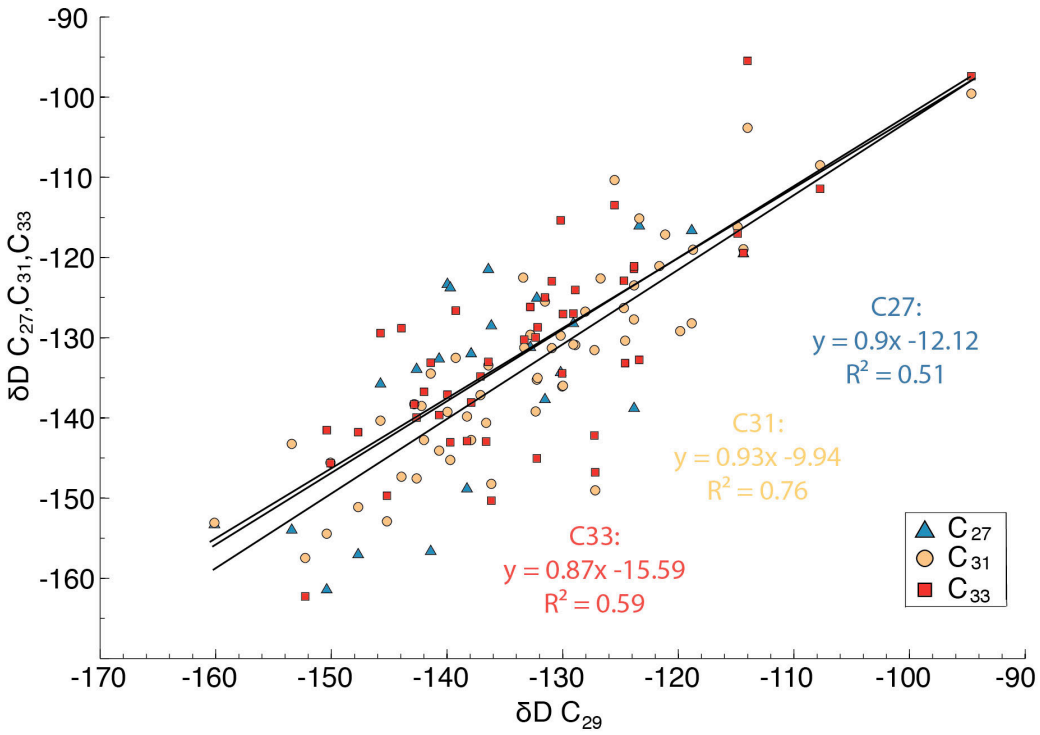

Fig. C.6. Plot of hydrogen for C_{29} versus C_{27}, C_{31} and C_{33} to decipher hydrogen sources and plant groups (e.g., higher plants, aquatic plants, grasses).

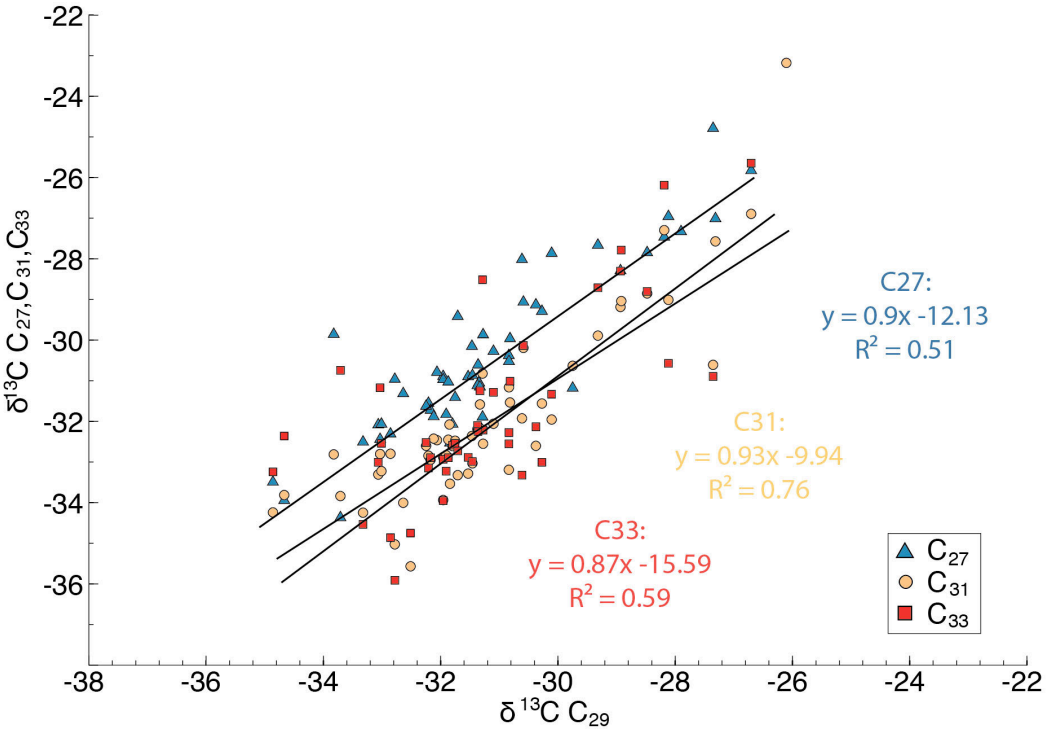

Fig. C.7. Plot of carbon C_{29} versus C_{27}, C_{31} and C_{33} to decipher carbon sources and plant groups.

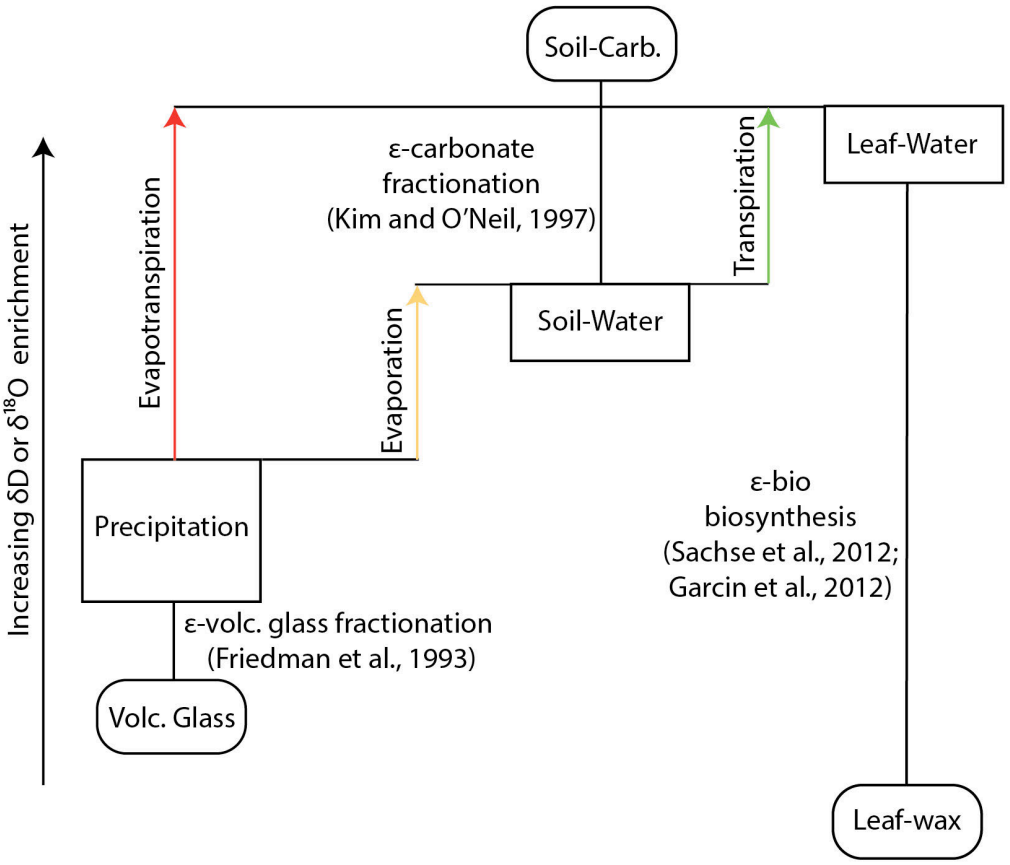

Fig. C.8. Isotopic relationships between source water δD and $\delta^{18}O$ of precipitation, soil-water and leaf-water, and stable isotope proxies of lipid biomarkers, soil-carbonates and volcanic glass.

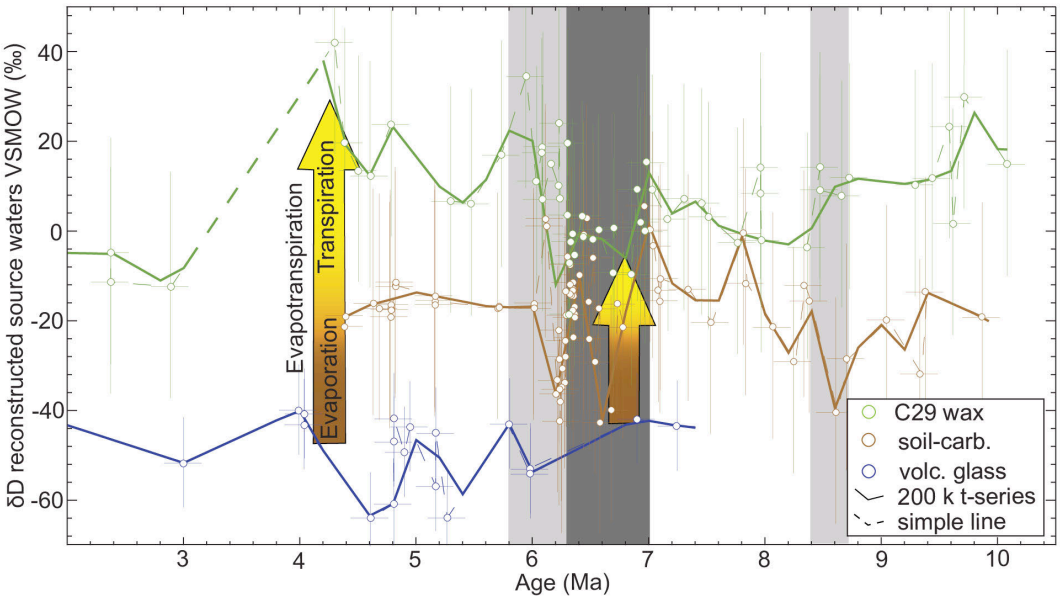

Fig. C.9. Reconstructed source water for lipid biomarkers, pedogenic carbonates, and volcanic glass. A. Reconstructed source water and estimates of evaporation, transpiration, and evapotranspiration over time (arrows). Note the differences in reconstructed source water for the different proxies, suggesting that all three proxies use different source water: volcanic glass: precipitation, pedogenic carbonates: soil water, lipid biomarkers: leaf /soil water. A time series is constructed using the reconstructed source waters with a time resolution of 200 k and used for calculating the source water differences for figure 4.3.

Table C.1. Lipid biomarker n-alkane results and source water reconstruction

TABLE 1. HYDROGEN AND CARBON ISOTOPE ANALYSIS OF N-ALKANE LIPID BIOMARKERS

Sample #	Lat. (S)	Long. (W)	Stratigraphic depth (m)	Age (Ma)	Error (Ma)	Sample type	Source	TOC %	ACL (C14-C37)	ACL (C25-C37)	CPI
AR-II-PS 1	25.6770	66.1020	20	10.21	0.1	Paleosoil/overbank deposit	This study	0.1	24.1	28.4	0.9
AR-II-PS 2	25.6767	66.1016	50	10.08	0.1	Paleosoil/overbank deposit	This study	0.1	27.7	28.9	1.5
AR-II-PS 17	25.6655	66.0968	138	9.71	0.1	Paleosoil/overbank deposit	This study	0.1	25.6	30.8	1.5
AR-13-46-1	25.6832	66.1010	161	9.62	0.1	Lacustrine sediment	This study	< 0.1	30.4	30.8	3.1
AR-II-PS 18	25.6659	66.0964	169	9.58	0.1	Paleosoil/overbank deposit	This study	2.2	28.7	30.1	2.4
AR-II-PS 4	25.6746	66.0986	204	9.44	0.1	Paleosoil/overbank deposit	This study	0.2	27.5	29.9	2.2
AR-II-PS 5	25.6749	66.0981	239	9.29	0.1	Paleosoil/overbank deposit	This study	0.2	24.3	29.0	1.4
AR-II-PS 6	25.6764	66.0966	375	8.73	0.1	Lacustrine sediment	This study	0.5	29.1	29.8	2.7
AR-13-55-1	25.6840	66.0977	391	8.66	0.1	Paleosoil/overbank deposit	This study	< 0.1	30.3	30.4	3.1
AR-13-54-1	25.6844	66.0977	412	8.57	0.1	Paleosoil/overbank deposit	This study	< 0.1	31.0	31.0	6.5
AR-II-PS 7	25.6772	66.0961	435	8.47	0.1	Lacustrine sediment	This study	5.5	26.6	27.5	4.1
AR-II-PS 7b	25.6772	66.0961	435	8.47	0.1	Lacustrine sediment	This study	5.5	26.6	27.6	10.0
AR-II-PS 7c	25.6772	66.0961	435	8.47	0.1	Paleosoil/overbank deposit	This study	5.6	22.6	29.2	0.7
AR-II-PS 8	25.6740	66.0949	462	8.36	0.1	Paleosoil/overbank deposit	This study	0.4	27.5	29.1	2.4
AR-13-53-1	25.6845	66.0960	532	8.07	0.1	Paleosoil/overbank deposit	This study	< 0.1	29.6	29.8	3.0
AR-13-45-2	25.6773	66.0943	556	7.97	0.1	Paleosoil/overbank deposit	This study	< 0.1	28.9	29.1	4.8
AR-II-PS 9	25.6773	66.0944	558	7.96	0.1	Paleosoil/overbank deposit	This study	8.8	24.0	29.1	1.2
AR-13-45-1	25.6773	66.0943	558	7.96	0.1	Paleosoil/overbank deposit	This study	0.1	29.6	29.6	3.9
AR-II-PS 10	25.6780	66.0938	605	7.77	0.1	Paleosoil/overbank deposit	This study	0.3	28.7	29.8	3.1
AR-II-PS 11	25.6784	66.0935	665	7.52	0.1	Paleosoil/overbank deposit	This study	0.2	27.8	29.7	2.2
AR-II-PS 12	25.6787	66.0936	679	7.46	0.1	Paleosoil/overbank deposit	This study	0.3	23.0	28.9	1.0
AR-II-PS 13	25.6778	66.0930	715	7.31	0.1	Paleosoil/overbank deposit	This study	0.2	26.9	29.7	2.5

AR-II-PS 14	25.6779	66.0929	750	7.16	0.1	Paleosoil/overbank deposit	This study	0.5	22.4	26.4	1.5
AR-II-PS 15	25.6782	66.0920	781	7.03	0.1	Paleosoil/overbank deposit	This study	0.1	19.8	28.1	0.9
AR-II-PS 16	25.6782	66.0920	793	6.98	0.1	Paleosoil/overbank deposit	This study	0.2	27.3	29.4	2.0
AR-13-52-1	25.6830	66.0926	796	6.97	0.1	Paleosoil/overbank deposit	This study	< 0.1	27.9	28.9	2.2
AR-13-51-1	25.6844	66.0914	805	6.93	0.1	Lacustrine sediment	This study	0.2	27.1	29.0	2.9
AR-13-51-2	25.6844	66.0914	812	6.90	0.1	Paleosoil/overbank deposit	This study	< 0.1	30.5	30.5	18.1
AR-II-PS 22	25.6773	66.0894	824	6.85	0.1	Paleosoil/overbank deposit	This study	0.4	28.2	29.1	2.4
AR-II-PS 23	25.6782	66.0889	880	6.70	0.1	Lacustrine sediment	This study	0.2	27.1	28.5	2.0
AR-II-PS 24	25.6782	66.0889	883	6.69	0.1	Paleosoil/overbank deposit	This study	0.3	30.9	30.9	23.4
AR-II-PS 25	25.6788	66.0893	935	6.57	0.1	Lacustrine sediment	This study	0.3	27.2	29.1	2.6
AR-II-PS 26	25.6791	66.0890	957	6.52	0.1	Paleosoil/overbank deposit	This study	0.1	27.0	29.4	1.4
AR-II-PS 27	25.6751	66.0863	992	6.44	0.1	Paleosoil/overbank deposit	This study	0.3	30.7	31.1	3.9
AR-II-PS 28	25.6747	66.0864	996	6.43	0.1	Lacustrine sediment	This study	0.2	27.0	29.0	2.4
AR-13-44-1	25.6753	66.0854	1024	6.36	0.1	Paleosoil/overbank deposit	This study	< 0.1	28.2	28.8	2.8
AR-II-PS 29	25.6754	66.0854	1031	6.35	0.1	Lacustrine sediment	This study	0.3	27.7	28.8	2.4
AR-13-48-1	25.6885	66.0878	1045	6.33	0.3	Paleosoil/overbank deposit	This study	< 0.1	27.2	27.7	2.6
AR-13-47-1	25.6892	66.0875	1059	6.32	0.3	Paleosoil/overbank deposit	This study	0.1	28.4	29.1	3.2
AR-13-47-2	25.6892	66.0875	1062	6.32	0.3	Paleosoil/overbank deposit	This study	0.3	27.4	28.6	3.1
AR-13-49-2	25.6890	66.0865	1078	6.30	0.3	Paleosoil/overbank deposit	This study	0.4	27.2	27.9	2.8
AR-13-49-3	25.6890	66.0865	1079	6.30	0.3	Lacustrine sediment	This study	0.4	27.2	28.6	2.3
AR-II-PS 31	25.6781	66.0829	1115	6.27	0.3	Paleosoil/overbank deposit	This study	0.1	21.3	29.9	1.8
AR-13-42-2	25.6770	66.0821	1157	6.24	0.3	Paleosoil/overbank deposit	This study	< 0.1	30.5	30.5	8.9
AR-II-PS 33	25.6773	66.0822	1165	6.23	0.3	Paleosoil/overbank deposit	This study	0.1	25.7	29.2	2.1
AR-13-42-1	25.6770	66.0821	1171	6.23	0.3	Paleosoil/overbank deposit	This study	< 0.1	29.6	29.8	3.8
AR-II-PS 32	25.6773	66.0813	1248	6.16	0.3	Paleosoil/overbank deposit	This study	1.6	26.4	28.8	1.6
AR-13-40-2	25.6793	66.0812	1335	6.09	0.3	Paleosoil/overbank deposit	This study	< 0.1	30.4	30.4	4.6
AR-13-40-1	25.6793	66.0812	1338	6.09	0.3	Paleosoil/overbank deposit	This study	< 0.1	28.9	28.9	3.7
AR-II-PS 36	25.6769	66.0805	1342	6.08	0.3	Lacustrine sediment	This study	0.1	28.5	30.4	3.2
AR-II-PS 35	25.6747	66.0785	1401	6.03	0.3	Paleosoil/overbank deposit	This study	0.1	29.6	29.6	1.6
AR-II-PS 34	25.6749	66.0774	1477	5.95	0.3	Paleosoil/overbank deposit	This study	0.1	22.9	29.5	1.4

Table C.1. Lipid biomarker n-alkane results and source water reconstruction (continued)

AR-II-PS 37	25.6759	66.0768	1564	5.73	0.3	Paleosoil/overbank deposit	This study	0.1	30.0	30.0	4.7
AR-II-PS 38	25.6764	66.0751	1670	5.47	0.3	Paleosoil/overbank deposit	This study	0.1	26.9	29.9	1.6
AR-II-PS 39	25.6771	66.0740	1741	5.30	0.3	Paleosoil/overbank deposit	This study	0.1	24.0	29.8	1.2
AR-II-PS 20	25.6853	66.0533	1871	4.79	0.2	Paleosoil/overbank deposit	This study	0.2	27.8	30.6	1.2
AR-13-BM-4	25.7295	66.0192	1965	4.61	0.2	Lacustrine sediment	This study	< 0.1	30.2	30.2	6.5
AR-13-BM-2	25.7295	66.0143	1982	4.50	0.2	Paleosoil/overbank deposit	This study	< 0.1	29.9	30.1	3.6
AR-13-BM-1	25.7285	66.0129	2000	4.39	0.2	Paleosoil/overbank deposit	This study	< 0.1	29.9	30.5	3.4
AR-II-PS 21	25.6922	66.0283	2013	4.30	0.2	Paleosoil/overbank deposit	This study	0.1	21.1	28.7	0.6
AR-13-37-1	25.7957	65.9734	2200	2.89	0.2	Lacustrine sediment	This study	< 0.1	29.7	29.8	7.5
AR-13-36-1	25.7955	65.9711	2280	2.38	0.2	Lacustrine sediment	This study	< 0.1	30.7	30.7	5.6
AR-13-36-2	25.7955	65.9711	2280	2.38	0.2	Lacustrine sediment	This study	< 0.1	30.8	30.8	9.0

aδDwax of C29 lipid biomarker source waters were calculated using the emperical equation δmw = (140 + δDC29) / 1.08 of Garcin et al. (2012) for n-alkanes calibrated along a large humidity and precipitation transect in tropical Africa (Ghana).

Table C.1. Lipid biomarker n-alkane results and source water reconstruction (continued)

Carbon $\delta^{13}C$ results

Sample #	C27	STDEV	C28	STDEV	C29	STDEV	C30	STDEV	C31	STDEV	C32	STDEV	C33	STDEV
AR-II-PS 1														
AR-II-PS 2	-30.4	0.2	-30.8	0.1	-30.8	0.1	-31.1	0.4	-33.2	0.4	-33.3	0.4	-32.6	0.2
AR-II-PS 17	-27.0	0.3	-27.0	0.3	-28.1	0.3	-27.7	0.3	-29.0	0.2			-30.6	2.9
AR-13-46-1	-32.3	0.1	-32.8	0.1	-32.9	0.1	-33.3	0.2	-32.8	0.0	-34.4	0.1	-34.9	0.2
AR-II-PS 18					-32.5	0.5			-35.6	0.1			-34.7	0.4
AR-II-PS 4	-30.9	0.4			-32.0	0.3			-32.9	0.1			-32.9	0.5
AR-II-PS 5	-29.3	0.2	-30.6	0.2	-30.3	0.1	-30.9	0.2	-31.6	0.2	-32.3	0.2	-33.0	0.6
AR-II-PS 6	-31.0	0.3	-32.3	0.2	-32.8	0.2	-31.2	3.1	-35.0	0.1	-35.9	0.1	-35.9	0.1
AR-13-55-1	-31.0	0.7			-31.3	0.5			-32.1	0.2				
AR-13-54-1	-32.1	0.5	-31.4	0.4	-31.8	0.0	-31.5	0.2	-32.6	0.1	-32.4	0.1	-32.6	0.0
AR-II-PS 7	-29.0	0.8												
AR-II-PS 7b	-25.8	0.1			-26.7	0.1			-26.9	0.1			-25.6	0.1
AR-II-PS 7c	-30.9	0.2	-31.2	0.3	-31.5	0.2	-31.4	0.1	-33.3	0.1	-34.8	0.2	-32.9	0.0
AR-II-PS 8	-30.9	0.4			-31.5	0.7			-33.0	0.2			-33.0	0.2
AR-13-53-1	-31.0	0.7			-31.3	0.5			-32.1	0.2				
AR-13-45-2	-31.6	0.0	-32.2	0.0	-32.2	0.0	-32.6	0.2	-32.8	0.0	-33.4	0.7	-33.1	0.1
AR-II-PS 9	-31.0	0.0	-30.7	0.0	-32.0	0.1	-32.6	0.1	-33.9	0.0	-34.5	0.3	-34.0	0.0
AR-13-45-1	-31.7	0.2	-32.0	0.2	-32.2	0.2	-32.3	0.6	-32.9	0.0			-32.9	0.2
AR-II-PS 10	-31.6	0.1			-32.2	0.2			-32.6	0.2			-32.5	0.1
AR-II-PS 11	-29.9	0.2			-31.3	0.1	-29.6	0.4	-32.6	0.1			-32.2	0.2
AR-II-PS 12	-29.4	0.1	-30.5	0.2	-31.7	0.2	-34.3	1.5	-33.3	0.2	-33.6	0.3	-32.7	0.1
AR-II-PS 13	-32.1	0.0	-32.6	0.1	-33.1	0.2	-32.6	0.1	-33.3	0.1	-33.2	0.1	-33.0	0.0
AR-II-PS 14	-30.8	0.1			-32.1	0.5			-32.5	0.4				
AR-II-PS 15	-28.0	0.3	-29.6	1.5	-30.6	1.5	-30.8	2.0	-31.9	1.8	-33.2	0.6	-33.3	0.4
AR-II-PS 16	-33.9	0.2	-33.7	0.4	-34.7	0.1	-33.4	0.6	-33.8	0.1	-32.1	0.2	-32.4	0.2
AR-13-52-1	-27.3	0.2			-27.9	0.1	-25.2	4.4						
AR-13-51-1	-31.1	0.5			-31.4	0.2			-32.2	0.2			-32.1	0.1

Table C.1. Lipid biomarker n-alkane results and source water reconstruction (continued)

AR-13-51-2	-31.0	0.1	-31.2	0.3	-31.9	0.1	-32.6	0.3	-32.5	0.1	-33.2	0.5	-32.9	0.2		
AR-II-PS 22	-33.5	0.2	-33.7	0.1	-34.9	0.2	-33.3	0.1	-34.2	0.1	-32.0	0.2	-33.2	0.0		
AR-II-PS 23	-32.4	0.4			-33.0	0.5			-32.8	0.4			-31.2	0.2		
AR-II-PS 24	-27.8	0.1	-27.4	0.0	-28.5	0.1			-28.9	0.1			-28.8	0.0		
AR-II-PS 25	-27.9	0.2	-30.0	0.1	-30.1	0.2	-32.4	0.1	-32.0	0.1			-31.3	0.1		
AR-II-PS 26	-30.6	0.3			-31.4	0.3			-32.2	0.1			-32.2	0.5		
AR-II-PS 27	-32.5	0.2	-32.7	0.2	-33.3	0.1	-33.1	0.3	-34.2	0.0	-34.3	0.2	-34.5	0.1		
AR-II-PS 28	-29.9	0.1	-30.4	0.1	-33.8	0.2	-33.7	0.2	-32.8	0.6	-32.1	0.1				
AR-13-44-1	-29.1	1.3			-30.4	0.2			-32.6	0.2			-32.1	0.3		
AR-II-PS 29	-24.8	0.0	-26.5	0.2	-27.4	0.3	-30.5	0.1	-30.6	0.1			-30.9	0.1		
AR-13-48-1	-31.3	0.2			-32.6	0.6			-34.0	0.2						
AR-13-47-1	-32.1	0.1			-33.0	0.2	-32.9	0.4	-33.2	0.0			-32.5	0.2		
AR-13-47-2	-31.4	0.5			-31.8	0.6			-32.5	1.2			-32.5	0.3		
AR-13-49-2	-34.4	0.3	-32.7	0.3	-33.7	0.2	-33.3	0.2	-33.8	0.1	-30.7	0.5	-30.7	0.2		
AR-13-49-3	-31.9	0.2	-30.9	0.1	-31.3	0.1	-30.9	0.3	-30.8	0.2	-27.6	0.9	-28.5	0.2		
AR-II-PS 31																
AR-13-42-2					-31.9	0.2			-32.1	0.0						
AR-II-PS 33	-31.9	0.0			-32.1	0.7			-32.4	0.2						
AR-13-42-1	-31.8	0.2			-31.9	0.1			-32.8	0.0			-33.2	0.6		
AR-II-PS 32	-31.2	0.1			-29.7	0.6			-30.6	0.2						
AR-13-40-2	-32.5	0.6	-31.3	0.6	-31.8	0.6	-31.8	0.3	-33.5	0.6	-32.7	0.3				
AR-13-40-1	-30.5	0.4	-31.4	0.7	-30.8	0.1	-31.3	0.1	-31.2	0.4	-31.2	0.3	-32.3	0.2		
AR-II-PS 36	-30.1	0.0			-31.5	0.1			-32.4	0.0						
AR-II-PS 35																
AR-II-PS 34																
AR-II-PS 37	-31.1	0.6			-31.3	0.1			-31.6	0.2			-31.2	0.2		
AR-II-PS 38																
AR-II-PS 39	-30.0	0.1	-30.8	0.1	-30.8	0.2	-30.9	0.0	-31.5	0.2			-31.0	0.1		
AR-II-PS 20	-27.5	0.9			-28.2	0.4			-27.3	0.0			-26.2	0.1		
AR-13-BM-4	-27.7	0.0			-29.3	0.4			-29.9	0.5			-28.7	0.0		

Table C.1. Lipid biomarker n-alkane results and source water reconstruction (continued)

AR-13-BM-2	-28.3	0.1		-28.9	0.1		-29.2	0.2	-28.3	0.1
AR-13-BM-1	-30.3	0.2		-31.1	0.7		-32.1	0.9	-31.3	0.1
AR-II-PS 21	-27.0	0.2		-27.3	0.0		-27.6	0.1		
AR-13-37-1				-26.1	0.2		-23.2	0.2		
AR-13-36-1	-29.1	0.1		-30.6	0.1		-30.2	0.1	-30.1	0.9
AR-13-36-2				-28.9	0.5		-29.0	0.5	-27.8	0.5

Table C.1. Lipid biomarker n-alkane results and source water reconstruction (continued)

	Hyrogen δD results														Source water reconstruction	
Sample #	C27	STDEV	C28	STDEV	C29	STDEV	C30	STDEV	C31	STDEV	C32	STDEV	C33	STDEV	Rec.C_{29} meteoric water δD VSMOW[b] (‰)	error ± 1 sig
AR-II-PS 1																
AR-II-PS 2					-123.8	1.4			-127.7	0.4			-121.4	3.1	15.0	25.0
AR-II-PS 17					-107.7	0.6			-108.5	0.2			-111.4	8.3	29.9	25.0
AR-13-46-1	-148.8	0.8			-138.3	1.8	-136.8	2.5	-139.8	0.3	-136.6	6.0	-142.9	0.1	1.6	25.0
AR-II-PS 18					-114.9	3.6			-116.2	1.8			-117.0	2.3	23.3	25.0
AR-II-PS 4					-127.3	2.4			-131.5	4.1			-142.2	1.0	11.8	25.0
AR-II-PS 5					-128.9	0.1			-130.9	0.6			-124.0	2.5	10.3	25.0
AR-II-PS 6					-127.2	4.1			-149.0	1.2			-146.8	7.2	11.9	25.0
AR-13-55-1	-137.7	2.4	-129.1	15.6	-131.5	0.0	-124.6	0.4	-125.5	0.2	-119.3	0.7	-125.0	1.6	7.8	25.0
AR-13-54-1																
AR-II-PS 7																
AR-II-PS 7b	-134.3	0.2			-130.2	1.8			-129.7	2.4			-115.3	0.7	9.1	25.0
AR-II-PS 7c					-124.6	2.9			-130.4	1.3			-133.2	1.9	14.3	25.0
AR-II-PS 8					-143.9	1.3			-147.3	8.5			-128.8	1.1	-3.6	25.0
AR-13-53-1																
AR-13-45-2					-142.2	3.6			-138.5	1.4					-2.0	25.0
AR-II-PS 9					-130.9	5.0			-131.3	5.0			-123.0	5.0	8.4	25.0
AR-13-45-1					-124.7	1.9	-125.0	3.9	-126.3	0.6			-122.9	0.4	14.2	25.0
AR-II-PS 10					-142.8	1.5	-136.8	4.3	-138.3	0.3	-131.4	0.5	-138.3	0.0	-2.6	25.0
AR-II-PS 11					-136.6	0.9			-140.6	0.9			-142.9	3.1	3.1	25.0
AR-II-PS 12					-133.3	0.3			-131.2	1.3			-130.2	0.3	6.2	25.0

Table C.1. Lipid biomarker n-alkane results and source water reconstruction (continued)

AR-II-PS 13	-125.1	3.9			-132.2	1.8			-135.2	2.4				-145.0	3.1	7.2	25.0
AR-II-PS 14					-137.1	9.8			-137.2	3.6				-134.8	9.1	2.7	25.0
AR-II-PS 15					-130.0	1.9			-136.1	1.9				-134.4	4.5	9.2	25.0
AR-II-PS 16	-116.0	1.3	-124.8	0.7	-123.4	0.5	-121.0	0.9	-115.1	2.0	-113.7	2.3		-132.8	1.8	15.4	25.0
AR-13-52-1	-123.3	0.9	-136.5	0.4	-140.0	1.3	-166.0	1.3	-139.2	0.4	-146.9	1.2		-137.1	0.6	0.0	25.0
AR-13-51-1	-132.0	0.9			-137.9	0.6			-142.7	0.2				-138.1	1.1	1.9	25.0
AR-13-51-2					-130.0	1.8			-136.0	0.2				-127.0	1.7	9.3	25.0
AR-II-PS 22	-161.4	2.8	-155.3	8.0	-150.4	4.2	-149.3	5.7	-154.4	1.5	-152.9	1.9		-141.5	2.9	-9.6	25.0
AR-II-PS 23					-139.3	1.7			-132.5	1.5				-126.6	0.8	0.7	25.0
AR-II-PS 24					-150.1	0.1			-145.6	1.1				-145.7	0.2	-9.3	25.0
AR-II-PS 25	-123.8	2.6	-136.7	1.1	-139.7	2.1	-172.3	2.3	-145.2	1.7	-150.5	2.0		-143.0	2.4	0.3	25.0
AR-II-PS 26					-142.0	2.0			-142.8	0.7				-136.7	2.7	-1.8	25.0
AR-II-PS 27	-156.6	0.8			-141.4	1.6			-134.5	2.2				-133.1	1.3	-1.3	25.0
AR-II-PS 28	-121.5	0.4	-135.3	1.9	-136.4	1.0	-141.6	0.4	-133.4	0.5	-137.8	1.5		-133.0	0.7	3.3	25.0
AR-13-44-1	-135.8	0.9	-138.5	1.9	-145.8	0.5	-137.5	1.9	-140.3	1.0	-135.8	1.7		-129.4	0.3	-5.3	25.0
AR-II-PS 29	-132.6	0.3	-139.9	0.7	-140.7	0.9	-160.1	0.6	-144.1	0.6	-155.7	3.4		-139.7	1.7	-0.6	25.0
AR-13-48-1	-133.9	1.0	-137.3	0.8	-142.6	0.6	-140.2	1.2	-147.5	0.6				-140.0	2.0	-2.4	25.0
AR-13-47-1	-157.0	1.3	-151.2	3.5	-147.7	0.9	-149.5	1.3	-151.1	0.9				-141.8	1.1	-7.1	25.0
AR-13-47-2	-153.3	2.6			-160.1	1.2			-153.1	3.6						-18.6	25.0
AR-13-49-2	-116.6	2.9	-120.4	5.9	-118.8	3.3			-128.2	4.4						19.6	25.0
AR-13-49-3	-128.5	3.7			-136.2	5.9			-148.2	6.8				-150.3	0.0	3.6	25.0
AR-II-PS 31																	
AR-13-42-2					-132.2	0.6			-135.0	0.9				-128.7	0.6	7.3	25.0
AR-II-PS 33					-114.0	0.9			-103.8	0.7				-95.5	0.3	24.1	25.0
AR-13-42-1	-128.2	5.6			-129.1	1.1			-130.8	1.4				-127.0	7.4	10.1	25.0
AR-II-PS 32	-138.8	1.7			-123.8	5.1			-123.5	5.1				-121.1	9.2	15.0	25.0
AR-13-40-2					-132.3	0.3			-139.2	0.9				-130.0	1.5	7.1	25.0
AR-13-40-1					-119.8	0.7			-129.2	1.0						18.7	25.0
AR-II-PS 36					-121.1	10.0			-117.1	1.2						17.5	25.0
AR-II-PS 35					-128.0	1.0			-126.8	1.0						11.1	25.0

Table C.1. Lipid biomarker n-alkane results and source water reconstruction (continued)

AR-II-PS 34			-102.7	1.0	-124.5	1.0									34.5	25.0
AR-II-PS 37			-121.6	0.9			-121.1	2.2							17.0	25.0
AR-II-PS 38			-133.4	1.0			-122.5	1.0							6.1	25.0
AR-II-PS 39	-131.2	4.2	-132.8	4.6			-129.6	1.3			-126.2	0.2			6.7	25.0
AR-II-PS 20	-119.5	1.8	-114.4	2.0			-119.0	3.1			-119.4	5.2			23.7	25.0
AR-13-BM-4			-126.7	1.0			-122.6	1.0							12.3	25.0
AR-13-BM-2			-125.5	1.0	-109.2	1.5	-110.3	0.8	-110.4	3.4	-113.5	0.9			13.4	25.0
AR-13-BM-1			-118.7	1.4			-119.0	0.8							19.7	25.0
AR-II-PS 21			-94.7	1.1	-88.0	3.7	-99.6	0.5	-78.9	10.3	-97.4	14.5			42.0	25.0
AR-13-37-1	-154.0	0.5	-153.4	0.9			-143.2	2.3							-12.4	25.0
AR-13-36-1			-152.3	0.5	-141.1	1.5	-157.5	1.4	-151.9	3.2	-162.3	1.1			-11.4	25.0
AR-13-36-2			-145.2	1.1			-152.9	0.3			-149.7	1.3			-4.8	25.0

Table C.1. Lipid biomarker n-alkane results and source water reconstruction (continued)

Sample #	Lat.(° S)	Long. (° W)	Stratigraphic position (m)	Age (Ma)	Source	δ^{13}C PDB (‰)	std dev.	δ^{18}O PDB (‰)	std dev.
AR-14-SC-49	-25.6724	-66.0995	202	9.86	This study	-17.3	0.3	-9.0	0.1
AR-14-SC-47	-25.6751	-66.0988	319	9.38	This study	-11.1	0.3	-8.4	0.1
AR-14-SC-46	-25.6750	-66.0982	330	9.33	This study	-12.5	0.3	-10.5	0.1
AR-14-SC-43	-25.6758	-66.0973	399	9.04	This study	*-4.1*	*0.3*	*-9.1*	*0.1*
AR-14-SC-41	-25.6764	-66.0964	481	8.70	This study	-15.6	0.3	-10.1	0.1
AR-14-SC-42	-25.6767	-66.0965	503	8.61	This study	-11.1	0.3	-11.6	0.1
AR-14-SC-40	-25.6742	-66.0950	558	8.38	This study	-14.0	0.3	-8.6	0.1
AR-14-SC-38	-25.6741	-66.0949	569	8.33	This study	-14.4	0.3	-8.2	0.1
AR-14-SC-39	-25.6745	-66.0948	590	8.25	This study	-13.7	0.3	-10.2	0.1
AR-14-SC-37	-25.6765	-66.0948	633	8.07	This study	-14.1	0.3	-9.3	0.1
AR-14-SC-35	-25.6779	-66.0941	689	7.83	This study	-12.9	0.3	-8.2	0.1
AR-14-SC-34	-25.6780	-66.0940	694	7.81	This study	-12.1	0.3	-6.8	0.1
AR-14-SC-33	-25.6784	-66.0936	761	7.53	This study	-15.1	0.3	-9.2	0.1
AR-14-SC-32	-25.6781	-66.0930	808	7.34	This study	-12.9	0.3	-8.3	0.1
AR-14-SC-31	-25.6781	-66.0927	865	7.10	This study	-13.0	0.3	-8.0	0.1
AR-14-SC-30	-25.6781	-66.0926	866	7.09	This study	-10.3	0.3	-8.6	0.1
AR-14-SC-29	-25.6781	-66.0926	870	7.08	This study	-12.6	0.3	-8.3	0.1
AR-14-SC-28	-25.6782	-66.0924	880	7.04	This study	-11.9	0.3	-7.2	0.1
AR-14-SC-27	-25.6782	-66.0921	886	7.01	This study	-17.4	0.3	-6.7	0.1
AR-14-SC-26	-25.6783	-66.0919	898	6.96	This study	-11.2	0.3	-6.1	0.1
AR-14-SC-25	-25.6777	-66.0894	951	6.78	This study	-13.8	0.3	-9.3	0.1
AR-14-SC-24	-25.6781	-66.0889	975	6.73	This study	-13.9	0.3	-8.7	0.1
AR-14-SC-23	-25.6783	-66.0892	1001	6.68	This study	-16.3	0.3	-11.5	0.1
AR-14-SC-21	-25.6790	-66.0888	1050	6.58	This study	-15.6	0.3	-11.8	0.1
AR-14-SC-18	-25.6735	-66.0871	1055	6.57	This study	-14.1	0.3	-8.8	0.1
AR-14-SC-17	-25.6743	-66.0869	1071	6.54	This study	-13.2	0.3	-10.2	0.1
AR-14-SC-16	-25.6746	-66.0866	1080	6.52	This study	-14.3	0.3	-7.5	0.1
AT7-7_c	-25.6752	-66.0864	1095	6.48	Bywater-Reyes et al. (2010)	-13.4	0.1	-8.6	0.1
AT7-7_d	-25.6752	-66.0864	1095	6.48	Bywater-Reyes et al. (2010)	-14.4	0.2	-9.6	0.1
AR-14-SC-15	-25.6755	-66.0864	1106	6.47	This study	-14.4	0.3	-6.4	0.1
AR-14-SC-14	-25.6757	-66.0859	1117	6.44	This study	*-11.7*	*0.3*	*-4.4*	*0.1*
AR-14-SC-12	-25.6749	-66.0855	1119	6.44	This study	-14.7	0.3	-6.9	0.1
AR-14-SC-13	-25.6751	-66.0851	1138	6.40	This study	-13.9	0.3	-7.9	0.1

Table C.2. Pedogenic-carbonate results and source water reconstruction

AR_13_15	-25.6885	-66.0876	1147	6.36	This study	-11.4	0.1	-7.6	0.1
AR_13_16	-25.6885	-66.0876	1147	6.36	This study	-11.2	0.1	-7.8	0.1
AR_13_16B	-25.6885	-66.0876	1147	6.36	This study	-11.4	0.1	-7.9	0.1
AR_13_14	-25.6885	-66.0876	1149	6.35	This study	-11.0	0.1	-7.2	0.1
AR_13_12	-25.6885	-66.0876	1149	6.35	This study	-11.6	0.1	-7.1	0.1
AR_13_13	-25.6885	-66.0876	1149	6.35	This study	-11.4	0.1	-7.2	0.1
AR_13_11	-25.6884	-66.0875	1151	6.35	This study	-12.4	0.1	-8.3	0.1
AR_13_10	-25.6884	-66.0876	1151	6.35	This study	-11.1	0.1	-7.0	0.1
AR_13_9	-25.6884	-66.0876	1152	6.35	This study	-13.1	0.1	-6.8	0.1
AR_13_7	-25.6884	-66.0876	1154	6.35	This study	-11.0	0.1	-7.0	0.1
AR_13_7B	-25.6884	-66.0876	1154	6.35	This study	-11.1	0.1	-7.0	0.1
AR_13_8	-25.6884	-66.0876	1154	6.35	This study	-11.7	0.1	-7.5	0.1
AR-14-SC-11	-25.6752	-66.0849	1142	6.33	This study	-10.7	0.3	-7.1	0.1
AT5-3_a	-25.6512	-66.0714	1145	6.32	Bywater-Reyes et al. (2010)	-15.4	0.2	-6.9	0.1
AT5-3_b	-25.6512	-66.0714	1145	6.32	Bywater-Reyes et al. (2010)	-15.0	0.2	-6.7	0.2
AT5-3_d	-25.6512	-66.0714	1145	6.32	This study	-13.8	0.1	-6.2	0.3
AR-14-SC-10	-25.6754	-66.0844	1154	6.32	This study	*-8.8*	*0.3*	*0.5*	*0.1*
AR-14-SC-9	-25.6763	-66.0840	1176	6.30	This study	-11.5	0.3	-5.9	0.1
AR-14-SC-8	-25.6765	-66.0838	1187	6.29	This study	-13.7	0.3	-7.5	0.1
AR-14-SC-7	-25.6763	-66.0836	1190	6.28	This study	-13.8	0.3	-6.8	0.1
AT5-4b-a	-25.6517	-66.0707	1196	6.28	Bywater-Reyes et al. (2010)	-10.2	0.3	-5.9	0.1
AT5-4b-b	-25.6517	-66.0707	1196	6.28	Bywater-Reyes et al. (2010)	-10.5	0.1	-6.4	0.2
AR-14-SC-6	-25.6758	-66.0831	1199	6.28	This study	-10.1	0.3	-7.0	0.1
AR-14-SC-5	-25.6766	-66.0830	1219	6.26	This study	-12.9	0.3	-6.7	0.1
AR-14-SC-4	-25.6767	-66.0828	1226	6.25	This study	-12.7	0.3	-7.2	0.1
AR-14-SC-3	-25.6769	-66.0827	1238	6.24	This study	-13.4	0.3	-7.5	0.1
AR_13_4	-25.6769	-66.0826	1238	6.23	This study	-13.1	0.1	-7.4	0.1
AR_13_4B	-25.6769	-66.0826	1238	6.23	This study	-12.9	0.1	-7.4	0.1
AR_13_6	-25.6769	-66.0826	1238	6.23	This study	-12.7	0.1	-8.3	0.1
AR-14-SC-2	-25.6769	-66.0825	1245	6.23	This study	-13.8	0.3	-6.6	0.1
AR-14-SC-1	-25.6770	-66.0824	1250	6.22	This study	-13.0	0.3	-5.9	0.1
AR_13_3b	-25.6770	-66.0821	1271	6.20	This study	-13.6	0.1	-7.8	0.1
AR_13_3a	-25.6770	-66.0821	1271	6.20	This study	-12.6	0.1	-7.6	0.1
AT7-7_a	-25.6770	-66.0810	1336	6.11	Bywater-Reyes et al. (2010)	-11.8	0.2	-4.0	0.1
AT7-7_b	-25.6770	-66.0810	1336	6.11	Bywater-Reyes et al. (2010)	-11.8	0.1	-4.1	0.2

Table C.2. Pedogenic-carbonate results and source water reconstruction (continued)

AT7-9-a	-25.6743	-66.0779	1424	6.01	Bywater-Reyes et al. (2010)	-12.4	0.1	-6.5	0.1
AT7-9-b	-25.6743	-66.0779	1424	6.01	Bywater-Reyes et al. (2010)	-12.3	0.1	-6.4	0.1
AT7-9-c	-25.6743	-66.0779	1424	6.01	Bywater-Reyes et al. (2010)	-12.0	0.1	-6.5	0.1
AT4-2-a	-25.6761	-66.0766	1592	5.70	Bywater-Reyes et al. (2010)	-11.4	0.3	-5.9	0.1
AT4-2-d	-25.6761	-66.0766	1592	5.70	Bywater-Reyes et al. (2010)	-10.5	0.1	-5.9	0.1
AT4-2-e	-25.6761	-66.0766	1592	5.70	Bywater-Reyes et al. (2010)	-10.3	0.1	-5.9	0.1
AT4-4-a	-25.6771	-66.0726	1815	5.16	Bywater-Reyes et al. (2010)	-9.4	0.1	-5.7	0.1
AT4-4-c	-25.6771	-66.0726	1815	5.16	Bywater-Reyes et al. (2010)	-9.5	0.1	-5.8	0.1
AT4-4-d	-25.6771	-66.0726	1815	5.16	Bywater-Reyes et al. (2010)	-9.4	0.1	-5.6	0.1
AT5-16a_a	-25.6491	-66.0533	1840	4.82	Bywater-Reyes et al. (2010)	-8.9	0.1	-6.1	0.1
AT5-16a_b	-25.6491	-66.0533	1840	4.82	Bywater-Reyes et al. (2010)	-9.2	0.1	-6.1	0.1
AT5-16a_c	-25.6491	-66.0533	1840	4.82	Bywater-Reyes et al. (2010)	-8.7	0.1	-6.0	0.1
AT2-4d-a	-25.7309	-66.0300	1960	4.78	Bywater-Reyes et al. (2010)	-9.1	0.1	-5.5	0.1
AT2-4d-b	-25.7309	-66.0300	1960	4.78	Bywater-Reyes et al. (2010)	-8.2	0.1	-5.3	0.1
AT2-4d-c	-25.7309	-66.0300	1960	4.78	Bywater-Reyes et al. (2010)	-8.3	0.3	-5.2	0.1
AT2-4d-d	-25.7309	-66.0300	1960	4.78	Bywater-Reyes et al. (2010)	-8.4	0.2	-5.3	0.1
RT-02	-25.6793	-66.0436	2030	4.68	This study	-7.6	0.3	-5.3	0.1
RT-04	-25.6774	-66.0416	2063	4.63	This study	-7.4	0.3	-5.1	0.1
AT6-2_a	-25.6734	-66.0345	2100	4.39	This study	-9.3	0.1	-5.3	0.3
AT6-2_b	-25.6734	-66.0345	2100	4.39	This study	-8.9	0.4	-5.6	0.1

aδD values were calculated using the LMWL of δD = 8.44*δ180 + 15.91 for 26° S from Rohrmann et al. (2014) , bδ18O of soil-carbonate meteoric water was calculated using the equation of Kim and O'Neil (1997) for calcite and Δ47 temperatures taken from Carrapa et al. (2014). Samples marked in red italic font were excluded from this study due to their low carbonate content during analysis test with HCL

Table C.2. Pedogenic-carbonate results and source water reconstruction (continued)

Sample #	δ18O VSMOW (‰)	calc. δD VSMOW[a] (‰)	Rec. meteoric water $\delta^{18}O$ VSMOW[b] (‰)	Error ± 1 SE (‰)	Rec. meteoric water δD VSMOW[b] (‰)	Error ± 1 SE (‰)
AR-14-SC-49	20.9	192.1	-4.1	1	-19.1	24.35
AR-14-SC-47	21.6	197.9	-3.5	1	-13.4	24.35
AR-14-SC-46	19.3	179.0	-5.7	1	-31.8	24.35
AR-14-SC-43	*20.8*	*191.4*	*-4.2*	1	*-19.8*	24.35
AR-14-SC-41	19.7	182.5	-5.3	1	-28.5	24.35
AR-14-SC-42	18.3	170.3	-6.7	1	-40.4	24.35
AR-14-SC-40	21.3	195.8	-3.7	1	-15.5	24.35
AR-14-SC-38	21.7	199.3	-3.3	1	-12.0	24.35
AR-14-SC-39	19.7	181.9	-5.3	1	-29.1	24.35
AR-14-SC-37	20.6	189.9	-4.4	1	-21.3	24.35
AR-14-SC-35	21.8	199.8	-3.3	1	-11.6	24.35
AR-14-SC-34	23.2	211.4	-1.9	1	-0.3	24.35
AR-14-SC-33	20.7	190.9	-4.3	1	-20.3	24.35
AR-14-SC-32	21.6	198.4	-3.4	1	-12.9	24.35
AR-14-SC-31	21.9	200.8	-3.1	1	-10.6	24.35
AR-14-SC-30	21.3	195.7	-3.7	1	-15.6	24.35
AR-14-SC-29	21.6	198.2	-3.4	1	-13.1	24.35
AR-14-SC-28	22.8	208.4	-2.3	1	-3.2	24.35
AR-14-SC-27	23.2	212.1	-1.8	1	0.4	24.35
AR-14-SC-26	23.9	217.5	-1.2	1	5.6	24.35
AR-14-SC-25	20.6	189.7	-4.4	1	-21.4	24.35
AR-14-SC-24	21.2	195.1	-3.8	1	-16.1	24.35
AR-14-SC-23	18.3	170.8	-6.6	1	-39.9	24.35
AR-14-SC-21	18.0	167.9	-6.9	1	-42.7	24.35
AR-14-SC-18	21.1	194.1	-3.9	1	-17.2	24.35
AR-14-SC-17	19.7	181.8	-5.3	1	-29.1	24.35
AR-14-SC-16	22.5	205.6	-2.6	1	-5.9	24.35
AT7-7_c	22.0	201.6	-3.7	1	-15.7	24.35
AT7-7_d	21.0	193.1	-4.7	1	-24.0	24.35
AR-14-SC-15	23.6	214.7	-1.5	1	3.0	24.35
AR-14-SC-14	*25.6*	*232.1*	*0.5*	1	*19.9*	24.35
AR-14-SC-12	23.1	211.0	-2.0	1	-0.7	24.35
AR-14-SC-13	22.0	201.7	-3.0	1	-9.7	24.35

Table C.2. Pedogenic-carbonate results and source water reconstruction

(continued)

AR_13_15	23.0	210.3	-3.9	1	-16.8		24.35
AR_13_16	22.8	208.6	-4.1	1	-18.5		24.35
AR_13_16B	22.7	207.8	-4.2	1	-19.2		24.35
AR_13_14	23.5	214.5	-3.6	1	-14.4		24.35
AR_13_12	23.6	214.9	-3.5	1	-14.0		24.35
AR_13_13	23.5	214.5	-3.6	1	-14.4		24.35
AR_13_11	22.4	205.0	-4.7	1	-23.7		24.35
AR_13_10	23.7	215.9	-3.4	1	-13.0		24.35
AR_13_9	23.9	217.6	-3.2	1	-11.4		24.35
AR_13_7	23.7	216.1	-3.4	1	-12.8		24.35
AR_13_7B	23.7	215.7	-3.4	1	-13.2		24.35
AR_13_8	23.1	211.1	-4.0	1	-17.7		24.35
AR-14-SC-11	22.8	208.5	-3.6	1	-14.3		24.35
AT5-3_a	23.8	216.6	-3.5	1	-14.0		24.35
AT5-3_b	24.0	218.8	-3.3	1	-11.9		24.35
AT5-3_d	24.6	223.3	-2.8	1	-7.5		24.35
AR-14-SC-10	*30.7*	*274.8*	*3.9*	1	*48.6*		24.35
AR-14-SC-9	24.1	219.1	-2.6	1	-5.6		24.35
AR-14-SC-8	22.5	205.7	-4.1	1	-18.7		24.35
AR-14-SC-7	23.1	211.2	-3.5	1	-13.4		24.35
AT5-4b-a	24.8	225.2	-4.8	1	-24.4		24.35
AT5-4b-b	24.4	221.5	-5.2	1	-28.0		24.35
AR-14-SC-6	22.9	209.6	-5.9	1	-33.8		24.35
AR-14-SC-5	23.3	212.8	-5.5	1	-30.6		24.35
AR-14-SC-4	22.8	208.5	-6.0	1	-34.8		24.35
AR-14-SC-3	22.4	205.2	-6.4	1	-38.0		24.35
AR_13_4	23.2	212.1	-6.1	1	-35.4		24.35
AR_13_4B	23.3	212.2	-6.1	1	-35.3		24.35
AR_13_6	22.4	204.9	-6.9	1	-42.4		24.35
AR-14-SC-2	23.4	213.1	-5.3	1	-28.5		24.35
AR-14-SC-1	24.2	219.8	-4.5	1	-22.1		24.35
AR_13_3b	22.9	209.3	-6.2	1	-36.3		24.35
AR_13_3a	23.1	210.8	-5.8	1	-33.2		24.35
AT7-7_a	26.8	242.4	-1.6	1	2.8		24.35
AT7-7_b	26.6	240.8	-1.7	1	1.2		24.35

Table C.2. Pedogenic-carbonate results and source water reconstruction (continued)

AT7-9-a	24.3	220.6	-3.9	1	-16.8	24.35
AT7-9-b	24.3	221.2	-3.8	1	-16.2	24.35
AT7-9-c	24.2	220.2	-3.9	1	-17.1	24.35
AT4-2-a	24.8	225.5	-3.9	1	-17.2	24.35
AT4-2-d	24.9	225.9	-3.9	1	-16.7	24.35
AT4-2-e	24.8	225.6	-3.9	1	-17.0	24.35
AT4-4-a	25.0	227.0	-3.7	1	-15.6	24.35
AT4-4-c	24.9	226.2	-3.8	1	-16.4	24.35
AT4-4-d	25.2	228.2	-3.6	1	-14.5	24.35
AT5-16a_a	24.6	223.7	-3.3	1	-12.0	24.35
AT5-16a_b	24.6	223.5	-3.3	1	-12.3	24.35
AT5-16a_c	24.7	224.4	-3.2	1	-11.4	24.35
AT2-4d-a	25.2	228.8	-4.1	1	-19.1	24.35
AT2-4d-b	25.5	230.8	-3.9	1	-17.2	24.35
AT2-4d-c	25.6	231.6	-3.8	1	-16.4	24.35
AT2-4d-d	25.4	230.4	-4.0	1	-17.6	24.35
RT-02	24.7	224.7	-3.9	1	-17.2	24.35
RT-04	24.9	226.0	-3.8	1	-16.0	24.35
AT6-2_a	25.5	230.8	-4.1	1	-19.0	24.35
AT6-2_b	25.2	228.4	-4.4	1	-21.3	24.35

Table C.2. Pedogenic-carbonate results and source water reconstruction (continued)

Table C.3. Volcanic glass and source water reconstruction

Sample	Latitude (° S)	Longitude (°W)	Elevation (m)	Age (Ma)	Error (Ma)	δDg (‰)	Error (‰)	δDsw (‰)†	Dating method	Age cited in:	δDg cited in:
Modern s. water	-	-	-	0.00	-	-64.6	10.0	-32.7	-	-	Rohrmann et al., 2014
B005	-25.697	-66.180	1900	1.05	0.07	-67.2	3.0	-35.4	U-Th/He zircon	Pingel unpublished	Pingel unpublished
ANG-070313-1	-25.764	-65.988	1731	3.00	0.50	-83.1	3.0	-51.8	stratigraphic	Pingel unpublished	Pingel unpublished
AT3-11-R	-25.727	-66.007	1820	3.99	0.15	-71.7	3.0	-40.0	U-Pb zircon	Bywater-Reyes et al., 2010	Pingel unpublished
AT3-9-R	-25.728	-66.008	1820	4.04	0.26	**-72.4**	3.0	-40.8	U-Pb zircon	Bywater-Reyes et al., 2010	Pingel unpublished
AT3-9	-25.728	-66.008	1820	4.04	0.26	**-74.8**	4.0	-43.3	U-Pb zircon	Bywater-Reyes et al., 2010	Carrapa et al., 2014
AT6-1	-25.675	-66.039	1880	4.61	0.16	-94.8	8.0	-64.0	U-Pb zircon	Bywater-Reyes et al., 2010	Carrapa et al., 2014
AR-11-ASH-5	-25.693	-66.037	1850	4.81	0.50	-91.8	3.0	-60.8	stratigraphic	Pingel unpublished	Pingel unpublished
AT2-7-R	-25.729	-66.019	1860	4.81	0.17	-78.4	3.0	-46.9	U-Pb zircon	Bywater-Reyes et al., 2010	Pingel unpublished
AT2-7	-25.729	-66.019	1855	4.81	0.17	-73.4	3.0	-41.8	U-Pb zircon	Bywater-Reyes et al., 2010	Carrapa et al., 2014
AR-11-ASH-2/3	-25.687	-66.055	1822	4.90	0.30	-80.7	3.0	-49.3	stratigraphic	Pingel unpublished	Pingel unpublished
AR-11-ASH-4	-25.679	-66.051	1862	4.90	0.30	-80.8	3.0	-49.4	stratigraphic	Pingel unpublished	Pingel unpublished
AT2-2-R	-25.731	-66.032	1914	4.95	0.16	-75.2	3.0	-43.7	U-Pb zircon	Bywater-Reyes et al., 2010	Pingel unpublished
AT4-3-R	-25.677	-66.073	1845	5.17	0.23	**-88.0**	3.0	-56.9	U-Pb zircon	Bywater-Reyes et al., 2010	Pingel unpublished
AT4-3	-25.677	-66.073	1845	5.17	0.23	**-76.5**	8.0	-45.0	U-Pb zircon	Bywater-Reyes et al., 2010	Carrapa et al., 2014
AI-29	-25.674	-66.072	1900	5.27	0.28	-94.8	3.0	-63.9	U-Pb zircon	Coutand et al., 2006	Pingel unpublished
AT7-10-R	-25.675	-66.077	1840	5.98	0.32	**-84.3**	3.0	-53.0	U-Pb zircon	Bywater-Reyes et al., 2010	Pingel unpublished
AT7-10	-25.675	-66.077	1840	5.98	0.32	**-85.3**	1.0	-54.1	U-Pb zircon	Bywater-Reyes et al., 2010	Carrapa et al., 2014
ANG-070313-3	-25.682	-66.079	1825	5.80	0.50	-74.7	3.0	-43.1	stratigraphic	Pingel unpublished	Pingel unpublished
AT4-1	-	-	1820	6.90	0.30	-73.6	1.0	-42.0	U-Pb zircon	Bywater-Reyes et al., 2010	Carrapa et al., 2014
AT1-1	-25.771	-66.060	1980	7.24	0.26	-75.0	2.0	-43.5	U-Pb zircon	Bywater-Reyes et al., 2010	Carrapa et al., 2014

Note: If not otherwise indicated, all samples were measured using TC/EA and Thermo-Finnigan MAT 253 stable-isotope mass spectrometer at Goethe University, Frankfurt in Germany. Bold sample names and δDg values indicate duplicate measurements from Carrapa et al., 2014 and our data (R--resampled), which show a generally good fit.

†Calculated using fractionation equation of Friedman et

Bibliography

Al-Dousari, A.M., Al-Elaj, M., Al-Enezi, E., Al-Shareeda, A., 2009. Origin and characteristics of yardangs in the Um Al-Rimam depressions (N Kuwait). Geomorphology 104, 93-104.

Allmendinger, R.W., Jordan, T.E., Kay, S.M., Isacks, B.L., 1997. ALTIPLANO-PUNA PLATEAU OF THE CENTRAL ANDES. Annual Review Earth Planetary Science 25, 139–174.

Alonso, R., Bookhagen, B., Carrapa, B., Coutand, I., Haschke, M., Hilley, G.E., Schoenbohm, L., Sobel, E.R., Strecker, M.R., Trauth, M.H., Villanueva, A., 2006. Tectonics, climate, and landscape evolution of the southern central Andes: the Argentine Puna Plateau and adjacent regions between 22 and 30 S, in: The Andes. Springer, Berlin Heidelberg, pp. 265–283.

An, Z., 2000. The history and variability of the East Asian paleomonsoon climate. Quaternary Science Reviews 19, 171–187.

Anderson, R.S., 1986. Erosion profiles due to particles entrained by wind: Application of an eolian sediment-transport model. Geological Society Of America Bulletin 97, 1270– 1278.

Aref, M.A.M., El-Khoriby, E., Hamdan, M.A., 2002. The role of salt weathering in the origin of the Qattara Depression, Western Desert, Egypt. Geomorphology 45, 181-195.

Baby, P., Rochat, P., Mascle, G. & Hérail, G., 1997. Neogene shortening contribution to crustal thickening in the back arc of the Central Andes. Geology 25, 883-886.

Baker, P. A., Fritz, S.C., Dick, C.W., Eckert, A.J., Horton, B.K., Manzoni, S., Ribas, C.C., Garzione, C.N., Battisti, D.S., 2014. The emerging field of geogenomics: Constraining geological problems with genetic data. Earth-Science Reviews 135, 38–47.

Balco, G., Rovey, C.W., 2008. An isochron method for cosmogenic-nuclide dating of buried soils and sediments. American Journal of Science 308, 1083-1114.

Barnes, J.B., Ehlers, T. A., 2009. End member models for Andean Plateau uplift. Earth-Science Reviews 97, 105–132.

Beniston, M., 2003. Climatic change in mountain regions: A review of possible impacts, in: Climate Variability and Change in High Elevation Regions: Past, Present & Future. pp. 5–31.

Beresford-Jones, D., Lewis, H., Boreham, S., 2009. Linking cultural and environmental change in Peruvian prehistory: Geomorphological survey of the Samaca Basin, Lower Ica Valley, Peru. Catena 78, 234-249.

Bierman, P., Turner, J., 1995. ^{10}Be and ^{26}Al evidence for exceptionally low rates of Australian bedrock erosion and the likely existence of Pre-Pleistocene landscapes. Quaternary Research 44, 378-382.

Bierman, P.R., Caffee, M., 2002. Cosmogenic exposure and erosion history of Australian bedrock landforms. Geological Society of America Bulletin 114, 787-803.

Blisniuk, P.M., Stern, L.A., 2005. Stable isotope paleoaltimetry: a critical review. American Journal of Science 305, 1033-1074.

Blöthe, J.H., Korup, O., 2013. Millennial lag times in the Himalayan sediment routing system. Earth Planetary Science Letters 382, 38–46.

Boers, N., Bookhagen, B., Marwan, N., Kurths, J., Marengo, J., 2013. Complex networks identify spatial patterns of extreme rainfall events of the South American Monsoon System. Geophysical Research Letters 40(16), 4386-4392.

Bona, P., Starck, D., Galli, C., Gasparini, Z., Reguero, M., 2014. Caiman CF . Latirostris (Alligatoridae, Caimaninae) in the Late Miocene Palo Pintado formation, Salta Province, Argentina: paleogeographic and paleoenvironmental considerations. Ameghiniana 51, 1–12.

Bookhagen, B., Burbank, D.W., 2006. Topography, relief, and TRMM-derived rainfall variations along the Himalaya. Geophysical Research Letters 33, 1–5.

Bookhagen, B, Strecker, M.R., 2008. Orographic barriers, high-resolution TRMM rainfall, and relief variations along the eastern Andes. Geophysical Research Letters 35(6), 1–6.

Bookhagen, B., Burbank, D.W., 2010. Toward a complete Himalayan hydrological budget: Spatiotemporal distribution of snowmelt and rainfall and their impact on river discharge. Journal of Geophysical Research Earth Surface 115.

Bookhagen, B., Strecker, M.R., 2012. Spatiotemporal trends in erosion rates across a pronounced rainfall gradient: Examples from the southern Central Andes. Earth Planetary Science Letters 327, 97–110.

Boos, W.R., Kuang, Z., 2010. Dominant control of the South Asian monsoon by orographic insulation versus plateau heating. Nature 463, 218–22.

Bossi, G.E., Georgieff, S.M., Gavriloff, I.J.C., Ibañez, L.M., Muruaga, C.M., 2001. Cenozoic evolution of the intramontane Santa Maria basin, Pampean Ranges, northwestern Argentina. Journal of South American Earth Sciences 14(7), 725-734.

Bowen, G.J., Wilkinson, B., 2002. Spatial distribution of d18 O in meteoric precipitation. Geology 30, 315–318.

Bowler, J. M., Chen, K., and Yuan, B., 1987. Systematic variations in loess source areas: Evidence from Qaidam and Qinghai basins, western China, in Tungsheng, L. ed., Aspects of Loess Research: Beijing, China Ocean Press, p. 39-51.

Bowman, I., 1924. Desert Trails of Atacama.

Bradley, R.S., Vuille, M., Diaz, H.F., Vergara, W., 2006. Climate change. Threats to water supplies in the tropical Andes. Science 312, 1755–1756.

Bridges, N. T., Laity, J. E., Greeley, R., Phoreman, J., Eddlemon, E.E., 2004. Insights on rock abrasion and ventifact formation from laboratory and field analog studies with applications to Mars. Planetary and Space Science 52, 199-213.

Bristow, C.S., Drake, N., Armitage, S., 2009. Deflation in the dustiest place on Earth: The Bodélé Depression, Chad. Geomorphology 105, 50-58.

Brookes, I. A., 2003. Geomorphic indicators of Holocene winds in Egypt's Western Desert. Geomorphology 56, 155-166.

Brown, E.T., Stallard, R.F., Larsen, M.C., Raisbeck, G.M., Yiou, F., 1995. Denudation rates determined from the accumulation of in situ-produced ^{10}Be in the Luquillo experimental forest, Puerto Rico. Earth and Planetary Science Letters 129, 193-202.

Bryson, R.A., 1986. Airstream climatology of Asia. Proceedings of International Symposium on the Qinghai-Xizang Plateau and Mountain Meteorology. American Meteorological Society, Boston, Ma, 604-617.

Burbank, D.W., Leland, J., Fieldings, E.J., Anderson, R.S., Brozovic, N., Reid, M.R., Duncan, C., 1996. Bedrock incision, rock uplift and threshold hillslopes in the northwestern Himalayas. Nature 379, 505–510.

Bywater-Reyes, S., Carrapa, B., Clementz, M. & Schoenbohm, L., 2010. Effect of late Cenozoic aridification on sedimentation in the Eastern Cordillera of northwest Argentina (Angastaco basin). Geology 38, 235–238.

Dictionary.Cambridge.org. Cambridge Dictionaries Online, 2014. Web. "plateau", 04 December 2014.

Canavan, R.R., Carrapa, B., Clementz, M.T., Quade, J., DeCelles, P.G., Schoenbohm, L.M., 2014. Early Cenozoic uplift of the Puna Plateau, Central Andes, based on stable isotope paleoaltimetry of hydrated volcanic glass. Geology 42, 447–450.

Carrapa, B., Trimble, J.D., Stockli, D.F., 2011. Patterns and timing of exhumation and deformation in the Eastern Cordillera of NW Argentina revealed by (U-Th)/He thermochronology. Tectonics 30, 1–30.

Carrapa, B., Huntington, K.W., Clementz, M., Quade, J., Bywater-Reyes, S. Schoenbohm, L.M., Canavan, R.R., 2014. Uplift of the Central Andes of NW Argentina associated with upper crustal shortening, revealed by multiproxy isotopic analyses. Tectonics 33(6), 1039-1054.

Carrera, N., Muñoz, J. A., Sàbat, F., Mon, R., Roca, E., 2006. The role of inversion tectonics in the structure of the Cordillera Oriental (NW Argentinean Andes). Journal of Structural Geology 28, 1921–1932.

Carretier, S., Regard, V., Vassallo, R., Aguilar, G., Martinod, J., Riquelme, R., Pepin, E., Charrier, R., Herail, G., Farias, M., Guyot, J.-L., Vargas, G., Lagane, C., 2013. Slope and climate variability control of erosion in the Andes of central Chile. Geology 41, 195–198.

Cassel, E. J., Graham, S. A., Chamberlain, C. P., (2009). Cenozoic tectonic and topographic evolution of the northern Sierra Nevada, California, through stable isotope paleoaltimetry in volcanic glass. Geology 37, 547–550.

Carvalho, L.M. V, Silva, A.E., Jones, C., Liebmann, B., Dias, P.L.S., Rocha, H.R., 2011. Moisture transport and intraseasonal variability in the South America monsoon system. Climate Dynamics 36, 1865–1880.

Carvalho, L.M. V., Jones, C., Liebmann, B., 2002. Extreme Precipitation Events in Southeastern South America and Large-Scale Convective Patterns in the South Atlantic Convergence Zone. Journal of Climate 15, 2377–2394.

Cerling, T.E., Wang, Y., Quade, J., 1993. Expansion of C4 ecosystems as an indicator of global ecological change in the late Miocene. Nature 361, 344-345.

Chikaraishi, Y., Naraoka, H., 2003. Compound-specific δD–δ13C analyses of n-alkanes extracted from terrestrial and aquatic plants. Phytochemistry 63, 361–371.

Clark, M.K., Schoenbohm, L.M., Royden, L.H., Whipple, K.X., Burchfiel, B.C., Zhang, X., Tang, W., Wang, E., Chen, L., 2004. Surface uplift, tectonics, and erosion of eastern Tibet from large-scale drainage patterns. Tectonics 23, 1–20.

Clark, M.K., House, M.A., Royden, L.H., Burchfiel, B.C., Whipple, K.X., Zhang, X., Tang, W., 2005. Late Cenozoic uplift of southeastern Tibet. Geology 33, 525–528.

Clarke, M.L., Wintle, A.G., Lancaster, N., 1996. Infra-red stimulated luminescence dating of sands from the Cronese Basins, Mojave Desert. Geomorphology 17, 199-205.

Cloos, M., 1993. Lithospheric buoyancy and collisional orogenesis - Subduction of oceanic plateaus, continental margins, island arcs, spreading ridges, and seamounts. Geological Society of America Bulletin 105, 715–738.

Coutand, I., Carrapa, B., Deeken, A., Schmitt, A.K., Sobel, E.R., Strecker, M.R., 2006. Propagation of orographic barriers along an active range front: insights from sandstone petrography and detrital apatite fission-track thermochronology in the intramontane Angastaco basin, NW Argentina. Basin Research 18, 1–26.

Cowie, S.M., Knippertz, P., Marsham, J.H., 2013. Are vegetation-related roughness changes the cause of the recent decrease in dust emission from the Sahel? Geophysical Research Letters 40, 1868–1872.

Craddock, W., Kirby, K., Nathan, H., Zhang, H., Shi, X., Liu, J., 2010. Rapid fluvial incision along the Yellow River during headward basin integration. Nature Geoscience 3, 209–213.

Crouvi, O., Amit, R., Enzel, Y., Porat, N., Sandler, A., 2008. Sand dunes as a major proximal dust source for late Pleistocene loess in the Negev Desert, Israel. Quaternary Research 70, 275-282.

Crouvi, O., Amit, R., Enzel, Y., Gillespie, A.R., 2010. Active sand seas and the formation of desert loess. Quaternary Science Reviews 29, 2087-2098.

Dansgaard, W., 1964. Stable isotopes in precipitation. Tellus 16(4), 436–468.

DeCelles, P.G., Kapp, P., Ding, L., Gehrels, G.E., 2007. Late Cretaceous to middle Tertiary basin evolution in the central Tibetan Plateau: Changing environments in response to tectonic partitioning, aridification, and regional elevation gain. Geological Society of America Bulletin 119, 654–680.

Deeken, A., Sobel, E.R., Coutand, I., Haschke, M., Riller, U., Strecker, M.R., 2006. Development of the southern Eastern Cordillera, NW Argentina, constrained by apatite fission track thermochronology: From early Cretaceous extension to middle Miocene shortening. Tectonics 25, 1–21.

De Silva, S.L., Bailey, J.E., Mandt, K.E., Viramonte, J.M., 2010. Yardangs in terrestrial ignimbrites: Synergistic remote and field observations on Earth with applications to Mars. Planetary Space Science 58, 459–471.

Dettman, D.L., Fang, X., Garzione, C.N., Li, J., 2003. Uplift-driven climate change at 12 Ma: a long δ18O record from the NE margin of the Tibetan plateau. Earth and Planetary Science Letters 2148(1-2), 267–277.

Diefendorf, A. F., Freeman, K. H., Wing, S. L. & Graham, H. V., 2011. Production of n-alkyl lipids in living plants and implications for the geologic past. Geochimica Cosmochimica Acta 75, 7472–7485.

Ding, Z., Sun, J.M., Yang, S.L., Liu, T.S., 2001. Geochemistry of the Pliocene and clay formation in the Chinese Loess Plateau and implications for its origin, source provenance, and paleoclimate change. Geochimica Cosmochimica Acta 65, 901–914.

Dong, Z., Lv, P., Lu, J., Qian, G., Zhang, Z., Luo, W., 2012. Geomorphology and origin of Yardangs in the Kumtagh Desert, Northwest China. Geomorphology 139–140, 145–154.

Dufresne, J. L., Foujols, M. A., Denvil, S., Caubel, A., Marti, O., Aumont, O., Balkanski, Y., Bekki, S., Bellenger, H., Benshila, R., Bony, S., Bopp, L., Braconnot, P., Brockmann, P., Cadule, P., Cheruy, F., Codron, F., Cozic, A., Cugnet, D., Noblet, N., Duvel, J. P., Ethé, C., Fairhead, L., Fichefet, T., Flavoni, S., Friedlingstein, P., Grandpeix, J. Y., Guez, L., Guilyardi, E., Hauglustaine, D., Hourdin, F., Idelkadi, A., Ghattas, J., Joussaume, S., Kageyama, M., Krinner, G., Labetoulle, S., Lahellec, A., Lefebvre, M. P., Lefevre, F., Levy, C., Li, Z.X., Lloyd, J., Lott, F., Madec, G., Mancip, M., Marchand, M., Masson, S., Meurdesoif, Y., Mignot, J., Musat, I., Parouty, S., Polcher, J., Rio, C., Schulz, M., Swingedouw, D., Szopa, S., Talandier, C., Terray, P., Viovy, N., Vuichard, N., 2013. Climate change projections using the IPSL-CM5 Earth System Model: from CMIP3 to CMIP5, Climate Dynamics 40, 2123-2165.

Duvall, A.R., Clark, M.K., Kirby, E., Farley, K. A., Craddock, W.H., Li, C., Yuan, D. Y., 2013. Low-temperature thermochronometry along the Kunlun and Haiyuan Faults, NE Tibetan Plateau: Evidence for kinematic change during late-stage orogenesis. Tectonics 32, 1190–1211.

Echavarria, L., Hernández, R., Allmendinger, R., Reynolds, J., 2003. Subandean thrust and fold belt of northwestern Argentina: Geometry and timing of the Andean evolution. American Associaction of Petroleum Geologist Bulletin 87, 965–985.

Eglington, G., Hamilton, R. J., 1967. Leaf epicuticular waxes. Science 156, 1322–35.

Ehlers, T.A., Poulsen, C.J., 2009. Influence of Andean uplift on climate and paleoaltimetry estimates. Earth and Planetary Science Letters 281(3-4), 238-248.

Enzel, Y., Amit, R., Crouvi, O., Porat, N., 2010. Abrasion-derived sediments under intensified winds at the latest Pleistocene leading edge of the advancing Sinai–Negev erg. Quaternary Research 74, 121-131.

European Space Agency, 2014. South America and the Andes mountains, ID: 310509, Proba-V, 07/05/2014 8:50 am, <http://www.esa.int/spaceinimages/Images/2014/05/South_America_and_the_Andes_mountains, 18 July 2014.

Fieldings, E.J., Isacks, B.L., Barazangi, M., Duncan, C., 1994. How flat is Tibet ? Geology 22, 163–167.

Fischer Weltalmanach 2003, 2003. Fischer Taschenbuchverlag, Frankfurt a. M. – CD-ROM.

Friedman, I., Gleason, J., Sheppard, R.A., and Gude, A.J. Deuterium fractionation as water diffuses into silicic volcanic ash, in Swart, P.K., eds., Climate change in continental isotopic records: American Geophysical Union Geophysical Monograph 78, pp. 321–321.

Froehlich, K., Kralik, M., Papesch, W., Scheifinger, H., Stichler, W., 2008. Deuterium excess in precipitation of Alpine regions – moisture recycling. Isotopes in Environmental and Health Studies 44(1), 61–70.

Froidevaux, C., Isacks, B.L., 1984. The mechanical state of the lithosphere in the Altiplano-Puna segment of the Andes. Earth Planetary Science Letters 71, 305–314.

Fu, C., Fletcher, J.O., 1985. The Relationship between Tibet-Tropical Ocean Thermal Contrast and Interannual Variability of Indian Monsoon Rainfall. Journal of Climate and Applied Meteorology 24, 841-847.

Gaiero, D.M., Simonella, L., Gassó, S., Gili, S., Stein, A.F., Sosa, P., Becchio, R., Arce, J., Marelli, H., 2013. Ground/satellite observations and atmospheric modeling of dust storms originating

in the high Puna-Altiplano deserts (South America): Implications for the interpretation of paleo-climatic archives. Journal of Geophysical Research: Atmosphere 118, 3817–3831.

Galewsky, J., Samuels-Crow, K., 2014. Water vapor isotopic composition of a stratospheric air intrusion : Measurements from the Chajnantor Plateau , Chile. Journal of Geophysical Research: Atmosphere 119, 9679–9691.

Galli, C.I., Coira, B., Alonso, R., Reynolds, J., Matteini, M., Hauser, N., 2014. Tectonic controls on the evolution of the Andean Cenozoic foreland basin: Evidence from fluvial system variations in the Payogastilla Group, in the Calchaquí, Tonco and Amblayo Valleys, NW Argentina. Journal South American Earth Science 52, 234–259.

Gao, Y., 1962. Some Problems on East-Asia Monsoon. Science Press, Beijing (in Chinese).

Garcin, Y., Schwab, V.F., Gleixner, G., Kahmen, A., Todou, G., Séné, O., Onana, J.M., Achoundong, G., Sachse, D., 2012. Hydrogen isotope ratios of lacustrine sedimentary n-alkanes as proxies of tropical African hydrology: Insights from a calibration transect across Cameroon. Geochimica Cosmochimica Acta 79, 106-126.

Garreaud, R.D., Aceituno, P., 2001. Interannual Rainfall Variability over the South American Altiplano. Journal of Climate 14, 2779–2789.

Garreaud, R., Vuille, M., Clement, A.C., 2003. The climate of the Altiplano: observed current conditions and mechanisms of past changes. Paleogeography, Paleoclimatology, Paleoecology 194(1-3), 5–22

Garreaud, R.D., Vuille, M., Compagnucci, R., Marengo, J., 2009. Present-day South American climate. Palaeogeography, Palaeoclimatology, Palaeoecology 281, 180–195.

Garzione, C.N., Hoke, G.D., Libarkin, J.C., Withers, S., MacFadden, B., Eiler, J., Ghosh, P., Mulch, A., 2008. Rise of the Andes. Science 320, 1304–1307.

Garzione, C.N., Auerbach, D.J., Jin-Sook Smith, J., Rosario, J.J., Passey, B.H., Jordan, T.E., Eiler, J.M., 2014. Clumped isotope evidence for diachronous surface cooling of the Altiplano and pulsed surface uplift of the Central Andes. Earth Planetary Science Letters 393, 173–181.

Gasparini, N.M., Whipple, K.X., 2014. Diagnosing climatic and tectonic controls on topography: Eastern flank of the northern Bolivian Andes. Lithosphere 6, 230–250.

Gonfiantini, R., Roche, M.-A., Olivery, J.-C., Fontes, J.-C., Zuppi, G.M., 2001. The altitude effect on the isotopic composition of tropical rains. Chemical Geology 181, 147–167.

Gosse, J.C., Phillips, F.M., 2001. Terrestrial in situ cosmogenic nuclides: theory and application. Quaternary Science Reviews 20, 1475-1560.

Goudie, A.S., Stokes, S., Cook, J., Samieh, S., El-Rashidi, O.A., 1999. Yardang landforms from Kharga Oasis, south-western Egypt. Z. Geomorphol., Suppl.-Bd., 116, 97–112.

Goudie, A.S., 2007. Mega-Yardangs: A Global Analysis. Geography Compass 1, 65-81.

Goudie, A.S., 2008. The history and nature of wind erosion in deserts. Annual Review of Earth and Planetary Sciences 36, 97-119.

Goudie, A.S., 2009. Dust storms: Recent developments. Journal of Environmental Management 90, 89–94.

Granger, D.E., Kirchner, J.W., Finkel, R., 1996. Spatially averaged long-term erosion rates measured from in-situ-produced cosmogenic nuclides in alluvial sediment. The Journal of Geology 104, 249-257.

Greene, L., 1995. Eolian landforms in the Central Andes: implications for the long-term stability of atmospheric circulation (Thesis).

Guo, Z.T., Ruddiman, W.F., Hao, Q.Z., Wu, H.B., Qiao, Y.S., Zhu, R.X., Peng, S.Z., Wei, J.J., Yuan, B.Y., Liu, T.S., 2002. Onset of Asian desertification by 22 Myr ago inferred from loess deposits in China. Nature 416, 159-163.

Hahn, D.G., Manabe, S., 1975. The role of mountains in the South Asian Monsoon Circulation. Journal of Atmospheric Science 32, 1515–1541.

Hain, M.P., Strecker, M.R., Bookhagen, B., Alonso, R.N., Pingel, H., Schmitt, A.K., 2011. Neogene to Quaternary broken foreland formation and sedimentation dynamics in the Andes of NW Argentina (25°S). Tectonics 30, 1–27.

Halimov, M., Fezer, F., 1989. Eight yardang types in central Asia. Zeitschrift fuer Geomorphologie **33**, 205-217.

Hanebuth, T.J.J., Henrich, R., 2009. Recurrent decadal-scale dust events over Holocene western Africa and their control on canyon turbidite activity (Mauritania). Quaternary Science Reviews 28, 261-270.

Harrer, H., 1952. Sieben Jahre in Tibet: Mein Leben am Hofe des Dalai Lama. Ullstein, Wien.

Haynes, C.V., 1980. Geologic evidence of pluvial climates in the El Nabta area of the Western Desert, Egypt. In: Wendorf, F., Schild, R. (Eds.), Prehistory of the Eastern Sahara. Academic Press, New York, pp. 353-371.

Hedin, S., 1903. Central Asia and Tibet. Hurst and Blackeet, London, pp. 1272.

Heermance, R.V., Pullen, A., Kapp, P., Garzione, C., Bogue, S., Ding, L., Song, P., 2013. Climatic and tectonic controls on sedimentation and erosion during the Pliocene–Quaternary in the Qaidam Basin (China). Geological Society of America Bulletin 125, 833-856.

Herbst, R., Anzótegui, L.M., Jalfin, G., 1987. Estratigrafía, paleoambientes y dos especies de Salvinia Adanson (Filicopsida) del Mioceno Superior de Salta, Argentina. Revista de la Facultad de Ciencias Exactas y Naturales y Agrimensura 7, 15–42.

Herzschuh, U., 2006. Palaeo-moisture evolution in monsoonal Central Asia during the last 50,000 years. Quaternary Science Reviews 25, 163-178.

Hilkert, A. W., Douthitt, C. B., Schluetter, H. J. & Brandt, W. A., 1999. Isotope Ratio Monitoring Gas Chromatography / Mass Spectrometry of D / H by High Temperature Conversion Isotope Ratio Mass Spectrometry. Rapid Commununication in Mass Spectrometry 13, 1226–1230.

Hilley, G.E., Strecker, M.R., 2005. Processes of oscillatory basin filling and excavation in a tectonically active orogen: Quebrada del Toro Basin, NW Argentina. Geological Society of America Bulletin 117, 887–901.

Hoke, G.D., Aranibar, J.N., Viale, M., Araneo, D.C., Llano, C., 2013. Seasonal moisture sources and the isotopic composition of precipitation, rivers, and carbonates across the Andes at 32.5-35.5°S. Geochemistry, Geophysics, Geosystems 14, 962–978.

Hoke, G.D., Giambiagi, L.B., Garzione, C.N., Mahoney, J.B., Strecker, M.R., 2014. Neogene paleoelevation of intermontane basins in a narrow, compressional mountain range, southern Central Andes of Argentina. Earth Planetary Science Letters 406, 153–164.

Hoorn, C., Wesselingh, F.P., Ter Steege, H., Bermudez, M. A, Mora, A., Sevink, J., Sanmartín, I., Sanchez-Meseguer, A., Anderson, C.L., Figueiredo, J.P., Jaramillo, C., Riff, D., Negri, F.R., Hooghiemstra, H., Lundberg, J., Stadler, T., Särkinen, T., Antonelli, A., 2010. Amazonia through time: Andean uplift, climate change, landscape evolution, and biodiversity. Science 330, 927–31.

Hoorn, C., Mosbrugger, V., Mulch, A., Antonelli, A., 2013. Biodiversity from mountain building. Nature Geoscience 6, 154.

Horton, B.K., 1998. Sediment accumulation on top of the Andean orogenic wedge : Oligocene to late Miocene basins of the Eastern Cordillera , southern Bolivia. Geological Society of America Bulletin 110, 1174–1192.

Horton, B.K., DeCelles, P.G., 2001. Modern and ancient fluvial megafans in the foreland basin system of the central Andes, southern Bolivia: implications for drainage network evolution in fold-thrust belts. Basin Research 13, 43–63.

Horton, B.K., 2012. Cenozoic evolution of hinterland basins in the Andes and Tibet, in: Tectonics of Sedimentary Basins: Recent Advances. pp. 427–444.

Houseman, G., England, P., 1996. A lithospheric-thickening model for the Indo-Asian collision, in: WORLD AND REGIONAL GEOLOGY. pp. 1–17.

Houze, R.A., 2012. Orographic effects on precipitating clouds. Review of Geophysics 50, 1–47.

Huffman, G.J., et al., 2007. The TRMM Multisatellite Precipitation Analysis (TMPA): Quasi-Global, Multiyear, Combined-Sensor Precipitation Estimates at Fine Scales. Journal of Hydrometeorology 8(1), 38–55.

Hren, M.T., Bookhagen, B., Blisniuk, P.M., Booth, A.L., Chamberlain, C.P., 2009. δ18O and δD of streamwaters across the Himalaya and Tibetan Plateau: Implications for moisture sources and paleoelevation reconstructions. Earth and Planetary Science Letters 288(1-2), 20–32.

Hynek, S., Passey, B.H., Prado, J.L., Brown, F.H., Cerling, T.E., Quade, J., 2012. Small mammal carbon isotope ecology across the Miocene–Pliocene boundary, northwestern Argentina. Earth and Planetary Science Letters 321-322, 177–188.

IAEA/WMO (April 2012) Global Network of Isotopes in Precipitation, The GNIP database. Accessible at: http://www.iaea.org/water.

Immerzeel, W.W., van Beek, L.P.H., Bierkens, M.F.P., 2010. Climate change will affect the Asian water towers. Science 328, 1382–1385.

Inbar, M., Risso, C., 2001. Holocene yardangs in volcanic terrains in the southern Andes, Argentina. Earth Surface Processes and Landforms 26, 657-666.

Indoitu, R., Orlovsky, L., Orlovsky, N., 2012. Dust storms in Central Asia: spatial and temporal variations. Journal of Arid Environments 85, 62–70.

Insel, N., Poulsen, C.J., Ehlers, T. a., 2009. Influence of the Andes Mountains on South American moisture transport, convection, and precipitation. Climate Dynamics 35, 1477–1492.

Insel, N, Poulsen, C.J., Ehlers, T.A., Sturm, C., 2012. Response of meteoric δ18O to surface uplift — Implications for Cenozoic Andean Plateau growth. Earth and Planetary Science Letters 317-318, 262–272.

IPCC, 2007. Climate Change 2007: Synthesis Report. Contribution of Working Groups I, II and III to the Fourth Assessment Report of the Intergovernmental Panel on Climate Change [Core Writing Team, Pachauri, R.K and Reisinger, A. (eds.)]. IPCC, Geneva, Switzerland, 104 pp.

Isacks, B.L., 1988. Uplift of the Central Andean Plateau and Bending of the Bolivian Orocline. Journal of Geophysical Research Solid Earth 93, 3211–3231.

Isacks, B.L., Bloom, A.L., Fielding, E.J., Fox, a., Gubbels, T., 1989. Tectonics of the central Andes. Advances in Space Research 9, 79–84.

Jarvis, A., Reuter, H.I., Nelson, A., Guevara, E., 2008. Hole-filled SRTM for the globe Version 4. available from the CGIAR-CSI SRTM 90 m Database. http://srtm.csi.cgiar.org

Jordan, T.E., Alonso, R.N., 1987. Cenozoic Stratigraphy and Basin Tectonics of the Andes Mountains, 20° -28° South Latitude. American Association of Petroleum Geologists Bulletin 71, 49–64.

Jordan, T.E., Isacks, B.L., Allmendinger, R.W., Brewer, J.A., Ramos, V.A., Ando, C.J., 1983. Andean tectonics related to geometry of subducted Nazca plate. American Association of Petroleum Geologists Bulletin 94, 341–361.

Jungers, M.C., Heimsath, A.M., Amundson, R., Balco, G., Shuster, D., Chong, G., 2013. Active erosion–deposition cycles in the hyperarid Atacama Desert of Northern Chile. Earth Planetary Science Letters 371-372, 125–133.

Kahmen, A., Hoffmann, B., Schefuß, E., Arndt, S.K., Cernusak, L. A., West, J.B., Sachse, D., 2013. Leaf water deuterium enrichment shapes leaf wax n-alkane δD values of angiosperm plants II: Observational evidence and global implications. Geochimica Cosmochimica Acta 111, 50–63.

Kalnay, E., Kanamitsu, M., Kistler, R., Collins, W., Deavean, D., Gandin, L., Iredell, M., Saha, S., White, G., Woollen, J., Zhu, Y., Leetmaa, A., Reynolds, R., Chelliah, M., Ebisuzaki, W., Higgins, W., Janowiak, J., Mo, K. C., Ropelewski, C., Wang, J., Jenne, R., and Joseph, D., 1996. The NCEP/NCAR Reanalysis 40-year Project. Bulletin of the American Meteorological Society 77(3), 437-471.

Kapp, P., Pelletier, J.D., Rohrmann, A., Heermance, R., Russell, J., Ding, L., 2011. Wind erosion in the Qaidam basin, central Asia: Implications for tectonics, paleoclimate, and the source of the Loess Plateau. GSA Today 21, 4–10.

Kay, R.W., Mahlburg Kay, S., 1993. Delamination and delamination magmatism. Tectonophysics 219, 177–189.

Kehl, M., 2009. Quaternary climate change in Iran – the state of knowledge. Erdkunde 63, 1-17.

Kim, S. T., O'Neil, J. R., 1997. Equilibrium and nonequilibrium oxygen isotope effects in synthetic carbonates. Geochimica et Cosmochimica Acta, 61(16), 3461-3475.

Kirby, E., Whipple, K.X., 2012. Expression of active tectonics in erosional landscapes. Journal of Structural Geology 44, 54–75.

Kirchner, J.W., Finkel, R.C., Riebe, C.S., Granger, D.E., Clayton, J.L., King, J.G., Megahan, W.F., 2001. Mountain erosion over 10 yr, 10 k.y., and 10 m.y. time scales. Geology 29, 591-594.

Kleinert, K., Strecker, M.R., 2001. Climate change in response to orographic barrier uplift: Paleosol and stable isotope evidence from the late Neogene Santa Maria basin, northwestern Argentina. Geological Society of America Bulletin 113(6), 728–742.

Kley, J., Rossello, E. A., Monaldi, C.R., Habighorst, B., 2005. Seismic and field evidence for selective inversion of Cretaceous normal faults, Salta rift, northwest Argentina. Tectonophysics 399, 155–172.

Knight, J., 2002. Wind abrasion (ventifaction) on Donegal and Oregon coasts and implications for the sediment dynamics of coastal systems. Journal of Coastal Research 36, 441-449.

Knight, J., 2008. The environmental significance of ventifacts: A critical review. Earth-Science Reviews 86, 89-105.

Kohl, C.P., Nishiizumi, K., 1992. Chemical isolation of quartz for measurement of in-situ -produced cosmogenic nuclides. Geochimica et Cosmochimica Acta 56, 3583-3587.

Koppes, M.N., Montgomery, D.R., 2009. The relative efficacy of fluvial and glacial erosion over modern to orogenic timescales. Nature Geoscience 2, 644-647.

Krinsley, D.B., 1970. A geomorphological and paleoclimatological study of the playas of Iran. US Geological Survey Final Report, Contract PRO CP, 70-800.

Kulhawy, F.H., 1975. Stress deformation properties of rock and rock discontinuities. Engineering Geology 9, 327-350.

Kurosaki, Y., Mikami, M., 2003. Recent frequent dust events and their relation to surface wind in East Asia. Geophysical Research Letters 30, 1–4.

Kurosaki, Y., Shinoda, M., Mikami, M., 2011. What caused a recent increase in dust outbreaks over East Asia? Geophysical Research Letters 38, 1–6.

Laity, J.E., 1994. Landforms of aeolian erosion. In: Abrahams, A.D., Parsons, A.J. (Eds.), Geomorphology of Desert Environments. Chapman & Hall, London, pp. 506-535.

Laity, J.E., Bridges, N.T., 2009. Ventifacts on Earth and Mars: Analytical, field, and laboratory studies supporting sand abrasion and windward feature development. Geomorphology 105, 202-217.

Laity, J.E., 2011. Wind erosion in drylands. In: Thomas, D.S (Ed.), Arid Zone Geomorphology: Process, Form and Change in Drylands. John Wiley & Sons, Oxford, U.K., pp. 539-568.

Lal, D., 1991. Cosmic ray labeling of erosion surfaces: in situ nuclide production rates and erosion models. Earth and Planetary Science Letters 104, 424-439.

Lal, D., Harris, N.B., Sharma, K.K., Gu, Z., Ding, L., Liu, T., Dong, W., Caffee, M.W., Jull, A.J.., 2003. Erosion history of the Tibetan Plateau since the last interglacial: constraints from the first studies of cosmogenic ^{10}Be from Tibetan bedrock. Earth and Planetary Science Letters 217, 33-42.

Langbein, W.B., Schumm, S.A., 1958. Yield of Sediment in Relation to Mean Annual Precipitation. Eos, Trans. Am. Geophys. Union 39, 1076–1084.

Larma, R.D., Vutukuri, V.S., 1978. Handbook on mechanical properties of rocks, vol. II. Trans. Tech. Publ., Schwitzerland.

Latorre, C., Quade, J, McIntosh, W.C., 1997. The expansion of C4, grasses and global change in the late Miocene: Stable isotope evidence from the Americas. Earth and Planetary Science Letters 146(1997), 83–96.

Lavé, J., Burbank, D., 2004. Denudation processes and rates in the Transverse Ranges, southern California: Erosional response of a transitional landscape to external and anthropogenic forcing. Journal of Geophysical Research 109, 1–31.

Lechler, A.R., Niemi, N.A., 2012. The influence of snow sublimation on the isotopic composition of spring and surface waters in the southwestern United States: Implications for stable isotope-based paleoaltimetry and hydrologic studies. Geological Society of America Bulletin 124(3-4), 318–334.

Lenters, J.D., Cook, K.H., 1995. Simulation and Diagnosis of the Regional Summertime Precipitation Climatology of South America. Journal of Climate 8, 2988–3005.

Lee-Thorpe, J.L., Van der Merwe, N.J., 1987. Carbon isotope analysis of fossil bone apatite. Inorganic, Organic, Physical and analytical Chemistry 83(11), 712-715.

Li, H. C., Ku, T. L., 1997. δ13C–δ18C covariance as a paleohydrological indicator for closed-basin lakes. Palaeogeography, Palaeoclimatology, Palaeoecology 133, 69–80.

Liu, C. Q., Masuda, A., Okada, A., Yabuki, S., Fan, Z.-L., 1994. Isotope geochemistry of Quaternary deposits from the arid lands in northern China. Earth and Planetary Science Letters 127, 25-38.

Mahowald, N., Ward, D.S., Kloster, S., Flanner, M.G., Heald, C.L., Heavens, N.G., Hess, P.G., Lamarque, J.F., Chuang, P.Y., 2011. Aerosol Impacts on Climate and Biogeochemistry. Annual Review of Environment and Resources 36, 45–74.

Marengo, J. A., Liebmann, B., Grimm, A. M., Misra, V., Silva Dias, P.L., Cavalcanti, I.F. A., Carvalho, L.M. V., Berbery, E.H., Ambrizzi, T., Vera, C.S., Saulo, A. C., Nogues-Paegle, J., Zipser, E., Seth, A., Alves, L.M., 2012. Recent developments on the South American monsoon system. International Journal Climatology 32, 1–21.

Marin, J., Sauer, J.A., 1954. Strengths of materials. Macmillan, New York.

Marticorena, B., 2014. Dust Production Mechanisms, in: Mineral Dust: A Key Player in the Earth System. pp. 93–120.

McCauley, J.F., Breed, C.S., Grolier, M.J., 1977. Yardangs. In: Doehring, D.O. (Ed.), Geomorphology in Arid Regions. George Allen and Unwin, Boston, pp. 233-269.

Meade, R.H, 1988. Movement and storage of sediment in river systems. In: Lerman, A., Meybeck, M. (Eds.), Physical and chemical weathering in geochemical cycles. Kluwer Academic Publishers, Dordrecht, Netherlands, pp.165-179.

Menon, S., Hansen, J., Nazarenko, L., Luo, Y., 2002. Climate effects of black carbon aerosols in China and India. Science 297, 2250–2253.

Mix, H., Winnick, M.J., Mulch, A., Chamberlain, C.P. (2013) Grassland expansion as an instrument of hydrologic change in Neogene western North America. Earth and Planetary Science Letters, 377-378, 73-83.

Molnar, P., 2004. Late Cenozoic increase in accumulation rates of terrestrial sediment: How might climate change have affected erosion rates? Annual Review of Earth and Planetary Sciences 32, 67-89.

Molnar, P., Boos, W.R., Battisti, D.S., 2010. Orographic Controls on Climate and Paleoclimate of Asia: Thermal and Mechanical Roles for the Tibetan Plateau. Annual Review of Earth and Planetary Sciences 38, 77–102.

Mulch, A., Sarna-Wojcicki, A.M., Perkins, M.E., Chamberlain, C.P., 2008. A Miocene to Pleistocene climate and elevation record of the Sierra Nevada (California). Proceedings of the National Academy of Science, USA, 105, 6819-6824.

Mulch A., Uba, C., Strecker, M.R., Schönberg, R., Chamberlain, C.P., 2010. Late Miocene climate variability and surface elevation in the central Andes. Earth and Planetary Science Letters, 290, 173-182.

NASA, 2013. Tibetan Plateau. http://visibleearth.nasa.gov, 19 September 2014.

Nishiizumi, K., Kohl, C.P., Arnold, J.R., Klein, J., Fink, D., Middleton, R., 1991. Cosmic ray produced ^{10}Be and ^{26}Al in Antarctic rocks: exposure and erosion history. Earth and Planetary Science Letters 104, 440-454.

Nishiizumi, K., Caffee, M.W., Finkel, R.C., Brimhall, G., Mote, T., 2005. Remnants of a fossil alluvial fan landscape of Miocene age in the Atacama Desert of northern Chile using cosmogenic nuclide exposure age dating. Earth and Planetary Science Letters 237, 499-507.

Nishiizumi, K., Imamura, M., Caffee, M. W., Southon, J. R., Finkel, R. C., & McAninch, J., 2007. Absolute calibration of 10 Be AMS standards. Nuclear Instruments and Methods in Physics Research Section B: Beam Interactions with Materials and Atoms 258(2), 403-413.

Ouimet, W., Whipple, K., Royden, L., Reiners, P., Hodges, K., Pringle, M., 2010. Regional incision of the eastern margin of the Tibetan Plateau. Lithosphere 2, 50–63.

Owen, L. A., Gualtieri, L., Finkel, R.C., Caffee, M.W., Benn, D.I., Sharma, M.C., 2001. Cosmogenic radionuclide dating of glacial landforms in the Lahul Himalaya, northern India: defining the timing of Late Quaternary glaciation. Journal of Quaternary Science 16, 555–563.

Owen, L. A., Finkel, R.C., Haizhou, M., Barnard, P.L., 2006. Late Quaternary landscape evolution in the Kunlun Mountains and Qaidam Basin, Northern Tibet: A framework for examining the links between glaciation, lake level changes and alluvial fan formation. Quaternary International 154, 73-86.

Penck, W., 1924. Über die Form andiner Krustenbewegungen und ihre Beziehungen zur Sedimentation. Geologische Rundschau 14, 301–315.

Peters, N. A., Huntington, K.W., Hoke, G.D., 2013. Hot or not? Impact of seasonally variable soil carbonate formation on paleotemperature and O-isotope records from clumped isotope thermometry. Earth Planetary Science Letters 361, 208–218.

Phillips, F.M., Zreda, M.G., Ku, T.-lung, Luo, S., Huang, Q.I., Elmore, D., Kubik, P.W., Sharma, P., 1993. ^{230}Th/^{234}U and ^{36}Cl dating of evaporite deposits from the western Qaidam Basin , China: Implications for glacial-period dust export from Central Asia. Geological Society of America Bulletin 105, 1606-1616.

Pingel, H., Alonso, R.N., Mulch, A., Rohrmann, A., Sudo, M., Strecker, M.R., 2014. Pliocene orographic barrier uplift in the southern Central Andes. Geology 42, 691–694.

Poage, M.A., Chamberlain C.P., 2001. Stable isotope composition of precipitation and surface waters: considerations for studies of paleoelevation change. American Journal of Science 301(1), 1–15.

Polissar, P. J., Freeman, K. H., Rowley, D. B., McInerney, F. A., Currie, B. S., 2009. Paleoaltimetry of the Tibetan Plateau from D/H ratios of lipid biomarkers. Earth Planetary Science Letters 287, 64–76.

Ponton, C., West, A. J., Feakins, S.J., Galy, V., 2014. Leaf wax biomarkers in transit record river catchment composition. Geophysical Research Letters 41, 6420–6427.

Portenga, E.W., Bierman, P.R., 2011. Understanding Earth's eroding surface with ^{10}Be. GSA Today 21, 4-10.

Porter, S., 2001. Chinese loess record of monsoon climate during the last glacial–interglacial cycle. Earth-Science Reviews 54, 115-128.

Poulsen, C.J., Ehlers, T. A, Insel, N., 2010. Onset of convective rainfall during gradual late Miocene rise of the central Andes. Science 328, 490–493.

Prell, W.L., Kutzbach, J.E., 1997. The impact of Tibet-Himalayan elevation on the sensitivity of the monsoon climate system to changes in solar radiation, in: Tectonic Uplift and Climate Change. Springer, pp. 171–201.

Prohaska, F., 1976. The climate of Argentina, Paraguay and Uruguay. Climates of Central and South America, 1976 – World Survey of Climatology.

Pullen, A., Kapp, P., McCallister, A. T., Chang, H., Gehrels, G.E., Garzione, C.N., Heermance, R. V., Ding, L., 2011. Qaidam Basin and northern Tibetan Plateau as dust sources for the Chinese Loess Plateau and paleoclimatic implications. Geology 39, 1031–1034.

Pye, K., 1995. The nature, origin and accumulation of loess. Quaternary Science Reviews 14, 653-667.

Qian, W., Quan, L., Shi, S., 2002. Variations of the dust storm in China and its climatic control. Journal of Climate 15, 1216–1229.

Rea, D.K., Snoeckx, H., Joseph, L.H., 1998. Late Cenozoic eolian deposition in the North Pacific: Asian drying, Tibetan uplift, and cooling of the northern hemisphere. Paleoceanography 13, 215-224.

Rech, J. A., Currie, B.S., Shullenberger, E.D., Dunagan, S.P., Jordan, T.E., Blanco, N., Tomlinson, A.J., Rowe, H.D., Houston, J., 2010. Evidence for the development of the Andean rain shadow from a Neogene isotopic record in the Atacama Desert, Chile. Earth Planetary Science Letters 292, 371–382.

Rehak, K., Bookhagen, B., Strecker, M.R., Echtler, H.P., 2010. The topographic imprint of a transient climate episode: The western Andean flank between 15.5° and 41.5°S. Earth Surface Processes and Landforms 35, 1516–1534.

Reynolds, J.H., Galli, C.I., Hernandez, R.M., Idleman, B.D., Kotila, J.M., Hilliard, R. V, Naeser, C.W., 2000. Middle Miocene tectonic development of the transition zone, Salta Province, Northwest Argentina: magnetic stratigraphy from the Metan Subgroup, Sierra de Gonzalez. Geological Society of America Bulletin 112, 1736–1751.

Ridgwell, A.J., 2002. Dust in the Earth system: the biogeochemical linking of land, air and sea. Philosophical Transactions of the Royal Society of London. Series A: Mathematical, Physical and Engineering Sciences 360, 2905–2924.

Risi, C., Bony, S., Vimeux, F., 2008. Influence of convective processes on the isotopic composition (δ 18 O and δ D) of precipitation and water vapor in the tropics: 2. Physical interpretation of the amount effect. Journal of Geophysical Research 113(D19), 1–12.

Ritley, K., Odontuya, E., 2004. Yardangs and dome dunes northeast of Tavan Har, Gobi, Mongolia.

Rohrmann, A., Kapp, P., Carrapa, B., Reiners, P.W., Guynn, J., Ding, L., Heizler, M., 2012. Thermochronologic evidence for plateau formation in central Tibet by 45 Ma. Geology 40, 187–190.

Rohrmann, A., Strecker, M.R., Bookhagen, B., Mulch, A., Sachse, D., Pingel, H., Alonso, R.N., Schildgen, T.F., Montero, C., 2014. Can stable isotopes ride out the storms? The role of convection for water isotopes in models, records, and paleoaltimetry studies in the central Andes. Earth Planetary Science Letters 407, 187–195.

Romatschke, U., Houze, R., 2013. A Characteristics of Precipitating Convective Systems Accounting for the Summer Rainfall of Tropical and Subtropical South America. Journal of Hydrometeorology 14(1), 25–46.

Rowley, D.B., Pierrehumbert, R.T., Currie, B.S., 2001. A new approach to stable isotope-based paleoaltimetry: implications for paleoaltimetry and paleohypsometry of the High Himalaya since the Late Miocene. Earth Planetary Science Letters 188, 253–268.

Rowley, D.B., Currie, B.S., 2006. Palaeo-altimetry of the late Eocene to Miocene Lunpola basin, central Tibet. Nature 439, 677–681.

Rowley, D.B., Garzione, C.N., 2007. Stable Isotope-Based Paleoaltimetry. Annual Review of Earth and Planetary Sciences 35(1), 463–508.

Rozanski, K., Araguás-Araguás, L., & Gonfiantini, R., 1993. Isotopic patterns in modern global precipitation. Climate change in continental isotopic records, 1-36.

Rubin, D. M., and Hesp, P. A., 2009. Multiple origins of linear dunes on Earth and Titan. Nature Geoscience 2, 653-658.

Ruddiman, W.F., Raymo, M.E., Prell, W.L., Kutzbach, J.E., 1997. The uplift-climate connection: a synthesis, in: Tectonic Uplift and Climate Change. Springer, pp. 471–515.

Ruszkiczay-Rüdiger, Z., Braucher, R., Csillag, G., Fodor, L.I., Dunai, T.J., Bada, G., Bourlés, D., Müller, P., 2011. Dating Pleistocene aeolian landforms in Hungary, Central Europe, using in situ produced cosmogenic ^{10}Be. Quaternary Geochronology 6, 515-529.

Ruthsatz, B., Hofmann, U., 1984. Die Verbreitung von C4-Pflanzen in den semiariden Anden NW-Argentiniens mit einem Beitrag zur Blattanatomie ausgewählter Beispiele. Phytocenologia 12, 219-249.

Sachse, D., Billault, I., Bowen, G.J., Chikaraishi, Y., Dawson, T.E., Feakins, S.J., Freeman, K.H., Magill, C.R., McInerney, F. A., van der Meer, M.T.J., Polissar, P., Robins, R.J., Sachs, J.P., Schmidt, H.-L., Sessions, A.L., White, J.W.C., West, J.B., Kahmen, A., 2012. Molecular Paleohydrology: Interpreting the Hydrogen-Isotopic Composition of Lipid Biomarkers from Photosynthesizing Organisms. Annual Review of Earth and Planetary Sciences 40, 221–249.

Salio, P., Nicolini, M., Saulo, A.C., 2002. Chaco low-level jet events characterization during the austral summer season. Journal of Geophysical Research 107, ACL-32.

Samuels-Crow, K.E., Galewsky, J., Hardy, D.R., Sharp, Z.D., Worden, J., Braun, C., 2014. Convective influences on the isotopic composition of atmospheric water vapor over the tropical Andes. Journal of Geophysical Research: Atmospere 119, 7051–7063.

Saulo, A.C. Seluchi, M.E., Nicolini, B., Aires, B., Previsa, C.D., Paulista, C., 2004. A case study of a Chaco low-level jet event. Monthly Weather Review 132(11), 2669-2683.

Saylor, J.E., Mora, A., Horton, B.K., Nie, J., 2009. Controls on the isotopic composition of surface water and precipitation in the Northern Andes, Colombian Eastern Cordillera. Geochim. Cosmochim. Acta 73, 6999–7018.

Schemmel, F., Mikes, T., Rojay, B., Mulch, A., 2013. The impact of topography on isotopes in precipitation across the Central Anatolian Plateau (Turkey). American Journal of Science 313, 61–80.

Schildgen, T.F., Yıldırım, C., Cosentino, D., Strecker, M.R., 2014. Linking slab break-off, Hellenic trench retreat, and uplift of the Central and Eastern Anatolian plateaus. Earth-Science Review. 128, 147–168.

Seinfeld, J.H., Pandis, S.N., 2012. Atmospheric Chemistry and Physics; From Air Pollution to Climate Change, Atmospheric Chemistry and Physics: from air pollution to climate change. John Wiley & Sons.

Sempere, T., Herail, G., Oller, J., Bonhomme, M.G., 1990. Late Oligocene-early Miocene major tectonic crisis and related basins in Bolivia. Geology 18, 946–949.

Shao, X., Huang, L., Liu, H., Liang, E., Fang, X., 2005. Reconstruction of precipitation variation from tree rings in recent 1000 years in Delingha, Qinghai. Science in China Series D Earth Sciences 48, 939- 949.

Shao, Y., Wyrwoll, K.-H., Chappell, A., Huang, J., Lin, Z., McTainsh, G.H., Mikami, M., Tanaka, T.Y., Wang, X., Yoon, S., 2011. Dust cycle: An emerging core theme in Earth system science. Aeolian Research 2, 181–204.

Sharp, R.P., 1980. Wind-driven sand in Coachella Valley, California: Further data Wind-driven sand in Coachella Valley, California: Further data. Geological Society of America Bulletin 91, 724- 730.

Shin, S.I., Otto-Bliesner, B., Brady, E.C., Kutzbach, J.E., Harrison, S.P., 2003. A Simulation of the Last Glacial Maximum climate using the NCAR-CCSM. Climate Dynamics 20, 127-151.

Silva, G. A. M., Ambrizzi, T., Marengo, J. A., 2009. Observational evidences on the modulation of the South American Low Level Jet east of the Andes according the ENSO variability. Annales geophysicae: atmospheres, hydrospheres and space sciences 27, 645–657.

Small, E.E., Anderson, R.S., Repka, J.L., Finkel, R., 1997. Erosion rates of alpine bedrock summit surfaces deduced from in situ ^{10}Be and ^{26}Al. Earth and Planetary Science Letters 150, 413-425.

Smith, J., Vance, D., Kemp, R. A., Archer, C., Toms, P., King, M., Zárate, M., 2003. Isotopic constraints on the source of Argentinian loess - With implications for atmospheric circulation and the provenance of Antarctic dust during recent glacial maxima. Earth Planetary Science Letters 212, 181–196.

Sobel, E.R., Hilley, G.E., Strecker, M.R., 2003. Formation of internally drained contractional basins by aridity-limited bedrock incision. Journal of Geophysical Research: Solid Earth 108, 1–23.

Sobel, E.R., Strecker, M.R., 2003. Uplift, exhumation and precipitation: tectonic and climatic control of Late Cenozoic landscape evolution in the northern Sierras Pampeanas, Argentina. Basin Research 15(4), 431–451.

Sobolev, S. V., Babeyko, a. Y., 2005. What drives orogeny in the Andes? Geology 33, 617–620.

Spate, A.P., Burgess, J.S., Shevlin, J., 1995. Rates of rock surface lowering, Princess Elizabeth Land, Eastern Antarctica. Earth Surface Processes and Landforms 20, 567-573.

Starck, D., Anzotegui, L.M., 2001. The late Miocene climatic change—persistence of a climatic signal through the orogenic stratigraphic record in northwestern Argentina. Journal of South American Earth Science 14, 763–774.

Stewart, M., 1975. Stable isotope fractionation due to evaporation and isotopic exchange of falling waterdrops: Applications to atmospheric processes and evaporation of lakes. Geophsyical Research 80(9), 1133-1146.

Stier, P., Feichter, J., Kinne, S., Kloster, S., Vignati, E., Wilson, J., Ganzeveld, L., Tegen, I., Werner, M., Balkanski, Y., Schulz, M., Boucher, O., Minikin, A., Petzold, A., 2005. The aerosol-climate model ECHAM5-HAM. Atmoseric Chemistry Physics 5, 1125–1156.

Strecker, M.R., Cerveny, P., Bloom, A.L., Malizia, D., 1989. Late Cenozoic tectonism and landscape development in the foreland of the Andes: Northern Sierras Pampeanas (26-28 S), Argentina. Tectonics 8(3), 517-534.

Strecker, M.R., Alonso, R.N., Bookhagen, B., Carrapa, B., Hilley, G.E., Sobel, E.R., Trauth, M.H., 2007. Tectonics and Climate of the Southern Central Andes. Annual Review of Earth and Planetary Sciences 35, 747–787.

Strecker, M.R., Alonso, R., Bookhagen, B., Carrapa, B., Coutand, I., Hain, M.P., Hilley, G.E., Mortimer, E., Schoenbohm, L., Sobel, E.R., 2009. Does the topographic distribution of the central Andean Puna Plateau result from climatic or geodynamic processes? Geology 37, 643–646.

Sullivan, R., Banfield, D., Bell, J.F., Calvin, W., Fike, D., Golombek, M., Greeley, R., Grotzinger, J., Herkenhoff, K., Jerolmack, D., Malin, M., Ming, D., Soderblom, L. a, Squyres, S.W., Thompson, S., Watters, W. a, Weitz, C.M., Yen, A., 2005. Aeolian processes at the Mars Exploration Rover Meridiani Planum landing site. Nature 436, 58-61.

Sun, J., 2002. Provenance of loess material and formation of loess deposits on the Chinese Loess Plateau. Earth Planetary Science Letters 203, 845–859.

Sun, Y., Tada, R., Chen, J., Liu, Q., Toyoda, S., Tani, A., Ji, J., Isozaki, Y., 2008. Tracing the provenance of fine-grained dust deposited on the central Chinese Loess Plateau. Geophysical Research Letters 35, 1–5.

Takahashi, K., Battisti, D.S., 2007. Processes Controlling the Mean Tropical Pacific Precipitation Pattern. Part I: The Andes and the Eastern Pacific ITCZ. Journal of Climate 20, 3434–3451.

Tapponnier, P., Zhiqin, X., Roger, F., Meyer, B., Arnaud, N., Wittlinger, G., Jingsui, Y., 2001. Oblique stepwise rise and growth of the Tibet plateau. Science 294, 1671-1677.

Thiede, R.C., Bookhagen, B., Arrowsmith, J.R., Sobel, E.R., Strecker, M.R., 2004. Climatic control on rapid exhumation along the Southern Himalayan Front. Earth Planetary Science Letters 222, 791–806.

Thiede, R.C., Ehlers, T.A., 2013. Large spatial and temporal variations in Himalayan denudation. Earth Planetary Science Letters 371, 278–293.

Thompson, L.G., Mosley-Thompsonm, E., Davis, M.E., Bolzan, J.F., Dai, J., Yao, T., Gundestrup, N., Wu, X., Klein, L., Xie, Z., 1989. Holocene-Late Pleistocene climatic ice core records from Qinghai-Tibetan Plateau. Science 246, 274- 477.

Thompson, L.G., Davis, M.E., Mosley-Thompson, E., Lin, P.-N., Henderson, K.A., Mashiotta, T.A., 2005. Tropical ice core records: evidence for asynchronous glaciation on Milankovitch timescales. Journal of Quaternary Science 20, 723-733.

Thomson, B.J., Bridges, N.T. Greeley, R., 2008. Rock abrasion features in the Columbia Hills, Mars. Journal of Geophysical Research 113, 1-13.

Toggweiler, J.R., Russell, J., 2008. Ocean circulation in a warming climate. Nature 451, 286- 288.

Uba, C. E., Strecker, M. R. and Schmitt, A. K., 2007. Increased sediment accumulation rates and climatic forcing in the central Andes during the late Miocene. Geology 35(11), 979–982.

Uno, I., Eguchi, K., Yumimoto, K., Takemura, T., Shimizu, A., Uematsu, M., Liu, Z., Wang, Z., Hara, Y., Sugimoto, N., 2009. Asian dust transported one full circuit around the globe. Nature Geoscience 2, 557-560.

Van Hunen, J., Van Den Berg, A.P., Vlaar, N.J., 2000. A thermo-mechanical model of horizontal subduction below an overriding plate. Earth Planetary Science Letters 182, 157–169.

Vanacker, V., von Blanckenburg, F., Govers, G., Molina, A., Poesen, J., Deckers, J., Kubik, P., 2007. Restoring dense vegetation can slow mountain erosion to near natural benchmark levels. Geology 35, 303–306.

Vandervoort, D.S., Jordan, T.E., Zeitler, P.K., Alonso, R.N., 1995. Chronology of internal drainage development and uplift, southern Puna plateau, Argentine central Andes. Geology 23, 145–148.

Vera, C., Higgins, W., Amador, J., Ambrizzi, T., Garreaud, R., Gochis, D., Gutzler, D., Lettenmaier, D., Marengo, J., Mechoso, C.R., Nogues-Paegle, J., Dias, P.L.S., Zhang, C., 2006. Toward a Unified View of the American Monsoon Systems. Journal of Climate 19, 4977–5000.

Viviroli, D., Archer, D.R., Buytaert, W., Fowler, H.J., Greenwood, G.B., Hamlet, A. F., Huang, Y., Koboltschnig, G., Litaor, M.I., López-Moreno, J.I., Lorentz, S., Schädler, B., Schreier, H., Schwaiger, K., Vuille, M., Woods, R., 2011. Climate change and mountain water resources: overview and recommendations for research, management and policy. Hydrology and Earth System Science 15, 471–504.

Von Blanckenburg, F., Hewawasam, T., Kubik, P.W., 2004. Cosmogenic nuclide evidence for low weathering and denudation in the wet, tropical highlands of Sri Lanka. Journal of Geophysical Research: Earth Surface 109 (F3).

Von Blanckenburg, F., 2005. The control mechanisms of erosion and weathering at basin scale from cosmogenic nuclides in river sediment. Earth and Planetary Science Letters 237, 462–479.

Von Humboldt, A., 1808. Ansichten der Natur mit wissenschaftlichen Erläuterungen, Band 1. ed. Tübingen.

Vuille, M., Bradley, R.S., Werner, M., Keimig, F., 2003. 20th century climate change in the tropical Andes: observation and model results. Advances in Global Chance Research 15, 75–99.

Wan, Z., Zhang, Y., Zhang, Q., Li, Z., 2002. Validation of the land-surface temperature products retrieved from Terra Moderate Resolution Imaging Spectroradiometer data. Remote Sensing of Environment 83(1-2), 163–180.

Wan, Z., 2008. New refinements and validation of the MODIS Land-Surface Temperature/Emissivity products. Remote Sensing of Enviroment 112(1), 59-74.

Wang, X., Dong, Z., Zhang, J., Liu, L., 2004. Modern dust storms in China: an overview. Journal of Arid Environments 58, 559–574.

Wang, Y., Cheng, H., Edwards, R.L., Kong, X., Shao, X., Chen, S., Wu, J., Jiang, X., Wang, X., An, Z., 2008. Millennial- and orbital-scale changes in the East Asian monsoon over the past 224,000 years. Nature 451, 1090- 1093.

Wang, Y., Zhen, J., Zhang, W., Li, S., Liu, X., Yang, X., and Liu, Y., 2012, Cenozoic uplift of the Tibetan Plateau: Evidence from the tectonic-sedimentary evolution of the western Qaidam Basin. Geoscience Frontiers 3, 175-187.

Ward, A.W., Greeley, R., 1984. Evolution of the yardangs at Rogers Lake, California. Geological Society of America Bulletin 95, 829-837.

Washington, R., Todd, M.C., Lizcano, G., Tegen, I., Flamant, C., Koren, I., Ginoux, P., Engelstaedter, S., Bristow, C.S., Zender, C.S., Goudie, a. S., Warren, a., Prospero, J.M., 2006. Links between topography, wind, deflation, lakes and dust: The case of the Bodélé Depression, Chad. Geophysical Research Letters 33, 1-4.

Whipple, K.X., Kirby, E., Brocklehurst, S.H., 1999. Geomorphic limits to climate-induced increases in topographic relief. Nature 401, 39–43.

Whipple, K.X., 2004. Bedrock rivers and the geomorphology of active orogens. Annual Review of Earth and Planetary Sciences 32, 151-185.

Whipple, K.X., Meade, B.J., 2006. Orogen response to changes in climatic and tectonic forcing. Earth Planetary Science Letters 243, 218–228.

Whipple, K.X., 2009. The influence of climate on the tectonic evolution of mountain belts. Nature Geoscience 2, 97–104.

Whipple, K.X., Gasparini, N.M., 2014. Tectonic control of topography, rainfall patterns, and erosion during rapid post-12 Ma uplift of the Bolivian Andes. Lithosphere 6, 251–268.

Wichura, H., Bousquet, R., Oberhänsli, R., Strecker, M.R., Trauth, M.H., 2010. Evidence for middle Miocene uplift of the East African Plateau. Geology 38, 543–546.

Wolfe, S. A., Nickling, W.G., 1993. The protective role of sparse vegetation in wind erosion. Progress in Physical Geography 17, 50–68.

Worden, J., Noone, D., Bowman, K., 2007. Importance of rain evaporation and continental convection in the tropical water cycle. Nature 445(7127), 528–32.

Wu, G., Zhang, C., Zhang, X., Tian, L., Yao, T., 2010. Sr and Nd isotopic composition of dust in Dunde ice core, Northern China: Implications for source tracing and use as an analogue of long-range transported Asian dust. Earth and Planetary Science Letters 299, 409–416.

Wulf, H., Bookhagen, B., Scherler, D., 2010. Seasonal precipitation gradients and their impact on fluvial sediment flux in the Northwest Himalaya. Geomorphology 118, 13–21.

Yao, Y., Liu, W., 2014. Hydrogen isotopic composition of plant leaf wax in response to soil moisture in an arid ecosystem of the northeast Qinghai-Tibetan Plateau, China. Journal of Arid Land 6, 592–600.

Yaofeng, J., Chunchang, H., Jiangli, P., Junjie, N., 2008. Chronology of the Holocene loess-paleosol section and its deposition and pedogenesis on the south of Chinese Loess Plateau. Journal of Geographical Sciences 18, 425-442.

Zeitler, P.K., Meltzer, A.S., Koons, P.O., Hallet, B., Chamberlain, C.P., Kidd, W., Park, S.K., Seeber, L., Bishop, M., Shroder, J., 2001. Erosion, Himalayan Geodynamics, and the Geomorphology of Metamorphism. GSA Today (1), 4–9.

Zhang, W., Appel, E., Fang, X., Yan, M., Song, C., Cao, L., 2012. Paleoclimatic implications of magnetic susceptibility in Late Pliocene–Quaternary sediments from deep drilling core SG-1 in the western Qaidam Basin (NE Tibetan Plateau). Journal of Geophysical Research 117, 1–16.

Zhao, Y., Yu, Z., Chen, F., Ito, E., Zhao, C., 2007. Holocene vegetation and climate history at Hurleg Lake in the Qaidam Basin, northwest China. Review of Palaeobotany and Palynology 145, 275-288.

Zhao, Y., Yu, Z., Liu, X., Zhao, C., Chen, F., Zhang, K., 2010. Late Holocene vegetation and climate oscillations in the Qaidam Basin of the northeastern Tibetan Plateau. Quaternary Research 73, 59-69.

Zhou, J., Xu, F., Wang, T., Cao, a, Yin, C., 2006. Cenozoic deformation history of the Qaidam Basin, NW China: Results from cross-section restoration and implications for Qinghai–Tibet Plateau tectonics. Earth and Planetary Science Letters 243, 195-210.

Zhuang, G., Brandon, M. T., Pagani, M. & Krishnan, S., 2014. Leaf wax stable isotopes from Northern Tibetan Plateau: Implications for uplift and climate since 15 Ma. Earth Planetary Science Letters 390, 186–198.

Zipser, E.J., Liu, C., Cecil, D.J., Nesbitt, S.W., Yorty, D.P., 2006. Where Are the Most Intense Thunderstorms on Earth? Bulletin of the American Meteorological Society 87(8), 1057–1071.